Advances in Planar and Integrated Magnetics

Ouyang, Ziwei

Publication date:
2011

Document Version
Publisher's PDF, also known as Version of record

Technical University of Denmark

Ziwei Ouyang

Advances in Planar and Integrated Magnetics

PhD thesis, October 2011

DTU Electrical Engineering
Department of Electrical Engineering

Ph.D. Thesis

Advances in Planar and Integrated Magnetics

Author:
Ziwei Ouyang

Supervisors:
Michael A. E. Andersen
Ole C. Thomsen

DTU Electrical Engineering
Technical University of Denmark
Ørsteds Plads
Building 349
DK-2800 Kgs. Lyngby
Denmark
www : http://www.elektro.dtu.dk/
Tel : (+45) 45 25 38 00
Fax: (+45) 45 93 16 34

Preface

This PhD project "Advances in Planar and Integrated Magnetics" is carried out under the PhD research program EnergyLabDK at the PhD school, Department of Electrical Engineering, at Technical University of Denmark (DTU), and in close cooperated with Flux A/S, Denmark. During this project, a research visit was carried out at "Electric Power Processing Lab" in Technical University of Delft, the Netherlands.

During this PhD project, I have become deeply indebted and grateful to all of those who has stood by me and helped me throughout this project. Special thanks go to:

- The supervisors Prof. Michael A. E. Andersen and Assoc. Prof. Ole C. Thomsen, for their inspiration, encouragement and endless confidence to me along the way.

- Niels O. Christensen, Jacob L. Philipsen, Ole Poulsen, Thomas Bjõrklund and Erik Matthiesen at Flux A/S, Denmark, for their constructive comments, suggestions and helps.

- All colleagues in DTU Electronics Group for their support and helps, especially Zhe Zhang, Gokhan Sen, and Kristian Lindberg-Poulsen, for their valuable discussions and enjoyable collaboration. Many thanks to group secretary Henriette D. Wolff, for her kindly assistance.

- Søren Petersen for his inspiration and valuable discussions in the integrated inductors with stacked I-core. And also thanks to Henrik Schneider for his encouragement and valuable discussions in the magnetics design.

- Prof. Braham Ferreira at TU Delft, for accepting me as a visiting student at his research group, and Dr. Jelena Popovic and Milos Acanski for their valuable discussions in ultra-thin coupled inductors for flexible PV module.

- My dear family, my wife Haiying Yang, my parents Yongzhong Ouyang and Xinwen Guo, their love and endless support, encouragements during this project.

Abstract

The trend toward high power density, high operating frequency, and low profile in power converters has exposed a number of limitations in the use of conventional wire-wound magnetic component structures. Transformers made of the planar principle eliminate virtually some shortcomings of old-fashioned wire wound types, and thus planar magnetics, has in recent years, become increasingly popular in high frequency power converters.

First, an overview of basic planar magnetics technology used in general dc-dc converters is presented. PCB or flexible PCB windings as a main construction together with planar cores yield a number of advantages over the conventional magnetics. Meanwhile, some limitations of planar magnetics are also introduced.

Secondly, fundamental characteristics of planar magnetics are investigated through winding conduction loss, core loss, leakage inductance and interwinding capacitance. Accordingly, a clear cognition for the intrinsic properties of planar magnetics has been given. Trade-offs is unavoidable in the magnetics design, and thus an analysis of trade-offs is necessary for an optimum design in a high quality dc-dc converter. In addition, an improved interwinding arrangement is proposed to further reduce winding conduction loss, leakage inductance, and even interwinding capacitance.

With the development of multilayer PCB, the integrated magnetics with planar structure can be easily implemented. Hence, planar integrated magnetics technique as a major part of this thesis is investigated. The history and the evolution of integrated magnetics in power converters have been described. It is recalled, that integrated magnetics allows less number of parts, lower volume and cost of the converter, and higher efficiency. Many innovative ideas are proposed and experimentally verified.

- E-I-E core structure with integrated transformers and inductors is applied into the two recent developed dc-dc topologies.
- A new method to integrate the current balancing transformer with common input inductor for the primary-parallel dc-dc converter is proposed.
- A low profile and low cost integrated inductors with stacked I-cores for multiple-phase interleaved dc-dc converters is proposed.
- Ultra-thin coupled inductors design for flexible PV module is introduced. A 1.5-mm thickness integrated coupled inductor with sandwich core structure is under investigation.
- A “four quadrants integrated transformer” utilizing orthogonal flux to decouple the two primary windings has been applied to a dual-input isolated boost dc-dc converter.

Dansk Resumé

Udviklingen i retning af høj effekttæthed, høj switchfrekvens og lav byggehøjde i switchmode strømforsyninger har afsløret en række begrænsninger ved anvendelse af konventionelle, trådviklede magnetiske komponenter. Transformere lavet med planar teknik eliminerer nogle af ulemperne ved gammeldags trådviklede typer, og planar transformatorer er derfor i de seneste år blevet stadig mere populære i switchmode strømforsyninger som arbejder ved høje frekvenser.

Først præsenteres en oversigt over de grundlæggende planar teknologier, som anvendes i almindelighed DC/DC konvertere. PCB eller fleksible PCB viklinger i kombination med planar kerner giver en række fordele i forhold til den konventionelle teknik. Nogle begrænsninger for planar transformatorer bliver også introduceret.

Derefter bliver de grundlæggende egenskaber af planar transformatorer i relation til ledetab i viklinger, kerne tab, sprednings induktans og viklingskapacitet undersøgt. Trade-offs er uundgåelige i magnetiske designs, og der præsenteres derfor en analyse af de trade-offs, som er nødvendige i forbindelse med et optimalt design af en højkvalitets DC/DC konverter. Yderligere introduceres et forbedret viklingsarrangement, som reducerer ledetab, spredningsinduktans og viklekapacitet.

Udviklingen af flerlags PCB har medført at det er blevet relativt nemt at lave integrerede magnetiske komponenter med planar kerner. Da integrerede løsninger åbner mulighed for et lavere komponentforbrug, lavere volumen og kost, samt en højere virkningsgrad udgør en undersøgelse af disse løsningsmetoder en stor del af denne afhandling. Historien og udviklingen af integrerede magnetiske komponenter til brug i switchmode strømforsyninger beskrives og mange innovative idéer bliver foreslået og verificeret eksperimentelt.

- E-I-E kerne struktur med integrerede transformere og induktorer implementeres i to nyligt udviklede DC/DC topologier.
- En ny metode til integrering af den strømtransformator, som anvendes i primær parallelkoblede DC/DC konvertere med fælles indgangsspole, demonstreres.
- En kost effektiv, lav profil integreret induktor med stablede I-kerner til brug i flerfasede DC-DC konvertere er demonstreres.
- Et design med ultra-tynde koblede spoler til et fleksibelt PV modul introduceres. En 1,5 mm tyk integreret koblet induktor med sandwich kerne struktur undersøges.
- En "fire kvadrant integreret transformator", som benytter ortogonal fluks til at undgå magnetisk kobling mellem to primærviklinger, implementeres på en dual-input, isoleret boost DC/DC konverter.

Table of Contents

Chapter 1: Introduction

1.1 Scope

The scope of this thesis is to present the research work obtained in the PhD project "Planar Magnetics for High Grade Converter," carried out during the period from December 2008 through October 2011. Many of the scientific results of the research have been published in form of peer reviewed conference papers, journal papers as well as patent applications. The publication list during this PhD study has been included in appendix A and selected publications form a major part of this thesis and are included in appendix B [B1]-[B11].

The objective of this thesis is to supplement the already published information and thereby present a more coherent and complete overview of the research work and results obtained in the project.

Furthermore, the thesis condenses a large number of advanced knowledge of magnetics design and magnetics integration in power electronics. It is a hope that the thesis is useful to those power engineers who are about to use planar magnetics.

1.2 Background and Motivation

From the late 1800s, when theatres wanted a method of dimming their new lighting systems, to the mid 1900s when people wanted to be able to control the speed of their model train sets, right through to modern day telecommunication applications, people have needed a means of controlling voltage from a standard mains supply. These systems have come a long way since the manual operated systems of the 1800s, but the basic concept of the transformer and inductor has always been integral to the development of electrical and electronic sub-systems.

Nowadays, high efficient and high power density converter is fundamental to continued profitable growth of the telecommunications, automotive, aerospace and data processing industries and of many others. For safety reasons, transformers must invariably be incorporated, to galvanically isolate with other equipments, as well as to adapt the output voltage to the proper level. In the past, operating frequencies above 20-kHz were precluded by the non-availability of suitable switching transistors. Now, with power MOSFETs (Metal-Oxide Semiconductor Field-Effect Transistor) capable of converting power at frequencies well above 500-kHz, the major obstacles to ongoing performance improvements in power supplies are the limitations inherent in conventional "wire-wound-on-a-bobbin" transformers and companion inductors. Transformers made of the planar principle such as copper foil lead frames, printed

circuit boards (PCB) or flexible PCB yield a host of benefits over the conventional transformer (the advantages of planar construction will be discussed in Chapter 2), and thus eliminate virtually some shortcomings of old-fashioned wire wound types. At present, planar magnetics has been widely used in modern power converters, particularly for brick dc-dc converters.

Furthermore, with the development of modern power electronics requiring higher power density and higher efficiency dc-dc converters, DTU and Flux A/S have a clear vision of the vital role of integrated magnetics (IM) technique with planar techniques. The shared vision of the partners is that new planar integrated magnetics (PIM) designs will enable unprecedented performance of dc-dc power converters, thereby creating a unique and highly competitive solution for certain markets, such as the automotive, aerospace and renewable energy sectors.

1.3 Project Objectives

- Planar magnetics have been touted as intrinsic advantages to winding conduction loss and leakage inductance, especially by some commercial companies. In fact, the low winding conduction loss and leakage inductance are not intrinsic properties of planar structures. This research will give a clear cognition for intrinsic properties of planar magnetics.
- Like a conventional magnetics design, the optimal design and trade-offs for planar magnetics also need to be investigated in order to pursue a high efficiency and low profile dc-dc converter. Hence, detailed analysis for winding conduction loss, core loss, leakage inductance and interwinding capacitance is also one of the research objectives.
- Integrated magnetics technique can reduce the number of parts and the volume of converter, and may even increase the power efficiency. As the rapid development of multi-layer PCB and thick copper PCB techniques, the integrated magnetics with PCB windings becomes a possible and easier implementation for embedded dc-dc converters. Emphasis on planar integrated magnetics will be major objective of this research.

1.4 Thesis Structure and Content

The structure, organization and content of this PhD thesis is visualized in the flow chart presented in Fig. 1-1 and Fig.1-2. The selected published or peer-reviewed journal papers, conference papers and patent applications are also illustrated in the two flow charts. The purpose of this report is therefore to complement the already published papers by providing a condensed and coherent presentation of the overall project and

related results. Special focus will be devoted to present a coherent derivation of the key fundamental theoretical aspects of this project.

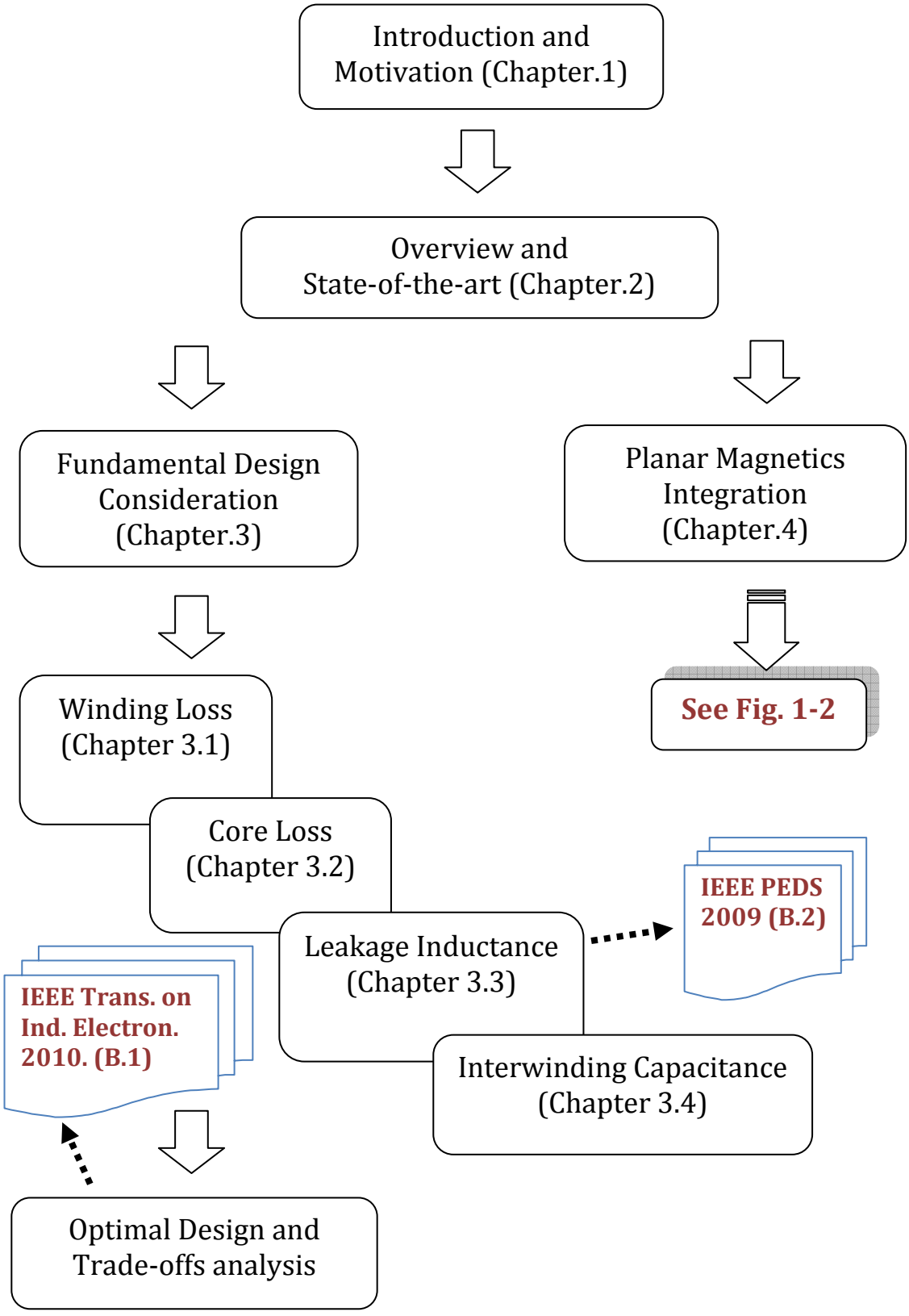

Fig. 1-1: PhD thesis structure and work contents (1)

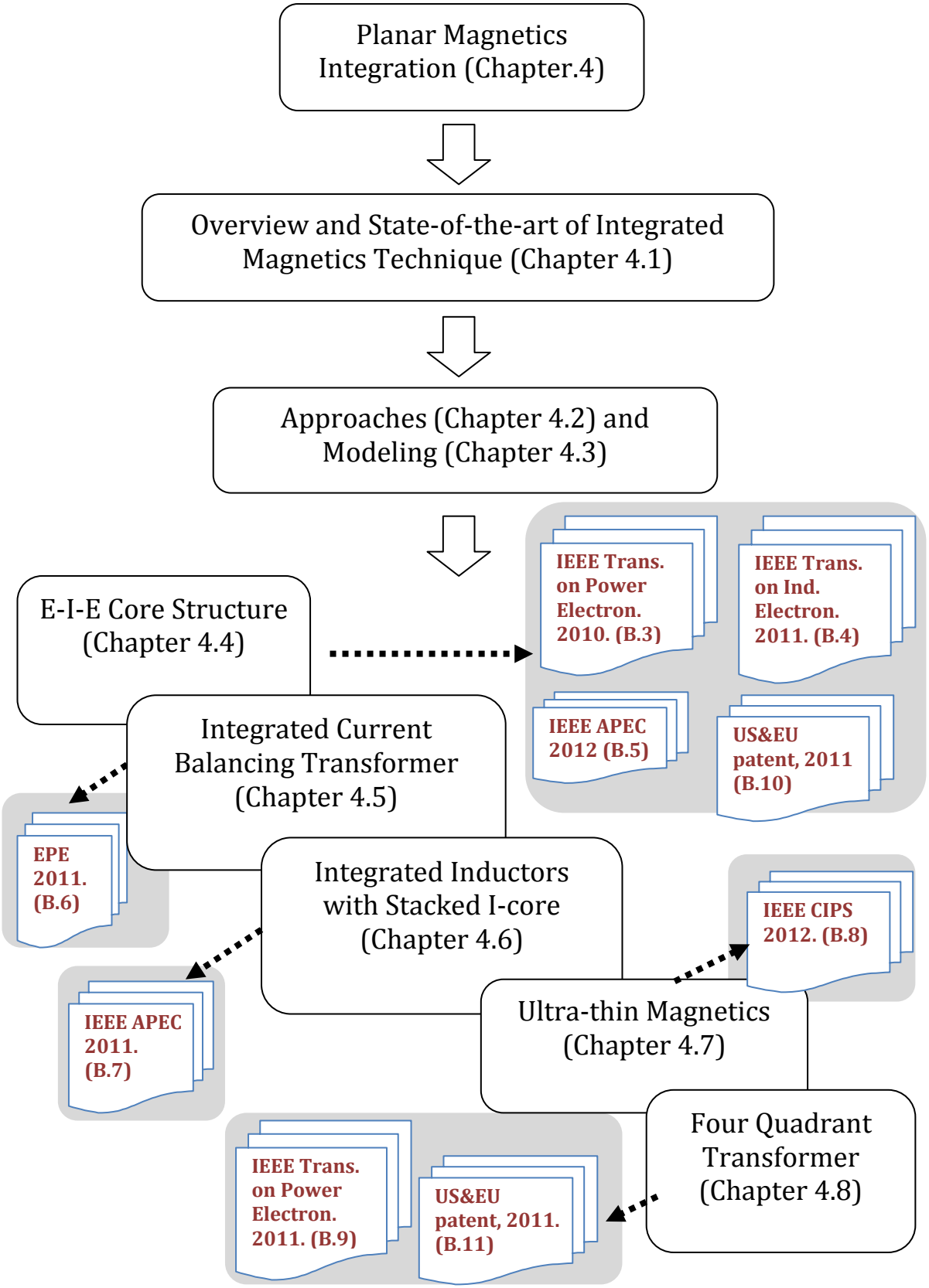

Fig. 1-2: PhD thesis structure and work contents (2)

Chapter 2: State-of-the-Art

2.1 Overview of Planar Magnetic Technology

The trend toward high power density, high operating frequency, and low profile in power converters has exposed a number of limitations in the use of conventional wire-wound magnetic component structures. In recent years, planar magnetics has become increasingly popular in high frequency power converters because of the unique advantages they achieve in terms of low profile, excellent thermal characteristic, extremely good repeatability, modularity, easy manufacturing and winding integration with PCB (print circuit board) based [2.1]–[2.5].

Nowadays, there are several different techniques to construct planar windings as shown in Fig. 2-1. The planar-wound structures are generally created by laminating planar copper windings and disk-like dielectrics into multilayer PCB that are enclosed by a flat magnetically permeable core. Manufacturing cost of embedded planar magnetics in a PCB-assembled power converter has been substantially reduced by introducing flexible-foil PCB (FPCB) to create the windings without increasing the remaining number of rigid PCB layers [2.1]. In order to handle a high current, thicker stamped copper turns are typically used in the planar structure as well.

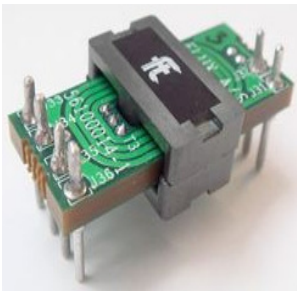

(a) Multilayer PCB winding.
Ref. [2.28]

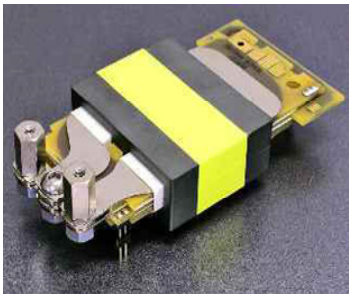

(c) Hybrid of PCB and stamped copper foil.
Search from Google

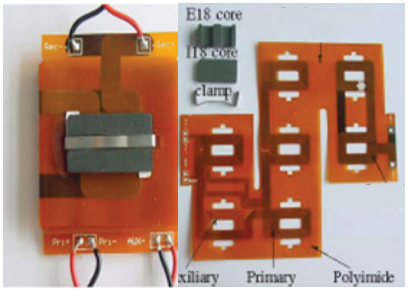

(e) Flexible PCB winding.
Ref. [2.1]

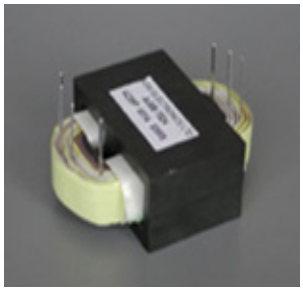

(b) Vertical winding with planar core.
Search from Google

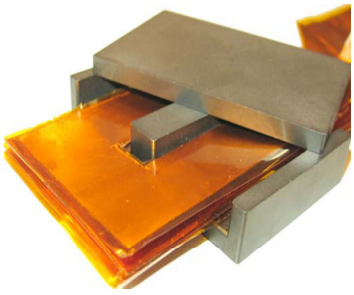

(d) Copper foil windings
Ref. [2.29]

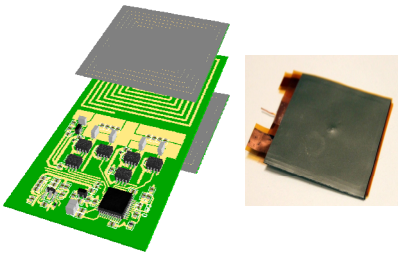

(f) Ultra-thin magnetics
Ref. [2.30]

Fig.2-1: Different techniques for implementation of planar windings.

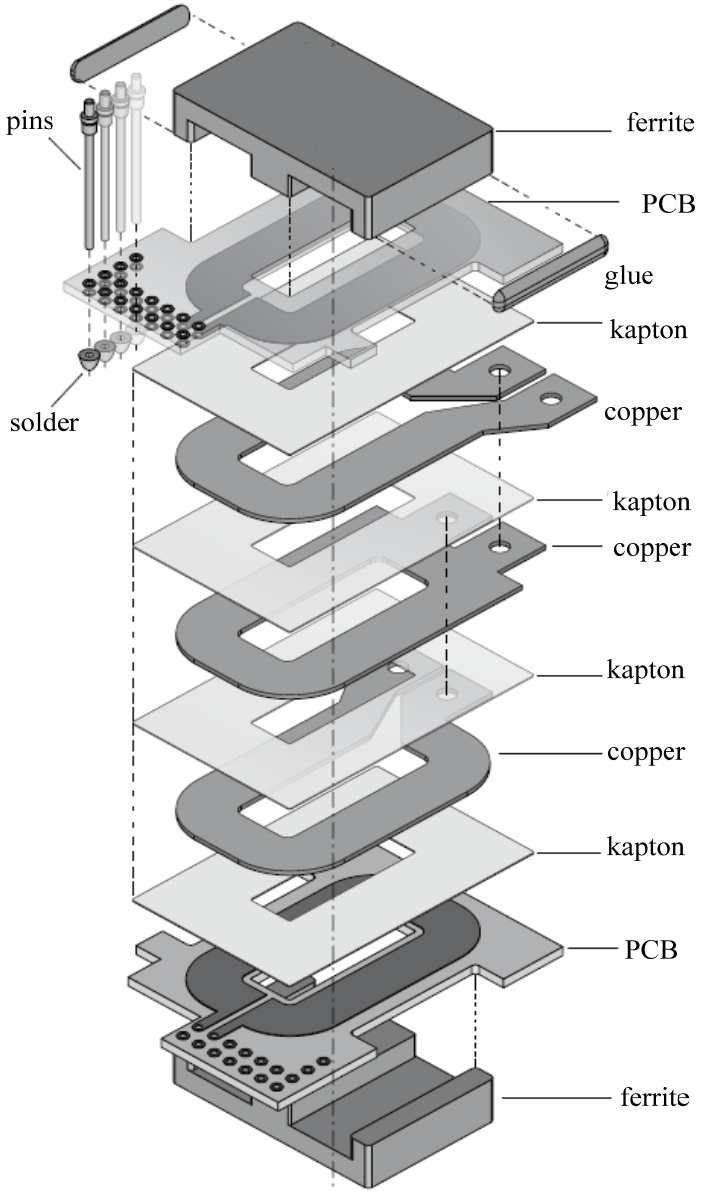

Fig. 2-2: Structure of a hybrid winding transformer.

Fig. 2-2 shows an unlaminated structure of hybrid winding transformer. The pair of low profile geometries with ferrite material is used as magnetic core of the transformer. PCB winding and stamped copper turns are used for primary or secondary windings respectively. In general, the handling current in PCB winding is smaller than thicker stamped copper turn. With recent development in PCB technology, the thick copper winding from 3-oz to 16-oz is possible to be laminated with PCB prepreg. The polyimide films (Kapton) are used in each layer to prevent the short circuit. Meanwhile, its characteristics of wide range temperatures and high voltage stress are attractive to transformer applications.

Compact and high-efficient power conversion is critical to the miniaturization of computer, telecommunication, vehicle and other industrial and military systems. Planar

magnetics have intrinsically much lower profile than conventional wire wound devices, which aids miniaturization. Fig. 2-3 shows some available commercial products using planar magnetics technology within the current industrial market, and planar magnetics technology can be applied to the industrial products from micro-system to kilo-watts system.

(a) 120 W Eighth-brick DC-DC Converter
Ref. [2.31]

(b) 400 W Half-brick DC-DC Converter
Ref. [2.32]

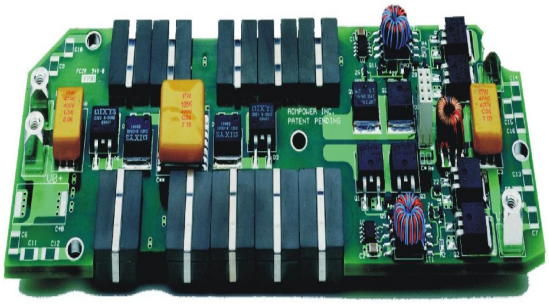

(c) 1 kW DC-DC Converter
Ref. [2.33]

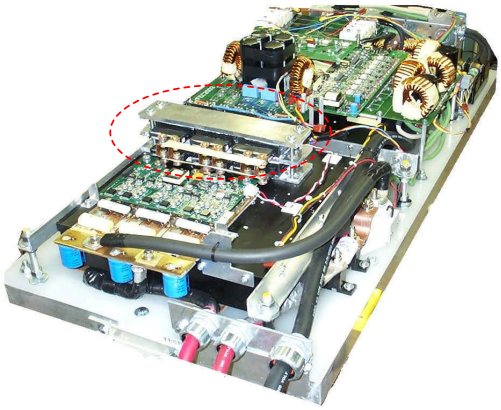

(d) 10 kW DC-DC Converter
Ref. [2.34]

Fig. 2-3: Industrial products with planar magnetics technology.

Recent published literature primarily in the form of journal papers, conference papers, international patents and tutorial notes, has been searched and analyzed to establish the present state-of-the-art. Research leading to planar magnetic components has been carried out since the 1960's [2.6]. The earlier research on planar magnetics mainly focused on the thin-film technology specific for integrated circuit (IC) design [2.6]-[2.8]. The early 90's saw many investigations into the characteristics, modeling and optimization of planar magnetics [2.9]-[2.11]. In recent years, with the development of PCB manufacture technology, research on miniature power converter with planar magnetics technology has attracted widespread international attention [2.1]-[2.3], [2.12]-[2.19]. Since planar structure performs a new concept in magnetics design and changed winding arrangements and core geometries can be extensively used to many different applications, a large number of international patents related to planar

magnetics have been invented in recent years [2.20]-[2.25]. Center of Power Electronics Systems (CPES) of Virginia Tech, Electrical Power Processing (EPP) group of Delft University of Technology, etc. are the leading universities in the world for the advanced planar magnetics integration and packaging technologies. Payton Planar Magnetics Ltd. is the world leader in developing and manufacturing of planar magnetic components. Delta Electronics Inc. and Emerson Network Power Inc. represent the state of the art for industrial power converters using planar magnetic components.

2.2 Advantages and Disadvantages

The advantages of planar magnetic components over conventional wire-wound components are as follows:

- **Low profile** — planar magnetic devices have intrinsically much lower profile than conventional wire-wound devices, which aids miniaturization. Typically, the height of a planar magnetic device is 25% to 50% less than its wire-wound counterpart.
- **Good thermal characteristic and high power density** — planar magnetic cores tend to have a higher surface-to-volume ratio than conventional magnetic cores. As a result, they are more effective at conducting heat and tend to have low thermal sensitivities compared with conventional wire-wound devices. Fig. 2-4 shows thermal comparison between conventional core and planar core. In order to make a fair comparison, the two cores have the same volume, the cross-section and the window area. 2-W power losses are dissipated in both cores and the same size aluminum plates are used. The simulations are operated under the same conditions where ambient temperature is 30°C and nature heat convection and radiation are used. It is obvious that planar core has a better thermal behavior than the conventional core. These heat removal benefits again add greatly to the power densities, particularly at frequencies ranging from 100-kHz up to several MHz.

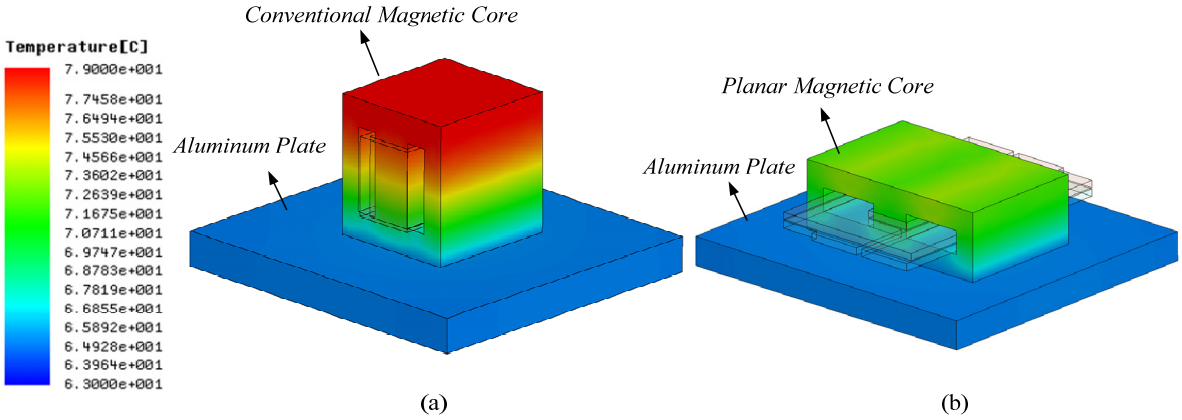

Fig. 2-4: Thermal comparison between (a) conventional core and (b) planar core.

- **Ease of manufacturability and cost reduction** — since manual steps or complex automatic steps such as winding are removed, and PCB techniques are easily adapted for mass production.
- **Unrivalled repeatability** — planar components are made from pre-formed assemblies, thus the assembly process itself has only a few stages. This simplification of assembly allows planar magnetics to be manufactured with very high repeatability and with increased accuracy.
- **Modularity —** since PCB winding are used for the planar magnetic devices, the semiconductors and other passive components can also be assembled into the PCB surfaces and thus no extra connections are required.
- **Ease of implementation on interleaved winding** — since multi-layer PCBs allow the interconnection of arbitrary layers, interleaved primary and secondary windings can be implemented much more easily than in conventional magnetics. This provides a significant reduction on leakage inductance and high frequency winding losses.

The characteristics of planar magnetics are, of course, not all advantageous. They have some limitations such as:

- **Large footprint** — large surface area offered by the flatter cores used in planar devices. On the other hand, if the core window width is fully utilized, almost one third of PCB windings area will be exposed to the ambient air due to the PCB windings are situated in the horizontal direction, which also contributes a portion of the large footprint.
- **Low copper fill factor** — if PCB is used to implement planar windings, the copper fill factor is typically low this is due to the fact that minimum inner-turn spacing of 150-μm and dielectric thickness of 100-μm are required. Copper on a thin flexible polymer substrate gives an improved fill factor, as the dielectric thickness can be made as low as 50-μm**.** Many layers of flexible circuit can be laminated together resulting in a similar structure to a rigid PCB but with higher fill factor.
- **Limited number of turns —** a low copper fill factor gives a limited number of turns for PCB winding. Furthermore, increased number of turns requires an increased number of layers, unless reducing the winding width at the expense of dc resistance. This is not a cost–effective way to implement the PCB winding because the cost of PCB manufacturing rises rapidly with increasing number of layers.
- **High interwinding capacitance** — windings stacked closely provides an increased interwinding capacitance, and PCB windings have intrinsically larger

surface area than conventional wire-winding which further increases the interwinding capacitance.

2.3 Use of PCB, flexible PCB and stamped copper turns

Besides the aforementioned advantages of PCB winding such as unrivalled repeatability, modularity, ease of implementation on interleaved winding etc, the PCB itself has matured far beyond its initial purpose of electrical interconnection: it allows passives integration of electromagnetic functionality by implementing enhanced substrate materials [2.26], allows packaging in 3-D power converters by using flexible PCB [2.1], and also enhances thermal management by means of thermally conducting layers in intimate contact with the heat source [2.27].

Flexible PCB can improve the copper fill factor in the planar magnetics due to a thin polymer substrate. Meanwhile, it can facilitate the use of "z-folding" technique to implement a large number of layers without the need for vias or soldering for layer interconnections**.**

Stamped copper turn provides a cost-effective way to implement high current, thick and single-turn windings. The main disadvantages are that insulation layers must be separately applied and extra terminations for layer interconnections are required.

2.4 Summary

This chapter has established the present state-of-the-art of planar magnetics technology according to literatures' review. Currently, PCB and FPCB winding technologies are widely used for the miniaturization of power converters. Stamped copper turns and its hybrid structure with PCB winding are usually used for high current applications. The advantages and disadvantages of planar magnetics have been presented. And other important parameters for planar magnetics including ac resistance, leakage inductance and interwinding capacitance will be discussed in Chapter 3. Since PCB winding is advantageous to magnetics integration, an emphasis on planar integrated magnetics will be presented in Chapter 4.

2.5 Reference

[2.1] E. de Jong, J. Ferreira, and P. Bauer, "Toward the next level of PCB usage in power electronic converters," *IEEE Trans. Power Electron.*, vol. 23, no. 6, pp. 3153–3163, Nov. 2008.

[2.2] C. Quinn, K. Rinne, T. O'Donnell, M. Duffy, and C. O. Mathuna, "A review of planar magnetic techniques and technologies," in *Proc. IEEE Appl. Power Electron. Conf. Expo.,* 2001, pp. 1175–1183.

[2.3] C. Buccella, C. Cecati, and F. deMonte, "A coupled electrothermal model for planar transformer temperature distribution computation," *IEEE Trans. Ind. Electron.*, vol. 55, no. 10, pp. 3583–3590, Oct. 2008.

[2.4] J.-P. Schauwers, C. Nunes, B. Velaerts, F. Robert, and P. Mathys, "Planar transformer technology applied to AC/DC conversion," in *Proc. IEEE Telecommunication Energy Conf., (INTELEC)*, 1999.

[2.5] M. T. Quirke, J. J. Barrett, and M. Hayes, "Planar magnetic component technology-a review," *IEEE Trans. Components, Hybrids, and Manufacturing Technology*, vol. 15, no. 5, pp.884-892, Oct. 1992.

[2.6] A. Olivei, "Optimized miniature thin-film planar inductors, compatible with integrated circuits," *IEEE Trans. Parts, Materials and Packaging*, vol. 5, no. 2, pp. 71- 88, Jun 1969.

[2.7] K. Kawabe, H. Koyama, K. Shirae, "Planar inductor," *IEEE Trans. Magn.*, vol. 20, no. 5, pp.1804- 1806, Sep. 1984.

[2.8] O. Oshiro, H. Tsujimoto, K. Shirae, "A novel miniature planar inductor," *IEEE Trans. Magn.*, vol.23, no.5, pp. 3759- 3761, Sep 1987.

[2.9] L. Heinemann, "Modelling and design of high frequency planar transformers," in *Proc. IEEE Power Electron. Spec. Conf.*, 1995, pp.651-657.

[2.10] N. Dai, A. W. Lofti, C. Skutt, W. Tabisz, and F. C. Lee, "A comparative study of high-frequency, low-profile planar transformer technologies," in *Proc. IEEE Appl. Power Electron. Conf. Expo.*, 1994, pp.226-232.

[2.11] D. van der Linde, C. A. M. Boon, and J. B. Klaassens, "Design of a high-frequency planar power transformer in multilayer technology," *IEEE Trans. Ind. Electron.*, vol. 38, no. 2, pp.135-141, Apr. 1991.

[2.12] R. Prieto, J. A. Cobos, O. Garcia, P. Alou, and J. Uceda, "Using parallel windings in planar magnetic components," in *Proc. IEEE Power Electron. Spec. Conf.*, 2001, pp.2055-2060.

[2.13] S. C. Tang, S. Y. R. Hui, H. S.-H. Chung, "A low-profile power converter using printed-circuit board (PCB) power transformer with ferrite polymer composite," *IEEE Trans. Power Electron.,* vol. 16, no. 4, pp.493-498, Jul. 2001.

[2.14] W. Chen, Y.-P. Yan, Y.-Q. Hu, and Q. Lu, "Model and design of PCB parallel winding for planar transformer," *IEEE Trans. Magn.*, vol. 39, no. 5, pp. 3202–3204, Sep. 2003.

[2.15] L. Dalessandro, N. Karrer, J. W. Kolar, "High-performance planar isolated current sensor for power electronics applications," *IEEE Trans. Power Electron.,* vol. 22, no. 5, pp.1682-1692, Sept. 2007.

[2.16] A. Prasai, W. G. Odendaal, "Fabrication and modeling of a planar magnetic structure with directly etched windings," in *Proc. IEEE Energy Convers. Congr. Expo.,* 2009, pp. 1895-1902.

[2.17] R. Prieto, J. A. Oliver, J. A. Cobos, M. Christini, "Magnetic component model for planar structures based on transmission lines," *IEEE Trans. Ind. Electron.*, vol. 57, no. 5, pp.1663-1669, May 2010.

[2.18] A. W. Roesler, J. M. Schare, S. J. Glass, and K. G. Ewsuk, G. Slama, D. Abel, and D. Schofield, "Planar LTCC transformers for high-voltage flyback converters," *IEEE Trans. Compon. Packag. Technol.*, vol. 33, no. 2, pp.359-372, June 2010.

[2.19] C. Panchal and J.-W. Lu, "High frequency planar transformer (HFPT) for universal contact-less battery charging platform," *IEEE Trans. Magn.*, vol. 47, no. 10, pp.2764-2767, Oct. 2011.

[2.20] R. S. Downing, G. I. Rozman, "Planar magnetics with integrated cooling," U.S. patent, 6278353, Aug. 21, 2001.

[2.21] G. Raghavan, M. G. Case, "Symmetric planar inductor," U.S. patent, 0077992, Apr. 14, 2005.

[2.22] C.-G. Cheng, "Low-profile planar transformer," U.S. patent, 7414510, Aug. 10, 2008.

[2.23] G. B. Koprivnak, T. D. Williams, “Planar transformer and method of manufacturing,” U.S. patent, 0079229, Apr. 1, 2010.

[2.24] P. Clayton, “Integrated planar transformer and inductor assembly,” U.S. patent, 6320490, Nov. 20, 2010.

[2.25] W. Herhold, “Planar transformer,” U.S. patent, 0140824, Jun. 16, 2011.

[2.26] E. Waffenschmidt and J. Ferreira, “Embedded passives integrated circuits for power converters,” in *Proc. IEEE Power Electron. Spec. Conf.*, 2002, pp.12–17.

[2.27] E. de Jong, J. Ferreira, and P. Bauer, “Improving the thermal management of AC-DC converters using integration technologies,” in *Proc. IEEE Ind. Appl. Conf.*, 2004, pp. 2315–2322.

[2.28] Flux A/S, Denmark, http://www.flux.dk

[2.29] E. J. Meurer and S. W. H. de Haan, "On the common mode resonant frequency of transformers," in *Proc. European Power Electronics (EPE),* pp.1-6, Sept. 2007.

[2.30] M. Acanski, Z. Ouyang, J. Popovic-Gerber and J. A. Ferreira. “Design of very low profile coupled inductors for PV module integrated converters,” in *Proc. IEEE Integrated Power system (CIPS),* Germany, March, 2012.

[2.31] Delta Electronics Inc., http://www.delta.com.tw

[2.32] Emerson Network Power Inc., http://www.powerconversion.com

[2.33] I. D. Jitaru, “Technology trends in automotive power,” Tutorial notes, APEC, 2011.

[2.34] C. Smith, “Simulation for fuel cell inverter using SIMPLORER and SIMULINK,” Ansoft Power Simulation Workshop, Oct. 2003.

Chapter 3: Design Considerations

3.1 Winding Conduction Loss

3.11 Transformer Winding Loss

The use of higher switching frequency results in a size reduction of passive component. As the same as the conventional magnetic structures, the demand of high frequency operation also causes increased winding losses in planar magnetic structures due to the skin and the proximity effects. In general, old-fashioned wire wound transformer has a high dc resistance due to a small diameter is used to avoid the high frequency eddy current effects (the diameter is chosen around skin depth), and thus operates at low power level. However, copper foil has a higher ratio of width to thickness and thus contributes a low dc resistance without compromising high frequency eddy current effects when the thickness is chosen around skin depth. Therefore, from this point, planar magnetics are more suitable for high frequency and high power converters than the old-fashioned wire wound magnetics. Of course, copper foil can also be vertically mounted in traditional core geometries.

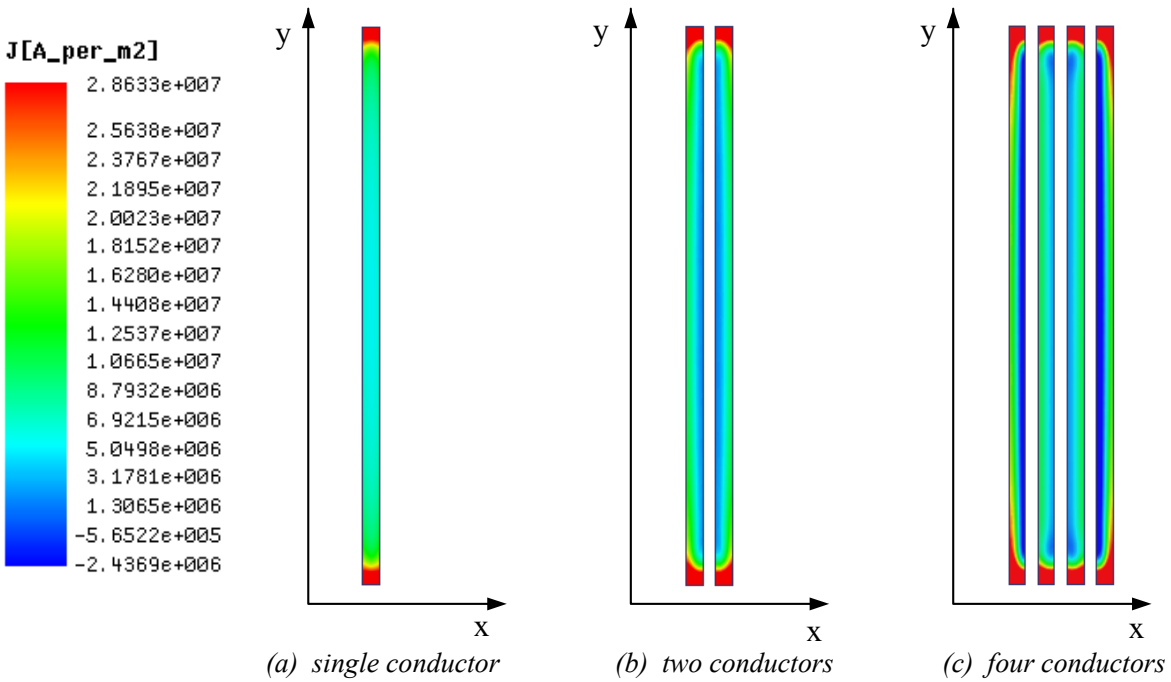

Fig. 3-1: Current density distribution in a single conductor and multiple conductors.

Winding losses are dramatically increased with high frequency due to eddy current effects. For design and optimization of transformers, there is a need for an accurate prediction of the winding losses over a wide frequency range and various winding

arrangements. Eddy current losses, including skin effect and proximity effect losses, seriously impair the performance of transformers in high-frequency power conversion applications. For ac current flowing in a conductor, the alternating field inside this conductor induces eddy currents in the conductor, which produces a field that tends to cancel the field produced by the original current. The tendency of the alternating current distributes itself within the conductor, so that the current density near the surface of the conductor is greater than that at its center. This is called skin effect, which causes the effective resistance of the conductor to be increased with the frequency of the ac current. The proximity effect is similar, but it is caused by the current carried by an adjacent conductor. The current in the adjacent conductor causes a time-varying field and induces a circulating current inside the conductor. Both the skin effect and the proximity effect cause the current density to be nonuniform in the cross section of the conductor and thus cause a high winding resistance at high frequency. Fig. 3-1 shows current density distribution in a single conductor and multiple conductors. The FEA simulation is carried out under Cartesian XY plane with eddy current solution and each conductor is excited with same currents. For a single conductor, the current flows to the two ends of conductor due to the skin effect. For the multiple conductors, the currents of conductors trend to the surface along the y-axis. This is due to the proximity effect caused by adjacent conductors, effectively enhancing the skin effect in an individual conductor.

Many efforts have been made to derive expressions allowing for an accurate representation of frequency behavior of ac resistance. The ac resistance effects due to high frequency currents are specifically tailored for transformers by Dowell [3.1]. This work is based on a 1-D solution of the diffusion equation, as applied to conducting parallel plates. Dowell's results apply only to winding portions. A winding portion is defined as a part of a transformer winding which, when examining the low-frequency magnetic-field-intensity diagram, extends in either direction along the axis of winding height from a position of zero field intensity to the first positive or negative peak of magnetic field intensity. This particular approach, being one dimensional in rectangular coordinates, is in principal applicable to foil conductors having a magnetic field parallel to the conductor surface, and is therefore subject to certain restrictions:

- The magnetic flux in the core window (leakage flux) is assumed to parallel to the foil conductor surface.
- The approach cannot be applied to the inductor design where the energy storage is included, as it results in a magnetic field component that is not parallel to the foil conductor surface.
- Voltages and currents excitations in both windings are sinusoidal.
- Twisted-wire bundles or Litz wire cannot be applied. And the effect of a partial layer, which spans substantially less than the core window breadth, is not considered.

- Infinite long solenoid windings are assumed. When the windings fill the window length completely, or the distances between consecutive turns, between adjacent layers and between the conductor edge and the magnetic core are small, the resultant field equivalently approaches that of infinite solenoid windings.
- The curvature of the conductors is neglected.

Until now, most of the literatures discussed for the high-frequency winding loss of transformers are based upon Dowell's work in 1966. Perry analyzes a general N-layer solenoid and derives winding loss expressions for each rectangle foil layer in 1979 [3.2]. Venkatraman applies Dowell's results to nonsinusoidal excitation using Fourier analysis in 1984 [3.3]. Vandelac and Ziogas's work incorporates aspects of Dowell and Venkatraman to extend Perry's analysis in 1987 [3.4]. Ferreira, in 1994, rewrites Perry's equation and proposes that the orthogonality between the skin effect and proximity effect which makes a more generalized approach for the analytical solution of ac resistance in transformer windings [3.5]. In 2000, Hurley presents a new formula for the optimum foil or layer thickness, without the need for Fourier coefficients and calculations at harmonic frequencies with arbitrary current waveforms [3.6]. All aforementioned efforts are based on one-dimensional method for calculating the ac resistance of multilayer windings. A squared-field-derivative (SFD) method proposed by Sullivan allows calculating losses in multi-winding transformers with 2-D and 3-D field effects and arbitrary waveforms in each winding [3.7].

Planar magnetics feature flat rectangle copper windings with a higher ratio of the width to the thickness of the conductors. The most commonly used expression for its ac resistance of the mth layer is derived as [3.5],

$$\frac{R_{ac,m}}{R_{dc,m}} = \frac{\varepsilon}{2} \cdot \left[\frac{\sinh \varepsilon + \sin \varepsilon}{\cosh \varepsilon - \cos \varepsilon} + (2m-1)^2 \cdot \frac{\sinh \varepsilon - \sin \varepsilon}{\cosh \varepsilon + \cos \varepsilon} \right] \tag{3-1}$$

where ε is an effective thickness of skin depth and defined as h/δ, h is the thickness of conductor and δ is the skin depth at a certain frequency. m is treated as a winding portion and defined as a ratio,

$$m = \frac{F(h)}{F(h) - F(0)} \tag{3-2}$$

where $F(0)$ and $F(h)$ are magneto motive forces (MMFs) at the limits of a layer surface. The first term in (3-1) describes the skin effect factor and the second term represents the proximity effect factor. The proximity effect loss, in a multilayer winding, may strongly dominate over the skin effect loss, depending on the value of m, which relates to the winding arrangements. Interleaved windings technology can significantly reduce the

proximity loss when the primary and secondary currents are in phase. A detailed analysis of the ac resistance and optimum thickness for interleaved windings arrangement in planar transformers can be found in [B.1]. Although the expression (3-1) can provide relatively good results in a certain frequency range, accurate results are still limited by the aforementioned Dowell's restrictions, particularly for sinusoidal excitations. In addition, the vias are a necessity of PCB windings, which also contribute ac resistances at high frequency. Considering these limitations, it is advisable to determine winding losses with Finite Element Analysis (FEA) simulations.

3.12 Inductor Winding Loss

From the Dowell's restriction, the 1-D based equation (3-1) is not valid for the 2-D calculation such as gapped inductors. This is due to the fact that external flux through the conductors has to be considered. This external flux is caused by the fringing field of air gaps, which further increases the eddy current effect inside the conductors. Hereby, besides the skin effect loss and proximity effect loss, an excessive power loss caused by the fringing field should be considered for gapped inductors. For transformers, it is relatively straightforward to understand the magnetic field and the resultant losses. However, for inductors, the magnetic field configuration is influenced by the core geometry, the position of air gaps and the position of conductors. A number of authors have addressed the problem of fringing field losses at high frequencies for planar magnetics [3.8]-[3.14]. The most outstanding work, [3.13] and [3.14], as a calculation method of the fringing field for planar inductors is recommend here. The fringing field is divided into two components, x component H_x and y component H_y. For the planar windings situated in horizontal direction, the x component is parallel to the wide surface of the conductors and the y component is perpendicular to it. Both x and y components induce the currents flowing toward the edges of conductor in order to exclude the external flux. The fringing field loss caused by the x component is small since the thickness of conductor is close to the skin depth. However, the fringing field loss caused by the y component is much higher due to a high ratio of the width to the thickness. An orthogonal winding structure is accordingly used in [3.15] to reduce the fringing field loss caused by the y components. An inductive sheet placed around the airgap of a ferrite core is shown to reduce the fringing effect in [3.12]. The inductive sheet replaced by an open-circuit copper screen can also reduce the winding loss [3.16]. Tapered-winding structure is used to keep the conductors out of the "keep-away regions" in order to minimize the fringing loss [3.17].

Fig. 3-2 shows FEA results of fringing effect for different formats of air gaps. The same inductances are required in order to make a fair comparison. Case-1 shows a 0.5-mm air gap used in the center leg and Case-2 represents two 0.5-mm air gaps situated at the outer legs of the core. Case-3 has distributed air gaps in the center leg with 5 interval 0.1-mm gaps, and all legs with 0.25-mm air gaps is shown in Case-4. Case-5 constructs

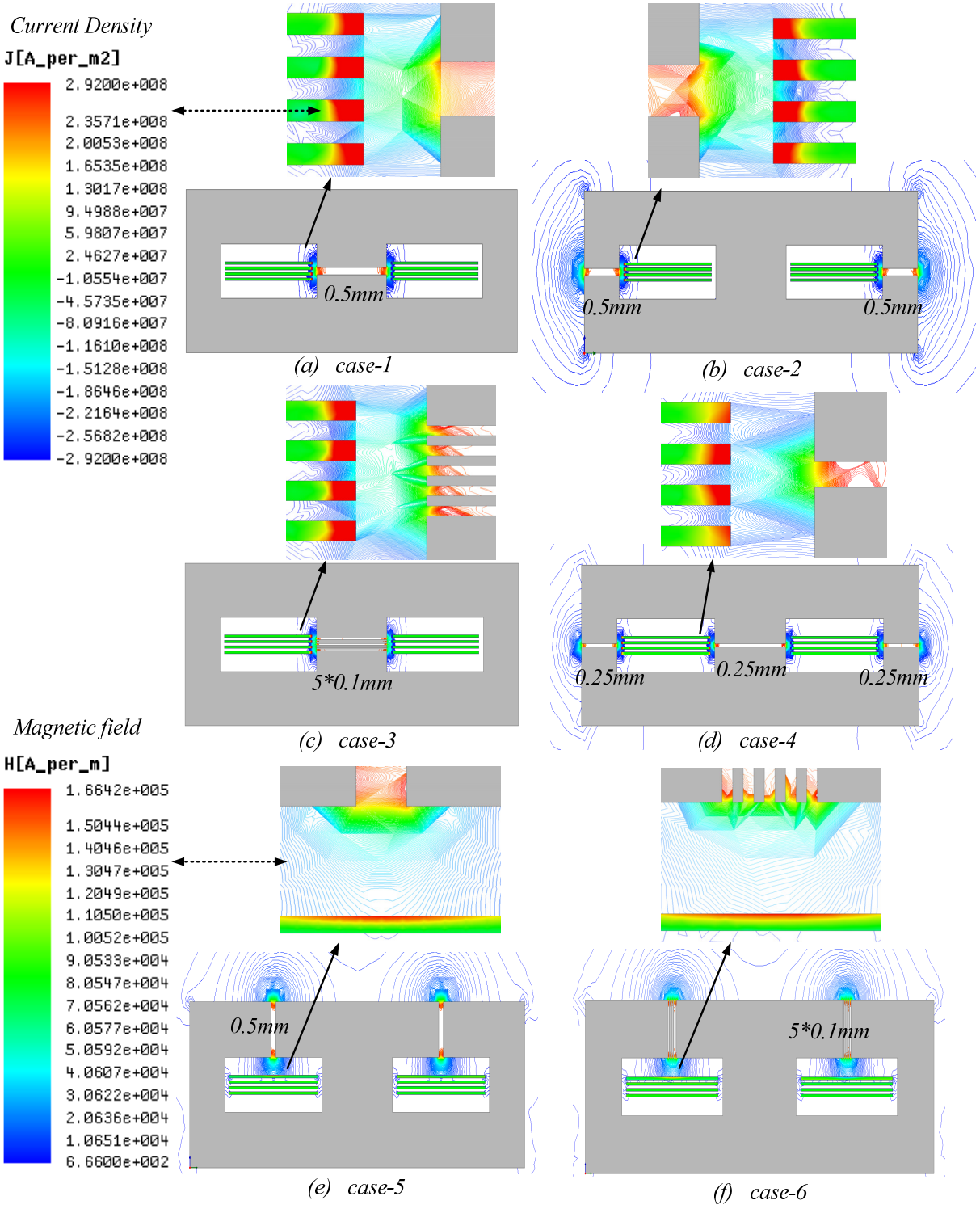

Fig. 3-2: Comparisons of fringing effect in different formats of air gaps under 2-D FEA simulation.

two 0.5-mm air gaps situated at top of core and Case-6 is with 0.5-mm distributed air gaps as a replacer of Caes-5. For all cases, windings with four turns are arranged at the center of the core window. Current density distribution *J* has been plotted in the conductors and the fringing magnetic field *H* has been plotted around the air gaps as well. For Case-1, Case-2, Case-3 and Case-4, the currents must flow toward to the edges

of conductors in order to exclude the tangential fringing magnetic field. In Case-5 and Case-6, the currents flow toward to the surfaces of conductors due to the tangential fringing magnetic field is parallel to the surfaces of conductors. Since planar conductors have higher ratio of width to thickness, the currents flowing to the edges will cause extremely higher ac resistance than the cases that currents flowing to the surfaces. Fig. 3-3 plots a comparative result for the ratio of ac resistance to dc resistance. Caes-1 is the worst case for high frequency winding loss where the ac resistance is 62.8 times the dc resistance at 500-kHz frequency. Case-2 and Case-3 have a slight reduction than Case-1. The ac resistance is only 32.6 times the dc resistance at 500-kHz frequency in Case-4. The best results are shown in Case-5 and Case-6. This benefit of the top air gap for planar conductors has attracted people's attention and thus some further researches on quasidistributed gap inductor have been investigated in [3.9]. In addition, the conductors situated far away to the air gaps can also significantly reduce winding loss, which has been illustrated in Fig. 11 of [B.4].

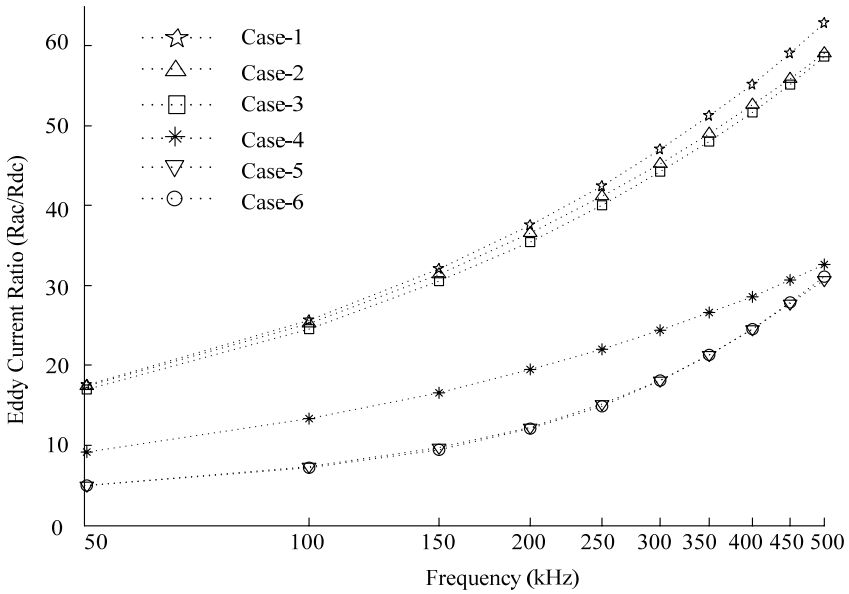

Fig. 3-3: Comparative FEA results on eddy current effect.

3.13 Parallel Winding

Parallel connection of multilayer for planar winding is usually employed to increase the current handling capacity. The currents in the series-windings remain the same, resulting in the same magnetic field strengths on both sides of the layers. However, with parallel winding connections, the currents in each layer may not be equally shared due to the leakage fluxes and the high-frequency effects, and thus the magnetic field around parallel-windings becomes more complicated. In other words, circulating currents may exist in the parallel layers, which contributes to an extra winding loss. Detailed analysis for the parallel effect loss is shown in [3.18]-[3.21]. Notice that the full interleaved winding arrangement may not be the best case for flyback transformer or inductor

design with parallel windings. This is due to the fact that gap effect (fringing field) strongly affects the unbalanced current distribution [3.21].

3.14 Summary

- Dowell's results and related improvement are main references for transformer conduction loss calculation in last 50 years. Although its accuracy cannot be perfectly guaranteed in practical planar transformer design due to some restrictions, the most commonly used equation for winding loss calculation, nowadays, is still based on Dowell's contribution. The accurate investigations on the modeling of winding loss, particularly for planar structure, should be taken into account since it directly relates to the optimization of power converters.
- Ease of implementation of interleaved winding is well-known advantage for planar magnetics. Therefore, interleaved winding arrangements have been investigated and related comparisons are shown in [B.1]. The results show that interleaved winding causes a significant reduction to the winding conduction loss of transformers. And an improved interleaved winding arrangement with m=0.5 has been proposed in [B.1], which can further reduce the proximity effect.
- The fringing field caused by the air gaps in planar inductor cannot be ignored since an excessive power loss is dissipated to the windings. Investigation on the fringing effect of planar inductors has been done in this study.
- Unbalanced current distribution in parallel windings has to be considered, particularly for gapped inductors, which also contribute to an excessive power loss. An appropriate winding arrangement needs to be used to balance the currents in parallel winding layers.

3.2 Core Loss

There are three main methods to model magnetic core loss:
1) Hysteresis models;
2) Loss separation approach;
3) Empirical methods.
The first method is usually based on the Jiles-Atherton model [3.22], [3.23] or Preisach model [3.24]. The core loss separation approach [3.25] assumes that three fundamental effects are contributing to the core losses: static hysteresis loss, eddy current loss and excess eddy current loss. This approach has a practical disadvantage that the models are based on parameters, which are not always available and difficult to extract. Although the hysteresis models and loss separation approach can lead to satisfactory results, they require extensive computations and measurement works. Empirical approach enables loss determination with manufacturer-provided data with an easy way to use expression. The most commonly used approach that characterizes core losses is the empirical

Steinmetz equation, which expresses core loss density as power law with fixed exponent of frequency and flux density.

$$P_v = k \cdot f^{\alpha} \cdot (\frac{\Delta B}{2})^{\beta} \tag{3-3}$$

where k, α, β are constants provided by manufacturer, ΔB is peak-to-peak flux density of a sinusoidal excitation with switching frequency f and P_v is time-average core loss per unit volume. Unfortunately, the Steinmetz equation is only valid for sinusoidal excitation. This is a significant drawback since in a majority of power electronics applications the core material is exposed to non-sinusoidal flux waveforms. Core loss due to non-sinusoidal waveforms can far exceed the loss due to sinusoidal waveforms, even if the frequencies and the peak-to-peak flux densities are identical [3.26]. In order to determine losses for a wider variety of waveforms, some modified expressions including modified Steinmetz expression (MSE) [3.27], generalized Steinmetz equation (GSE) [3.28], improved GSE (IGSE) [3.29], improved IGSE (I²GSE) [3.30], natural Steinmetz extension (NSE) [3.31], equivalent elliptical loop (EEL) [3.32] and waveform coefficient Steinmetz equation (WCSE) [3.33] are introduced. A comparison among these modified empirical methods shows that the IGSE have the best loss determination with a wide variety of waveforms [3.26].

$$P_v = \frac{1}{T} \cdot \int_0^T k_i \cdot \left|\frac{dB(t)}{dt}\right|^{\alpha} \cdot (\Delta B)^{\beta-\alpha} \cdot dt$$

$$k_i = \frac{k}{(2\pi)^{\alpha-1} \cdot \int_0^{2\pi} |\cos\theta|^{\alpha} \cdot 2^{\beta-\alpha} \cdot d\theta} \tag{3-4}$$

Eq. (3-4) shows the IGSE expression where k, α, and β are determined by equating the loss expression for a sinusoidal excitation case with Eq. (3-3). The angle θ represents the phase angle of the sinusoidal waveform. Applying a piecewise linear model (PWL) to the non-sinusoidal waveform and then combining with the IGSE, leads to an easy-to-use expression for accurate determination of core loss without requiring extra characterization of material parameters and measurement works beyond the basic parameters of the Steinmetz equation. This approach has been applied in this work [B.3].

Zero voltage across the magnetic components in some periods can be frequently observed in most of power converters, particularly for H-bridge converter. The time period of zero voltage depends on the duty cycle. Cores losses still occur a short period after switching the winding voltage to zero due to magnetic relaxation. However, this is in contradiction to Eq. (3-4). In [3.30], a further improvement of the IGSE that takes this

effect into consideration is suggested and accordingly named I^2GSE. But some extra empirical parameters are required, which are not easy to find.

Another important drawback of IGSE or I^2GSE is that they neglect the fact that core losses vary under dc bias conditions, i.e. the Steinmetz parameters change under dc bias condition. When a magnetic core operates under dc bias condition, core loss still can be described using Steinmetz Equation or IGSE. However, the Steinmetz parameters must be adjusted according to the dc bias present. For many materials, the impact of a dc bias cannot be neglected as it may increase the core loss by a factor of more than two [3.34]. Two means of considering dc bias losses are suggested in [3.34], [3.35]. Based on the contribution of [3.34], a core loss consideration under dc bias has been applied to my work for a planar integrated magnetics module in [B.3].

3.3 Leakage Inductance

Not all the magnetic flux generated by ac current excitation on the primary windings follows the magnetic circuit and link with the secondary windings. The flux linkage between two windings or parts of the same winding is never complete. Some flux leaks from the core and returns to the air, winding layers and insulator layers, and thus these flux causes imperfect coupling.

The leakage inductance causes the main switch current at the device input to vary at a low slope between zero and the rated value, and reduces the rate of commutation between the output diodes. In addition, the stored energy in the leakage inductance leads to a generation of voltage spikes on the main switches, which, aside from creating electromagnetic interference (EMI) problems, increases the switching losses and thus reduces the power efficiency [3.36]. For a low leakage construction, nearly all of the leakage energy is stored within the windings and the space between the windings. Furthermore, the leakage energy stored within and between the windings is basically only a function of the winding geometry and turns, and is intrinsically independent of the core geometry. But notice that different core geometries may cause a difference in winding geometry and thus change the leakage inductance. An in-depth analysis of leakage inductance in planar transformer is suggested in [B.2].

Planar transformers have been touted to have a low leakage inductance, particularly by some commercial companies. The perception that planar transformers have a low leakage inductance has remained as they have gained in popularity, giving the impression that this is an intrinsic property of the design. Fig. 3-4 shows a comparison of leakage inductance between planar structure and conventional structure. In order to make a fair comparison, the cross-section and the volume of core, the number of turns, the conductor thickness, the space between the conductors and the area of core window are kept the same. Observing from the FEA simulation, the leakage inductance of planar structure is twice as large as that of conventional structure. The change of the leakage

inductances between the two structures will be enlarged with increased core geometry. This is due to the fact that the planar structure provides a longer length of mean turn and thus results in a higher leakage inductance. More core structures compared with the planar structure for leakage inductance are presented in [3.37], resulting in planar structure is not intrinsically a low leakage inductance construction. However, planar transformer can achieve low leakage inductance by interleaving primary and secondary windings. How interleaved winding arrangements highly reduce the leakage inductance is presented in [B.2]. If a similar level of winding interleaving is used with the other transformer constructions, they will retain their relative leakage inductance advantages over the planar transformer. As a conclusion, planar transformer does not have intrinsic property of low leakage inductance. The only benefit of the planar transformer in this regard is the relative ease with which primary and secondary windings can be heavily interleaved.

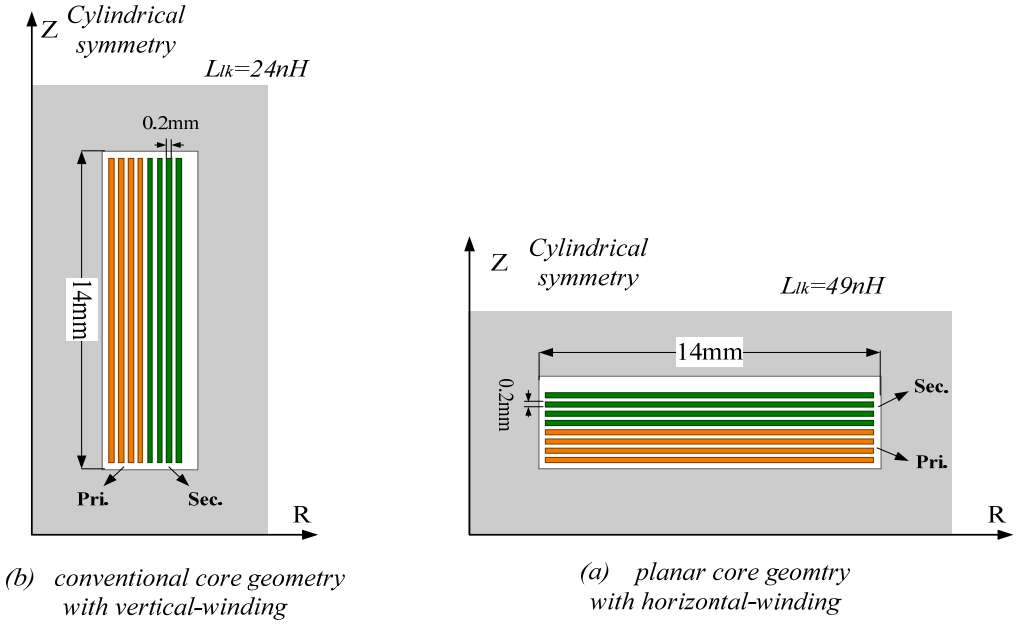

Fig. 3-4: Leakage inductance comparison between planar structure and conventional structure.

The methods to reduce the leakage inductance are:

- **Reduce the number of turns**. From [B.2], neglecting the contribution of fringe fields, the leakage inductance is then simply proportional to the number of turns. However, the reduction of number of turn may cause a core saturation or higher core loss, even though there will be advantageous to the winding conduction loss. Hence, analysis of the trade-offs and determination of the optimum number of turns become necessary [B.1].
- **Reduce the thickness of conductors and insulators**. Thin copper sheet and insulator can reduce the leakage inductance at the expense of a high dc resistance and high interwinding capacitance [B.1], [B.2].

- **Reduce the length of mean turn**.
- **Increase the width of conductors**.
- **Interleaving winding arrangement**.

However, in some applications such as a phase-shift-modulated soft-switching dc-dc converter, the magnitude of leakage inductance determines the achievable load range under zero-voltage-switching operation, and thus a relatively high leakage inductance is required. The aforementioned methods can be reversely used to achieve a desirable high leakage inductance but at the expense of a magnetic field that differs significantly from being parallel to the layers and gives additional losses. Besides, two additional methods to increase the leakage inductance are introduced as follows:

- **Insert ferrite polymer compounds (FPC)** between the primary and secondary windings. As shown in Fig. 3-5, a 0.2-mm FPC material with the relative permeability μ_r=30 is inserted between the primary and secondary windings, providing a lower reluctance return path for the magnetic flux. This returned magnetic flux will not link with the other windings and thus cause a high leakage and low coupling coefficient. The parameters of core geometry and winding geometry in this transformer are kept the same with the case in Fig. 3-4(b). The FEA simulation shows the inserted FPC leads to a 5 times higher leakage inductance than the case without FPC. The magnitude of leakage inductance can be controlled by the thickness and the permeability of FPC material. Leakage inductance and eddy current effect of the windings are respectively plotted as a function of relative permeability μ_r of the FPC material in Fig. 3-6. The leakage inductance and the eddy current effect are both increased with a higher permeability or a thicker FPC sheet. Not only ferrite polymer compounds, but also other magnetism material such as μ-metal, amorphous iron or nanocrystalline iron foil can be used to control the leakage inductance. This is often called "integrated magnetics" since a large leakage inductance is formed without adding extra windings, which has been widely used in the LLC resonant converters [3.38]-[3.42].

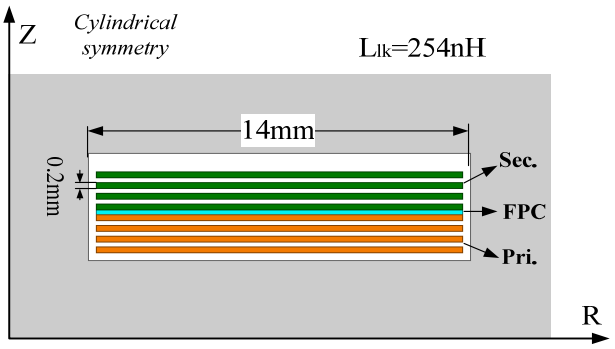

Fig. 3-5: Leakage result with inserted FPC sheet.

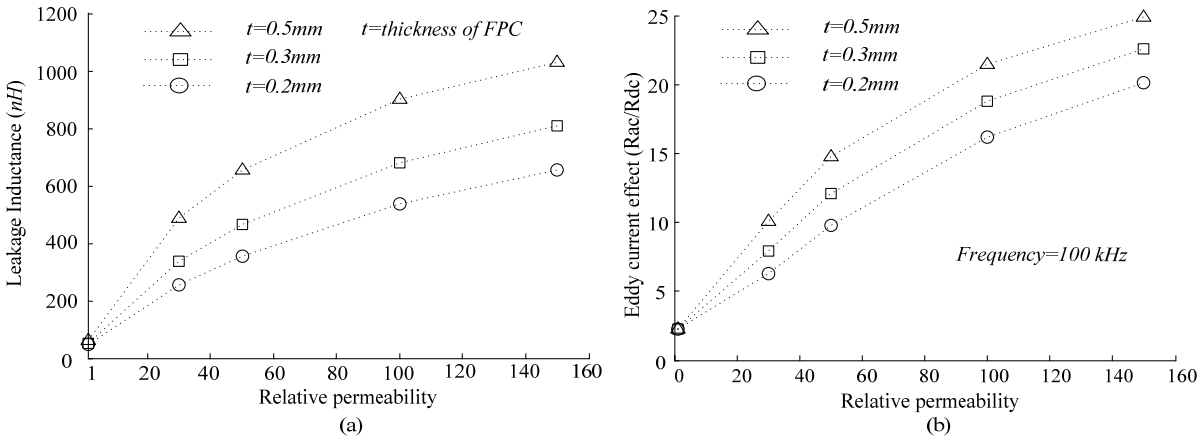

Fig. 3-6: Functions of leakage inductance (a), eddy current effect (b) with relative permeability of FPC material in terms of different thicknesses.

- **Fractional turn.** A fractional turn is really a full turn around a fraction of the total center leg flux. As an example in Fig. 3-7, each outer leg has half of the total center leg flux as an E-I core shape having two outer legs of equal areas. A single turn around either outer leg will have an induced voltage equal to half of the primary volts per turn. Such a turn is therefore equivalent to half turn. This type core splits the magnetics flux into two equal portions and only one portion are linked with secondary and thus results in a high leakage inductance. Fractional turns applied to an X-type core is presented in [3.43] and concrete explanation of the existence of high leakage inductance is given. A similar technique with a high leakage inductance has been applied into a high power resonant converter [3.44].

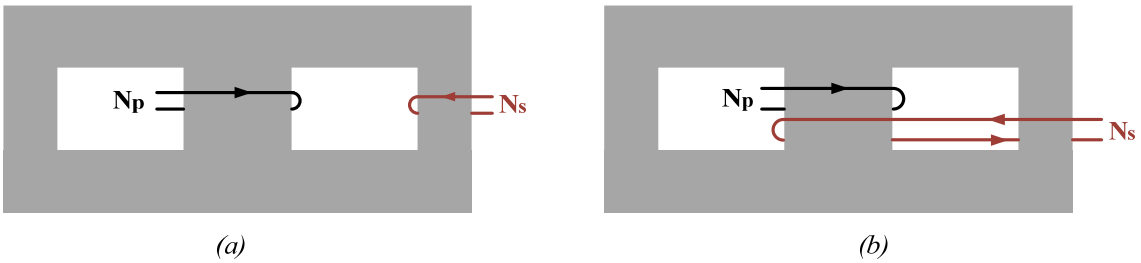

Fig. 3-7: Examples for fractional turn.

3.4 Interwinding Capacitance

There is a contradiction between the leakage inductance and the stray capacitance. A lower leakage inductance is achieved at the expense of the interwinding capacitance. Interwinding capacitance cannot be ignored, particularly for planar transformers. The voltage potential between turns, between winding layers, and between windings and core create this parasitic element. Most of literatures for planar transformer design concentrate on the reduction of leakage inductances, but interwinding capacitances have not effectively been considered. In fact, this parasitic capacitance significantly affects the magnetic component performance in such a way that the current waveform on the

excitation side would be distorted and the overall efficiency of converters would be decreased. Subjected to high-voltage stresses, interwinding capacitance between the windings causes leakage currents and consequently contributes EMI problem [3.45]-[3.47]. For planar transformer, detailed analysis of interwinding capacitance is presented in [B.1]. Notice that heavy winding interleaving carries the price of high capacitance coupling between primary and secondary windings, typically increasing common mode noise current problems.

Here, we have to point out there is a mistake for calculating the equivalent capacitances in [B.1]. The static capacitance C_0 is assumed to be constant in each pair of parallel conductive plates. Since the average length of a turn varies with its mean distance to the center of the core, the static capacitance per overlapping turn actually varies as well. It is actually a function of number of overlapping turns, n, the conductor width, b, and the length of cross-section of center leg, l.

$$C_i = \varepsilon_r \cdot \varepsilon_0 \cdot \frac{(l + 4b \cdot i) \cdot b}{h_\Delta}, \qquad (i = 1,2,3 \dots, n) \tag{3-5}$$

In either case, the equivalent capacitance is related to the number of overlapping turns, the overlapping surface area, the distance between the overlapping plates and voltage potential between the primary and the secondary.

3.5 Summary

Four important parameters including winding resistance, core loss, leakage inductance and interwinding capacitance have been described in this Chapter. Detailed analysis can be referred to [B.1] and [B.2]. The trade-offs among these parameters needs to be recognized in order to implement an optimum design for planar magnetics.

3.6 Reference

[3.1] P. L. Dowell, "Effects of eddy currents in transformer windings," *Proc. Inst. Elect. Eng.*, vol. 113, no. 8, pp. 1387–1394, Aug. 1966.

[3.2] M. P. Perry, "Multiple layer series connected winding design for minimum losses," *IEEE Trans. Power Apparatus and Systems*, vol.PAS-98, no.1, pp. 116-123, Jan. 1979.

[3.3] P. S. Venkatraman, "Winding eddy current losses in switch mode power transformers due to rectangular wave currents," in *Proc. Powercon 11*, sec. Section A-1, 1984, pp. 1–11.

[3.4] J. P. Vandelac and P. D. Ziogas, 'A novel approach for minimizing high frequency transformer copper losses," *IEEE Trans. Power Electron.*, vol. 3, no. 3, pp. 266-277, Jul. 1988.

[3.5] J. Ferreira, “Improved analytical modeling of conductive losses in magnetic components,” *IEEE Trans. Power Electron.*, vol. 9, no. 1, pp. 127–131, Jan. 1994.

[3.6] W. G. Hurley, E. Gath, and J. G. Breslin, “Optimizing the AC resistance of multilayer transformer windings with arbitrary current waveforms,” *IEEE Trans. Power Electron.*, vol. 15, no. 2, pp. 369–376, Mar. 2008.

[3.7] C. R. Sullivan, "Computationally efficient winding loss calculation with multiple windings, arbitrary waveforms, and two-dimensional or three-dimensional field geometry," *IEEE Trans. Power Electron.*, vol. 16, no. 1, pp. 142-150, Jan. 2001.

[3.8] N. H. Kutkut and D. M. Divan, "Optimal air-gap design in high-frequency foil windings," *IEEE Trans. Power Electron.*, vol. 13, no. 5, pp. 942-949, Sep. 1998.

[3.9] J. Hu and C. R. Sullivan, “AC resistance of planar power inductors and the quasidistributed gap technique,” *IEEE Trans. Power Electron.*, vol. 16, no. 4, pp. 558–567, Jul. 2001.

[3.10] P. Wallmeier, "Improved analytical modeling of conductive losses in gapped high-frequency inductors," *IEEE Trans. Ind. Appl.*, vol. 37, no. 4, pp. 1045-1054, Jul/Aug. 2001.

[3.11] M. Albach and H. Robmanith, “The influence of air gap size and winding position on the proximity losses in high frequency transformers,” in *Proc. IEEE Power Electron. Spec. Conf.*, 2001, pp. 1485–1490.

[3.12] X. Mao, W. Chen and Y. Li, "Winding loss mechanism analysis and design for new structure high-frequency gapped inductor," *IEEE Trans. Magn.,* vol. 41, no. 10, pp. 4036- 4038, Oct. 2005.

[3.13] W. A. Roshen, "Fringing field formulas and winding loss due to an air gap," *IEEE Trans. Magn.,* vol. 43, no. 8, pp.3387-3394, Aug. 2007.

[3.14] W. A. Roshen, "High-frequency fringing fields loss in thick rectangular and round wire windings," *IEEE Trans. Magn.,* vol. 44, no. 10, pp. 2396-2401, Oct. 2008.

[3.15] J. Sun and V. Mehrotra, “Orthogonal winding structures and design for planar integrated magnetics,” *IEEE Trans. Ind. Electron.*, vol. 55, no. 3, pp. 1463–1469, Mar. 2008.

[3.16] J. Fletcher, B. Williams, and M. Mahmoud, "Airgap fringing flux reduction in inductors using open-circuit copper screens," in *IEE Proc. Electric Power Appl.,* vol. 152, no. 4, pp. 990- 996, July 2005.

[3.17] L. Ye, G. R. Skutt, R. Wolf, and F. C. Lee, "Improved winding design for planar inductors," In *IEEE Proc. Power Electron. Spec. Conf.,* 1997, pp.1561-1567.

[3.18] W. Chen, Y.-P. Yan, Y.-Q. Hu, and Q. Lu, “Model and design of PCB parallel winding for planar transformer,” *IEEE Trans. Magn.*, vol. 39, no. 5, pp. 3202–3204, Sep. 2003.

[3.19] X. Margueron, J.-P. Keradec, and A. Besri, “Current sharing between parallel turns of a planar transformer: prediction and improvement using a circuit simulation software,” in *Proc. IEEE Ind. Appl. Conf.*, 2007, pp. 1787–1793.

[3.20] R. Prieto, J. A. Cobos, O. Garcia, P. Alou, and J. Uceda, "Using parallel windings in planar magnetic components," in *Proc. IEEE Power Electron. Spec. Conf.*, 2001, pp. 2055-2060.

[3.21] R. Prieto, R. Asensi, J. A. Cobos, "Selection of the appropriate winding setup in planar inductors with parallel windings," in *Proc. IEEE Energy Convers. Congr. Expo.*, 2010, pp. 4599-4604.

[3.22] D. C. Jiles and D. L. Atherton, “Theory of ferromagnetic hysteresis,” *Journal of Magnetism and Magnetic Materials*, Vol. 61, 1986, pp. 48-60.

[3.23] D. C. Jiles, J. B. Thoelke and M. K. Devine, “Numerical determination of hysteresis parameters for modeling of magnetic properties using the theory of ferromagnetic hysteresis,” *IEEE Trans. Magn.,* Vol. 28, No. 1, pp. 27-34, Jan. 1992.

[3.24] A. R. Zare, R. Iravani, M. S. Pasand, H. Mohseni, and S. Farhangi, “An accurate hysteresis model for ferroresonance analysis of a transformer,” *IEEE Trans. Power Del.*, vol. 23, no. 3, pp. 1448–1456, Jul. 2008.

[3.25] W. A. Roshen, “A practical, accurate and very general core loss model for nonsinusoidal waveforms,” *IEEE Trans. Power Electron.*, vol. 22, no. 1, pp. 30–40, Jan. 2007.

[3.26] I. Villar, U. Viscarret, I. E.-Otadui, and A. Rufer, “Global loss evaluation methods for nonsinusoidally fed medium-frequency power transformers,” *IEEE Trans. Ind. Electron.*, vol. 56, no.10, pp. 4132–4140, Oct. 2009.

[3.27] J. Reinert, A. Brockmeyer, and R. W. De Doncker, “Calculation of losses in ferro- and ferrimagnetic materials based on the modified Steinmetz equation,” *IEEE Trans. Ind. Appl.*, vol. 37, no. 4, pp. 1055–1060, Jul-Aug. 2001.

[3.28] J. Li, T. Abdallah, and C. R. Sullivan, “Improved calculation of core loss with nonsinusoidal waveforms,” in *Proc. IEEE Ind. Appl. Conf.*, 2001, pp. 2203–2210.

[3.29] K. Venkatachalam, C. R. Sullivan, T. Abdallah, and H. Tacca, “Accurate prediction of ferrite cores loss with nonsinusoidal waveforms using only Steinmetz parameters,” in *Proc. IEEE Workshop Comput. Power Electron.*, 2002, pp. 36–41.

[3.30] J. Muehlethaler, J. Biela, J. Kolar, and A. Ecklebe, "Improved core loss calculation for magnetic components employed in power electronic systems," *IEEE Trans. Power Electron.*, 2011. (in press)

[3.31] A. Van den Bossche, V. C. Valchev, and G. B. Georgiev, “Measurement and loss model of ferrites with non-sinusoidal waveforms,” in *Proc. IEEE Power Electron. Spec. Conf.*, 2004, pp. 4814–4818.

[3.32] D. Lin, P. Zhou, W. N. Fu, Z. Badics, and Z. J. Cendes, “A dynamic core loss model for soft ferromagnetic and power ferrite materials in transient finite element analysis,” *IEEE Trans. Magn.*, vol. 40, no. 2, pp.1318–1321, Mar. 2004.

[3.33] W. Shen, F.Wang, D. Boroyevich, and C. W. Tipton, “Loss characterization and calculation of nanocrystalline cores for high-frequency magnetics applications” *IEEE Trans. Power Electron.*, vol. 23, no. 1, Jan. 2008.

[3.34] J. Muhlethaler, J. Biela, J. W. Kolar, and A. Ecklebe, “Core losses under dc bias condition based on Steinmetz parameters,” *IEEE Trans. Power Electron.*, 2011. (in press)

[3.35] G. Niedermeier and M. Esguerra, “Measurement of power losses with DC-bias - The Displacement Factor,” in *Proc. of PCIM*, pp. 169–174, 2000.

[3.36] W. G. Hurley and D. J. Wilcox. “Calculation of leakage inductance in transformer windings” *IEEE Trans. Power Electron.*, vol. 9, no. 1, pp. 121–126, January, 1994.

[3.37] B. W. Carsten, "The low leakage inductance of planar transformers; fact or myth?," in *Proc. IEEE Appl. Power Electron. Conf. Expo.*, 2001, pp.1184-1188.

[3.38] M. Meinhardt, M. Duffy, T. O'Donnell, S. O'Reilly, J. Flannery, and C. O Mathuna, "New method for integration of resonant inductor and transformer-design, realisation, measurements," in *Proc. IEEE Appl. Power Electron. Conf. Expo.*, 1999, pp. 1168-1174.

[3.39] I. W. Hofsajer, J. A. Ferreira, and J. D. van Wyk, "Design and analysis of planar integrated L-C-T components for converters," *IEEE Trans. Power Electron.*, vol. 15, no. 6, pp. 1221-1227, Nov. 2000.

[3.40] R. Chen, J. T. Strydom, and J. D. van Wyk, “Design of planar integrated passive module for zero-voltage-switched asymmetrical half-bridgePWM converter,” *IEEE Trans. Ind. Appl.*, vol. 39, no. 36, pp. 1648–1655, Nov./Dec. 2003.

[3.41] W. Liu and J. D. van Wyk, "Design of integrated LLCT module for LLC resonant converter," in *Proc. IEEE Appl. Power Electron. Conf. Expo.*, 2005, pp. 362- 368.

[3.42] Y. Liang, W. Liu, B. Lu, and J. D. van Wyk, "Design of integrated passive component for a 1 MHz 1 kW half-bridge LLC resonant converter," in *Proc. IEEE Ind. Appl. Conf.*, 2005. pp. 2223- 2228.

[3.43] G. Perica, "Elimination of leakage effects related to the use of windings with fractions of turns," *IEEE Trans. Power Electron.*, vol.PE-1, no.1, pp.39-47, Jan. 1986.

[3.44] J. Biela and J. W. Kolar, "Electromagnetic integration of high power resonant circuits comprising high leakage inductance transformers," in *Proc. IEEE Power Electron. Spec. Conf.*, 2004, pp. 4537-4545.

[3.45] H.-Y. Lu, J.-G. Zhu, and S. Y. R. Hui, “Experimental determination of stray capacitances in high frequency transformers,” *IEEE Trans. Power Electron.*, vol. 18, no. 5, pp. 1105–1112, Sep. 2003.

[3.46] L. Dalessandro, F. S. Cavalcante, and J. W. Kolar, “Self-capacitance of high-voltage transformers,” *IEEE Trans. Power Electron.*, vol. 22, no. 5, pp. 2081–2092, Sep. 2007.

[3.47] J. Biela and J. W. Kolar, “Using transformer parasitics for resonant converters—A review of the calculation of the stray capacitance of transformers,” *IEEE Trans. Ind. Appl.*, vol. 44, no. 1, pp. 223–233, Jan./Feb. 2008.

Chapter 4: Planar Integrated Magnetics

4.1 Overview of Integrated Magnetic Technology

One of the more interesting magnetics design techniques applied by today's power electronics engineers is the "blending" or "mixing" of the transformer and inductive functions of dynamic power conversion circuits on a single magnetic core structure. This technique has come to be known as Integrated Magnetics (IM) design. With the increased requirements of modern power electronics, integrated magnetics with planar core has proven to be an effective means of reducing dc-dc converter size, weight and cost and increasing converter efficiency [4.1]–[4.22].

The IM technique historically can be dated back to 1930s, when the coupled inductor was applied in basic filter design [4.1]. The IM technique had no improvement until the integrated transformer and inductor was introduced to voltage-fed push-pull converter in 1971 [4.2]. The IM technique started to attract the international attentions since that time, and then extended to use in Cuk converter [4.3], forward converter [4.4] and a great number of other topologies [4.5]-[4.7]. Although the concept of IM has been proposed around 50 years ago, the widespread application of this technique has been limited due to complicated manufacture until the appearance of planar magnetic cores in the end of last century. Planar core together with PCB winding or combined with other hybrid winding methods provides excellent solution for the IM technique, hence results in a new name of Planar Magnetic Integration (PIM).

In recent years, most efforts in the IM concentrate on current doubler rectifier due to its suitability for low-output-voltage and high-output-current applications. Unlike earlier IM techniques focusing only on core integration, both core and winding integration can be realized in the current doubler rectifier design, causing lower conduction loss and core loss. As a result, lower overall cost, size as well as higher efficiency can be obtained by using the IM technique for the current-doubler circuit [4.8]–[4.14]. Fig. 4-1 shows a course of development for the IM technique in the current doubler rectifier. Among these IM structures, the first proponent O. Seiersen [4.8] uses separate windings for the transformer and the two inductors, shown in Fig. 4-1(c). The transformer primary and secondary windings are both wound in the center leg, and two inductors are wound in the two outer legs with certain air gaps respectively. This is a typical core integration application where a single conventional E-E or E-I core is used. In contrast, the split secondary windings act as the inductors at the same time [4.10], shown in Fig. 4-1(d). Not only magnetic cores are shared, but also the windings are shared in this structure and thus the power efficiency would be enhanced. However, this structure encounters a large leakage inductance due to the primary windings and the secondary windings are

situated at different legs. In order to reduce the leakage inductance of transformer, another structure with all windings situated at the two outer legs is proposed [4.11] and [4.12], shown in Fig. 4-1(e). This proposed IM structure features a simple core structure, a small leakage inductance and low winding and core losses. However, an important drawback of limited filtering inductance is neglected, which leads to high current and voltage ripples in the output side. Accordingly, an improved IM structure [4.13], [4.14] allows the equivalent filtering inductance to be increased with significantly less increase in total winding conduction loss. The increased inductance leads to reduced current and voltage ripples, thereby reducing the size of capacitors required for output filtering. The lower current and flux ripple also helps to reduce the conduction loss and the magnetic core loss. As the result, the overall converter efficiency can be improved, especially under light load when the losses due to ripple current and ripple flux are more significant.

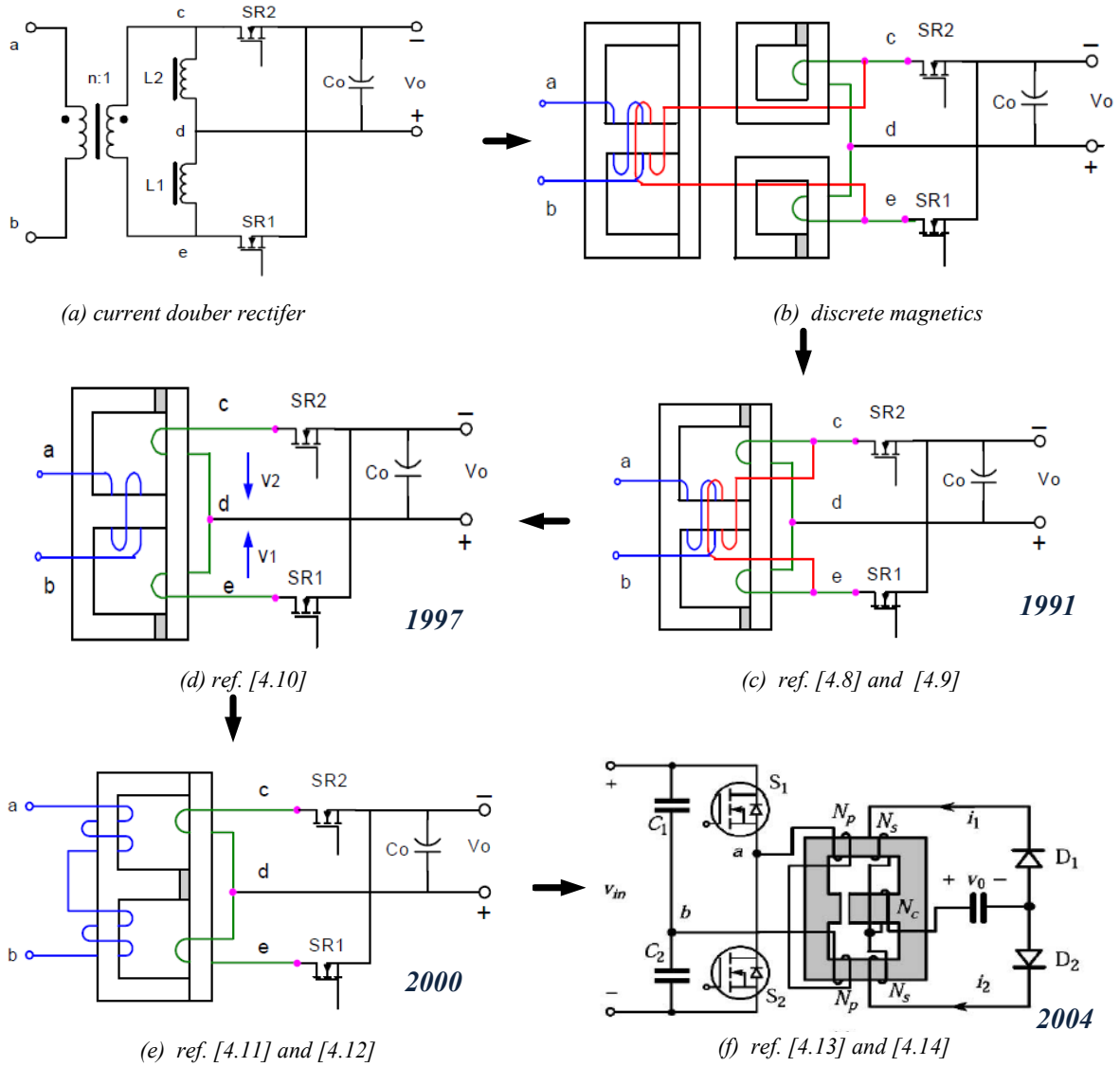

(a) current douber rectifer *(b) discrete magnetics*

(d) ref. [4.10] *(c) ref. [4.8] and [4.9]*

(e) ref. [4.11] and [4.12] *(f) ref. [4.13] and [4.14]*

Fig. 4-1: course of development for the IM technique in current doubler rectifiers.

A new Matrix Integrated Magnetics (MIM) structure is proposed in [4.15] and [4.16] for low voltage, high current applications. The cellular structure enables the design of low profile magnetics resulting in better core utilization, higher inductance per secondary winding and improved efficiency. An integrated dual-inductors isolated boost converter with one magnetic assembly is proposed in [4.17]. A 1-kW with 300~400-V input voltage and 48-V output voltage asymmetrical half-bridge pulse-width modulation converter employing an integrated L–L–C–T module is constructed in [4.18]. Detailed suggestions are given of how one generic, integrated L-C-T component could be used to implement various resonant converter topologies by merely reconfiguring the external terminals of the integrated components [4.19], [4.20]. An integrated transformer consisted of four step-down transformers wound on a single magnetic core for an interleaved four-phase forward converter has been proposed in [4.21]. Coupled inductors greatly reduce the steady-state inductor current ripples without sacrificing transient response of the converter [4.22], [4.23], [4.24].

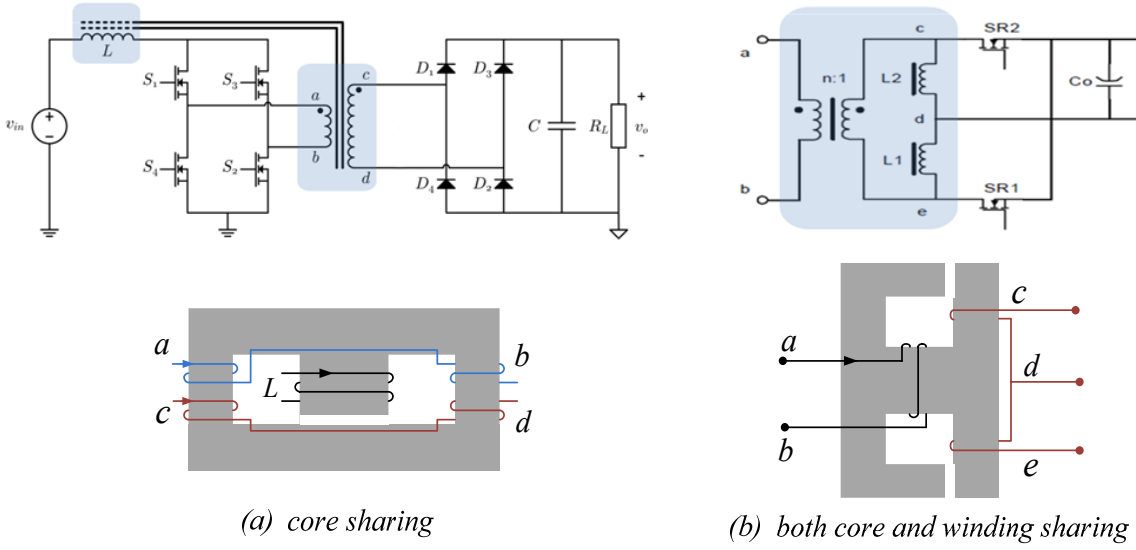

Fig. 4-2: Examples of IM approaches

4.2 Approaches of Integrated Magnetics

There are two main concepts in magnetic integration: core sharing and winding sharing. Core sharing is obtained when different discrete magnetic components merges into a single one, keeping the turns number of each winding. Fig. 4-2(a) shows a core sharing method where an inductor and a transformer are integrated into a single E-I core. [B.3] and [B.4] represent the applications of core sharing method. Winding sharing is obtained when a winding in the integrated magnetic component contributes to the magnetization of more than one equivalent discrete magnetics. Thus, not only core saving but also copper saving is achieved. Fig. 4-2(b) shows a winding sharing method in a current doubler circuit where the secondary windings not only performance a transformer but also two output inductors [4.10]. Both methods result in a low size, low cost and high efficiency power converter. In addition, the ideas of IM can also be divided

into coupled integration and uncoupled integration. The coupled integration means the windings of each individual inductive component are coupled together, which equivalently changes their self inductances. The typical application is the coupling inductors [4.22]-[4.24], which reduce the current ripple in multiple-phase interleaved dc-dc converters. Multiple-winding transformers [4.25] and current balancing transformers [B.7] also feature examples of the coupled integration. The uncoupled integration means the windings of each individual inductive component can be independently integrated into a single core. This kind of integration can also be widely used in many topologies due to their independent operation behaviors. An uncoupled method for transformer and inductor assembled into a single core is suggested in [B.3] and [B.4], and an innovational method of uncoupled integration for multiple transformers is presented in [B.9] and [B.11].

4.3 Modeling of Integrated Magnetics

The general analytical method for IM technique is inductive modeling, which is based on a reluctance-resistance analogy. This analytical method has been used in my papers [B.3], [B.4] and [B.7]. When considering magnetic circuits from the viewpoint of electronics, it is natural to regard magnetomotive force (MMF) as analogous to the voltage, and magnetic flux, Φ, as analogous to the current. As shown in Fig. 4-3, the MMF ($F = N \cdot I$) is visualized as a force like quantity that pushes a magnetic flux, Φ, around the magnetic circuit. Reluctance, R, in a magnetic circuit is then the counterpart of resistance of an electrical circuit. $\Phi = F/R$, corresponding directly to Ohm's law. Moreover, a sample of magnetic material permeability, $\mu = \mu_0 \cdot \mu_r$, path length l, and cross-sectional area A has a reluctance of $R = l/\mu \cdot A$, a formula that is closely similar to that for electrical resistance.

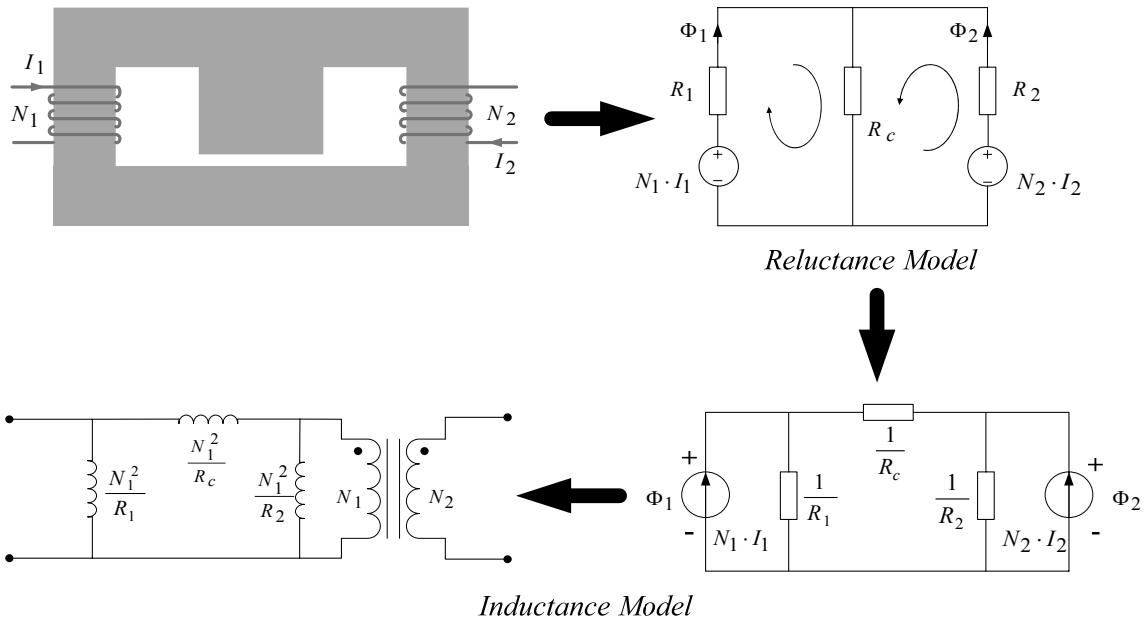

Fig. 4-3: Magnetic reluctance modeling and inductance modeling.

In many cases of practical interest, the magnetic and electrical circuits interact, and the system has to be analyzed as a whole. To allow this, the reluctance model is converted into an inductance model, which consists of a network of simple inductors and ideal transformers. This conversion can be implemented by using duality transformation rules. Unlike the reluctance model, the inductance model can be connected directly into the surrounding electrical circuits [4.26], [4.27]. However, the reluctance model and the corresponding inductance model have several deficiencies for the analysis of IM modeling.

(1) The energy interchange between windings and cores is lost due to the voltages on windings are not expressed directly in this model.
(2) The approach is not universally successful to all core geometries, particularly for non-planar networks [4.28].
(3) It leads to confusion for understanding energy relations and dynamics in the context of power electronics since there is no energy stored in the reluctance model.

In order to avoid aforementioned deficiencies, the gyrator-capacitor approach [4.28], [4.29] has been introduced for the IM model because it describes the interaction between the electrical and the magnetic circuit, including the dynamic flux change. This analytical method has been used in my paper [B.6]. In practice, this modeling method begins with the establishment of gyrators and capacitors. The gyrator links the magnetic path and the electrical circuit by representations of analogs from windings. Capacitors represent the permeance of core, gap and leakage inductance as energy storage devices in the magnetic path. This model is generally used as a SPICE simulation tool. For an analysis, it becomes complicated if there are multiple integrated windings.

4.4 Integrated Magnetics with E-I-E Core Structure

---Introduction: This study has been taken as a major part of investigations on planar integrated magnetics. This integrated technique has been applied to the two recent developed topologies described by two transaction papers, [B.3] and [B.4], one US&EU patent application [B.10] and four related conference papers (only [B.5] is attached).

A determination of IM approach relies on the applied topology. In [B.3], an integrated magnetics approach for one boost inductor and two transformers with E-I-E core geometry is proposed to reduce the number of parts, the total ferrite volume and core loss, which is used for a phase-shift plus duty-cycle-controlled hybrid bidirectional dc-dc converter. The detailed modeling of the integrated approach is presented in [B.3]. Since the boost inductor and the isolated transformers have no common termination (direct connection), the winding integration is not allowed for the boost inductor and the transformers in this topology. In this IM design, only core integration is allowable and the boost inductor is magnetically uncoupled with the two transformers. Currently, for the traditional core geometries, there are only two methods to decouple the individual

windings: flux cancellation and shared low reluctance path. Fig. 4-4 (a) and (b) shows examples of winding decoupling with shared low reluctance path and flux cancellation respectively. Due to a low reluctance path provided by high permeability core, the flux generated from each winding will flow in the low reluctance path rather than the high reluctance path with air gaps, and thus the windings will not magnetically affect each other. For the flux cancellation method, the winding-1 is symmetrically split into the outer legs of E-cores and the winding-2 is wound in the center leg. The flux Φ_1 generated from winding-1 are cancelled in the center leg and also the flux Φ_2 generated from winding-2 flowing through the winding-1 is zero, and thus the two windings are not magnetically coupled. In this Ph.D study, another innovational uncoupled idea based on 3-D orthogonal flux is proposed for multiple-input dc-dc converters, which will be described in the later section.

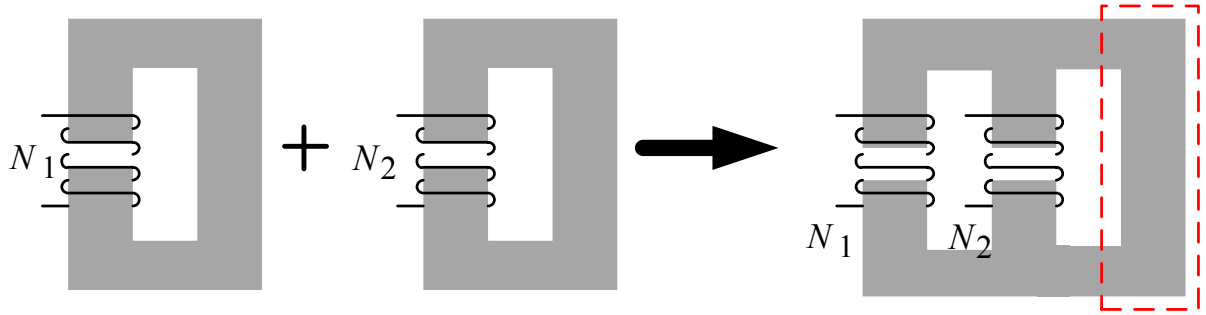

(a) shared low reluctance path

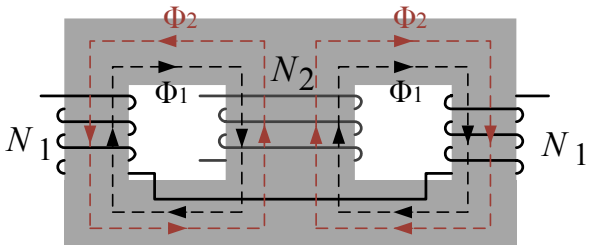

(b) flux cancellation

Fig. 4-4: Two methods for decoupling the individual windings.

The flux cancellation method has been applied into the integrated E-I-E core structure in [B.3] in order to magnetically uncouple the boost inductor and transformers. The middle I-core is used for partial coupling between the two transformers T_1 and T_2. When the middle I-core is removed, the two transformers will be fully coupled if the leakage inductance is negligible. The rate of change of the flux in each transformer leg is the same in order to meet Faraday's law. However, external switch sequence forces the voltage across on the winding of transformer T_2 to be zero during some periods depending on the duty cycle control, and thus a short circuit current comes out during these periods which may damage the converter. This can be proven as follows,

$$\begin{cases} v_{T1} = L_1 \cdot \dfrac{di_1}{dt} + M \cdot \dfrac{di_2}{dt} \\ v_{T2} = M \cdot \dfrac{di_1}{dt} + L_2 \cdot \dfrac{di_2}{dt} \end{cases} \tag{4-1}$$

where v_{T1} and v_{T2} are excitation voltages across on the two transformer windings, L_1 and L_2 represent self-inductances of the two transformer windings respectively, and M is mutual inductance between the two transformers. When $v_{T2} = 0$, the following expressions can be obtained,

$$v_{T1} = (L_1 - \frac{M^2}{L_2}) \cdot \frac{di_1}{dt} \tag{4-2}$$

And thus, the equivalent inductance of transformer T_1 is,

$$L_{eq1} = L_1 - \frac{M^2}{L_2} \tag{4-3}$$

Since the middle I-core is removed, the coupling coefficient k between the two transformers is equal to 1 if leakage inductance is negligible,

$$k = \frac{M}{\sqrt{L_1 \cdot L_2}} = 1 \tag{4-4}$$

Putting (4-3) and (4-4) together, finally a zero equivalent inductance is obtained, which causes extremely high current. The actual coupling coefficient $k = 0.4$ between the two transformers based on the E-I-E core structure has been derived in the appendix of [B.4]. Hereby, $L_{eq1} = 0.84 \cdot L_1$, is obtained during this zero voltage period, slightly increasing current ripples of the transformers. However, during the other periods, lower current ripples can be observed due to higher equivalent inductances are achieved.

This IM technique with E-I-E core structure has been re-used in the primary-parallel isolated boost converter [B.4]. All magnetic components in the converter including two input boost inductors and two transformers with primary-parallel and secondary-series windings are integrated into an E-I-E core geometry, reducing the number of parts, the total ferrite volume and core loss. With the same principle, only core integration is

allowable and the two boost inductors and two transformers are magnetically uncoupled by using the flux cancellation method. However, since the two transformers are operated in phase, the middle I-core is not used to avoid a short circuit current any more. Due to a low reluctance path provided by the middle I-core, the two input inductors can be integrated independently. The use of the middle I-core in this case is to decouple the two boost inductors, L_1 and L_2. The two inductors are fully direct-coupled if the middle I-core is removed. This results in a huge spike of inductor current at commutation point if there is any small mismatch in two primary stages [B.6]. Notice that the analysis is analogous to use the expressions (4-1)—(4-4). With this E-I-E core structure, many flux cancellation achieved in the middle I-core cause a reduction of the total core loss. The detailed core loss analysis can be referred in [B.4]. Further detailed analysis, modeling, design, experimental verification and comparisons are presented in [B.3] and [B.4] as well.

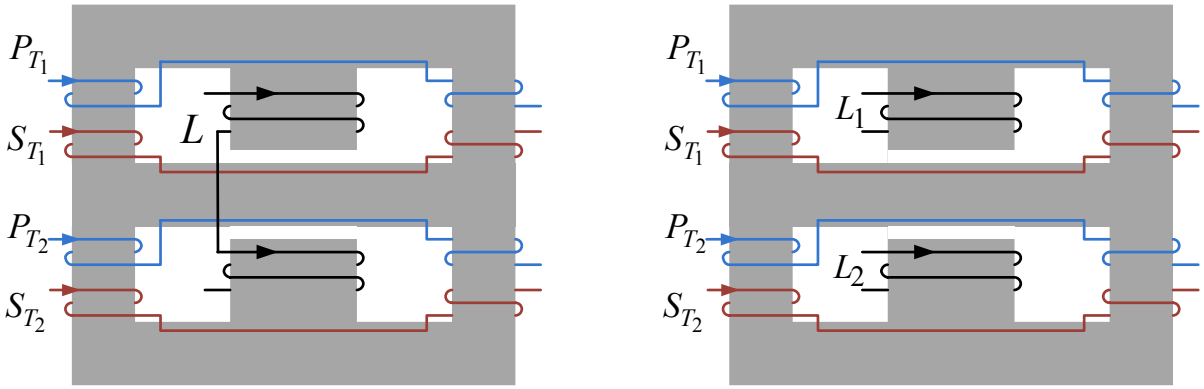

(a) structure in [B.3] *(b) structure in [B.4]*

Fig. 4-5: Integrated structures in [B.3] and [B.4].

Furthermore, by using the proposed IM approach, the transformer secondary winding can be re-used during start-up as a flyback winding coupled to the boost inductor [B.5]. The traditional added flyback winding [4.30] coupled to the boost inductor is thus eliminated from the circuit, bringing substantial cost savings, increased efficiency and simplified design. This patent pending [B.11] start-up method effectively addresses the start-up issue of isolated boost converters, potentially paving the way for increased industry adoption of this highly promising topology family, which so far has been limited by the start-up issue.

4.5 Integrated Current Balancing Transformer

---Introduction: This study has been inspired by previous Ph.D thesis [4.31] from ELE group of DTU. This integrated technique has been applied to the primary-parallel isolated boost converter described by one conference paper, [B.6].

Current sharing among converters or paralleled channels in a single converter is highly demanded because uneven current distribution may cause inductor saturation, uneven thermal stresses, degraded converter performance, and even failure of converter [4.32]. Transformer-based current balancing topologies without any current detector and control complexity have been presented in [4.33] and [4.34]. Fig. 4-6 shows a basic current balancing transformer topology and simple schematic diagrams of principle. The components after the current balancing transformer are considered as the load. The current balancing transformer must be designed as 1:1 turns ratio to ensure the currents are equally distributed, where the same rate of change of magnetic flux through the primary and secondary windings of the balancing transformer T_B is utilized.

$$v_{in} = v_L + v_T + v_1 = v_L - v_T + v_2 \tag{4-5}$$

The voltage across on the current balancing transformer v_T can be expressed,

$$v_T = \frac{v_2 - v_1}{2} \tag{4-6}$$

If $R_1 = R_2$, the voltages across on the load are the same, $v_1 = v_2$, since the currents are equal in the two branches. And thus the voltage across on the current transformer, $v_T = 0$, and no flux is induced in the core. If $R_1 \neq R_2$, the current balancing is held by the transformer and the voltages across on the load are different, $v_1 \neq v_2$. And thus the voltage across on the current transformer is equal to half of voltage difference between v_1 and v_2, shown in (4-6). Hence, a flux is induced in the core. In fact, it can be imaged that there is an invisible differential current through the transformer windings, causing the induced flux. Notice that the total balancing currents actually are the sum of the differential current and the forward current.

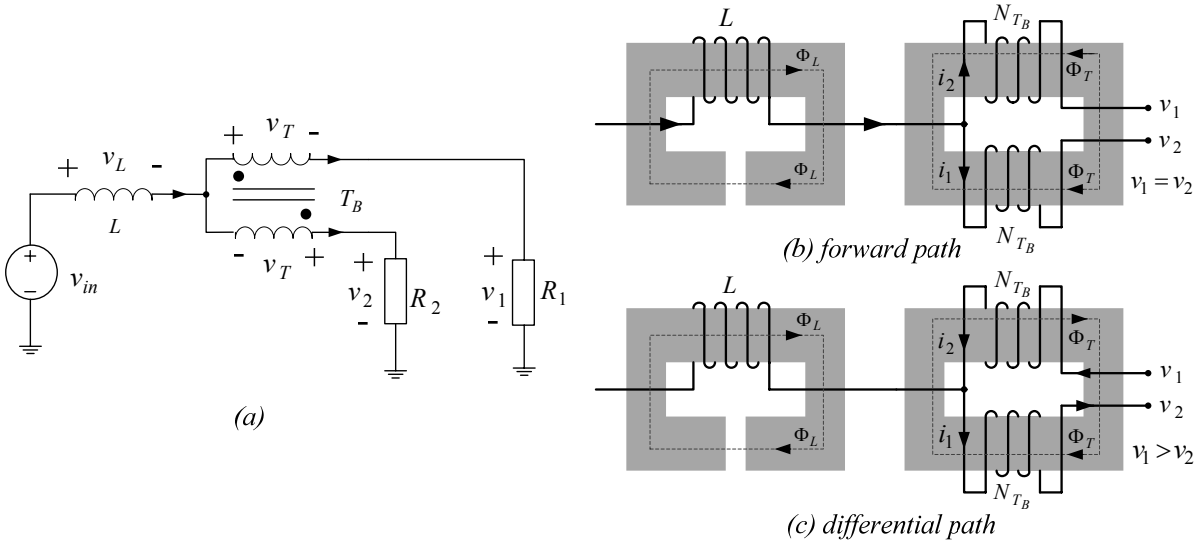

Fig. 4-6: Basic current balancing transformer topology and simple schematic diagrams of principle.

In the primary-parallel isolated boost converter [4.34], the series connected secondary windings, force the currents of isolated transformers to be identical during energy transfer cycles thus also guaranteeing current sharing between all active switches. During inductor charging period, when all switches are turned on, the current sharing between primary switches are maintained by the cascaded current balancing transformers. Small volt-time product imbalances between the paralleling power stages as caused by small differences in gate driver delays, power MOSFET switching speed, and/or parasitic circuit elements are absorbed by the current balancing transformers. A direct paralleling of such power stages, having low parasitic stray inductances, would lead to unpredictable current distribution between switches and potentially catastrophic failures.

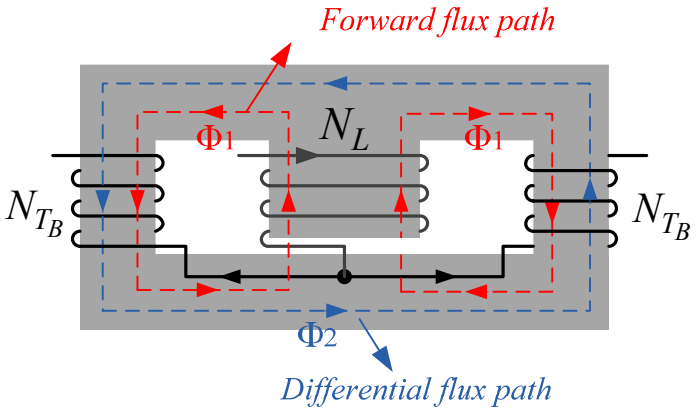

Fig. 4-7: Structure of integrated current balancing transformer.

In [4.34], the current balancing transformers are implemented as planar based discrete components. However, considering the small mismatch times of the switches due to the propagation delays of the ICs and parasitic elements in the gate drive circuitry, the planar cores of the discrete current balancing transformers are not being used during most of the switching period. This results in an inefficient use of the core and not cost-effective way. Therefore the idea of sharing a core with another magnetic element can be proposed, shown in Fig. 4-7. The integrated solution has an advantage of eliminating the extra core for the current balancing transformer, reducing the cost and the volume of the converter. Meanwhile, additional inductances are appearing in the forward path due to the direct coupling between the input inductor L and the current balancing transformer T_B, which reduces the input inductor current ripple. Further detailed analysis, simulation and experimental comparisons for the proposed integrated current balancing transformer are given in [B.6].

4.6 Integrated Inductors with Stacked I-cores

---Introduction: This study has been inspired by the commercial products for space application from International Rectifier (IR), Denmark and related publication [4.35]. This integrated technique has been

applied to the two-phase interleaved bidirectional dc-dc converter described by two conference papers (only [B.7] is attached).

Inspired by the new geometry IM technique for Hybridge topology in [4.35], a low profile and low cost integrated inductors with stacked I-cores for multiple-phase interleaved dc-dc converters is suggested in [B.7]. The new geometry modeling of the integrated inductors is depicted in Fig. 4-8. The module is implemented by three stacked I-cores. Air gaps are constructed by separating the I-cores using copper foil windings with well-defined thickness. The windings are wound in the top I-core and the bottom I-core separately with solenoid-wound structure, and the middle I- core provides a shared flux path with low reluctance. For further details readers are referred to the included publication [B.7].

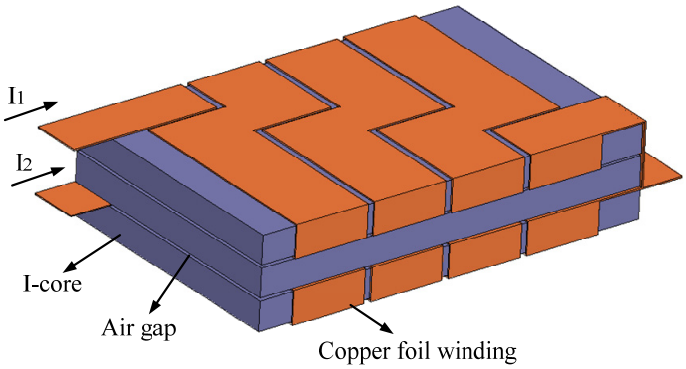

Fig. 4-8: Integrated inductors with stacked I-cores.

Unlike the conventional core types, the stacked I-cores structure provides a gradual saturated behavior due to a non-uniform flux distribution in the cores. If the two inductors are reverse-coupled and the currents are operated with 180° phase shift, or the two inductors are direct-coupled and the currents are in phase, the saturation firstly occurs at center point of the middle I-core, and then the saturated area gradually extends to the end with increasing current. And thus variable inductors whose inductances fall off with increasing current are formed. This behavior might be utilized in some application such as active power factor correction (PFC) [4.36] etc, providing adequate harmonic reduction, and saving considerable space and cost over a conventional inductor as employed in passive power factor correction.

A significant drawback of this structure is that a higher eddy current effect is induced in the conductors and thus causes a higher winding conduction loss. This is due to the fact that the windings are situated in the gaps where an external flux is approximated as purely vertical directed to the surface of the conductors. Since the external flux is tangential to the vertical edges of the conductors, a current must flow toward to the edges in order to exclude the magnetic field from the inside of conductor. The cross-sectional area of its ac current distribution in the conductor is therefore proportional to

δ^2 (δ is skin depth), so the effective ac resistance is much higher than dc resistance. This is a common problem for planar magnetics with sandwich structure [B.8]. A reduction to ac resistance can be obtained by using narrow copper tracks. The width of track close to the skin depth might be the best choice for the ac resistance, but a high dc resistance is compromised. Hereby, an auxiliary winding solution [4.37] to balance the ac resistance and dc resistance is recommend, where the auxiliary winding is optimally designed with lower ac resistance to carry the ac current while the main winding with low dc resistance is designed for the large dc current.

4.7 Ultra-thin Magnetics

---Introduction: This study has been taken as part of results of visiting at Electric Power Processing (EPP) group of TU Delft, the Netherlands (May. 2011- Aug. 2011). This magnetic design has been applied to flexible PV modules described by two conference papers (only [B.8] is attached).

In recent, there is a trend in photovoltaic (PV) systems toward a more granulated processing of the PV array power by means of distributed maximum power point tracking (DMPPT) [4.38]. This is achieved by connecting a dc-dc converter to each PV module in a large PV system and thus performing maximum power tracking on a module level, as opposed to centralized power processing in traditional PV system architectures. To reduce the cost and to improve the level of integration, the power converter is directly integrated on the back side of the PV module, eliminating additional wires and connections. Fig. 4-9 illustrates a concept of a dc-dc converter integrated into a flexible PV module. Since flexible PV modules are frameless and require a supporting structure, flexibility and very low profile (ultra-thin) become main construction design goals for the module integration.

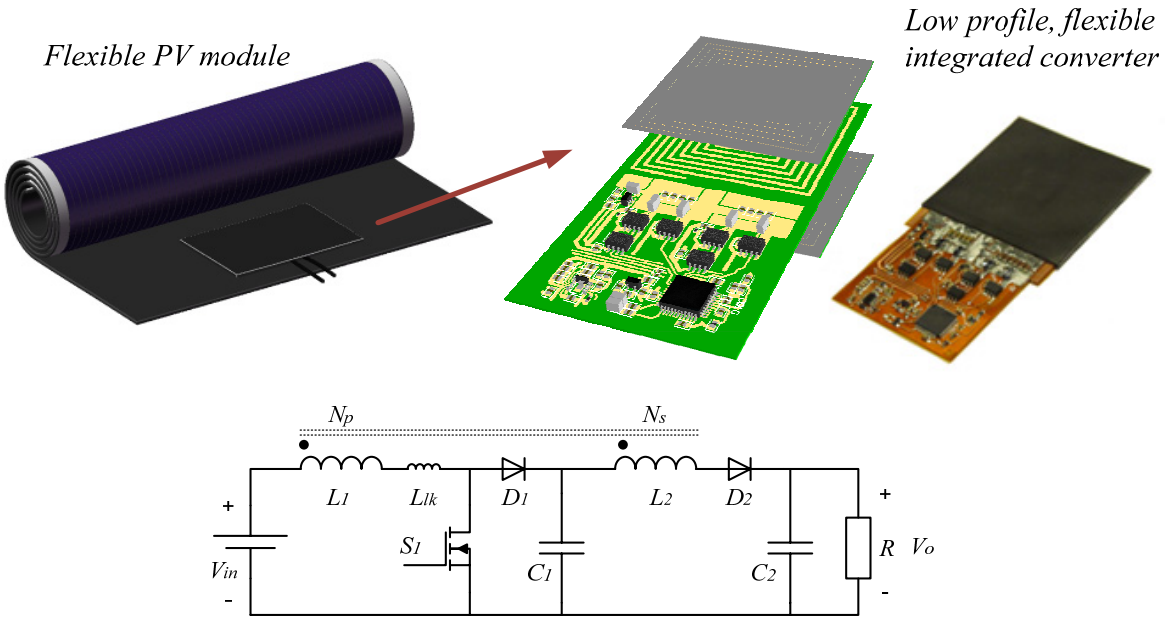

Fig. 4-9: Ultra-thin dc-dc converter integrated into a flexible PV module.

The design target is to construct an integrated high efficiency, high frequency boost converter for the DMPPT PV system. The considered converter is based on a high step-up multiphase boost topology with coupled inductors and passive lossless clamp circuit [4.39], [4.40]. The challenge for the PV converter is the magnetics design, meeting the low profile and flexible requirements. In this study, a 1.5-mm thickness integrated coupled inductor with sandwich core structure is under investigation. Several important design issues for the ultra-thin magnetics including self-inductance, leakage inductance, eddy current effect and core loss are analyzed in-depth in [B.8]. In order to reduce the high frequency eddy current effect in sandwich core structure, [B.8] also initiates a discussion with adjustable core structures and winding arrangements, such as closed core structure, hollow type structure and meander winding.

In [B.8], a precise impedance formula for the ultra-thin structure with consideration of non-uniform current distribution and lossy magnetic media has been proposed by Hurley [4.41]. A comparison of self-inductance between the calculation based on Hurley's contribution and FEA simulation is presented in order to illustrate the correction of eqn.(6) in [B.8].

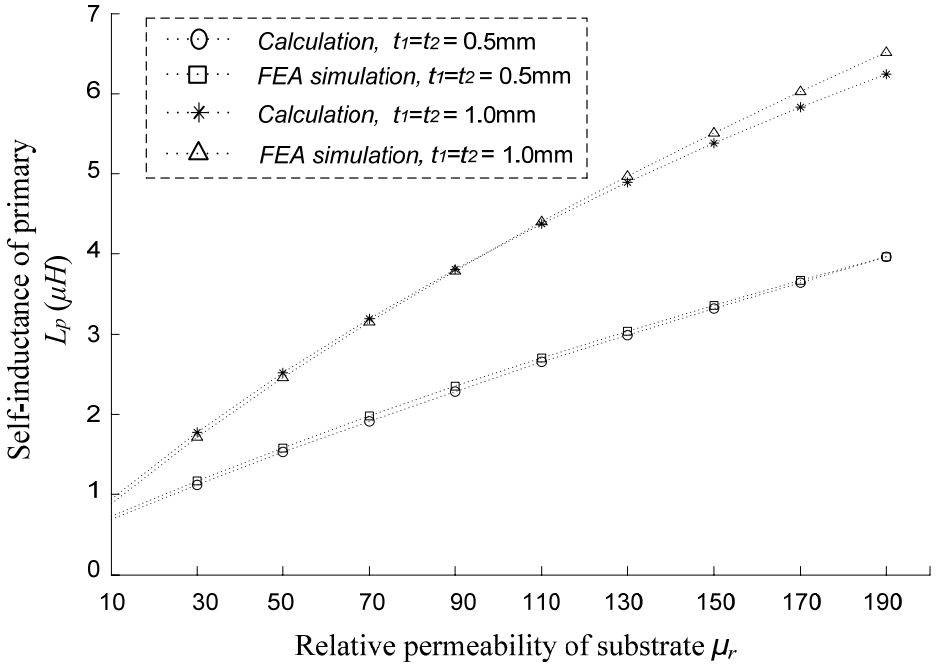

Fig. 4-10: A comparison of self-inductance between calculation and FEA simulation for sandwich structure.

4.8 Four Quadrants Integrated Transformers

---Introduction: This study has been inspired by previous Ph.D thesis [4.42] from ELE group of DTU. This integrated technique has been applied to the dual-input isolated bidirectional dc-dc converter. It has been described by one submitted transaction paper, [B.9], and one US&EU patent application [B.11].

Multiple-input converters (MICs) have been proposed as a cost-effective and flexible way to interface various sources such as solar array, wind turbine, fuel cell, and

commercial ac line, to get a regulated output voltage, and in some cases, energy-storage devices, with a load [4.43]-[4.45]. A common limitation of some known MICs is that only one input power source is allowed to transfer the power energy to the output at a time to prevent power coupling effect. Recently, in order to overcome this limitation, it has been proposed to use multiple-winding transformers based on flux additivity technology with phase-shifted PWM control [4.46]. This technology can transfer power from two or multiple different input voltage sources to the output load simultaneously meanwhile reverse blocking diodes are required at the input power stage sides. The reverse blocking diodes are needed to prevent a reverse power flow from one of the input voltage sources to another input voltage source through the coupled primary sides of the transformer as well as body diodes of semiconductor switches of the input power stages. Without these reverse blocking diodes, different input sources coupled to the multiple-input power converter cannot deliver power to the load simultaneously. Furthermore, this technology cannot be applied in the buck type isolated MICs unless the input voltages are strictly limited according to the turns ratio of multiple primary windings. Otherwise, an undesirable voltage difference stresses on one of the input power stages, causing an extremely high current on the semiconductors and thus damages the circuit. In addition, some other prior art approaches nowadays to overcome this limitation result in a large number of power switches and complicated control schemes [4.47], [4.48].

The main reason for the problem in the MICs is multiple primary windings are coupled. Consequently, it would be advantages to provide an integrated transformer with uncoupled primary windings for use in the MICs to allow multiple input power sources to be operated independently without compromising any functions of the power converter or required complex control or protection circuitry to be added to the input power stages. However, current decoupling approaches applied to traditional core geometries such as E-I or E-E rely on a shared lower reluctance path or flux cancellation mechanisms that have been mentioned before. In practical, both approaches applied to the traditional cores will cause lower magnetizing inductances, higher winding loss and EMI problem etc. Hereby, [B.9] proposes a new concept for decoupling the primary windings in the integrated multiple-winding transformers based on 3-dimensional (3D) space orthogonal flux decoupling. This requires a sort of nontraditional core geometries to carry out the orthogonal flux paths, shown in Fig. 4-11. A name of “four quadrants integrated transformer” (FQIT) is given to the proposed integrated transformer since the four legs with enclosed secondary windings are arranged in a quadratic pattern at the base core plate with the two perpendicular primary windings. Detailed analysis, discussion of advantages and experimental verification has been presented in [B.9], and further embodiments can be referred to the pending patent application [B.11].

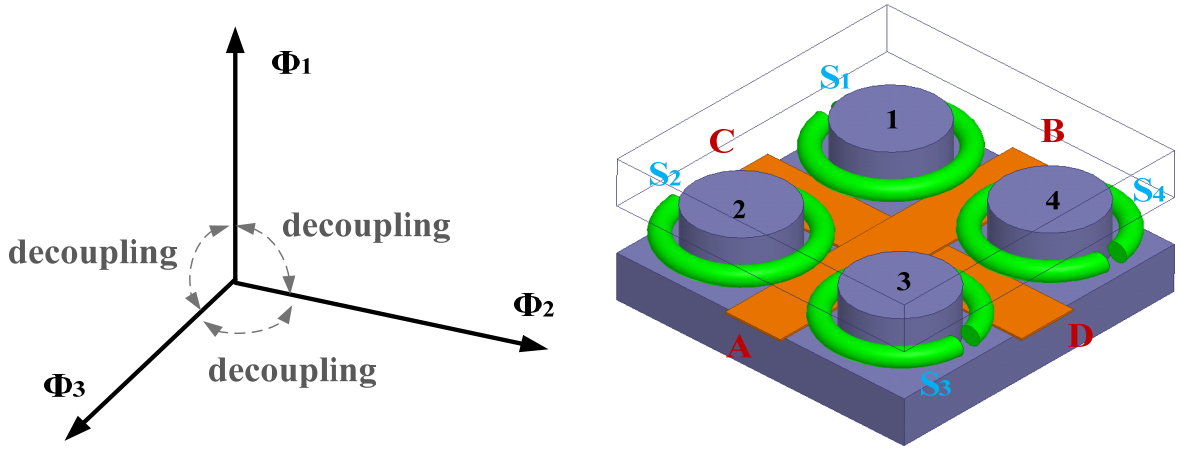

Fig. 4-11: 3-dimensional space orthogonal flux decoupling and its applied core geometry.

4.9 Summary

In this chapter, planar integrated magnetics technology has been studied.

- Approaches and analytical modeling of the IM technique are presented.
- The E-I-E core structure has been proposed to integrate multiple elements with inductive function, reducing the number of parts, the total ferrite volume and core loss. Two general decoupling methods, flux cancellation and a low reluctance path, are analyzed, and the flux cancellation method is utilized to make the integrated transformer and inductor operate independently. The middle-I core is used for avoiding a fully coupled effect between the two transformers which may cause catastrophic failures in the used application. This integrated technique has been used in the two recent developed topologies and the details are referred to [B.3] and [B.4].
- Current balancing transformer are integrated with common input inductor in the primary-parallel isolated boost converter, saving the number of cores, reducing the cost, and also additional inductance can help a reduction of input current ripple.
- A low profile and low cost integrated inductor with stacked I-core is proposed. A gradual saturation behavior is found due to non-uniform flux is distributed in the core. And a significant drawback of high winding conduction loss is described.
- Ultra-magnetics components for flexible PV module have been studied. A 1.5-mm thickness integrated coupled inductor with sandwich core structure is under investigation. Several important design issues for the ultra-thin magnetics including self-inductance, leakage inductance, eddy current effect and core loss are analyzed in-depth.

- A new concept for decoupling multiple windings in the integrated transformers based on 3-dimensional (3D) space orthogonal flux decoupling has been proposed. Accordingly, a new core geometry named “four quadrants integrated transformer” has been applied to a dual-input isolated boost dc-dc converter to allow the two input power sources to be operated independently.

4.10 Reference

[4.1] G. B. Crouse, “Electrical filter,” *U.S. Patent*, 1920948, Aug. 1, 1933.

[4.2] J. Cielo and H. Hoffman, "Combined transformer & inductor device," *U.S. Patent*, 3553620, Jan. 5, 1971, and *U.S Patent*, 3694726, Sep. 26, 1972.

[4.3] S. Cuk, "A new zero-ripple switching dc-to-dc converter and integrated magnetics," *IEEE Trans. Magn.*, vol.19, no.2, pp. 57-75, March 1983.

[4.4] G. E. Bloom, “New multi-chambered power magnetics concepts” *IEEE Trans. Magn.*, vol. 34, no. 4, pp.1342-1344, Jul. 1998.

[4.5] G. E. Bloom and D. M. Mitchell, “Integrated-magnetic gain-enhancement input filter for switch-mode power converter circuits,” in *Proc. IEEE Ind. Electron. Soc. Conf.*, 1990, pp.976-981.

[4.6] G. E. Bloom and R. P. Severns, "The generalized use of integrated magnetics and zero-ripple techniques in switch-mode power converters," in *Proc. IEEE Power Electron. Spec. Conf.*, 1984, pp. 15-33.

[4.7] R. P. Severns and G. E. Bloom, *“*Modern dc-to-dc switch-mode power converter circuits,” ISBN 0-442-21396-4, New York, 1985.

[4.8] C. Peng, M. Hannigan, and O. Seiersen, “A new efficient high frequency rectifier circuit”, in *Proc. High Frequency Power Conversion (HFPC) Conf.*, 1991, pp. 236-243.

[4.9] O. Seiersen, “Power supply circuit with integrated magnetic components,” *U. S. Patent*, *5335165*, Aug. 2, 1994.

[4.10] W. Chen, G. Hua, D. Sable, and F. C. Lee, “Design of high efficiency, low profile, low voltage converter with integrated magnetics,” in *Proc. IEEE Appl. Power Electron. Conf. Expo.*, 1997, pp. 911-917.

[4.11] P. Xu, Q. Wu, P. Wong, and F. C. Lee, “A novel integrated current doubler rectifier,” in *Proc. IEEE Appl. Power Electron. Conf. Expo.*, 2000, pp. 735–740.

[4.12] P. Xu, M. Ye, P. Wong, and F. C. Lee, “Design of 48 V voltage regulator modules with a novel integrated magnetics,” *IEEE Trans. Power Electron.*, vol. 17, no. 6, pp. 990- 998, Nov. 2002.

[4.13] J. Sun, K. F. Webb, and V. Mehrotra, “Integrated magnetics for current-doubler rectifiers,” *IEEE Trans. Power Electron.*, vol. 19, no. 3, pp.582-590, May, 2004.

[4.14] J. Sun and V. Mehrotra, “Orthogonal winding structures and design for planar integrated magnetics,” *IEEE Trans. Ind. Electron.*, vol. 55, no. 3, pp.1463-1469, March, 2008.

[4.15] S. Chandrasekaran, V. Mehrotra, and J. Sun, "A new matrix integrated magnetics (MIM) structure for low voltage, high current DC-DC converters," in *Proc. IEEE Power Electronics Specialists Conference,* pp. 1230- 1235, 2002.

[4.16] S. Chandrasekaran, V. Mehrotra, and J. Sun, “Core structure,” *U.S. Patent*, 6873237, Apr. 18, 2002.

[4.17] L. Yan and B. Lehman, "An integrated magnetic isolated two-inductor boost converter: analysis, design and experimentation" *IEEE Trans. Power Electron.*, vol. 20, no. 2, pp.332–342, March.2005.

[4.18] R. Chen, J. T. Strydom, and J. D. van Wyk, "Design of planar integrated passive module for zero-voltage-switched asymmetrical half-bridge PWM converter," *IEEE Trans. Ind. Appl.*, vol. 39, no. 36, pp. 1648–1655, Nov./Dec. 2003.

[4.19] P. A. J. van Rensburg, J. D. van Wyk, and J. A. Ferreira, "Design, prototyping and assessment of a 3 kW integrated LCT component for development in various resonant converters," *IET Power Electron.*, vol. 2, no. 5, pp. 535–544, 2009.

[4.20] J. T. Strydom, J. A. Ferreira, J. D. van Wyk, I. W. Hofsajer, and E. Waffenschmidt, "Power electronic subassemblies with increased functionality based on planar sub-components," in *Proc. IEEE Power Electron. Spec. Conf.,* 2000, pp. 1273–1278.

[4.21] L-P. Wong, Y-S. Lee, M. H. L. Chow, and D. K-W Cheng, "A four-phase forward converter using an integrated transformer," *IEEE Trans. Ind. Electron.*, vol. 55, no. 2, pp. 817–831, Mar. 2008.

[4.22] S.-Y. Lee, A. G. Pfaelzer, and J. D. van Wyk, "Comparison of different designs of a 42-V/14-V dc/dc converter regarding losses and thermal aspects," *IEEE Trans. Ind. Appl.*, vol. 43, no. 2, pp. 520–530, Mar. 2007.

[4.23] P.-L. Wong, Q.-Q. Wu, P. Xu, B. Yang, and F. C. Lee, "Investigating coupling inductors in the interleaving QSW VRM," in *Proc. IEEE Appl. Power Electron. Conf. Expo.,* 2000, pp. 973–978.

[4.24] H. Kosai, S. McNeal, B. Jordan, J. Scofield, B. Ray, and Z. Turgut, "Coupled inductor characterization for a high performance interleaved boost converter," *IEEE Trans. Magn.*, vol. 45, no. 10, pp. 4812–4815, Oct. 2009.

[4.25] Q. Chen, F. C. Lee, J.-Z. Jiang, and M. M. Jovanovic, "A new model for multiple-winding transformer," in *Proc. IEEE Power Electron. Spec. Conf.*, 1994, pp.864-871.

[4.26] G. W. Ludwig and S.-A. El-Hamamsay, "Coupled inductance and reluctance models of magnetic components," *IEEE Trans. Power Electron.*, vol. 6, no. 2, pp.240-250, Apr. 1991.

[4.27] S.-A. El-Hamamsy and E. I. Chang, "Magnetics modeling for computer-aided design of power electronics circuits," in *Proc. IEEE Power Electron. Spec. Conf.*, 1989, pp.635-645.

[4.28] D. C. Hamill, "Lumped equivalent circuits of magnetic components: the gyrator-capacitor approach," *IEEE Trans. Power Electron.*, vol. 8, no. 2, pp.97-103, Apr. 1993.

[4.29] L. Yan and B. Lehman, "Better understanding and synthesis of integrated magnetics with simplified gyrator model method," in *Proc. IEEE Power Electron. Spec. Conf.*, 2001, pp.433-438.

[4.30] L. Zhu, K. Wang, F. C. Lee, and J-S. Lai, "New start-up schemes for isolated full-bridge boost converters." *IEEE Trans. Power Electron.*, vol. 18, no. 4, pp. 946- 951, July 2003.

[4.31] M. Nymand, "High efficiency power converter for low voltage high power applications", PhD dissertation, ISBN: 978-87-92465-33-7, 2010.

[4.32] H. Mao, L.-B. Yao, C.-S. Wang, and I. Batarseh, "Analysis of inductor current sharing in nonisolated and isolated multiphase dc–dc converters," *IEEE Trans. Ind. Electron.*, vol. 54, no. 6, pp.3379-3388, Dec. 2007.

[4.33] K. I. Hwu, Y. H. Chen, "Applying differential-mode transformer to current sharing with current ripple considered," *IEEE Trans. Ind. Electron.*, vol. 58, no. 7, pp.2755-2771, July 2011.

[4.34] M. Nymand and M. A. E. Andersen, "A new very-high-efficiency R4 converter for high-power fuel cell applications," in *Proc. IEEE Power Electron. Drive Syst.,* 2009, pp. 997-1001.

[4.35] S. Petersen, “Improved geometry of integrated magnetics for the hybridge topology,” in *Proc. of the Sixth European Conference*, *European Space Agency*, ESA SP-502, p.241-247, May, 2002.

[4.36] W. H. Wölfle and W. G. Hurley, "Quasi-active power factor correction with a variable inductive filter: theory, design and practice," *IEEE Trans. Power Electron.*, vol. 18, no. 1, pp.248–255, Jan. 2003.

[4.37] M. Nymand, U. K. Madawala, M. A. E. Andersen, B. Carsten, and O. Seiersen, “Reducing ac winding losses in high-current high-power inductors,” in *Proc. IEEE Ind. Electron. Soc. Conf.*, 2009, pp. 774-778.

[4.38] G. R. Walker and P. C. Sernia, “Cascaded dc–dc converter connection of photovoltaic modules,” *IEEE Trans. Power Electron.,* vol. 19, no. 4, pp.1130–1139, Jul. 2004.

[4.39] Q. Zhao and F.C. Lee, “High-efficiency, high step-up dc–dc converters,” *IEEE Trans. Power Electron.,* vol. 18, no. 1, pp. 65- 73, Jan 2003.

[4.40] W-H. Li and X-N. He, "An interleaved winding-coupled boost converter with passive lossless clamp circuits," *IEEE Trans. Power Electron.*, vol. 22, no. 4, pp.1499-1507, July 2007.

[4.41] W. G. Hurley and M. C. Duffy, “Calculation of self- and mutual impedances in planar sandwich inductors,” *IEEE Trans. on Mag.*, vol.33, no.3, pp.2282-2290, May. 1997.

[4.42] Z. Zhang, “Powering the future data center,” PhD dissertation, ISBN: 978-87-92465-35-1, 2010.

[4.43] Y-C. Liu and Y-M. Chen, "A systematic approach to synthesizing multi-input dc–dc converters," *IEEE Trans. Power Electron.*, vol. 24, no. 1, pp.116-127, Jan. 2009.

[4.44] K. Kobayashi, H. Matsuo, and Y. Sekine, “Novel solar-cell power supply system using a multiple-input DC–DC converter,” *IEEE Trans. Ind. Electron.*, vol. 53, no. 1, pp. 281–286, Feb. 2006.

[4.45] H. Matsuo, T. Shigemizu, F. Kurokawa, and N. Watanabe, "Characteristics of the multiple-input dc-dc converter," *IEEE Trans. Ind. Electron.*, vol. 51, no. 3, pp. 625- 631, June 2004.

[4.46] Y-M. Chen, Y-C. Liu, and F-Y. Wu, “Multi-input dc/dc converter based on the multiwinding transformer for renewable energy applications” *IEEE Trans. Ind. Appl.*, vol. 38, no. 4, pp. 1096-1104, July 2002.

[4.47] J. Ruan, F. Liu, X. Ruan, D. Yang, Y. Li, and K. Jin, "Isolated multipleinput dc/dc converter using alternative pulsating source as building cells," in *Proc. IEEE International Power Electron. conf. (IPEC),* pp.1463-1470, 2010.

[4.48] H-J. Chiu, H-M. Huang, L-W. Lin and M-H. Tseng, "A multiple-input dc/dc converter for renewable energy systems," in *Proc. IEEE International Conf. on Industrial Technology (ICIT)*, pp.1304-1308, Dec. 2005.

Chapter 5: Conclusion and Future works

5.1 Conclusion

This work has investigated the fundamental characteristics of planar magnetics and advanced planar integrated magnetics technique for dc-dc converters.

This thesis first describes an overview of basic planar magnetics technology used in general dc-dc converters. PCB or flexible PCB windings as a main construction together with planar cores yield a number of advantages over the conventional magnetics. Meanwhile, some limitations of planar magnetics are also introduced.

A clear cognition for the intrinsic properties of planar magnetics has been given by investigating the winding conduction loss, core loss, leakage inductance and interwinding capacitance.

- Unlike traditional wire-wound transformer using the equivalent porosity factor, ac resistance calculation for planar windings is relatively straightforward to use Dowell's contribution. But power engineers must understand some restrictions of Dowell's equations so that improved equations might be used to get an accurate result, i.e. combining with Fourier analysis. Interleaved winding arrangement can significantly reduce the ac resistance. In addition, the fringing effect in the gapped inductor must be taken into account since an extremely high eddy current effects are induced in the windings.

- Simple core loss calculation with Steinmetz equation is not valid in most power electronics application. The improved generalized Steinmetz equation needs to be taken into account. Until now, there are still many efforts on the precise calculation and measurement for core loss, particularly at high frequency.

- A low leakage inductance in planar transformer has been touted by the commercial operation. The thesis has illustrated that low leakage inductance is not an intrinsic property of planar transformer, whereas a higher leakage inductance is provided. The only benefit of planar transformer in this regard is the relative ease with which primary and secondary windings can be heavily interleaved. Detailed leakage inductance calculation and suggested methods for reducing leakage inductance are introduced. In some application, a high leakage inductance is required, and thus two additional methods for increasing leakage are also introduced in this thesis.

- High interwinding capacitance is an intrinsic property of planar winding transformer, and thus it cannot be neglected. The interwinding capacitance is always contradiction with leakage inductance. The voltage potential between turns, between winding layers, and between windings and core create this parasitic element. Detailed analysis of interwinding capacitance for planar transformer has been presented.

- There are many trade-offs among winding loss, core loss, leakage inductance and capacitance. The trade-offs analysis has been described, and also an improved interleaved winding arrangement with m=0.5 (MMF ratio) has been proposed to further decrease winding conduction loss and leakage inductance.

Planar integrated magnetics technique as a major part of this thesis has been investigated. In the beginning of this chapter, the history and the evolution of integrated magnetics in power converters have been described. It is recalled, that integrated magnetics is to allow less number of parts, lower volume and cost of the converter, and higher efficiency. With the development of multilayer PCB, the integrated magnetics with planar structure can be easily implemented. The integrated approaches and the modeling have been introduced.

- E-I-E core structure with integrated transformers and inductors has been applied into the two recent developed dc-dc topologies. Detailed analysis of principle, design considerations and power losses are presented. Results from the experimental comparisons demonstrate that the PIM module is fully functional and electromagnetically equivalent to the discrete magnetics and a significant reduction of size can be achieved by using the PIM module.

- By using the proposed integrated magnetics approach in E-I-E core structure, the transformer secondary winding can be re-used during start-up as a flyback winding coupled to the boost inductor. The traditional added flyback winding coupled to the boost inductor is thus eliminated from the circuit, bringing substantial cost savings, increased efficiency and simplified design.

- A new method to integrate the current balancing transformer with common input inductor for the primary-parallel dc-dc converter is proposed. The integrated solution has an advantage of eliminating the extra core for the current balancing transformer, reducing the cost and the volume of the converter. Meanwhile, additional inductances appearing in the forward path reduce the input inductor current ripple.

- A low profile and low cost integrated inductors with stacked I-cores for multiple-phase interleaved dc-dc converters has been proposed. The characteristic of the stacked I-cores has been analyzed, and some advantages and disadvantages have

been described. A special gradual saturation behavior has been found, and thus a variable inductor is formed.

- Ultra-thin coupled inductors design for flexible PV module has been introduced. A 1.5-mm thickness integrated coupled inductor with sandwich core structure is under investigation.

- A "four quadrants integrated transformer" utilizing orthogonal flux to decouple the two primary windings has been applied into a dual-input isolated boost dc-dc converter. This allows the two input power sources to be operated independently, solving the common problem in current multiple-input dc-dc converters. Many advantages of the proposed transformer have been described such as independent operation, cost-effective, low size, high efficiency, wide range input/output voltages and special waveforms characteristics etc.

5.2 Future Works

- The continued fundamental researches for planar magnetics are necessary. In order to have an optimum design of dc-dc converter, accurate modeling for winding loss, core loss, leakage inductance and interwinding capacitance needs to be further investigated.

- The primary-parallel isolated boost converter employing the proposed E-I-E integrated core structure needs a re-design version in order to heave the advantage of planar core. Sandwich converter structure with flat heatsinks and Direct-FETs might be used. The new version will minimize the stay inductance in primary loop to reduce the switching loss. And the proposed start-up function will be included as well. The expected aim is 60 W/in^3 and 98% power efficiency.

- Ultra-thin coupled inductor design for flexible PV module needs an experimental demonstration. Continued collaboration with EPP group of TU delft is expected.

- More investigations on the four quadrant integrated transformer are expected. It is predicted that IM technique with new core geometry may have a great potential on the development of advanced converter topologies, and even bring a revolutionary advancement in power electronics.

Appendix A

Appendix A is a list of publications accomplished during this PhD study.

Journal Papers:

[1] **Z. Ouyang**, Z. Zhang, M. A. E. Andersen and O. C. Thomsen, "Four quadrants integrated transformers for dual-input isolated dc-dc converters," *IEEE Transactions on Power Electronics Letter*, 2011. (Accepted, TPEL-Letter-2011-10-0082)

[2] **Z. Ouyang**, G. Sen, O. C. Thomsen and M. A. E. Andersen, "Analysis and design of fully integrated planar magnetics for primary-parallel isolated boost converter," *IEEE Transactions on Industrial Electronics*, 2011. (Accepted, 11-1386-TIE)

[3] Z. Zhang, **Z. Ouyang**, O. C. Thomsen and M. A. E. Andersen, "Analysis and design of a bidirectional isolated dc-dc converter for fuel cell and super-capacitor hybrid system," *IEEE Transactions on Power Electronics*, 2011. (In press, digital object identifier: 10.1109/TPEL.2011.2159515)

[4] **Z. Ouyang**, Z. Zhang, O. C. Thomsen and M. A. E. Andersen, "Planar integrated magnetics (PIM) module in hybrid bidirectional dc-dc converter for fuel cell application," *IEEE Transactions on Power Electronics*, vol.26, no.11, pp.3254-3264, Nov. 2011.

[5] **Z. Ouyang**, O. C. Thomsen and M. A. E. Andersen, "Optimal design and tradeoff analysis of planar transformer in high-power dc–dc converters," *IEEE Transactions on Industrial Electronics*, 2010. (In press, digital object identifier: 10.1109/TIE.2010.2046005)

Conference Papers:

[6] **Z. Ouyang**, M. Acanski, J. Popovic-Gerber, J. A. Ferreira, O. C. Thomsen and M. A. E. Andersen, "Design consideration of ultra-thin coupled inductors for photovoltaic application," in *Proc. IEEE CIPS,* Nuremberg, Germany, March, 2012. (Accepted)

[7] M. Acanski, **Z. Ouyang**, J. Popovic-Gerber and J. A. Ferreira, "Design of very low profile coupled inductors for PV module integrated converters," in *Proc. IEEE CIPS,* Nuremberg, Germany, March, 2012. (Accepted)

[8] K. L.-Poulsen, **Z. Ouyang**, G. Sen and M. A. E. Andersen, "A new method for start-up of isolated boost converters using magnetic- and winding-integration," *in Proc. IEEE APEC*, Orlando, Florida, U.S.A, Feb., 2012. (Accepted)

[9] G. Sen, **Z. Ouyang**, O. C. Thomsen, M. A. E. Andersen and L. Møller, "Integrated current balancing transformer for primary parallel isolated boost converter," *in Proc. EPE,* Birmingham, U.K, Sept. 2011.

[10] **Z. Ouyang**, G. Sen, O. C. Thomsen and M. A. E. Andersen, "Fully integrated planar magnetics for primary-parallel isolated boost converter," *in Proc. IEEE APEC*, pp.174-181, Fort Worth, TX, U.S.A, March, 2011.

[11] **Z. Ouyang**, O. C. Thomsen, M. A. E. Andersen and T. Björklund, "Low profile, low cost, new geometry integrated inductors," *in Proc. IEEE APEC*, pp.150-156, Fort Worth, TX, U.S.A, March, 2011.

[12] **Z. Ouyang**, O. C. Thomsen, M. A. E. Andersen and T. Björklund, "A new geometry integrated inductors for two-phase interleaved buck converter," *in Proc. IEEE IECON*, pp. 582-586, Phoenix, AZ, U.S.A, Nov., 2010.

[13] **Z. Ouyang**, Z. Zhang, O. C. Thomsen, M. A. E. Andersen, O. Poulsen and T. Björklund, "Planar integrated magnetics design in wide input range dc-dc converter for fuel cell application," *in Proc. IEEE ECCE*, pp. 4611-4618, Atlanta, U.S.A, Sept., 2010.

[14] G. Sen, **Z. Ouyang**, O. C. Thomsen, M. A. E. Andersen and L. Møller, "A high efficient integrated planar transformer for primary-parallel isolated boost converters," *in Proc. IEEE ECCE*, pp. 4605-4610, Atlanta, U.S.A, Sept., 2010.

[15] **Z. Ouyang**, O. C. Thomsen and M. A. E. Andersen, "Optimal design and tradeoffs analysis of planar transformer in high power dc-dc converters," *in Proc. IEEE IPEC (ECCE-ASIA)*, pp. 3166-3173, Sapporo, Japan, Jun. 2010.

[16] **Z. Ouyang**, O. C. Thomsen and M. A. E. Andersen, "The analysis and comparison of leakage inductance in different winding arrangements for planar transformer," *in Proc. IEEE PEDS*, pp. 1143–1148, Taipei, Taiwan, Nov. 2009.

Patent Applications:

[17] **Z. Ouyang**, M. A. E. Andersen and Z. Zhang, "An integrated magnetics component," *EU & US Patent*, US application no. 61534202, and EU application no. EP11181106.3, 2011 (pending).

[18] K. L.-Poulsen, **Z. Ouyang** and G. Sen, "An isolated boost flyback power converter," *EU & US Patent*, US application no. 61505205, and EU application no. EP11172997.6, 2011 (pending).

Appendix B

Appendix B contains a list of selected publications made as part of this thesis i.e. conference papers, journal papers and patent applications.

[B.1] Z. Ouyang, O. C. Thomsen and M. A. E. Andersen, "Optimal design and tradeoff analysis of planar transformer in high-power dc–dc converters," *IEEE Transactions on Industrial Electronics*, 2010. (In press, digital object identifier: 10.1109/TIE.2010.2046005)

[B.2] Z. Ouyang, O. C. Thomsen and M. A. E. Andersen, "The analysis and comparison of leakage inductance in different winding arrangements for planar transformer," *in Proc. IEEE PEDS*, pp. 1143–1148, Taipei, Taiwan, Nov. 2009.

[B.3] Z. Ouyang, Z. Zhang, O. C. Thomsen and M. A. E. Andersen, "Planar integrated magnetics (PIM) module in hybrid bidirectional dc-dc converter for fuel cell application," *IEEE Transactions on Power Electronics*, 2011. (In press, digital object identifier: 10.1109 /TPEL.2011.2129598)

[B.4] Z. Ouyang, G. Sen, O. C. Thomsen and M. A. E. Andersen, "Analysis and design of fully integrated planar magnetics for primary-parallel isolated boost converter," *IEEE Transactions on Industrial Electronics*, 2011. (Submitted, 11-1386-TIE)

[B.5] K. L.-Poulsen, Z. Ouyang, G. Sen and M. A. E. Andersen, "A new method for start-up of isolated boost converters using magnetic- and winding-integration," *in Proc. IEEE APEC*, Orlando, Florida, U.S.A, Feb., 2012. (Accepted)

[B.6] G. Sen, Z. Ouyang, O. C. Thomsen, M. A. E. Andersen and L. Møller, "Integrated current balancing transformer for primary parallel isolated boost converter," *in Proc. EPE,* Birmingham, U.K, Sept. 2011.

[B.7] Z. Ouyang, O. C. Thomsen, M. A. E. Andersen and T. Björklund, "Low profile, low cost, new geometry integrated inductors," *in Proc. IEEE APEC*, pp.150-156, Fort Worth, TX, U.S.A, March, 2011.

[B.8] Z. Ouyang, M. Acanski, J. Popovic-Gerber, J. A. Ferreira, O. C. Thomsen and M. A. E. Andersen, "Design consideration of ultra-thin coupled inductors for photovoltaic application," in *Proc. IEEE CIPS,* Nuremberg, Germany, March, 2012. (Submitted)

[B.9] Z. Ouyang, Z. Zhang, M. A. E. Andersen and O. C. Thomsen, "Four quadrants integrated transformers for dual-input isolated dc-dc converters," *IEEE Transactions on Power Electronics Letter*, 2011. (Submitted, TPEL-Letter-2011-10-0082)

[B.10] K. L.-Poulsen, Z. Ouyang and G. Sen, "An isolated boost flyback power converter," *EU & US Patent*, US application no. 61505205, and EU application no. EP11172997.6, 2011 (pending).

[B.11] Z. Ouyang, M. A. E. Andersen and Z. Zhang, "An integrated magnetics component," *EU & US Patent*, US application no. 61534202, and EU application no. EP11181106.3, 2011 (pending).

Appendix B.1

[B.1] Z. Ouyang, O. C. Thomsen and M. A. E. Andersen, "Optimal design and tradeoff analysis of planar transformer in high-power dc–dc converters," *IEEE Transactions on Industrial Electronics*, 2010. (In press, digital object identifier: 10.1109/TIE. 2010.2046005)

Optimal Design and Tradeoff Analysis of Planar Transformer in High-Power DC–DC Converters

Ziwei Ouyang, *Student Member, IEEE*, Ole C. Thomsen, *Member, IEEE*, and Michael A. E. Andersen, *Member, IEEE*

***Abstract*—The trend toward high power density, high operating frequency, and low profile in power converters has exposed a number of limitations in the use of conventional wire-wound magnetic component structures. A planar magnetic is a low-profile transformer or inductor utilizing planar windings, instead of the traditional windings made of Cu wires. In this paper, the most important factors for planar transformer (PT) design including winding loss, core loss, leakage inductance, and stray capacitance have individually been investigated. The tradeoffs among these factors have to be analyzed in order to achieve optimal parameters. Combined with an application, four typical winding arrangements have been compared to illustrate their advantages and disadvantages. An improved interleaving structure with optimal behaviors is proposed, which constructs the top layer paralleling with the bottom layer and then in series with the other turns of the primary, so that a lower magnetomotive force ratio m can be obtained, as well as minimized ac resistance, leakage inductance, and even stray capacitance. A 1.2-kW full-bridge dc–dc converter prototype employing the improved PT structure has been constructed, over 96% efficiency is achieved, and a 2.7% improvement, compared with the noninterleaving structure, is obtained.**

***Index Terms*—Core loss, dc–dc converter, finite-element analysis (FEA), interleaving, leakage inductance, magnetomotive force (MMF), planar transformer (PT), stray capacitance, winding loss.**

I. Introduction

THE trend toward high power density, high operating frequency, and low profile in power converters has exposed a number of limitations in the use of conventional wire-wound magnetic component structures. In recent years, planar transformer (PT) has become increasingly popular in high-frequency power converters because of the unique advantages that they achieved in terms of low profile, excellent thermal characteristic, modularity and manufacturing simplicity, increased reliability, and power density [1]–[3]. The use of higher switching frequency can result in passive component size reduction, which achieves higher power density in power converter. However, also for the conventional magnetic structures, the demand of high-frequency operation also causes a number of limitations in planar magnetic structures, such as the problem of increased losses due to the skin and the proximity effects, particularly at frequencies above 100 kHz. Regarding winding ac resistance, many efforts have been made to derive expressions allowing for an accurate representation of frequency behavior of ac resistance. The ac resistance effects due to high-frequency current are specifically tailored for transformers by Dowell [4]. This work is based on a 1-D solution of the diffusion equation, as applied to conducting parallel plates. The expression for ac resistance has been rearranged in [5] due to the squared porosity factor η. The comparison of various methods for calculating the ac resistance of windings is given in [6]. The papers [7]–[9] analyze and improve the ac resistance expression specifically for different situations. Based on Dowell's equation, an optimum layer thickness of conductors minimizing winding loss can be found, which also significantly affects the leakage inductance, as shown in [20]. Regarding core loss, there are three main methods to calculate: 1) hysteresis models [11], [12]; 2) loss separation approach [13]; and 3) empirical methods. The empirical approach enables loss determination with manufacturer-provided data with an easy way to use expression. The typical expression, i.e., the Steinmetz equation, is limited by some constraints, so that many publications focus on improving Steinmetz equation to extend its use [14]–[19].

In this paper, a detail analysis in winding loss, core loss, leakage inductance, and stray capacitance has been presented. The tradeoffs among these factors have to be analyzed in order to achieve an optimal design. Furthermore, winding arrangements can, in part, bring an optimal behavior in the tradeoffs without any sacrifices, which play an important role in optimizing PT. Combining with an application in 1.2-kW full-bridge dc–dc converter, four different winding arrangements have been compared to illustrate each their merits and drawbacks. An improved interleaving structure 0.5P-S-P-S-P-S-P-S-0.5P is proposed, which constructs the top layer paralleling with the bottom layer and then in series with the other turns of the primary, so that a lower magnetomotive force (MMF) ratio m can be obtained, as well as minimized ac resistance, leakage inductance, and even stray capacitance. The detail experimental results have been shown in Section IV.

II. Detail Design Consideration

A. Winding Loss

Winding losses in transformers dramatically increase with high frequency due to eddy current effects. For design and optimization of transformers, there is a need for an accurate prediction of the winding losses over a wide frequency range and for various winding arrangements. Eddy current losses,

Manuscript received November 27, 2009; revised March 10, 2010; accepted January 25, 2010. This work was supported by Flux A/S.

The authors are with the Department of Electrical Engineering, Technical University of Denmark, 2800 Kongens Lyngby, Denmark (e-mail: zo@elektro.dtu.dk; oct@elektro.dtu.dk; ma@elektro.dtu.dk).

Color versions of one or more of the figures in this paper are available online at http://ieeexplore.ieee.org.

Digital Object Identifier 10.1109/TIE.2010.2046005

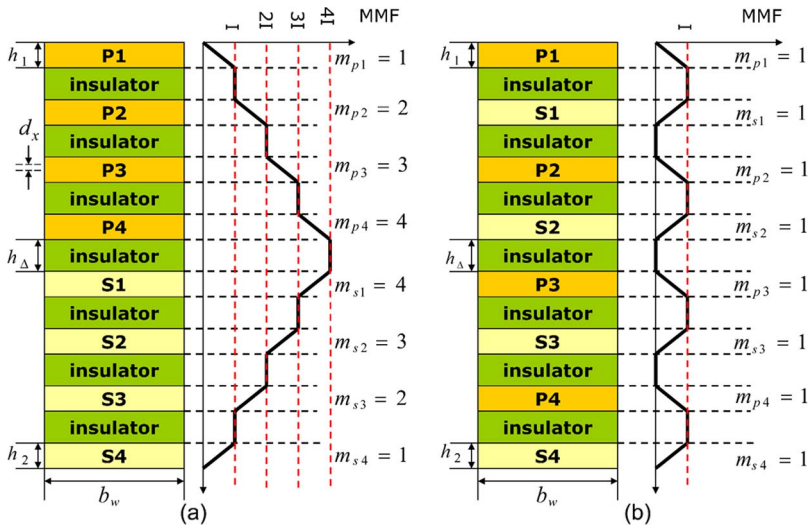

Fig. 1. MMF distributions. (a) Noninterleaving arrangement. (b) Interleaving arrangement.

including skin effect and proximity effect losses, seriously impair the performance of transformers in high-frequency power conversion applications. For ac current flowing in a conductor, the alternating field inside this conductor induces eddy currents in the conductor, which produce a field that tends to cancel the field produced by the original current. The tendency of the alternating current distributes itself within the conductor, so that the current density near the surface of the conductor is greater than that at its center. This is called skin effect, which causes the effective resistance of the conductor to increase with the frequency of the current. The proximity effect is similar, but it is caused by the current carried by an adjacent conductor. The current in the adjacent conductor causes a time-varying field and induces a circulating current inside the conductor. Both the skin effect and the proximity effect cause the current density to be nonuniform in the cross section of the conductor and thus cause a higher winding resistance at higher frequency.

The skin effect of an infinite foil conductor with sinusoidal excitation can be represented by the ratio of ac resistance to dc resistance as in [9]

$$\frac{R_{\rm ac}}{R_{\rm dc}} = \frac{\xi}{2} \cdot \frac{\sinh\xi + \sin\xi}{\cosh\xi - \cos\xi} \tag{1}$$

where $\xi = h/\delta$, and δ is the skin depth in the conductor.

Based on Dowell's assumptions and the general field solutions for the distribution of current density in a single layer of an infinitely foil conductor, the expression for the ac resistance of the mth layer is derived as [5], [9]

$$\frac{R_{{\rm ac},m}}{R_{{\rm dc},m}} = \frac{\xi}{2}\left[\frac{\sinh\xi + \sin\xi}{\cosh\xi - \cos\xi} + (2m-1)^2 \cdot \frac{\sinh\xi - \sin\xi}{\cosh\xi + \cos\xi}\right] \tag{2}$$

where m is defined as a ratio in

$$m = \frac{F(h)}{F(h) - F(0)} \tag{3}$$

where $F(0)$ and $F(h)$ are the MMFs at the limits of a layer, as shown in Fig. 1. The first term in (2) is identical to (1), which describes the skin effect. In addition, the second term represents the proximity effect factor. The proximity effect loss, in a multilayer winding, may strongly dominate over the skin effect loss, depending on the value of m, which is related to the winding arrangement. Interleaving transformer windings can significantly reduce the proximity loss when the primary and secondary currents are in phase. Fig. 1(a) and (b) shows the MMF distributions along the vertical direction for noninterleaving arrangement and fully interleaving arrangement, respectively. The value of m can be calculated according to (3), and quite different results are also shown in Fig. 1.

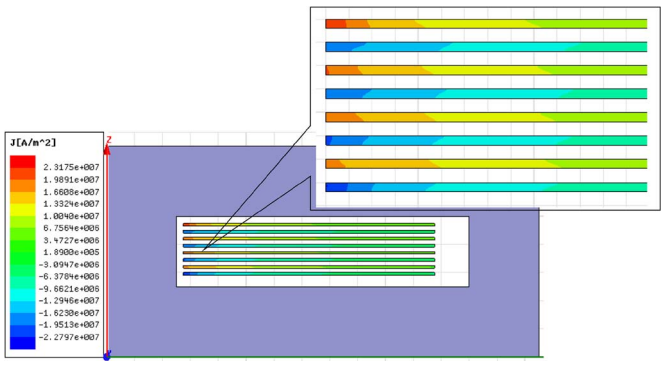

Fig. 2. Current distribution in fully interleaving arrangement.

In order to further illustrate the eddy current effect in different arrangements, a finite-element analysis (FEA) tool is used to analyze current distribution inside the conductors. Figs. 2 and 3 individually represent current distributions for interleaving windings and noninterleaving windings when the excitation frequency is 50 kHz. A 2-D PT model with cylindrical symmetry about the Z-axis has been built, and all of the conditions are the same in both figures, except the winding arrangement. It can be seen from the two figures that current density is higher toward the symmetrical Z-axis due to the dc spirality effect. The skin and the proximity effects can further increase the nonuniform distribution of current density when the frequency goes high. In other words, the color division of current distribution is caused not only by the dc spirality effect but also by the

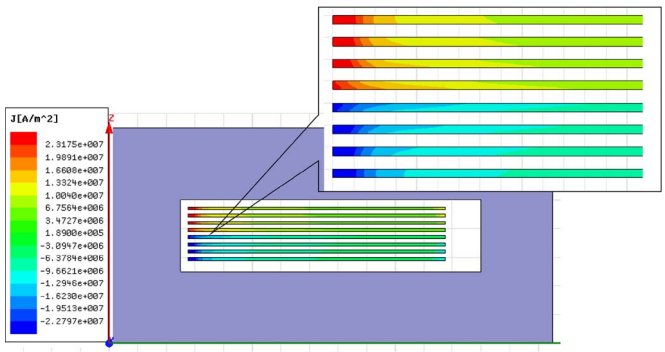

Fig. 3. Current distribution in noninterleaving arrangement.

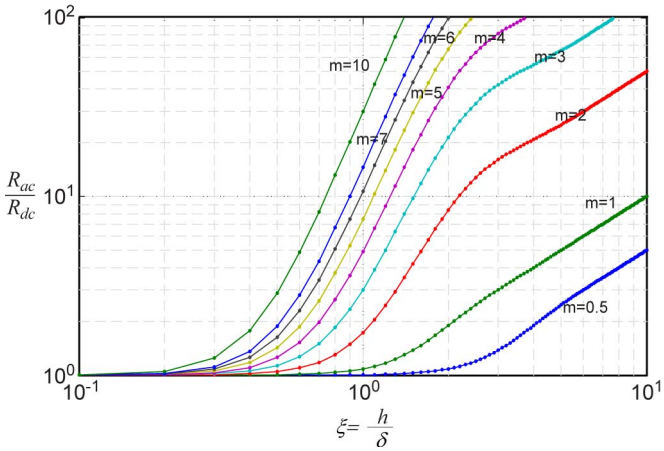

Fig. 4. Ratio of ac resistance to dc resistance as a function of ξ and MMF ratio m.

skin and the proximity effects. It is noteworthy that ac resistance will not be contributed by the dc spirality effect. For the noninterleaving arrangement in Fig. 3, the tendency of current density toward conductor surface is enhanced due to higher proximity effect. The strongest tendency toward conductor surface appears in the layer close to the interface between the primary and the secondary, and thus, the area of color division becomes smaller, which means that a higher ac resistance will be produced.

As seen in (2), ac resistance is not only related to MMF ratio m but also dependent on the ratio ξ. With a given frequency, the minimal ac resistance can be determined by the layer thickness of windings. The choice of thickness as a physical parameter has been a key in optimizing PT. Fig. 4 shows that the ratio of ac resistance to dc resistance increases with increasing thickness at a fixed frequency. For a large m, the proximity effect dominates over the skin effect, which leads to a higher winding resistance. With decreasing thickness of the conductor, the ratio is close to 1, which represents a low eddy current effect in the conductor, but the dc resistance will be increased. Hereby, minimal ac resistances can be figured out for different MMF ratios m, as shown in Fig. 5. Regarding the case that several number of turns are involved in a layer, the proximity effect among them in the horizontal direction can almost be negligible if the width is much more than the thickness; otherwise, the porosity factor η needs to be introduced [5], [9]. As shown in Fig. 5, the MMF ratio m is referred to be as small as possible, so that a minimal

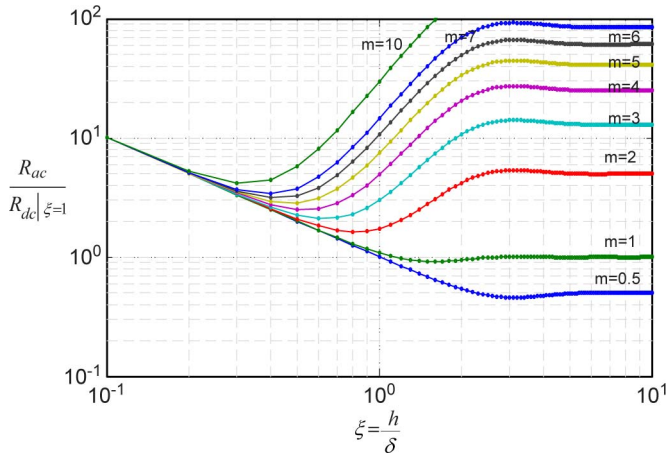

Fig. 5. AC resistance relative to dc resistance in a layer having an effective thickness of skin depth.

ac resistance can be obtained. In fact, it is not practical in the middle frequency, because a relative thicker conductor needs to be used. The window space of the core is also a limitation on this issue. However, in high-frequency application (above 500 kHz), the MMF ratio m of 0.5 can practically be implemented because of a very small skin depth.

Parallel connection of multilayer for planar winding is now usually employed to increase the current handling capacity of the winding. However, with parallel winding connections, the magnetic field around windings becomes more complicated. Due to the leakage fluxes and the high-frequency effects, the currents may not be equally shared among the paralleled layers. In other words, circulating currents may exist in parallel layers, which contributes to an extra winding loss. References [1] and [10] present the extra winding loss caused by "parallel effect loss" (circulating currents) in detail.

There are many limitations on the validity of (2) such as the minimum distances between consecutive turns, between adjacent layers, and between the conductor edge and the magnetic core, as well as sinusoidal waveform. The most outstanding work as a calculation method of the ac resistance for any current waveform to correct Dowell's assumptions can be found in [8]. In addition, several publications also get generalized correction factors to be applied in Dowell's resistance factor expression. However, these factors are usually derived from elaborated formulas and have to be determined from complicated coefficient tables [9]. Outside these minimum boundaries, it is advisable to determine winding losses with FEA simulations.

B. Core Loss

Referring to most of the literature, there are three main methods to deal with magnetic loss: 1) hysteresis models; 2) loss separation approach; and 3) empirical methods. The former is usually based on the Jiles–Atherton or Preisach models [11], [12]. The loss separation approach assumes that three fundamental effects are contributing to core losses: 1) static hysteresis loss; 2) eddy current loss; and 3) excess eddy current loss [13]. Finally, the empirical approaches are based on the Steinmetz equation, which is a curve-fitting expression

of measured data under sinusoidal excitation. Although the hysteresis models and loss separation approach can lead to satisfactory results, they require extensive computations and measurement works. Empirical approach enables loss determination with manufacturer-provided data with an easy way to use expression.

Nowadays, Steinmetz equation is widely used in the design of magnetic components in power converters, which expresses core loss density as power law with fixed exponent of frequency and flux density

$$P_v = K \cdot f^{\alpha} \cdot (\Delta B/2)^{\beta} \tag{4}$$

where K, α, and β are constants provided by the manufacturer, and ΔB is the peak-to-peak flux density that can be obtained from Faraday's law

$$\Delta B = \frac{V \cdot \Delta t}{N \cdot A_e} \tag{5}$$

where N is the number of turns, A_e is the cross section of the core, and $V \cdot \Delta t$ means volt-seconds.

However, (4) is only valid for sinusoidal waveform, and in some cases, loss for nonsinusoidal waveform can far exceed the loss due to sinusoidal ones, even when the frequencies and the peak flux densities are both equal. Reference [19] has proven that core loss can lead to an error of up to 45% in relation to the measured results for an H-bridge converter case operating with square waveform with zero-voltage period. In order to deal with any waveforms, some modified expressions including modified Steinmetz expression (MSE) [14], generalized Steinmetz equation (GSE) [15], improved GSE (IGSE) [16], natural Steinmetz extension [17], equivalent elliptical loop [18], and waveform coefficient Steinmetz equation [19] were introduced. A complete comparison among these modified empirical methods for a bidirectional isolation dc–dc converter shows that the MSE and the IGSE have the best loss determination; however, the IGSE copes better with a wide variety of voltage waveform [19]

$$P_v = \frac{1}{T}\int_0^T k_i \cdot \left|\frac{dB(t)}{dt}\right|^{\alpha} \cdot (\Delta B)^{\beta-\alpha} \cdot dt$$

$$k_i = \frac{K}{(2\pi)^{\alpha-1} \cdot \int_0^{2\pi} |\cos\theta|^{\alpha} \cdot 2^{\beta-\alpha} \cdot d\theta}. \tag{6}$$

K, α, and β are determined by equating the loss expression for a sinusoidal excitation case with (4). The angle θ represents the phase angle of the sinusoidal waveform. Applying a piecewise linear model (PWL) to the nonsinusoidal waveform and then combining it with the IGSE leads to an easy-to-use expression for the determination of core loss. Furthermore, it is believed that the IGSE is the most practical method for calculating core loss with nonsinusoidal waveforms in most high-frequency magnetic design work, because it requires only readily available sinusoidal loss data, in the form of parameters for the Steinmetz equation characterizing the material. For the full-bridge dc–dc converter operating with the symmetrical square waveforms, a new extension of Steinmetz equation can be deduced based on the IGSE and the PWL model

$$P_v = 2^{2\alpha-1} \cdot K \cdot f^{\alpha} \cdot B_{\mathrm{sqm}}^{\beta} \cdot D^{\beta-\alpha+1} \tag{7}$$

where D is the switching duty cycle. B_{sqm} is the peak flux density when the square waveform is with 50% duty cycle, which can be obtained from (5), i.e., $B_{\mathrm{sqm}} = (V \cdot T)/(4N \cdot A_e)$.

According (7), core loss can be determined by the number of turns, core cross section, excitation voltage, duty cycle, core volume, and material. The peak flux is inversely proportional with the frequency, and the exponent β is higher than the exponent α in general magnetic materials. Therefore, core loss will decrease with increasing frequency. The frequency leads to a tradeoff between winding loss and core loss, because high frequency significantly increases ac resistance, as presented before. With increasing number of turns, core loss can be benefited from the lower peak flux density but sacrificing winding loss. Using several cores to be cascaded to increase the core cross section can minimize the flux density, but it also increases winding loss, because an extra length of winding is added.

C. Leakage Inductance

Not all the magnetic flux generated by ac current excitation on the primary side follows the magnetic circuit and link with the secondary winding. The flux linkage between two windings or parts of the same winding is never complete. Some flux leaks from the core and returns to the air, winding layers, and insulator layers; thus, these flux causes imperfect coupling.

The energy associated with leakage inductance can be calculated according to analytical MMF distribution and energy distribution. From Fig. 1, the differential volume of each turn is $l_w \cdot b_w \cdot dx$; therefore, the total energy is the sum of the energy stored in each elementary layer, which can be given by

$$E_{lk} = \frac{\mu_0}{2} \sum \int_0^h H^2 \cdot l_w \cdot b_w \cdot dx \tag{8}$$

where l_w is the length of each turn, b_w is the width of each turn, and h represents the thickness of each winding layer. The thickness dx is situated at a distance x from the inner surface of conductor. The field strength H depends on the number of ampere turns linked by the leak flux path. Since the flux rapidly disperses on leaving the winding, the associated energy is much reduced, and the reluctance of the path within the magnetic core can be ignored, compared with that of the path in the windings; thus, the flux path can be expressed by the width b_w rather than the full closed flux path [20], [21]. According to (8), for

a noninterleaving structure in Fig. 1(a), the leak energy in the total winding space can be deduced then as

$$E_{lk}=\frac{\mu_0}{2}\cdot l_w\cdot b_w\left[4\int_0^{h_1}\left(\frac{I_1}{b_w}\cdot\frac{x}{h_1}\right)^2\cdot dx+4\int_0^{h_2}\left(\frac{I_1}{b_w}\cdot\frac{x}{h_2}\right)^2\cdot dx+\left(\frac{I_1}{b_w}\right)^2\cdot(h_1+h_2+2h_\Delta)+\left(\frac{2I_1}{b_w}\right)^2\cdot(h_1+h_2+2h_\Delta)+\left(\frac{3I_1}{b_w}\right)^2\cdot(h_1+h_2+2h_\Delta)+\left(\frac{4I_1}{b_w}\right)^2\cdot h_\Delta\right]$$

$$E_{lk}=\frac{\mu_0}{2}\cdot\frac{l_w}{b_w}\left[\frac{46(h_1+h_2)}{3}+44h_\Delta\right]\cdot I_p^2 \tag{9}$$

where h_1 and h_2 are the lay thicknesses of the primary and the secondary, respectively, and h_Δ is the height of the insulator layer. However, as for fully interleaving arrangement in Fig. 1(b), with the same approach, leakage inductance can be deduced as follows:

$$L_{\text{leakage}}=\mu_0\cdot\frac{l_w}{b_w}\cdot 4\left[\frac{h_1+h_2}{3}+h_\Delta\right]. \tag{10}$$

Apparently, the fully interleaving arrangement provides a significant advantage in reducing leakage inductance. As a conclusion, aside from winding structures, leakage inductance in PT can be changed by adjusting some physical parameters, including conductor thickness and its width, insulator thickness, and the number of turns. As a parasitic element exists in transformers, the leakage inductance causes the main switch current at the device input to vary at a low slope between zero and the rated value and reduces the rate of commutation between the output diodes. In addition, the stored energy in the leakage inductance leads to a generation of voltage spikes on the main switch, which, aside from creating electromagnetic interference (EMI) problems, increases the switching losses and lowers the efficiency. However, in some applications such as a phase-shift-modulated soft-switching dc/dc converter, the magnitude of leakage inductance determines the achievable load range under zero-voltage-switching operation, and a relatively large leakage inductance is desirable. In order to avoid an additional magnetic component, a leakage layer with low permeability has been inserted between the primary and the secondary to form a resonant inductor [22].

D. Stray Capacitance

Stray capacitance in designing PT cannot be ignored. The potential between turns, between winding layers, and between windings and core create this parasitic element. In most papers about optimizing PT, the main purpose is to reduce leakage inductances, but stray capacitances have not seriously been considered. In fact, stray capacitances significantly affect the magnetic component performance in such a way that the current waveform on the excitation side would be distorted and the overall efficiency of converters would be decreased. Subjected to high-voltage stresses, stray capacitance between windings causes leakage currents and consequently contributes EMI problem [25].

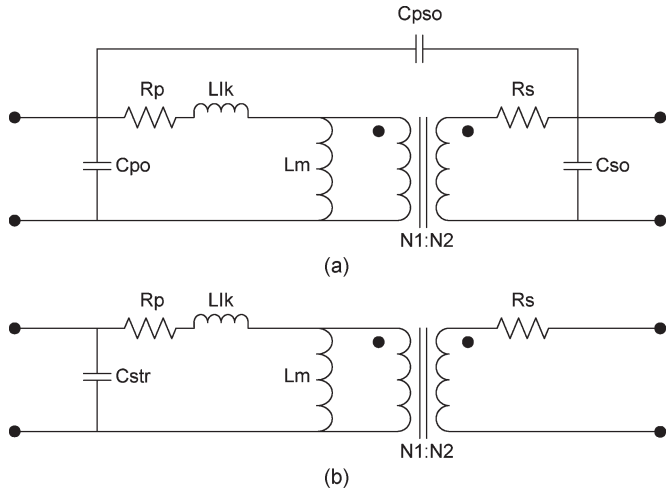

Fig. 6. Equivalent circuit of the transformer model (a) with self-capacitances and mutual capacitance and (b) with a single lumped stray capacitance referred to the primary side.

Considering an equivalent model of two-winding PT, as shown in Fig. 6, where R_p and R_s are the resistances of the primary and secondary windings. C_{po}, C_{so}, and C_{pso} are used to account for the self-capacitances of the primary and the secondary windings and the mutual capacitance between the two windings, respectively. It is desirable to keep C_{pso} to be as small as possible, and good EMI results could be achieved. The equivalent capacitors referred to the primary side can approximately be determined by the following relations [26]:

$$\begin{aligned}C_p&=C_{\text{po}}+(1-k)\cdot C_{\text{pso}}\\ C_s&=k^2\cdot C_{\text{so}}-k\cdot(k-1)\cdot C_{\text{pso}}\\ C_{\text{str}}&\approx C_p+C_s\end{aligned} \tag{11}$$

where k is the turns ratio. The mutual capacitance C_{pso} due to the electrical coupling between the primary and secondary windings can approximately be measured directly by shorting both primary and secondary sides. The single equivalent capacitance referred to the primary side C_{str} in Fig. 7 can approximately be computed by (11).

In the case of PTs, static layer capacitances can easily be estimated since the windings consist of parallel and flat conductors. The formula for the capacitance between two parallel conductive plates is given by

$$C_0=\varepsilon_r\cdot\varepsilon_0\cdot\frac{S}{h_\Delta} \tag{12}$$

where ε_0 is the permittivity of free air space, and ε_r is the relative permittivity of the material. In addition, S represents the overlapping surface area of the two plates. The distance between the plates is h_Δ. Fig. 7(a) shows an equivalent potential distribution model in dependence on the internal two layers of

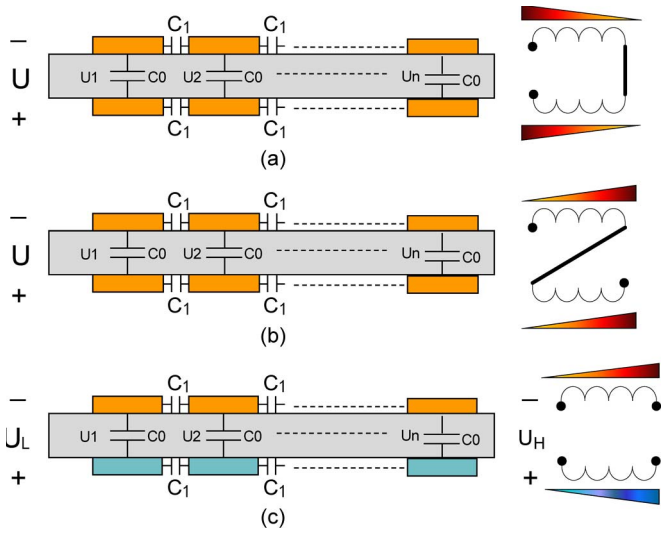

Fig. 7. Equivalent potential distribution model in dependence on (a) the internal two layers of the same winding with opposite directions, (b) the internal two layers of the same winding with the same direction, and (c) the two layers of the different windings.

the same winding with opposite directions. Assuming that the potential distribution along the turns linearly varies, i.e.,

$$U_i = \frac{(n+1)-i}{n} \cdot U, \qquad (i = 1, 2, 3, \ldots, n) \tag{13}$$

where n is the number of turns in each layer, and U_i represents the potential in each pair of plates. U is the voltage potential between the two terminations of the winding. The turn-to-turn capacitance C_1 can be ignored by comparing with the layer-to-layer capacitance C_0 due to a very small overlapping surface area. The total energy associated with the electric field in the two layers is given by

$$\begin{aligned} E = \sum_{i=1}^{n} E_i &= \frac{1}{2} C_0 U^2 \sum_{i=1}^{n} \left(\frac{n+1-i}{n} \right)^2 \\ &= \frac{(n+1)(2n+1)}{12n} C_0 U^2. \end{aligned} \tag{14}$$

The equivalent capacitance of the same winding can be expressed by

$$C_d = \frac{2E}{U^2} = \frac{(n+1)(2n+1)}{6n} C_0. \tag{15}$$

If there are m layers in series for the same winding as the same connection as Fig. 7(a), the overall equivalent capacitance could be deduced by equating the electric energy stored in all layer capacitors [29]

$$C_d' = \frac{4(m-1)}{m^2} C_d \tag{16}$$

for the connection in Fig. 7(b), which provides an equivalent constant voltage distribution along the turns in each layer. Hereby, a lower equivalent capacitance $C_d = (n/4) \cdot C_o$ in the winding with the same direction has been shown. Regarding stray capacitance in different windings, the voltage difference between the high potential side and the low potential side can be expressed by $U_\Delta = U_H - U_L$, as shown in Fig. 7(c), with the assumption that the linear distributed voltage along different windings is still valid. With the same procedure, the equivalent stray capacitance referred to the primary winding can be deduced by

$$C_w = \frac{2E}{U^2} = \frac{nU_L^2 + \frac{n(2n-1)}{6(n-1)} U_\Delta^2 + nU_L U_\Delta}{U^2} C_0. \tag{17}$$

Based on the preceding analysis for the stray capacitance, the optimal solutions can be concluded as follows: 1) reducing static layer capacitance by enhancing the distance or lowering the overlapping surface area between the two conductor plates; 2) reducing the number of turns in each layer or/and increasing the number of layers; 3) reducing the number of intersections between the primary and the secondary; 4) arranging the winding configurations to obtain the minimal energy associated with the electric field.

III. Tradeoff Analysis

Combining with the analysis of winding loss, core loss, leakage inductance, and stray capacitance, some overlapping occur in affecting each other, as described here.

1) Number of turns N. The lesser the N, the lesser the winding loss but the more the core loss that will be produced due to higher peak flux density; furthermore, a lower leakage inductance can also be obtained. The stray capacitance is also probably benefited, depending on the winding configuration. The choice of N will have to be a key in optimizing design.
2) Excitation frequency f. Although a higher frequency can cause a lower core loss as mentioned before, ac resistance will be increased due to eddy current effect. The leakage inductance slightly decreases with increased frequency because of a small change in the permeability of conductors. The designed frequency has to be considered the carrying capacity of the switching devices and the switching losses.
3) Thickness of conductors h and insulator h_Δ. The optimal thickness h for winding loss has been introduced in Section II. A larger h also causes a larger leakage inductance. There is a contradiction for h_Δ between the leakage inductance and the stray capacitance. The larger the h_Δ, the larger the leakage inductance and the smaller the capacitance. It is impossible to achieve both low values by optimizing the physical parameters. The only way to obtain optimal behaviors of both leakage inductance and stray capacitance is to change the winding configurations. Considering the loss in parasitic elements, a low leakage inductance has priority over a low stray capacitance in high-current low-voltage application. Reversely, in low-current high-voltage application, a low stray capacitance has to be required rather than a low leakage inductance.
4) Core geometry. For a certain number of turns, a bigger cross section A_e of core can bring a lower core loss, but the length of windings will have to be sacrificed, which increases the winding loss.

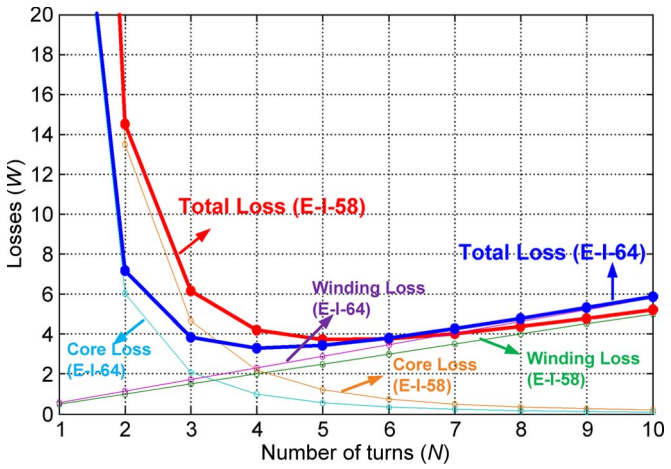

Fig. 8. Total loss, winding loss, and core loss vary with different numbers of turns in comparison of two planar cores.

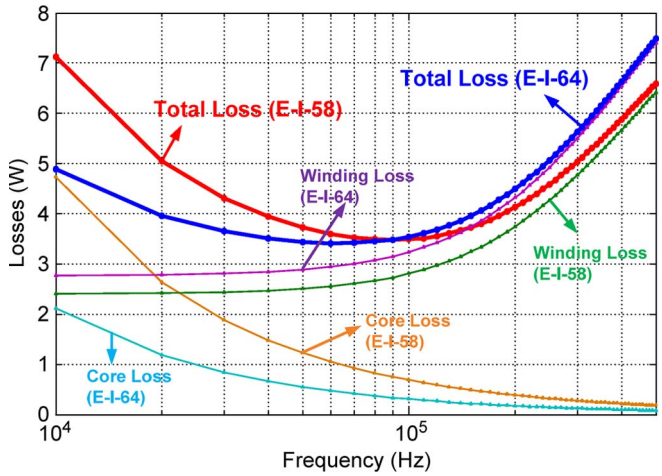

Fig. 9. Total loss, winding loss, and core loss vary with different frequencies in comparison of two planar cores.

In order to facilitate a clear understanding of tradeoffs in PT design, a 1 : 1 turn ratio transformer will be analyzed as an example of simplification. The assumed specification of a full-bridge buck dc–dc converter with primary excitation of 50 V/20 A, 50% duty cycle, and a switching frequency of 50 kHz is used. Full interleaving is employed to make the MMF ratios m in each layer equal to 1. According to the analysis of winding loss and Fig. 5, 0.25-mm-thick conductors are chosen in this example. The authors write a small program in virtue of Matlab to figure out the tradeoffs. Fig. 8 shows that the total loss, the winding loss, and the core loss vary as a function of different numbers of turns when the other parameters are fixed. The red curve and blue curve individually represent the total loss for the E-I-58 core and E-I-64 core. The core losses decrease with the increased number of turns; this is due to the fact that the flux density is reduced. The winding losses, however, increase, because higher dc resistances are achieved. Apparently, an optimal number of turns in this example can be found. In addition, Fig. 9 reflects a relationship between losses and frequency. An optimal frequency for the total loss can be found as well. Taken together as Figs. 8 and 9, the intersection points between the red line and the blue line illuminate the tradeoff also caused by the core geometry.

Following the analysis of ac resistance and core loss, the relationship between the losses and the number of turns N can be written by

$$P_w = K_1 \cdot N$$

$$P_c = K_2 \cdot N^{-\beta}$$

$$K_1 = 2 \cdot I^2 \cdot R_{\mathrm{dc}} \cdot \frac{\xi}{2}\left[\frac{\sinh\xi + \sin\xi}{\cosh\xi - \cos\xi} + \frac{\sinh\xi - \sin\xi}{\cosh\xi + \cos\xi}\right]$$

$$K_2 = 2^{2\alpha-1} \cdot K \cdot f^{\alpha} \cdot \left(\frac{V}{4 \cdot f \cdot A_e}\right)^{\beta} \cdot D^{\beta-\alpha+1}. \tag{18}$$

The total loss is

$$P_t = K_1 \cdot N + K_2 \cdot N^{-\beta}. \tag{19}$$

The minimum of (19) is achieved by taking the partial derivative N and setting to zero, i.e.,

$$\frac{\partial P_t}{\partial N} = K_1 - \beta \cdot K_2 \cdot N^{-\beta-1} = 0. \tag{20}$$

The optimal number of turns N

$$N^{\beta+1} = \frac{\beta \cdot K_2}{K_1} \tag{21}$$

$$P_{wo} = \beta \cdot P_{co}. \tag{22}$$

The minimum loss occurs when the winding loss is β times the core loss. Fig. 8 also proves the place where the minimum loss occurs.

IV. Experimental Comparison

Winding arrangements can also, in part, bring an optimal behavior in the tradeoffs without any sacrifices, which play an important role in optimizing PT. In the following work, four typical winding arrangements are compared to illustrate their advantages and disadvantages. Fig. 10 individually shows their 3-D models. A full-bridge buck dc–dc converter employing these PTs has been built with the specifications presented in Table I.

Model A: Noninterleaving has very high ac resistance and leakage inductance, compared with other arrangements, as shown in Figs. 11 and 12. However, it merits the stray capacitance because of only one intersection between the primary and the secondary. Table II shows that the lowest stray capacitance can be achieved in the noninterleaving arrangement.

Model B: Based on Table II and Figs. 11 and 12, ac resistance and leakage inductance are dramatically reduced in general full-interleaving P-S-P-S-P-S-P-S. A lower MMF ratio m causes a weaker proximity effect in the adjacent layers, which contributes a lower ac resistance. The energy associated with leakage inductance is reduced due to the fact that the magnetizing force is reduced in each layer, as shown in Fig. 1(b). However, seven intersections between the primary and the secondary can be found, which is caused by a higher

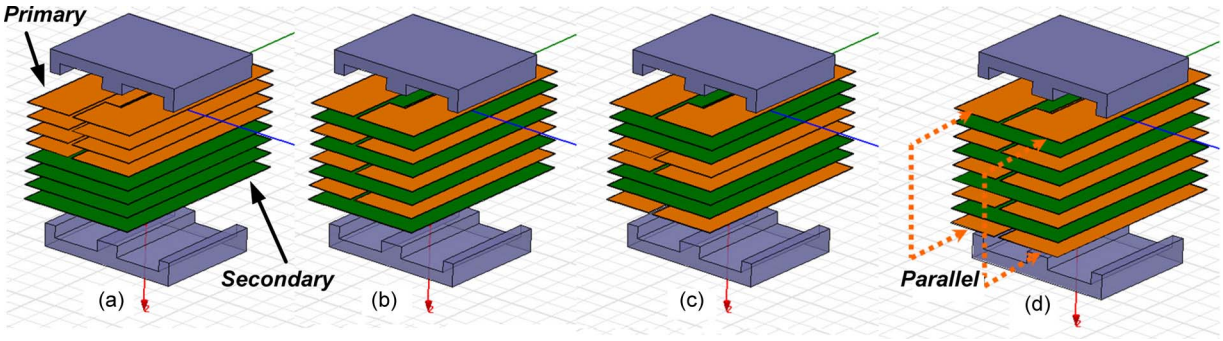

Fig. 10. 3-D models. (a) Noninterleaving. (b) P-S-P-S-P-S-P-S. (c) P-S-S-P-P-S-S-P. (d) Improved interleaving 0.5P-S-P-S-P-S-P-S-0.5P.

TABLE I
SPECIFICATIONS OF THE TRANSFORMER

Parameters	Values
Input voltage	50 V
Input current	20 A
Turns ratio (*N2/N1*)	2:1 (8:4)
Core type	EELP 64
Core material	Ferrite N87
Operating frequency	50 kHz
Duty cycle	50%
Cross-section of core	519 mm^2
Volume of core	41500 mm^3
Thickness of copper foil (primary)	0.25 mm
Thickness of PCB winding (secondary)	70 um * 4 (4 layers in parallel)
Insulator	0.1mm Kapton Tape

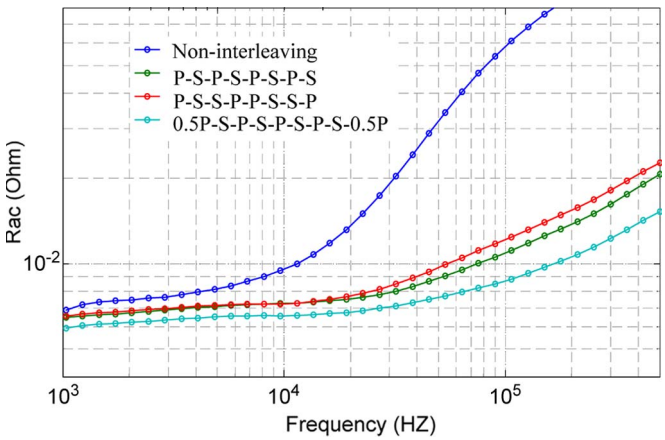

Fig. 11. AC resistance measurement.

stray capacitance. As shown in Table II, the stray capacitance in P-S-P-S-P-S-P-S is almost ten times that in noninterleaving.

Model C: P-S-S-P-P-S-S-P is another kind of fully interleaving arrangement, because the MMF ratios m in each layer are still equal to 1, as shown in Fig. 13(a). Comparing with the general full-interleaving P-S-P-S-P-S-P-S, it has similar ac resistance and leakage inductance, because their MMF distributions have the same functions. However, it is very noteworthy that stray capacitance is getting better without sacrificing any other behaviors (leakage inductance or ac resistance) due to the fact that fewer intersections (four) between the primary and the secondary can be found.

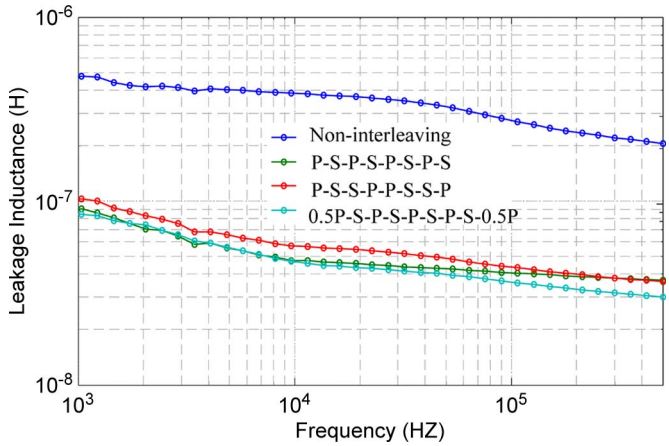

Fig. 12. Leakage inductance measurement.

TABLE II
MEASUREMENT RESULTS OF THE PARASITIC PARAMETERS

Frequency is 50 kHz	R_{ac}/R_{dc} (mOhm)	L_{leak} (nH)	C_{str} (nF)
Non-interleaving	32.2/6.55	324	1.15
P-S-P-S-P-S-P-S	9.14/6.14	43.8	9.41
P-S-S-P-P-S-S-P	10.1/6.21	47.4	4.24
P/2-S-P-S-P-S-P-S-P/2	7.68/5.69	40.6	3.89

Model D: Model d represents an improved interleaving arrangement that constructs the top layer paralleling with the bottom layer and then in series with the other turns of the primary, so that the MMF ratio m can further be reduced. Fig. 13(b) shows the analytical MMF distribution of 0.5P-S-P-S-P-S-P-S-0.5P. Since the unavoidable error of impedances on the top and bottom layers, the currents in each branch are probably not equal, and hence, the MMF ratios m may not be 0.5. Anyhow, a lower MMF ratio m below 1 can be achieved. Thereby, as shown in Fig. 11, a lower ac resistance appears in a high-frequency situation, and a slow increasing tendency can clearly be identified when the frequency is above 100 kHz. The most impressive thing is that not only ac resistance and leakage inductance can be reduced but stray capacitance can also be benefited, compared with other interleaving arrangements. The paper [31] proposed that quadruple interleaving also achieves $m = 0.5$ by splitting the secondary. However, the even turn ratio is limited in this construction, and the stray capacitance might not be improved.

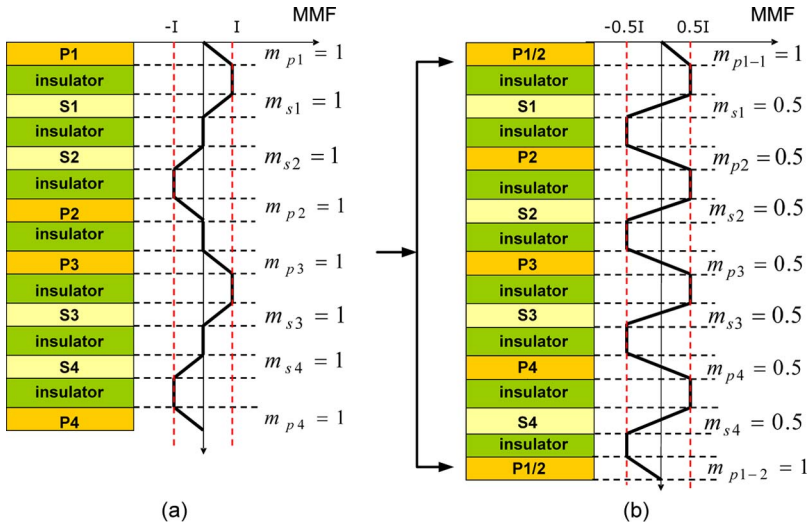

Fig. 13. MMF distributions for (a) P-S-S-P-P-S-S-P and (b) 0.5P-S-P-S-P-S-P-S-0.5P, respectively.

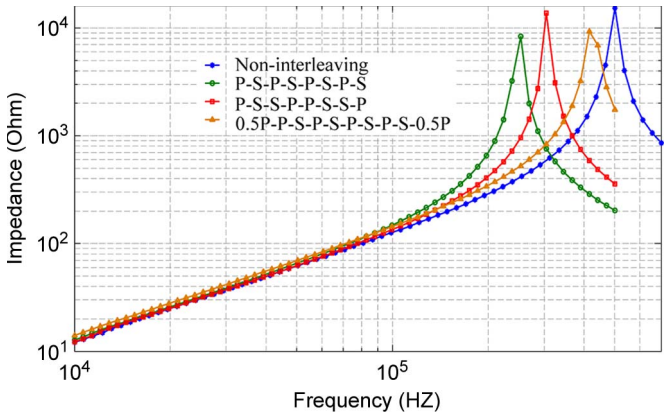

Fig. 14. Measured impedance with opening secondary winding in P-P-P-P-S-S-S-S, P-S-P-S-P-S-P-S, P-S-S-P-P-S-S-P, and 0.5P-S-P-S-P-S-P-S-0.5P, respectively.

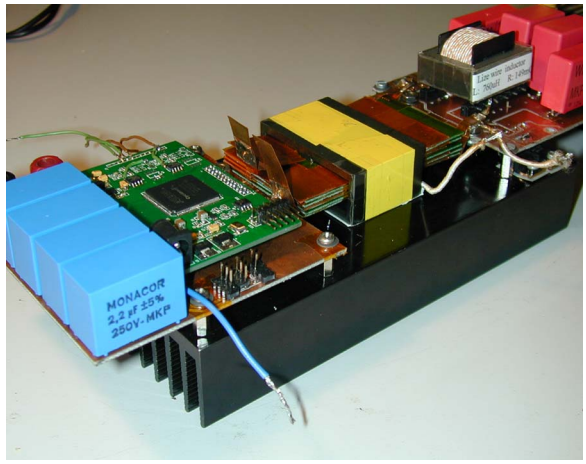

Fig. 15. Photo of 1.2-kW full-bridge dc–dc prototype employing an improved PT.

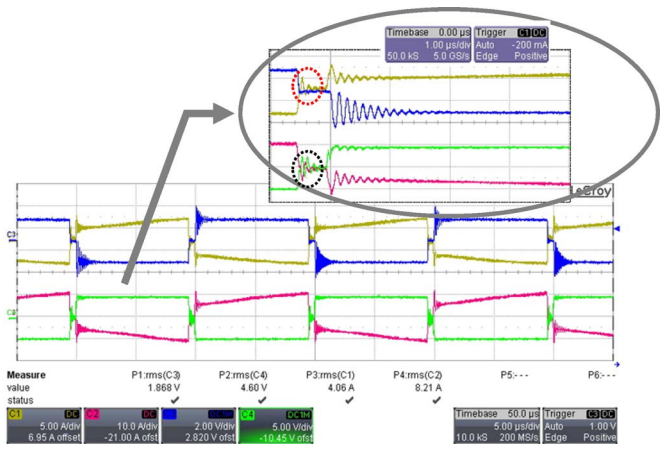

Fig. 16. Experimental waveforms for noninterleaving PT.

Fig. 14 shows the measured impedance with opening secondary winding in P-P-P-P-S-S-S-S, P-S-P-S-P-S-P-S, P-S-S-P-P-S- S-P, and 0.5P-S-P-S-P-S-P-S-0.5P arrangements, respectively. The noninterleaving has the best parallel *LC* resonance frequency (L = magnetizing inductance; C = stray capacitance of primary), and the worst case occurs in the full-interleaving P-S-P-S-P-S-P-S. Because the magnetizing inductance in the four arrangements are the same, the parallel *LC* resonance frequencies reflect the magnitude of the stray capacitors as the same results, as shown in Table II.

A 1.2-kW full-bridge converter prototype employing the improved PT structure has been constructed, as shown in Fig. 15. Figs. 16–19 show the plots of the transformer primary voltage, primary winding current, and secondary voltage and current in different winding arrangements. In these figures, C3 and C4 represent the voltage across the transformer secondary winding and primary winding, respectively. C1 and C2 represent the current on the transformer primary and secondary, respectively. A bigger ringing spike occurs in the dead time (or zero-voltage length if the duty cycle is not 0.5) for the noninterleaving arrangement due to the fact that the energy stored in the leakage inductance oscillates with the other parasitic elements in the circuit. The improved 0.5P-S-P-S-P-S-P-S-0.5P arrangement has the best high-frequency property in the ringing problem, which can bring low switching losses and low EMI problem. The

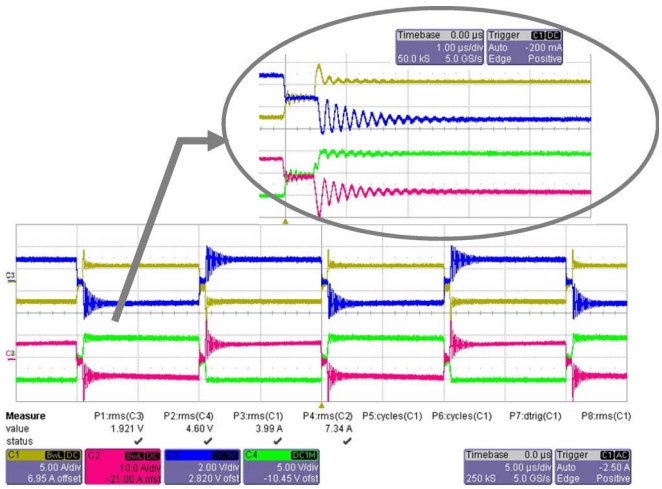

Fig. 17. Experimental waveforms for P-S-P-S-P-S-P-S PT.

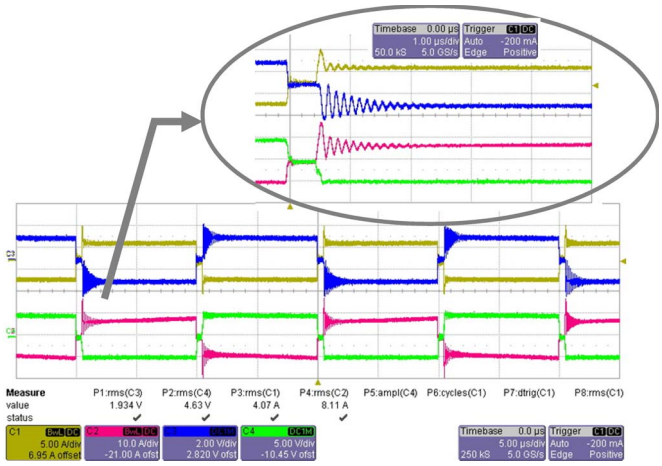

Fig. 18. Experimental waveforms for P-S-S-P-P-S-S-P PT.

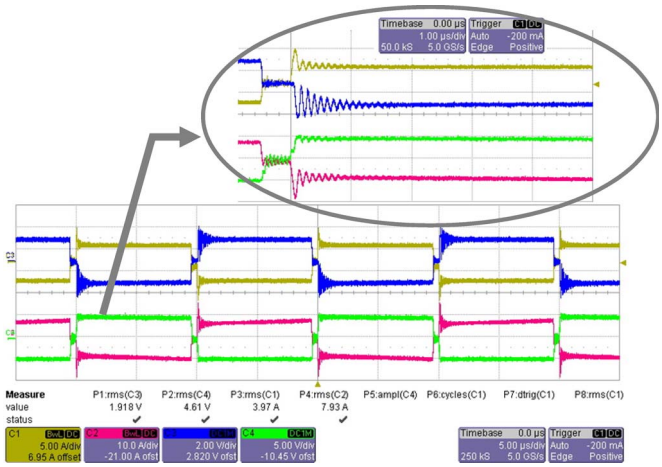

Fig. 19. Experimental waveforms for improved 0.5P-S-P-S-P-S-P-S-0.5P PT.

measured converter efficiencies are shown in Fig. 20. Over 96% efficiency can be achieved for the improved transformer, and a 2.7% improvement, compared with that of the noninterleaving structure, is obtained when the output power is 1.2 kW.

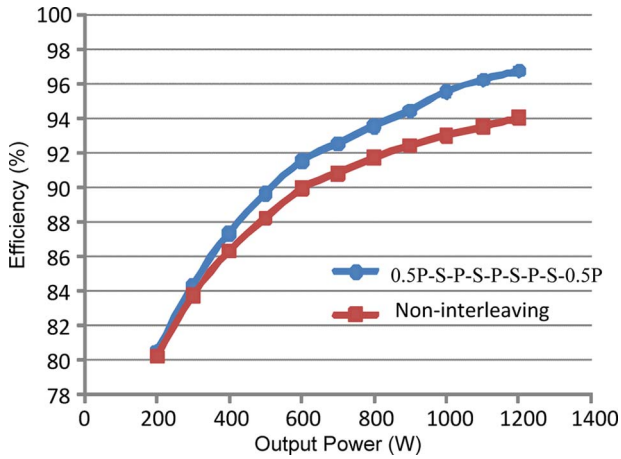

Fig. 20. Measured converter efficiencies.

V. Conclusion

A detailed consideration for designing PT including winding loss, core loss, leakage inductance, and stray capacitance has been presented. Unavoidable tradeoffs by the physical reasoning have been analyzed in this work as well. Winding arrangements can, in part, bring an optimal behavior in the tradeoffs without any sacrifices. Four typical winding arrangements have been compared to show their advantages and disadvantages. An improved structure 0.5P-S-P-S-P-S-P-S-0.5P has been proposed to illustrate that a low ac resistance, low leakage inductance, and even a relatively low stray capacitance can be obtained.

Acknowledgment

The authors would like to thank Flux A/S, N. O.-Christensen, O. Poulsen, E. B. Hansen, and T. Bjorklund for their support, and G. Sen for the manuscript discussion.

References

[1] W. Chen, Y.-P. Yan, Y.-Q. Hu, and Q. Lu, "Model and design of PCB parallel winding for planar transformer," *IEEE Trans. Magn.*, vol. 39, no. 5, pp. 3202–3204, Sep. 2003.

[2] C. Quinn, K. Rinne, T. O'Donnell, M. Duffy, and C. O. Mathuna, "A review of planar magnetic techniques and technologies," in *Proc. IEEE APEC*, 2001, pp. 1175–1183.

[3] E. de Jong, J. Ferreira, and P. Bauer, "Toward the next level of PCB usage in power electronic converters," *IEEE Trans. Power Electron.*, vol. 23, no. 6, pp. 3153–3163, Nov. 2008.

[4] P. L. Dowell, "Effects of eddy currents in transformer windings," *Proc. Inst. Elect. Eng.*, vol. 113, no. 8, pp. 1387–1394, Aug. 1966.

[5] J. Ferreira, "Improved analytical modeling of conductive losses in magnetic components," *IEEE Trans. Power Electron.*, vol. 9, no. 1, pp. 127–131, Jan. 1994.

[6] A. Reatti and M. K. Kazimierczuk, "Comparison of various methods for calculating the AC resistance of inductors," *IEEE Trans. Magn.*, vol. 38, no. 3, pp. 1512–1518, May 2002.

[7] A. D. Podoltsev, I. N. Kucheryavaya, and B. B. Lebedev, "Analysis of effective resistance and eddy-current losses in multiturn winding of high-frequency magnetic components," *IEEE Trans. Magn.*, vol. 39, no. 1, pp. 539–548, Jan. 2002.

[8] W. G. Hurley, E. Gath, and J. G. Breslin, "Optimizing the AC resistance of multilayer transformer windings with arbitrary current waveforms," *IEEE Trans. Power Electron.*, vol. 15, no. 2, pp. 369–376, Mar. 2008.

[9] X. Nan and C. R. Sullivan, "An improved calculation of proximity-effect loss in high-frequency windings of round conductors," in *Proc. IEEE Power Electron. Spec. Conf.*, 2003, pp. 853–860.
[10] X. Margueron, J.-P. Keradec, and A. Besri, "Current sharing between parallel turns of a planar transformer: Prediction and improvement using a circuit simulation software," in *Conf. Rec. IEEE IAS Annu. Meeting*, 2007, pp. 1787–1793.
[11] T. D. Kefalas and A. G. Kladas, "Harmonic impact on distribution transformer no-load loss," *IEEE Trans. Ind. Electron.*, vol. 57, no. 1, pp. 193–200, Jan. 2010.
[12] A. R. Zare, R. Iravani, M. S. Pasand, H. Mohseni, and S. Farhangi, "An accurate hysteresis model for ferroresonance analysis of a transformer," *IEEE Trans. Power Del.*, vol. 23, no. 3, pp. 1448–1456, Jul. 2008.
[13] W. A. Roshen, "A practical, accurate and very general core loss model for nonsinusoidal waveforms," *IEEE Trans. Power Electron.*, vol. 22, no. 1, pp. 30–40, Jan. 2007.
[14] J. Reinert, A. Brockmeyer, and R. W. A. A. De Doncker, "Calculation of losses in ferro- and ferrimagnetic materials based on the modified Steinmetz equation," *IEEE Trans. Ind. Appl.*, vol. 37, no. 4, pp. 1055–1060, Jul./Aug. 2001.
[15] J. Li, T. Abdallah, and C. R. Sullivan, "Improved calculation of core loss with nonsinusoidal waveforms," in *Conf. Rec. IEEE IAS Annu. Meeting*, 2001, pp. 2203–2210.
[16] K. Venkatachalam, C. R. Sullivan, T. Abdallah, and H. Tacca, "Accurate prediction of ferrite cores loss with nonsinusoidal waveforms using only Steinmetz parameters," in *Proc. IEEE Workshop Comput. Power Electron.*, 2002, pp. 36–41.
[17] A. Van den Bossche, V. C. Valchev, and G. B. Georgiev, "Measurement and loss model of ferrites with non-sinusoidal waveforms," in *Proc. IEEE Power Electron. Spec. Conf.*, 2004, pp. 4814–4818.
[18] D. Lin, P. Zhou, W. N. Fu, Z. Badics, and Z. J. Cendes, "A dynamic core loss model for soft ferromagnetic and power ferrite materials in transient finite element analysis," *IEEE Trans. Magn.*, vol. 40, no. 2, pp. 1318–1321, Mar. 2004.
[19] I. Villar, U. Viscarret, I. E. Otadui, and A. Rufer, "Global loss evaluation methods for nonsinusoidally fed medium-frequency power transformers," *IEEE Trans. Ind. Electron.*, vol. 56, no. 10, pp. 4132–4140, Oct. 2009.
[20] Z.-W. Ouyang, O. C. Thomsen, and M. A. E. Andersen, "The analysis and comparison of leakage inductance in different winding arrangements for planar transformer," in *Proc. IEEE PEDS*, 2009, pp. 1143–1148.
[21] E. C. Snelling, *Soft Ferrites—Properties and Applications,* 2nd ed. London, U.K.: Butterworth, 1988.
[22] R.-G. Chen, J. T. Strydom, and J. D. van Wyk, "Design of planar integrated passive module for zero-voltage-switched asymmetrical half-bridge PWM converter," *IEEE Trans. Ind. Appl.*, vol. 39, no. 36, pp. 1648–1655, Nov./Dec. 2003.
[23] W. G. Hurley and D. J. Wilcox, "Calculation of leakage inductance in transformer windings," *IEEE Trans. Power Electron.*, vol. 9, no. 1, pp. 121–126, Jan. 1994.
[24] X. Margueron, J.-P. Keradec, and D. Magot, "Analytical calculation of static leakage inductances of HF transformers using PEEC formulas," *IEEE Trans. Ind. Appl.*, vol. 43, no. 4, pp. 884–892, Jul. 2004.
[25] H.-Y. Lu, J.-G. Zhu, and S. Y. R. Hui, "Experimental determination of stray capacitances in high frequency transformers," *IEEE Trans. Power Electron.*, vol. 18, no. 5, pp. 1105–1112, Sep. 2003.
[26] L. Dalessandro, F. S. Cavalcante, and J. W. Kolar, "Self-capacitance of high-voltage transformers," *IEEE Trans. Power Electron.*, vol. 22, no. 5, pp. 2081–2092, Sep. 2007.
[27] M. J. Prieto, A. Fernandez, J. M. Diaz, J. M. Lopera, and J. Sebastian, "Influence of transformer parasitics in low-power applications," in *Proc. IEEE Appl. Power Electron. Conf.*, 1999, pp. 1175–1180.
[28] J. Biela and J. W. Kolar, "Using transformer parasitics for resonant converters—A review of the calculation of the stray capacitance of transformers," *IEEE Trans. Ind. Appl.*, vol. 44, no. 1, pp. 223–233, Jan./Feb. 2008.
[29] R. Petkov, "Optimum design of a high-power, high-frequency transformer," *IEEE Trans. Power Electron.*, vol. 11, no. 1, pp. 33–42, Jan. 1996.
[30] W. G. Hurley, "Optimizing core and winding design in high frequency transformers," in *Proc. IEEE CIEP*, 1996, pp. 2–13.
[31] M. Nymand and M. A. E. Andersen, "High-efficiency isolated boost dc–dc converter for high-power low-voltage fuel-cell applications," *IEEE Trans. Ind. Electron.*, vol. 52, no. 2, pp. 505–514, Feb. 2010.

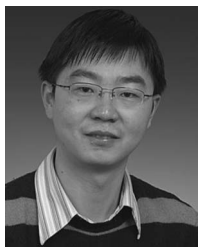

Ziwei Ouyang (S'07) received the B.S. degree from the Naval University of Engineering, Wuhan, China, in 2004 and the M.S. degree from Tianjin University of Technology, Tianjin, China, in 2007. He is currently working toward the Ph.D. degree in power electronics from the Department of Electrical Engineering, Technical University of Denmark, Kongens Lyngby, Denmark.

His research interests include magnetics design, modeling and integration in power supplies, dc/dc converters, and digital control in high-power reversible converters.

Ole C. Thomsen (M'06) received the B.S.E.E. degree in electronics from the Engineering Academy of Denmark (DIA), Kongens Lyngby, Denmark, in 1970.

From 1970 to 1976, he was with Skandinavisk Teleindustri A/S, as a RF R&D Engineer. From 1976 to 1980, he was with Christian Rovsing A/S, as a Power Electronic Project Manager in the Space Department. In 1980, he founded Powerlab A/S, operating within R&D and manufacturing of professional power electronic, and was a General Manager until 2004. Since 2005, he has been with the Department of Electrical Engineering, Technical University of Denmark, Kongens Lyngby, where he is currently an Associate Professor. His research interests include switch-mode power supplies, power factor correction, and EMC.

Michael A. E. Andersen (M'88) received the M.Sc.E.E. and Ph.D. degrees in power electronics from the Technical University of Denmark, Kongens Lyngby, Denmark, in 1987 and 1990, respectively.

He is currently a Professor of power electronics with the Technical University of Denmark, where he is the Deputy Director of the Department of Electrical Engineering and the Head of the Danish Ph.D. Research School in Electrical Energy Systems "EnergyLabDK." He has authored or coauthored more than 90 papers. His research interests include switch-mode power supplies, piezoelectric transformers, power factor correction, and switch-mode audio power amplifiers.

Appendix B.2

[B.2] Z. Ouyang, O. C. Thomsen, and M. A. E. Andersen. “The analysis and comparison of leakage inductance in different winding arrangements for planar transformer,” *in Proc. IEEE PEDS*, pp. 1143–1148, Taipei, Taiwan, Nov., 2009.

PUBLISHED IN PROCEEDING OF IEEE POWER ELECTRONICS AND DRIVE SYSTEM (PEDS), 2009

The Analysis and Comparison of Leakage Inductance in Different Winding Arrangements for Planar Transformer

Ziwei Ouyang, Ole C. Thomsen and Michael A. E. Andersen

Electrical Engineering Department, Technical University of Denmark, Kgs. Lyngby, Denmark

***Abstract* -- The coupling of the windings can be easily increased by using multiply stacked planar windings connection. Interleaving is a well-known technique used to reduce leakage inductance and minimize high-frequency winding losses. The paper aims to analyze leakage inductance of planar transformer based on magneto motive force (MMF) and energy distribution, and correct the formula of leakage inductance proposed by previous publications. The investigation of different winding arrangements shows significant advantages of interleaving structure. In this work, a novel half turn structure is proposed to further reduce leakage inductance. Some important issues are presented to acquire desirable leakage inductance. The design and modeling of 1-kW planar transformer is presented. In order to verify the analytical method for leakage inductance in this paper, finite element analysis (FEA) and measurement with impedance analyzer are presented. Good matching between calculation, FEA 2D simulation and measurement results is achieved.**

***Index Terms*-- leakage inductance, magneto motive force (MMF), finite element analysis (FEA), interleaving, half turn, planar transformer**

I. INTRODUCTION

In recent years, planar transformers have become increasingly popular in high frequency power converter design because of the advantages they achieved in terms of increased reliability, reproducibility, and increased power density. In terms of circuit performance one of the advantages of planar transformer is low profile and repeatable leakage inductance [1]. The leakage inductance causes the main switch current at the device input to vary at a low slope between zero and rated value and reduces the rate of commutation between output diodes. In addition, the stored energy in the leakage inductance leads to the generation of voltage spikes on the main switch which, besides creating EMI problems, increases the switching losses and lowers the efficiency [2]. Therefore, most designers expect the leakage inductance to be as small as possible. However, in some applications such as a phase-shift-modulated soft switching DC/DC converter, the magnitude of the leakage inductance determines the achievable load range under zero-voltage operation, and a relatively large leakage inductance is desirable. This paper aims to calculate the leakage inductance stored in planar transformer by analyzing magneto motive force (MMF) and energy distribution. Section II defines leakage inductance using the perspective of energy. The energy associated with leakage inductance should be equal to the sum of energy stored in each element layer inside the core window. The section also analyzes the magnetic field strength in each layer and finite element analysis 2D model is simulated to demonstrate the correctness of the analytical method. The formula presented in previous publications [3-5] is generally used to calculate the leakage inductance. However, it is noted that those formula don't contribute precise results. It assumes that the magnetic field strength along the height of insulator layer between non-interleaved sections varies linearly but actually it should keep constant during the whole area of insulator layer. A new formula suited for symmetrical winding arrangement is suggested in this paper. Section III proposes a novel half turn structure to further reduce the leakage inductance. The MMF distribution curve for half turn arrangement is presented and leakage inductance is computed. Section IV describes some important issues to require desirable leakage inductance including copper thickness, the thickness of insulator layer and the number of turns. Section V evaluates a good matching among the calculation, 2D FEA simulation and measurement with impedance analyzer, which indicates the correctness of the analytical method and the proposed calculation. Section V provides a conclusion.

II. BASIC DEFINITION AND CALCULATION FOR LEAKAGE INDUCTANCE

A. Basic Definition of Leakage Inductance

Not all the magnetic flux generated by AC current excitation on the primary side follows the magnetic circuit and link with the other windings. The flux linkage between two windings or parts of the same winding is never complete. Some flux leaks from the core and returns to the air, winding layers and insulator layers, thus these flux causes imperfect coupling. If the secondary is short-circuited, the main flux which links both windings will be negligible because the primary and secondary ampere turns almost cancel. So the leakage flux parts don't lose their individual identities. It is seen from Fig.1 that within the winding area the mutual repulsion causes the leakage flux to lie approximately parallel to the winding interface. The leakage inductance referred to the primary can be accessed by the energy stored in a magnetic field,

$$E = \frac{1}{2} \int_{total} B \cdot H \cdot dV = \frac{1}{2} \cdot L_{lk} \cdot {I_p}^2 \tag{1}$$

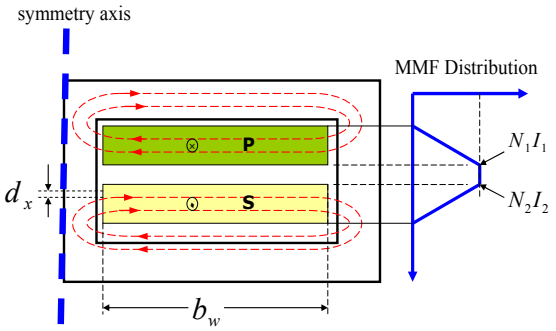

Fig. 1 The leakage flux paths and magneto motive force variation (MMF).

B. *Leakage Inductance Calculation*

For simplification to analyze MMF created by the windings, turns ratio 1:1 and total number of turns 8 are used as an example. As shown in Fig.2, the MMF varies linearly in winding layers can be assumed when operation frequency is not very high. When the frequency is increased, MMF distribution will concentrate on the surface of rectangle conductor due to eddy current effect. In practice, when the frequency grows, the leakage inductances will slightly decrease. Indeed, relative variation of leakage inductance as the frequency changes is quite small [6]. The leakage inductance for non-interleaving structure can be calculated as follows,

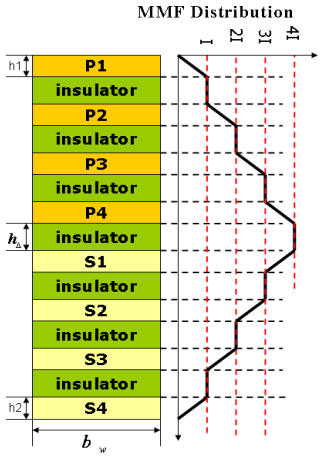

Fig. 2 Analytical scheme of MMF distribution for non-interleaving structure.

The differential volume of each turn is $l_w \cdot b_w \cdot dx$, therefore the total energy is sum of the energy stored in each elementary layer which can be expressed by

$$E = \frac{\mu_0}{2} \sum \int_0^h H^2 \cdot l_w \cdot b_w \cdot dx \tag{2}$$

where l_w is the length of each turn, b_w is the width of each turn, h represents the thickness of each winding layer. Fig.1 shows the thickness dx, situated at a distance x from the inner surface of the secondary winding. The field strength along the flux path which includes this layer depends on the number of ampere turns linked by the path. Since the flux disperses rapidly on leaving the winding, the associated energy is much reduced and the reluctance of the path within the magnetic core can be ignored compared with that of the path in the winding, therefore the flux path can be expressed by the width b_w rather than the full closed flux path. H may be taken as the field strength in the winding layer which is assumed to be constant along the plane of layer, thus, for first primary layer,

$$H = \frac{I_1}{b_w} \cdot \frac{x}{h_1} \tag{3}$$

According to the Eqn.2, the energy in the total winding space can be deduced then

$$\begin{aligned} E = \frac{\mu_0}{2} \cdot l_w \cdot b_w \Bigg[& 4 \int_0^{h_1} \left(\frac{I_1}{b_w} \cdot \frac{x}{h_1} \right)^2 \cdot dx + 4 \int_0^{h_2} \left(\frac{I_1}{b_w} \cdot \frac{x}{h_2} \right)^2 \cdot dx \\ & + \left(\frac{I_1}{b_w} \right)^2 \cdot (h_1 + h_2 + 2 \cdot h_\Delta) + \left(\frac{2 \cdot I_1}{b_w} \right)^2 \\ & \cdot (h_1 + h_2 + 2 \cdot h_\Delta) + \left(\frac{3 \cdot I_1}{b_w} \right)^2 \\ & \cdot (h_1 + h_2 + 2 \cdot h_\Delta) + \left(\frac{4 \cdot I_1}{b_w} \right)^2 \cdot h_\Delta \Bigg] \\ = & \frac{\mu_0}{2} \cdot l_w \cdot b_w \left[\frac{46(h_1 + h_2)}{3} + 44 \cdot h_\Delta \right] \cdot {I_1}^2 \end{aligned} \tag{4}$$

where h_1 and h_2 are the thickness of primary and secondary respectively, h_Δ is the height of insulator layers. Fig.3, Fig.4 and Fig.5 show the energy distribution (a) and the magnetic field distribution (b) in the non-interleaving structure, partial interleaving P-P-S-S-P-P-S-S structure and fully interleaving P-S-P-S-P-S-P-S structure respectively. Apparently, the interleaving structure provides significant advantage in reducing leakage inductance. The analytical MMF distribution (c) can be verified by magnetic field distribution based on FEA simulation results (b). A good matching between (b) and (c) illuminates the correctness of analytical method. Based on the above calculation, a new general formula suited for symmetrical winding arrangement (symmetrical MMF distribution) is suggested, which is expressed as follows,

$$L_{lk} = \mu_0 \cdot \frac{l_w}{b_w}\left[\frac{k_1 \cdot h_1 + k_2 \cdot h_2}{3} + M \cdot (\frac{k_1}{b_w})^2 \cdot h_\Delta + \sum_{k_1=0}^{k_1-1} (\frac{k_1}{b_w})^2 \cdot (h_1 + h_\Delta) + \sum_{k_2=0}^{k_2-1} (\frac{k_2}{b_w})^2 \cdot (h_2 + h_\Delta)\right] \quad (5)$$

where $k_1=N_1/M$ and $k_2=N_2/M$, N_1 and N_2 are the number of turns on the primary and secondary windings respectively, M is the number of section interfaces.

C. *The error analysis*

The formula published in the reference [3-5] to compute the leakage inductance for the symmetrical interleaving structure is shown in Eqn.6, which has been commonly used to compute leakage inductance for most of designers.

$$L_{lk} = \mu_0 \cdot \frac{l_w}{b_w} \cdot (\frac{N}{M})^2 \cdot \left[\frac{\sum x}{3} + \sum x_\Delta\right] \quad (6)$$

where N is the number of turns on the winding which the leakage inductance is to be referred; M is the number of section interfaces; Σx is the sum of all section dimensions perpendicular to the section interfaces and Σx_Δ is the sum of all inter-section layer thickness. It is noted that the partial interleaving P-P-S-S-S-S-P-P and fully interleaving P-S-S-P-

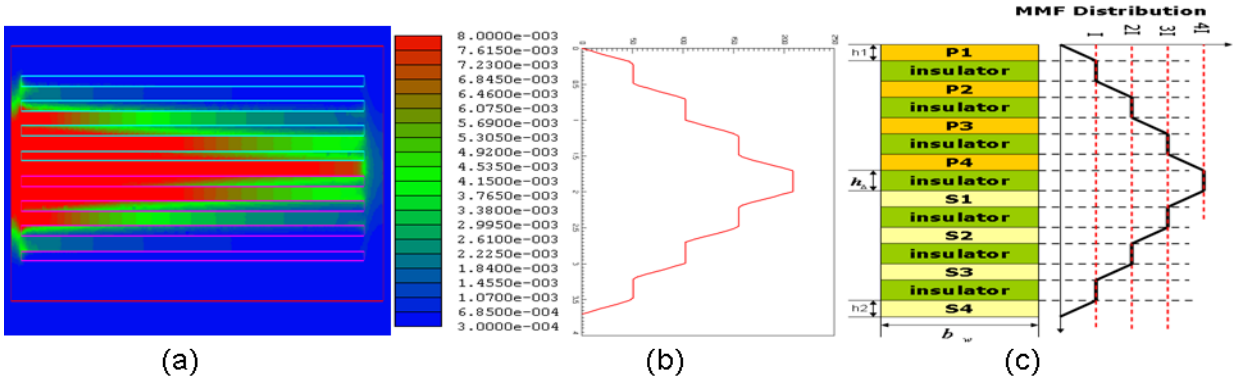

Fig.3 Non-interleaving structure (a) Energy distribution in FEA 2D simulation (b) Magnetic field strength distribution in FEA simulation (c) Analytical MMF distribution

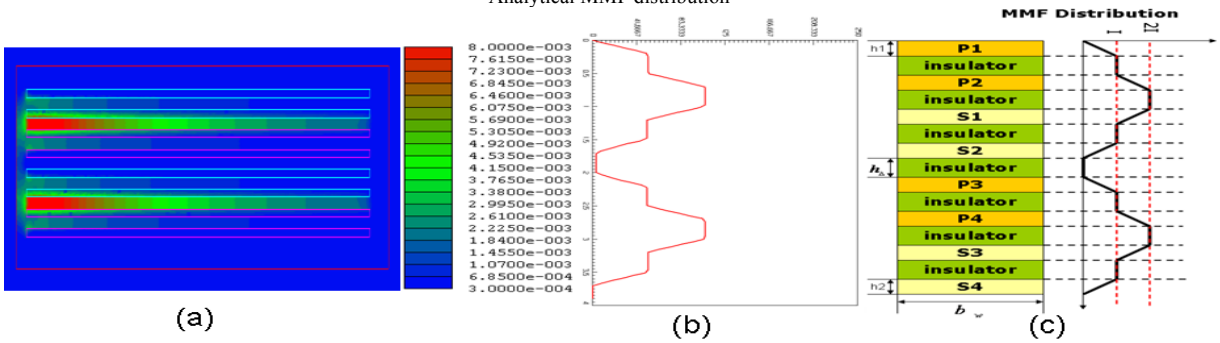

Fig.4 P-P-S-S-P-P-S-S structure (a) Energy distribution in FEA 2D simulation (b) Magnetic field strength distribution in FEA simulation (c) Analytical MMF distribution

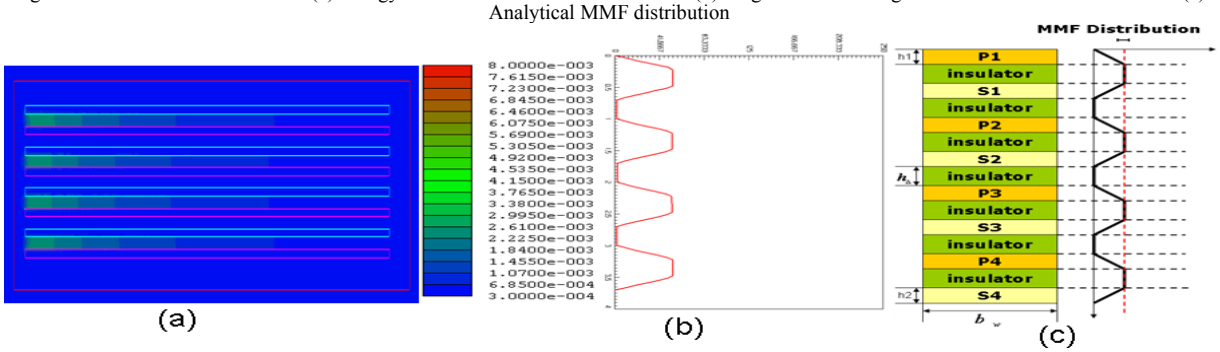

Fig.5 P-S-P-S-P-S-P-S structure (a) Energy distribution in FEA 2D simulation (b) Magnetic field strength distribution in FEA simulation (c) Analytical MMF distribution

P-S-S-P structures have equivalent leakage energy with the P-P-S-S-P-P-S-S and P-S-P-S-P-S-P-S structures respectively.

However, it assumes that the magnetic field strength along the height of insulator layer between non-interleaved sections varies linearly which is shown by the blue line in the Fig.6. Actually there is no extra flux path link with the insulator layer, the MMF curve should, therefore, keep constant in the area of insulator layer (see black line in Fig.6). The correctness of the latter analytical MMF distribution has been verified by FEA 2D simulation.

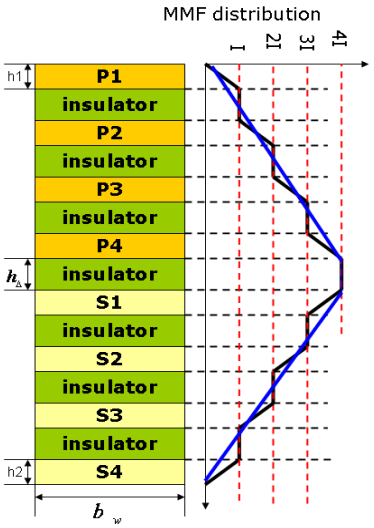

Fig.6 Comparison of MMF distribution in two different analytical methods

As an example, a planar transformer has been built with EI 64/5/50 core, the mean turn length is 202mm, copper width is 20mm and the thickness of primary and secondary are both 0.2mm, the thickness of insulator layer is 0.3mm. The winding arrangements P-P-P-P-S-S-S-S, P-P-S-S-P-P-S-S and P-S-P-S-P-S-P-S will be treated as case 1, case 2 and case 3 respectively. Table I describes the error between the proposed eqn.5 and the previous eqn.6.

TABLE I. THE ERROR ANALYSIS TABLE

	Calculation (eqn.5)	Previous Calculation (eqn.6)	The error
Case 1	*245 nH*	*291 nH*	*19%*
Case 2	*62.6 nH*	*82.9 nH*	*32%*
Case 3	*22 nH*	*25.8 nH*	*17%*

III. NOVEL HALF TURN STRUCTURE

The interleaving, partial interleaving and non-interleaving structures have a significant difference in leakage inductance due to the MMF distribution. From the MMF distribution curve, maximal magnetizing force in each layer determines the value of leakage inductance. Therefore half turn structure is proposed to further reduce the leakage inductance. The solution is to place an extra layer in the top layer, and then in parallel with the bottom layer so as to allow half current to flow, and the other layers are still kept in series.

As shown in Fig.7, the MMF distribution has been shifted to be a symmetrical curve on the X axis. The maximal magnetizing force is reduced to half of primary current. Taken together eqn.1-3, the energy in the total winding space can be found as follows,

$$E = \frac{\mu_0}{2}\cdot l_w \cdot b_w \left[2\int_0^{h_1} \left(\frac{I_1}{2\cdot b_w}\cdot\frac{x}{h_1}\right)^2 \cdot dx + 8\int_0^{0.5\cdot h_2} \left(\frac{I_1}{2\cdot b_w}\cdot\frac{x}{h_2}\right)^2 \cdot dx + 6\int_0^{0.5\cdot h_1} \left(\frac{I_1}{2\cdot b_w}\cdot\frac{x}{h_1}\right)^2 \cdot dx + 8\cdot\left(\frac{I_1}{2\cdot b_w}\right)^2 \cdot h_\Delta \right] = \frac{\mu_0}{2}\cdot l_w \cdot b_w \left[\frac{11h_1+4h_2}{48} + 2\cdot h_\Delta\right]\cdot {I_1}^2 \quad (7)$$

Obviously, the energy enclosed by the winding space gets a significant deduction, and thus 8.4-nH leakage inductance therefore can be obtained.

This structure not only reduces the leakage inductance, but also is advantageous to the winding loss caused by skin effect and proximity effect. Referring to Dowell equation [7], the quantity *m* represents the ratio of the MMF to the layer ampere-turns. The value of *m* can directly affect proximity

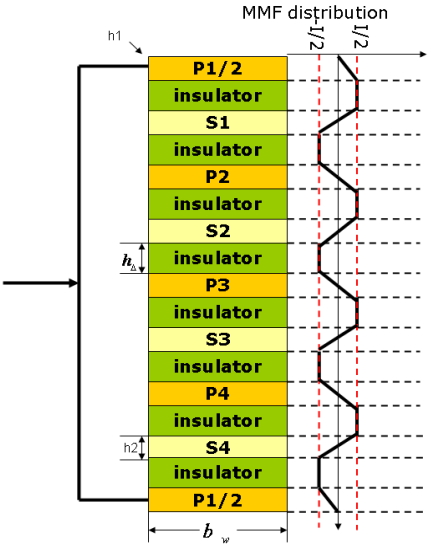

Fig.7 Analytical scheme of MMF distribution for half turn structure

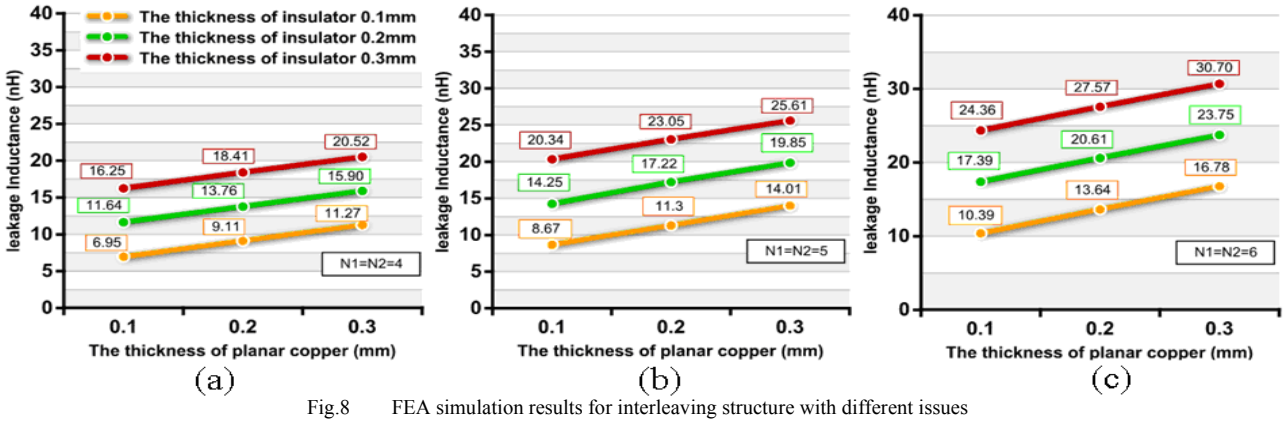

Fig.8 FEA simulation results for interleaving structure with different issues

loss of the windings [7-10]. Interleaving windings can significantly reduce the proximity loss when the primary and secondary currents are in phase. For the interleaving structure, the value of *m* is equal to 1 for each layer. When the aforementioned half turn structure is used, the value of *m=0.5* can be obtained. This causes a further reduction in the winding loss.

IV. Important Issues for Leakage Inductance

A. *The thickness of copper foil*

From eqn.5, leakage inductance can be influenced by the thickness of copper foil. It should be as thin as possible if a small leakage inductance is expected. Fig. 8 shows that the thicker the copper, the higher leakage inductance will be achieved. However, the winding loss might be sacrificed if the thin copper foil is used. It is note that if the thinner one is used, the ratio of ac-resistance to dc-resistance will be reduced due to a lower skin effect, even although the dc-resistance is increased. Therefore, there is an optimal value on the thickness of copper foil which can balance leakage inductance and winding loss.

B. *The thickness of insulator layer*

Leakage inductance can be also influenced by the thickness of insulator layer. From Fig.8, the leakage inductance decreases when a thinner insulator layer is used. Considering capacitor effect between inner-windings and insulator strength, the thickness of insulator won't be too low. There is also a trade-off between leakage inductance and interwinding capacitance. The thickness of insulation layer thickness reduced to a certain level results in a considerable dielectric loss [11].

C. *The number of turns*

Comparing the charts (a), (b) and (c) in Fig.8, it can be seen that the number of turns provide a significant difference in leakage inductance. More number of turns, higher leakage inductance. However, if the number of turns is increased, winding loss is also increased. In reverse, core loss will be reduced because a small variation of flux density is obtained. Therefore the trade-off becomes an essential design property.

D. *The others*

As known from eqn.5, the permeability of copper foil and insulator, the length and width of conductor are also related to the leakage inductance. The relative permeability can be controlled by different materials. Therefore, a leakage layer which consists of ferrite film could be used to realize higher leakage inductance. This leakage layer has been used in half –bridge resonant converter and many phase-shift applications to realize ZVS.

V. Experimental Verification

In order to verify the analysis, a 1-kW full bridge isolated buck converter employing planar transformer has been built. Fig.9 shows a photo of the converter. The fold technique for planar copper foil is adopted to avoid some undesirable problem caused by the terminal connection. Moreover, the different winding arrangements are easily implemented if the fold technique is used.

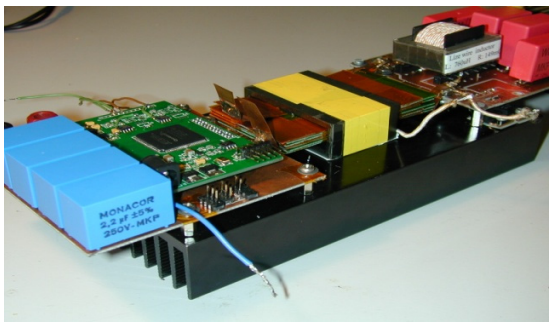

Fig. 9 The prototype of 1 kW planar transformer using in DC-DC converter

In order to verify the analytical method for leakage inductance, the results based on the measurement using impedance analyzer PSM1735 are presented. Fig.10 shows good matching between calculation, FEA 2D simulation and measurement results is achieved. The proposed novel half

turn structure has been treated as case 4. From Fig.10, half turn arrangement has best result in leakage inductance. Of course, small error exists in between measurement and calculation because of complex magnetic flux in the actual model. The tolerance of insulator thickness and short-loop in secondary side may also cause a slight error between measurement and calculation. In addition, extra connection also leads inaccuracy result.

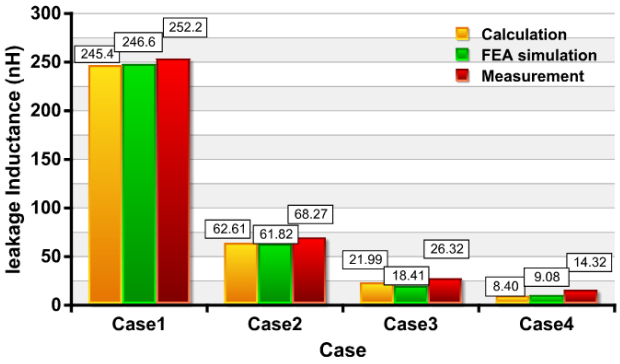

Fig.10 Comparison between calculation, FEA simulation and measurement

VI. Conclusion

The purpose for this paper is to find a solution to acquire a desired leakage inductance. An analytical computation of leakage inductance has been introduced. Several different winding arrangements have been investigated. Computed results are in good agreement with those obtained by FEA 2D simulation. The interleaving structure provides significant advantage in reducing leakage inductance. In order to further reduce leakage inductance and winding loss, a novel half turn was proposed in this paper. The results show the half turn structure contributing a low leakage inductance. Some important issues including copper thickness, insulator thickness and number of turns were analyzed to guide the designer to obtain desired value. The analytical method has been experimentally validated based on 1-kW planar transformers. Good matching is achieved between calculation, FEA simulation and measurement.

Acknowledgment

The authors gratefully acknowledge the support of this work by Niels O. Christensen, Ole Poulsen, and Ebbe B. Hansen, Flux A/S, Denmark.

References

[1] Meinhardt. M, Duffy. M, O'Donnell. T, O'Reilly. S, Flannery. J, O Mathuna. C. "New method for integration of resonant inductor and transformer-design, realisation, measurements" *IEEE Applied Power Electronics Conference and Exposition, APEC '99*, vol. 2, pp. 1168–1174, March 1999.

[2] William G. Hurley, David J. Wilcox. "Calculation of leakage inductance in transformer windings" *IEEE Transactions on Power Electronic*, vol. 9, no. 1, pp. 121–126, January, 1994.

[3] E. C. Snelling. *Soft Ferrites, Properties and Applications*, Butterworths, second edition, 1988.

[4] Ferrell. J, Lai. J.-S, Nergaard. T, Huang. X, Zhu. L, Davis. R. "The role of parasitic inductance in high-power planar transformer design and converter integration" *IEEE Applied Power Electronics Conference and Exposition, APEC '04*, vol. 1, pp. 510–515, 2004.

[5] Ning. Zhu, van Wyk. J. D, Wang. F. "Design of integrated parallel resonant transformers" *IEEE Power Electronics Specialists Conference, PESC '05*, vol. 2, pp. 1787 – 1792, June, 2005.

[6] Margueron. X, Keradec. J.-P, Magot. D. "Analytical caculation of satic leakage inductances of HF transformers using PEEC formulas" *IEEE Transactions on Industry Applications*, vol. 43, no. 4, pp. 884–892, July, 2004.

[7] Robert W.Erickson, Dragan Maksimovic. *Fundamentals of Power Electronics,* second edition, 2004.

[8] William Gerard Hurley, Eugene Gath, John G. Breslin, "Optimizing the ac resistance of multilayer transformer windings with arbitrary current waveforms" *IEEE Transactions on Power Electronics*, vol. 15, No. 2, March 2000.

[9] Alberto Reatti, Marian K. Kazimierczuk, "Comparison of various methods for calculating the ac resistance of inductors" *IEEE Transactions on Magnetics*, vol. 38, No. 3, May 2002.

[10] Jan A**.** Ferreira, "Improved analytical modeling of conductive losses in magnetic components" *IEEE Transactions on Power Electronics*, Vol. 9, No. 1, January 1994.

[11] Ackermann. B, Lewalter. A, Waffenschmidt. E. "Analytical modelling of winding capacitances and dielectric losses for planar transformers" *Proceedings of Computers in Power Electronics, 2004 IEEE Workshop,* vol. 1, pp.2–9, Aug, 2004.

[12] *Maxwell 2D Field Simulator*, Ansoft Corporation, http://www.ansoft.com

Appendix B.3

[B.3] Z. Ouyang, Z. Zhang, O. C. Thomsen and M. A. E. Andersen, "Planar integrated magnetics (PIM) module in hybrid bidirectional dc-dc converter for fuel cell application," *IEEE Transactions on Power Electronics*, vol.26, no.11, pp.3254-3264, Nov. 2011.

Planar-Integrated Magnetics (PIM) Module in Hybrid Bidirectional DC–DC Converter for Fuel Cell Application

Ziwei Ouyang, *Student Member, IEEE*, Zhe Zhang, *Member, IEEE*, Ole C. Thomsen, *Member, IEEE*, and Michael A. E. Andersen, *Member, IEEE*

***Abstract*—In most power electronics converters, the overall volume is mainly determined by the number of parts and the size of passive components. Integrated magnetics and planar magnetics techniques, therefore, have been an excellent option in order to reduce the counts and the size of magnetic components, hereby increasing the power density of converters. In this paper, a new planar-integrated magnetics (PIM) module for a phase-shift plus duty-cycle-controlled hybrid bidirectional dc–dc converter is proposed, which assembles one boost inductor and two transformers into an E-I-E core geometry, reducing the number of parts, the total volume of converter, as well as the total core loss of the magnetic components. AC losses in the windings and leakage inductance of the transformers are kept low by interleaving the primary and secondary turns of the transformers. To verify the validity of the design approach and theoretical analysis, a laboratory prototype employing the PIM module is implemented for a fuel cell application with 20–40-V input voltage and 400-V output voltage. Detailed results from the experimental comparisons demonstrate that the PIM module is fully functional and electromagnetically equivalent to the discrete magnetics and a significant reduction of size can be achieved by using the PIM module.**

***Index Terms*—DC–DC converter and fuel cell, hybrid, inductor, interleaving, planar-integrated magnetics (PIM), transformer.**

I. Introduction

In order to satisfy the requirements of modern power electronics application, magnetics integration with planar core has proven to be an effective means of reducing the converter size, the cost and increasing the converter efficiency [1]–[9]. Planar magnetics have unique advantages in terms of increased power density, better cooling capability, modularity and manufacturing simplicity, as well as easy implementation of interleaved windings, which make them attractive for high current dc–dc power converter applications [10]–[12].

Manuscript received August 31, 2010; revised December 20, 2010; accepted March 1, 2011. Date of current version November 18, 2011. This work was supported by the Flux A/S. The paper was presented at the IEEE Energy Conversion Congress and Exposition (ECCE) Conference, Atlanta, GA, 2010. Recommended for publication by Associate Editor S. Choi.

The authors are with the Department of Electrical Engineering, Technical University of Denmark, Kongens, Lyngby DK-2800, Denmark (e-mail: zo@elektro.dtu.dk; zz@elektro.dtu.dk; oct@elektro.dtu.dk; ma@elektro.dtu.dk).

Color versions of one or more of the figures in this paper are available online at http://ieeexplore.ieee.org.

Digital Object Identifier 10.1109/TPEL.2011.2129598

In recent years, most efforts in integrated magnetics (IM) focus on the current-doubler rectifier due to its suitability for low-output-voltage and high-output-current applications. Unlike conventional magnetic integration focusing only on core integration, both core and winding integration can be realized in the current-doubler rectifier design, causing lower conduction loss and core loss. As a result, lower overall cost, size as well as higher efficiency can be obtained by the IM design for the current-doubler circuit [1]–[5]. A 1 kW with 300–400-V input voltage and 48-V output voltage asymmetrical half-bridge pulse-width modulation converter employing an integrated L–L–C–T module is constructed in [6]. Detailed suggestions are given of how one generic, integrated L-C-T component could be used to implement various resonant converter topologies by merely reconfiguring the external terminals of the integrated components [7], [8]. An integrated transformer consisted of four step-down transformers wound on a single magnetic core for an interleaved four-phase forward converter has been proposed [13]. Coupled inductors can greatly reduce the steady-state inductor current ripples without compromising the transient response [14]–[18].

A new planar-integrated magnetics (PIM) module for a phase-shift plus duty-cycle-controlled hybrid bidirectional dc–dc converter is proposed in this paper. One boost inductor and two transformers are integrated into an E-I-E core geometry. The modeling of the PIM structure is presented in Section III. The flux generated from each magnetic component assembled into the PIM module can be partially cancelled, resulting in a lower core loss. Integrated transformers in this geometry have higher magnetizing inductance compared to separated transformers in terms of the same winding arrangements at the outer legs, reducing current stress. AC losses in the windings and leakage inductance of the transformers are kept low by interleaving the primary and secondary turns of the transformers. The design considerations for the PIM module are presented in depth in Section IV. Finally, in order to verify the validity of the design approach and theoretical analysis, a laboratory prototype employing the PIM module is implemented for a fuel cell (FC) application with 20–40-V input voltage and 400-V output voltage. Detailed results from the experimental comparisons demonstrate the PIM module is fully functional and electromagnetically equivalent to the discrete magnetics, and a significant reduction of the size can be achieved by using the PIM module.

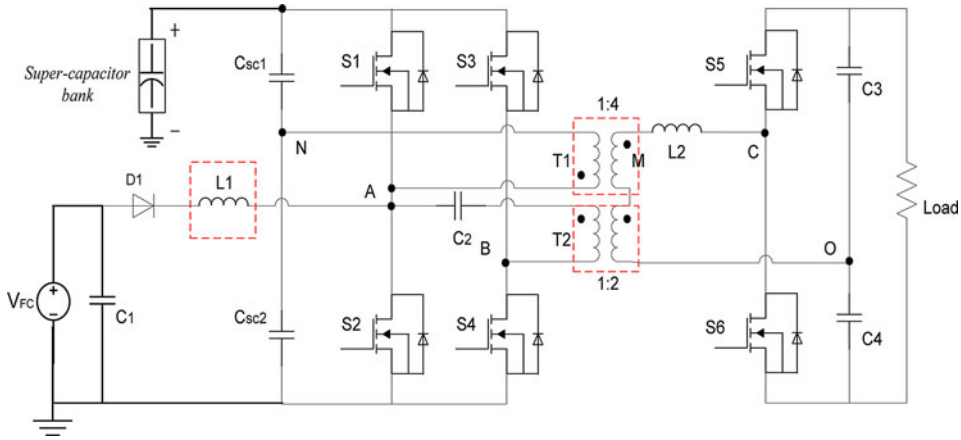

Fig. 1. Hybrid bidirectional dc–dc converter topology.

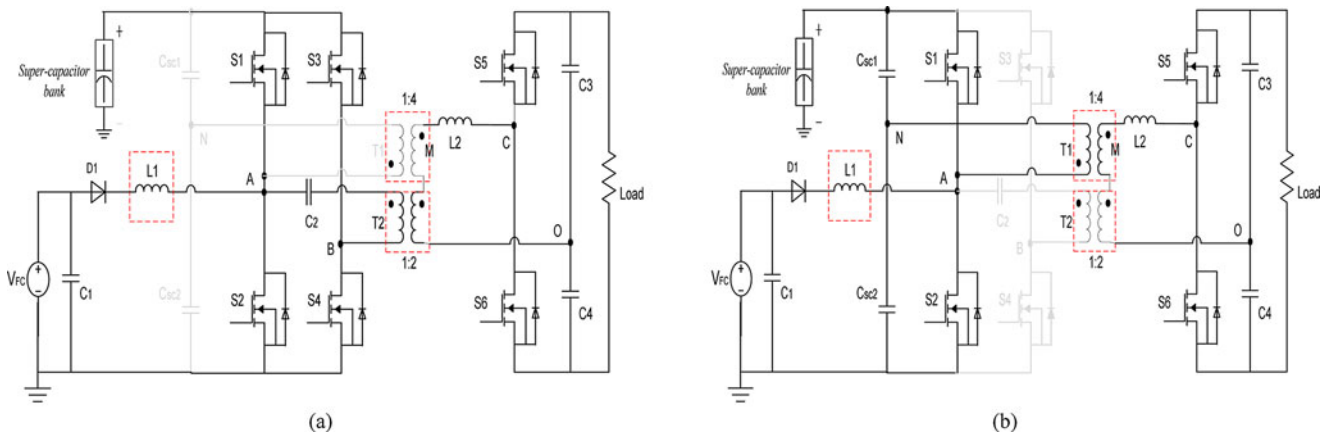

Fig. 2. Equivalent circuits of the converter: (a) full-bridge structure and (b) half-bridge structure.

II. Operation Principles of the Hybrid Bidirectional DC–DC Converter

Nowadays, the hybrid system based on FCs and supercapacitors as an environmentally renewable energy system has been applied in many fields, such as hybrid electric vehicle, uninterruptible power supply, and so on [19], [20]. Boost-derived topologies are preferred in FC applications due to their low input current ripple [21]. Fig. 1 shows a novel phase-shift plus duty-cycle-controlled hybrid bidirectional dc–dc converter, which is originally proposed in [22]. The converter utilizes a boost-type input structure to limit the current ripple drawn from the FCs. For better understanding, Fig. 2 shows equivalent circuits of the converter. Two transformers T_1 and T_2 are employed to associate with a half-bridge circuit [see Fig. 2(b)] and a full-bridge circuit [see Fig. 2(a)], respectively. The phase-shift technique is used in the converter since it can realize zero voltage switching (ZVS) for all switches without auxiliary switches. However, if the amplitude of input voltage is not matched with that of output voltage, the voltage on the phase-shift inductor L_2 consisting of the leakage inductance of the transformers on the secondary side and an auxiliary inductor becomes high, resulting in a higher current stress on all components. In order to operate in a wide input range, duty-cycle control for S_3 and S_4, therefore, can be used to reduce the current stress and conduction losses [23]–[27].

As shown in Fig. 1, a boost type half-bridge structure associated with the switches S_1 and S_2 operating at 50% duty cycle is located on the primary side of the transformer T_1. The supercapacitor bank crossing on the two series-connected capacitors C_{SC1} and C_{SC2} is connected on a variable low-voltage dc bus as an auxiliary energy source. Bidirectional operation can be realized between the supercapacitor bank and the output load. S_3 and S_4 are controlled by the duty cycle D to reduce the current stress when the input voltage V_{FC} is variable over a wide range. The two transformers T_1 and T_2 with independent primary windings as well as series-connected secondary windings are utilized to realize galvanic isolation and boost a low input voltage to the high-voltage secondary side. To avoid dc bias current of the transformer T_2 caused by asymmetrical operation in the full-bridge circuit (flux-walking problem), a dc blocking capacitor C_2 is added in series with the primary winding of T_2. Voltage-doubler circuit is used in the secondary side to further improve the voltage conversion ratio. The phase-shift inductor L_2 in the secondary side is utilized as power delivering interface element from low-voltage input side to high-voltage side. The delivered power is controlled by the phase-shift angle δ between

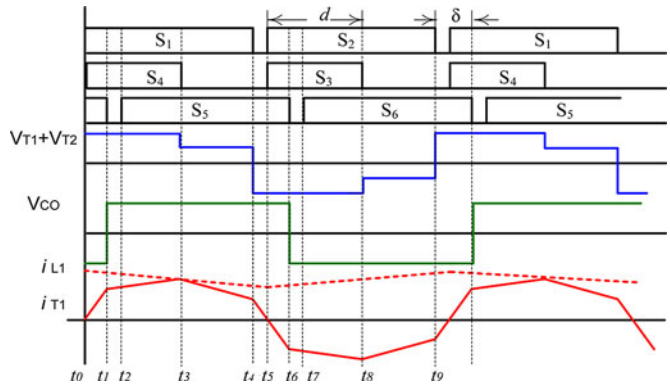

Fig. 3. Key waveforms of the converter under duty-cycle control.

S_1 and S_5, and can be expressed as (1) if the duty cycle D is 0.5 [24]

$$P = \frac{V_{\rm CO} \cdot V_{\rm MO} \cdot \delta \cdot (\pi - \delta)}{\omega \cdot \pi \cdot L_2} \tag{1}$$

where $V_{\rm MO}$ is the voltage on the secondary side of the transformers and $V_{\rm CO}$ is the high-side voltage as shown in Fig. 1. To facilitate the explanation of the operation of the circuit in Fig. 1, Fig. 3 shows key waveforms of the converter under duty-cycle control. A simplified stage analysis during a half switching period is presented as follows.

1) *Stage 1* (t_0–t_1): S_1, S_4, and S_6 are conducting. The voltage on L_2 is $V_{T1s}+V_{T2s}+V_{\rm CO}$, so the i_{L2} will increase linearly. I_{L1} goes though the body diode $D_{\rm S1}$ of switch S_1.
2) *Stage 2* (t_1–t_2): At t_1, S_6 is turned off. The inductor L_2 begins to resonate with the stray capacitors C_{S5} and C_{S6} of switches S_5 and S_6. When the voltage on C_{S5} reduces to zero, the body diode of S_5 starts to conduct, and the voltage $V_{\rm CO}$ changes the direction. Hereby, V_{L2} equals to $V_{T1s}+V_{T2s}-V_{\rm CO}$.
3) *Stage 3* (t_2–t_3): At t_2, S_5 is turned on under ZVS. The current paths are the same as those in the stage 2.
4) *Stage 4* (t_3–t_4): At t_3, S_4 is turned off. The inductor L_2 begins to resonate with the stray capacitors C_{S3} and C_{S4} of switches S_3 and S_4. When the voltage cross S_3 reduces to zero, D_{S3} is, therefore, forward biased. The voltage crossing the primary winding of T_2 is clamped to zero. So V_{L2} equals to $V_{T2s}-V_{\rm CO}$.
5) *Stage 5* (t_4–t_5)*:* At t_4, S_1 is turned off. The inductor L_2 begins to resonate with the stray capacitors C_{S1} and C_{S2} of switches S_1 and S_2. C_{S2} is discharged from $2V_{\rm FC}$. The rate of change depends on the magnitude $I_{T1p}+I_{T2p}-I_{Ldc}$. At t_5, V_{CS2} attempts to overshoot the negative rail. D_{S2} is forward biased. During this period, S_2 can be turned on under ZVS.

After t_5, the same operational principles are repeated in the second half cycle. Detailed stage analysis and the characteristics of the converter can be referred in [22].

III. New PIM Module Structure

The conventional IM design currently uses soft-ferrite E-I or E-E core. In this study, a new PIM structure is proposed to integrate two transformers T_1 and T_2 and boost inductor L_1 with a combined E-I-E core geometry. The PIM module is shown in Fig. 4. The windings of each transformer are symmetrically distributed into the outer legs of E-cores. The inductor L_1 is constructed by two series-connected inductors wound in each center leg of E-cores, respectively, with certain air gaps. The middle I-core provides a low reluctance return path, where flux cancellation can be achieved. Due to a high reluctance in the center legs, most alternating flux Φ_1 and Φ_2 generated from the transformer windings flows out of the center leg of E-core as shown in Fig. 4(b). The flux Φ_3 generated from the inductor windings flows in the center legs of E-cores, and then distributes equally into the two outer legs. None of the flux Φ_3 exists in the shared I-core. Half of Φ_3 increases the total flux in the right side together with Φ_1 and Φ_2 and the other half of Φ_3 decreases them in the left side at a certain instantaneous time. As a result, although the flux Φ_3 couples with Φ_1 and Φ_2 on the two outer legs, the transformers' behavior will not be affected. Since partial ac flux cancellations are achieved in the core as well as smaller total ferrite volume, lower core loss might be obtained compared with discrete magnetics. However, notice that partial saturation may occur due to the flux overlapping on the right side leg, which limits the nominal power of the converter.

In terms of this new geometry, many advantages can be concluded as follows.

1) Air gaps located in the center legs cause a lower fringing effect as well as electromagnetic interference (EMI) problem compared with the case that air gaps located in the outer leg [1], [3]. Mechanically stabilization is also counted as an advantage.
2) Magnetizing inductance will not be affected by the air gaps this is due to the fact that the flux Φ_1 and Φ_2 only circulate in the outer legs rather than the center legs with air gaps. Certainly, the magnetizing inductance in the PIM is much lower than the case where the same windings are wound on the center leg due to the equivalent cross section of the outer leg is only half of the center leg. However, magnetizing inductance can be improved by using the integrated approach compared to the separated transformers in terms of the same winding locations. This is because the flux cancellation occurring in the shared I-core effectively reduces the length of the transformer flux path [28], [29]. It is mathematically proved in Section IV and the measurement results in Section V also demonstrate the same conclusion.
3) Since partial ac flux cancellations are achieved in the core as well as smaller total ferrite volume, lower core loss might be obtained compared with discrete magnetics.
4) Less number of cores is used, causing a lower cost for the converter.
5) The integrated approach provides a low volume for the converter, which increases the power density required by space restrictions in automotive and integrated application.
6) *Flexibility:* The integrated approach can be extended into many other topologies such as the primary-parallel

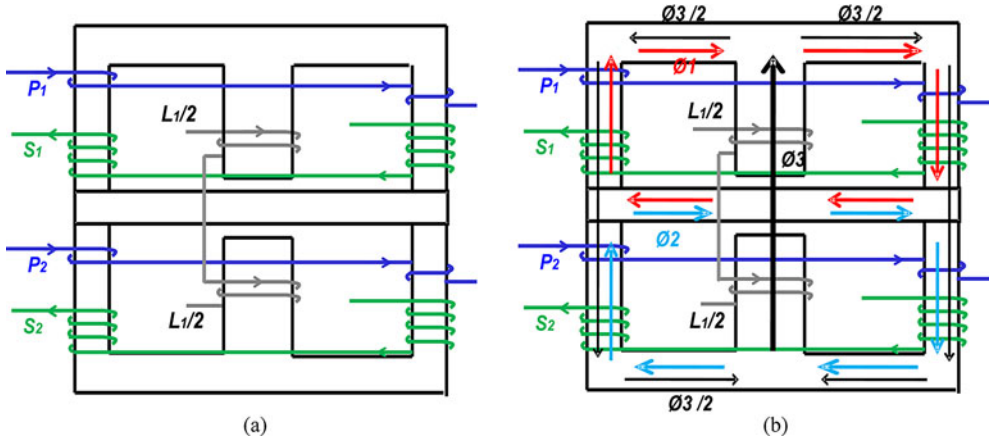

Fig. 4. (a) Proposed E-I-E integrated magnetic structure and (b) its instantaneous flux distribution.

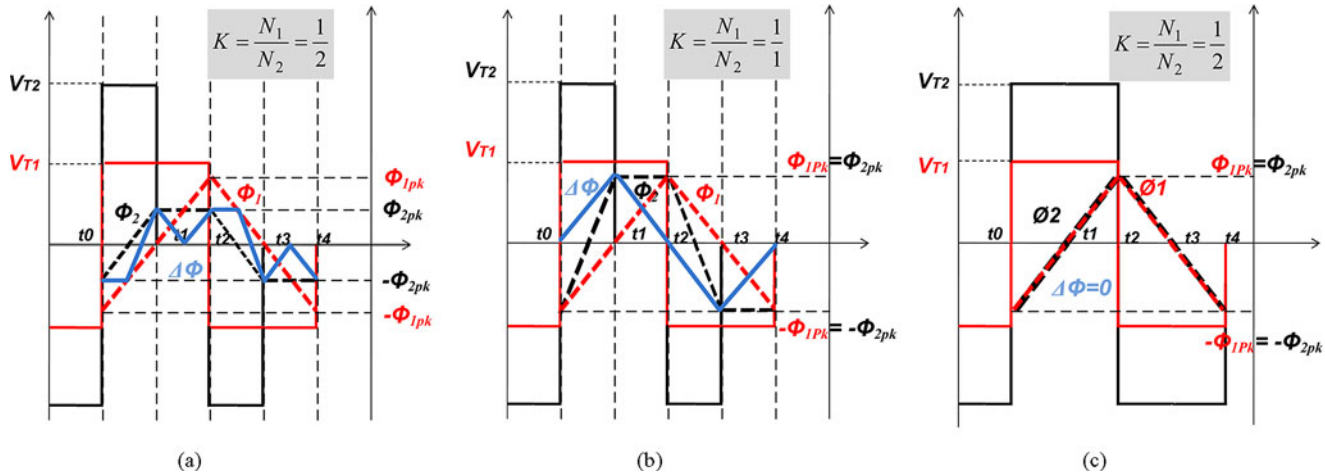

Fig. 5. Excitation voltages of the transformers and their ac flux waveforms: (a) when the primary turns factor is $K = 0.5$ under duty-cycle control; (b) when the primary turns factor is $K = 1$ under duty-cycle control; and (c) when the primary turns factor is $K = 0.5$ under nonduty-cycle control.

isolated boost converter [30], multitransformers converters, and so on.

IV. Magnetics Design Consideration

A. Primary Turns Factor

If the duty cycle D of S_3 and S_4 is smaller than 50% (duty-cycle control), it is impossible to obtain a complete flux cancellation in the shared I-core. A proper primary turns factor $K = N_1/N_2$ should be chosen in order to minimize the core loss as well as maximize the delivered power capability. N_1 and N_2 are the number of turns on the primary side of T_1 and T_2, respectively. Fig. 5 reflects the ac flux of the transformers Φ_1 and Φ_2 and variation of flux in the shared I-core $\Delta\Phi$ with different primary turns factors. Applying a piecewise linear model (PWL) to the nonsinusoidal waveform and combining this with the improved generalized Steinmetz equation (IGSE) [31] shows that the converter working under duty-cycle control ($D < 50\%$) has a lower core loss in the shared I-core when the primary turns factor is $K = 0.5$; furthermore, zero core loss (ideally) can be obtained in the shared I-core if the duty cycle D is 50% (nonduty-cycle control).

B. Magnetic Reluctance Model

Fig. 6 shows an equivalent magnetic model of the PIM module, where R_1 is the reluctance of the outer leg of E-core, R_2 is the reluctance of I-core, and R_C represents the reluctance of the center leg of E-core. R_C is much bigger than R_1 and R_2 due to the air gaps in the center legs. Since the transformers and the inductor do not affect each other, the equivalent magnetic model can be divided into two parts as shown in the bottom of Fig. 6. The left part represents the magnetic model associated with T_1 and T_2. The flux Φ_1 and Φ_2 will not flow in the center legs of E-core. The flux Φ_1 and Φ_2 in the shared I-core might be either partially or fully cancelled depending on the duty cycle D. The right part represents the magnetic model of the inductor L_1.

With assumption that leakage flux through the air is negligible, (2)–(4) can be obtained according to the magnetic model

$$N_1 \cdot i_{m1} = \phi_1 \cdot (2R_1 + R_2) + (\phi_1 - \phi_2) \cdot R_2 \quad (2)$$

$$N_2 \cdot i_{m2} = \phi_2 \cdot (2R_1 + R_2) + (\phi_2 - \phi_1) \cdot R_2 \quad (3)$$

$$N_L \cdot i_L = \phi_3 \cdot 2R_c + 0.5 \cdot \phi_3 \cdot (2R_1 + R_2). \quad (4)$$

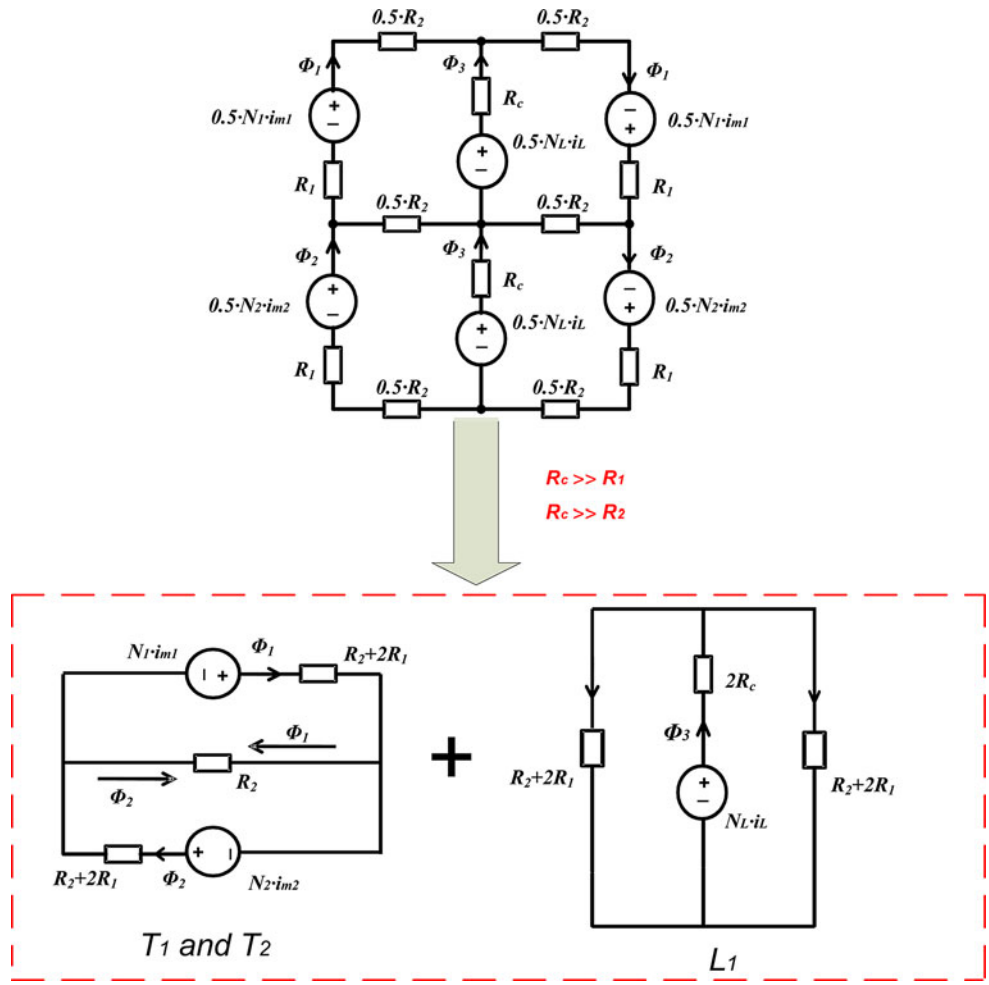

Fig. 6. Equivalent magnetic reluctance model of the PIM module.

As seen in Fig. 5, the rate of change on Φ_1 and Φ_2 are different over an entire period when the duty-cycle control is used. Accordingly, the following two cases with four intervals are analyzed ($D < 0.5$, T is the period)

1) Case 1 [0 ~ D·T] and [0.5·T ~ (0.5+D)·T]: the rate of change on Φ_1 and Φ_2 are the same. Based on Faraday's law, magnetizing inductances can be obtained

$$L_{m1} = \frac{N_1^2}{2R_1 + R_2}, \quad L_{m2} = \frac{N_2^2}{2R_1 + R_2},$$
$$L_1 = \frac{N_L^2}{2R_c + R_1 + 0.5 \cdot R_2}.$$

2) Case 2 [D·T ~ 0.5·T] and [(0.5+D)·T ~ T] : the rate of change on Φ_2 is zero. Without excitation current on T_2 in this period, there is no sense in calculating the magnetizing inductance of T_2

$$L_{m1} = \frac{N_1^2}{2 \cdot (R_1 + R_2)}; \quad L_1 = \frac{N_L^2}{2R_c + R_1 + 0.5 \cdot R_2}.$$

For a single separated transformer with the same winding arrangement at the outer leg, the magnetizing inductance is equal to $L_m = N^2/2(R_1 + R_2)$. As can be seen, such integrated transformers have higher magnetizing inductances than the single case when both T_1 and T_2 have excitation (*case 1*). This is because of the fact that the flux cancellation occurring in the shared I-core effectively reduces the length of the transformer flux path. Whereas, there is no improvement on magnetizing inductances if any one of the transformers has no excitation (*case 2*).

C. Saturation Consideration

It has been mentioned in the previous section that a saturation problem may appear due to the half of Φ_3 (including dc component) and their overlapping flux together with Φ_1 or Φ_2 in the right part. According to Faraday's law and Ampere's law, the peak flux densities for each magnetic component in the PIM module can be derived

$$B_{\mathrm{pk}\_T1} = \frac{V_{\mathrm{FC}}}{4 \cdot f \cdot N_1 \cdot A_e} \tag{5}$$

$$B_{\mathrm{pk}\_T2} = \frac{V_{\mathrm{FC}} \cdot D}{f \cdot N_2 \cdot A_e} \tag{6}$$

$$B_{\mathrm{pk}\_L} = \frac{\mu_0 \cdot N_L \cdot I_{\mathrm{pk}}}{l_g} \tag{7}$$

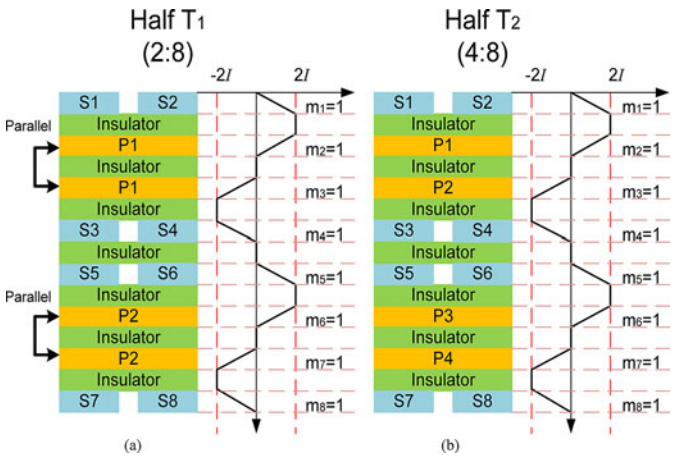

Fig. 7. Winding arrangements and MMF distributions (a) for a half winding of T_1 wound in one of the outer legs and (b) for a half winding of T_2 in one of the outer legs.

where f is the switching frequency and A_e is the cross section of the outer leg of E-core. l_g is the total length of air gaps in the center legs of E-core. In order to avoid flux saturation in the PIM module, the following equations are required if B_{pk_T2} is smaller than B_{pk_T1}

$$B_{\mathrm{pk}\_T1} + B_{\mathrm{pk}\_L} = \frac{V_{\mathrm{FC}}}{4 \cdot f \cdot N_1 \cdot A_e} + \frac{\mu_0 \cdot N_L \cdot I_{\mathrm{pk}}}{l_g} \leq B_{\mathrm{sat}}. \tag{8}$$

Therefore, one of the drawbacks for the PIM module is a limited power capability. The power capability of the PIM module can be increased by minimizing the peak flux density of T_1, B_{pk_T1}, which can be implemented by increasing either the switching frequency or the number of turns. Although both methods might achieve lower core loss, increased switching frequency contributes to a higher eddy current effect in the conductors as well as higher switching loss, and also an increased number of turns will cause a higher winding loss.

The maximum allowed flux density ripple ΔB_L is given by the maximum peak flux density for the inductor B_{pk_L} and the ratio of allowed peak-to-peak ripple current ΔI to the peak current I_{pk}

$$\Delta B_L = B_{\mathrm{pk}\_L} \cdot \frac{\Delta I}{I_{\mathrm{pk}}}. \tag{9}$$

The flux density ripple shall be less than or equal to the maximum allowed value given by (9). Accordingly the required number of turns is

$$N \geq \frac{V_{\mathrm{FC}} \cdot T}{4A_e \cdot B_{\mathrm{pk}\_L}} \cdot \frac{I_{\mathrm{pk}}}{\Delta I}. \tag{10}$$

High ripple current increases the core loss for the inductor L_1, and power loss in the MOSFETs. But low ripple current requires a high number of inductor turns, which results in high winding loss. Experience has shown that a good tradeoff in high current application is a current ripple factor ($I_{\mathrm{pk}}/\Delta I$) of 2 to 3.

D. Winding Arrangement

Winding losses in transformers increase dramatically with high frequency due to eddy current effects. Eddy current losses, including skin effect and proximity effect losses seriously impair the performance of transformers in high-frequency power conversion applications. Both the skin effect and the proximity effect cause the current density to be nonuniformly distributed in the cross section of the conductor and, thus, cause a higher winding resistance at higher frequency. The proximity effect loss, in a multilayer winding, may strongly dominate over the skin effect loss depending on the winding arrangement. Interleaving transformer windings can reduce the proximity loss significantly when the primary and secondary currents are in phase [32]–[34]. Fig. 7 shows the winding arrangements and magneto motive force (MMF) distributions along a vertical direction for a half winding of T_1 and T_2 wound in one of the outer legs, respectively. The value of m [35] in each layer is equal to 1 that contributes to lower ac resistances.

Not only ac resistance can be reduced, but also leakage inductance can be significantly decreased by the interleaving winding technique [36]. However, the reduced leakage inductance is not needed because the converter is working under phase-shift control, where a high leakage inductance is desirable. Considering a high current application, ac resistance is more important because it significantly affects the efficiency of the converter. Therefore, the interleaving technique is still adopted in order to reduce ac resistance. An auxiliary inductor is added in series with the secondary windings to establish a desired phase-shift inductor L_2. Notice that interwinding capacitance in this kind of interleaving arrangement is much better than that in a full interleaving arrangement without compromising any other performances including leakage inductance and ac resistance because of fewer intersections between the primary and the secondary, contributing to a relative lower EMI problem [35].

V. Simulation and Experimental Results

The specification of the hybrid dc–dc converter is shown in Table I. The converter works with variable input voltage of 20–40 V, and 400-V output voltage. The duty cycles of S_1 and S_2 is 50% to double input voltage to the dc bus of supercapacitor bank. The duty-cycle control is used to reduce the peak currents. Switching frequency is 100 kHz. A series dc blocking capacitor C_2 accommodates any volt-second mismatching and flux walking problem in the full bridge circuit. The resonant circuit consisting of C_2 and the primary leakage inductance of T_2 is designed to have a resonant frequency much lower than the switching frequency. A 40-μH auxiliary inductor plus the leakage inductance obtained on the secondary side of transformers are utilized as the phase-shift inductor L_2, which determines the power as expressed in (1). A good choice for the value of the boost inductor L_1 is, as aforementioned, to use a current ripple factor between 2 and 3.

To verify the validity of design approach, a 2-D finite element analysis (FEA) simulation model linked with external simulation circuit has been built. The simulation parameters fully coincide with the specifications shown in Table I. Fig. 8 shows

TABLE I
SPECIFICATIONS OF THE HYBRID DC–DC CONVERTER

Parameters	Values
Input voltage V_{FC} (V)	20-40
Output voltage V_o (V)	400
Duty cycle of S_1,S_2 and S_5,S_6	0.5
Duty cycle of S_3 and S_4	0.2-0.5
Switching frequency f_s (kHz)	100
DC blocking capacitance C_2 (μF)	10
Auxiliary inductor L_2 (μH)	40
Boost inductor L_1 (μH)	12
Turns ratio of T_1	1:4
Turns ratio of T_2	1:2

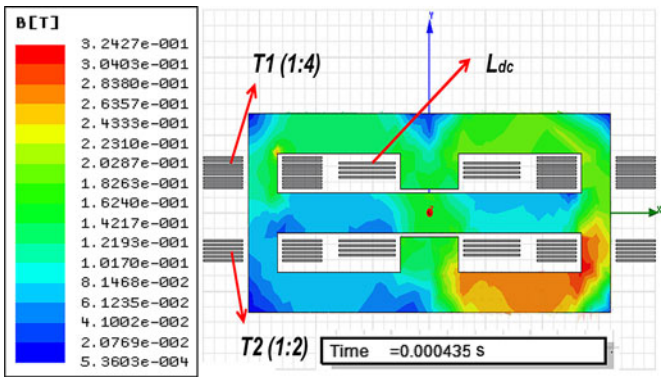

Fig. 8. Instantaneous flux density distribution in the core using 2-D FEA simulation.

an instantaneous distribution of the flux density B in the core. Apparently, the right part with a heavy color stress illustrates that half of Φ_3 increases the total flux in the right side together with Φ_1 and Φ_2. Reversely, the other half of Φ_3 decreases the flux in the left part. A partial flux cancellation on Φ_1 and Φ_2 occurs in the shared I-core and none of flux Φ_3 goes through it.

The proposed PIM module is further validated by two experimental designs. Fig. 9 shows pictures of (a) laboratory prototypes with discrete magnetic components and (b) its integrated converter employing the PIM module, respectively. Accordingly, almost half size is achieved in the integrated converter. Primary switching MOSFETs S_1–S_4 are implemented by IRFP4568 and high-voltage side MOSFETs S_5 and S_6 are realized by Vishay SIHG20N50 C. In order to make a relative fair comparison, all switching devices, gate drivers, capacitors, and auxiliary inductor are kept the same. In the integrated converter, the PIM module have 4 turns on the primary side of transformer T_1 and 8 turns on the primary side of T_2. The winding arrangements are shown in Fig. 7. Two ELP-64 cores and one ILP-64 core all with N87 core material are used in the PIM module. The inductor L_1 has 4 turns and 0.5-mm air gap in both center legs of E-cores to form a 10-μH inductance. All of windings are structured by a printed circuit board with 4-oz copper thickness. In the discrete converter, all magnetic components are independent. The inductor L_1 is designed with a Kool-Mμ-40μ core (distributed air gap core). 11 turns with 0.2-mm copper foil are wound in the 00K4020E core type to obtain the same inductance as the PIM module. Both T_1 and T_2 in the discrete converter use EILP-64 core types as well. Without the problem of limited power capability and flux cancellation, 4 turns, therefore, are used on the primary side of T_2. Interleaving technique is still used to reduce ac resistance. Notice that the transformer windings for the discrete converter are wound on the center legs of E-cores.

The measurement results on the magnetic components for both converters are shown in Tables II and III, respectively, obtained by an impedance analyzer PSM1735. As seen from the results, the PIM module has a higher leakage inductance that is due to the fact that the separated windings cause an imperfect coupling. Furthermore, the higher number of turns on T_2 also can be used to explain the higher leakage inductance [12]. With half cross section of the center leg, magnetizing inductance in the PIM module is obviously smaller than that in the discrete magnetics. However, it is worth to notice that magnetizing inductance in the PIM module is higher than half of the one in the discrete magnetics, which coincides with the previous analysis in Section III. 2.7-mH magnetizing inductance referred to the secondary side is enough to be used in this application where only 0.44-A magnetizing current ripple is induced when the converter works in the nominal operation. With regard to ac resistance of the transformers, a longer winding length, higher number of turns on T_2 as well as a few fringing flux effects may cause a higher value in the PIM module. This contributes almost 1 W more of transformer winding loss than that in the discrete converter as shown in Table IV.

To facilitate a comparison of the efficiency of the two designs, the losses of major magnetic components are estimated. The results are tabulated in Table IV for the case when the input voltage is 30 V and the output power is 600 W. Although L_1 in the discrete converter has a higher number of turns that causes a higher ratio of ac resistance to dc resistance due to the proximity effect, the winding loss of inductor L_1 in the discrete converter is much lower than that in the PIM-integrated converter as indicated in the breakdown analysis. This is because a very low dc resistance can be obtained for L_1 in the discrete magnetics due to a thick and wide copper foil, and the dc loss dominates the winding losses of the inductor. The core loss is evaluated by calculating with the combination of the PWL and the IGSE. The total core loss of the discrete magnetics is much higher than that of the PIM module. One reason is the distributed air gap core contributes a relative higher core loss in the discrete magnetics. The other reason is that the flux cancellation leads to a lower core loss. The authors would like to point out that the size, the winding loss, the core loss, etc., are always in contradiction. A low core loss probably can also be realized in the discrete magnetics but the size and the winding loss might be compromised. In fact, a real fair comparison should be built on top of optimized magnetics design. In the present case, the comparison

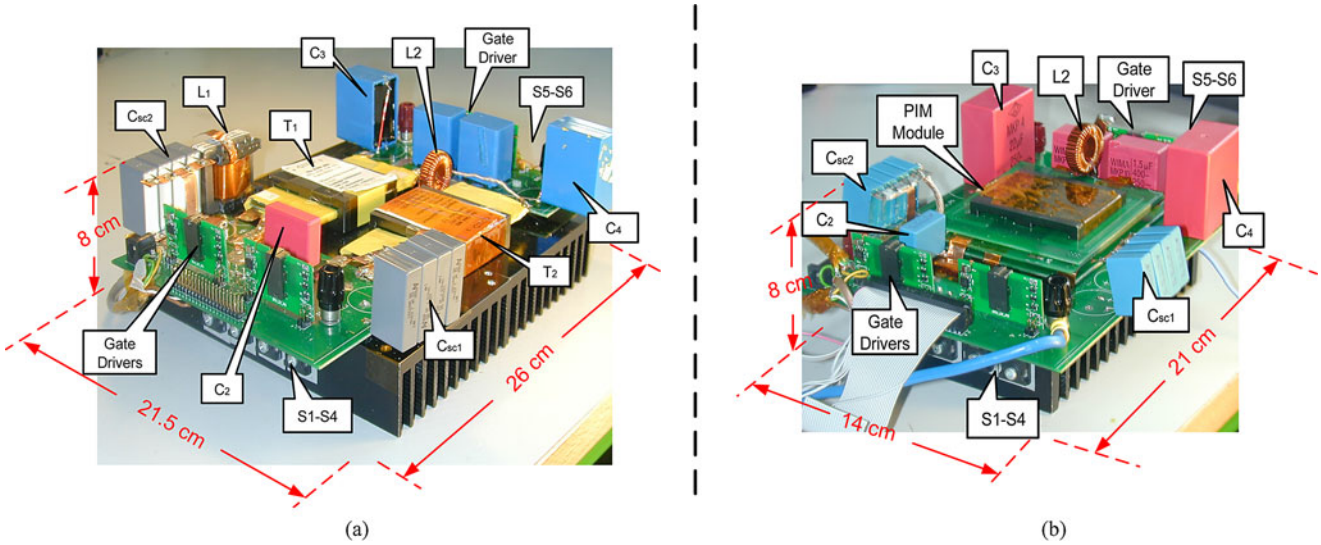

Fig. 9. (a) Hybrid dc–dc converter with discrete magnetic components and (b) hybrid dc–dc converter with proposed PIM module.

TABLE II
MEASUREMENT RESULTS FOR THE DISCRETE MAGNETICS

Parameters for the discrete magnetics	Values
Leakage inductance of T_1 (*ref. to pri.*)	101 (*nH*)
Magnetizing inductance of T_1 (*ref. to pri.*)	236.6 (*uH*)
AC resistance of T_1 at 100 *kHz* (*ref. to pri.*)	22.1 ($m\Omega$)
Leakage inductance of T_2 (*ref. to pri.*)	109.3 (*nH*)
Magnetizing inductance of T_2 (*ref. to pri.*)	190.8 (*uH*)
AC resistance of T_2 at 100 *kHz* (*ref. to pri.*)	30.8 ($m\Omega$)
Inductance of L_1	13.1 (*uH*)
AC resistance of L_1 at 100 *kHz*	34.6 ($m\Omega$)
DC resistance of L_1	3.7 ($m\Omega$)
Leakage inductance when the secondaries of the two transformers are in series (*ref. to sec.*)	1.9 (*uH*)
Magnetizing inductance when the secondaries of the two transformers are in series (*ref. to sec.*)	4.6 (*mH*)
AC resistance at 100 *kHz* when the secondaries of the two transformers are in series (*ref. to sec.*)	476.2 ($m\Omega$)

TABLE III
MEASUREMENT RESULTS OF THE PIM MODULE

Parameters for the PIM module	Values
Inductance of L_1 in the PIM Module	11.9 (*uH*)
AC resistance of L_1 in the PIM Module at 100 *kHz*	45.6 ($m\Omega$)
DC resistance of L_1 in the PIM Module	12.6 ($m\Omega$)
Leakage inductance of the PIM Module (*ref. to sec.*)	5.6 (*uH*)
Magnetizing inductance of the PIM Module (*ref. to sec.*)	2.7 (*mH*)
AC resistance at 100 *kHz* of the PIM Module (*ref. to sec.*)	535 ($m\Omega$)

TABLE IV
LOSS EVALUATION BREAKDOWN ON THE MAGNETIC COMPONENTS FOR TWO DIFFERENT PROTOTYPES UNDER 30-V INPUT, 600-W OUTPUT

Loss	Discrete Magnetics			PIM Module	
	T_1	T_2	L_1	T_1& T_2	L_1
Winding loss	4.33 W	1.51 W	2.16 W	6.55 W	6.49 W
	Total winding loss: 8 W			Total winding loss: 13.04 W	
Core loss	0.36 W	0.91 W	2.70 W	Total core loss: 1.73 W	
	Total core loss: 3.97 W				
Total loss	11.97 W			14.77 W	

may not be real fair but it still shows that the PIM module has an advantage on core loss and has an impressive size deduction.

Figs. 10–12 show (a) the measured waveforms in both the discrete converter and (b) the integrated converter under duty-cycle control at 30-V input voltage and 600-W output power. Fig. 10 shows the plots of the primary voltages (CH_1: V_{AN} and CH_2: V_{AB}) and currents (CH_3: i_{T1} and CH_4: i_{T2}) for T_1 and T_2, respectively. As can be seen, the peak currents of the transformers have been dropped during the period of duty-cycle control. Fig. 11 shows the waveforms of the voltages (CH_1: V_{CO} and CH_2: V_{MO}) on the secondary side and currents of the boost inductor (CH_3: i_{L1}) and the auxiliary inductor (CH_4: i_{L2}). Zero-voltage turn on for the MOSFETs can be seen from Fig. 12. For simplification, only S_4 and S_6 are chosen to

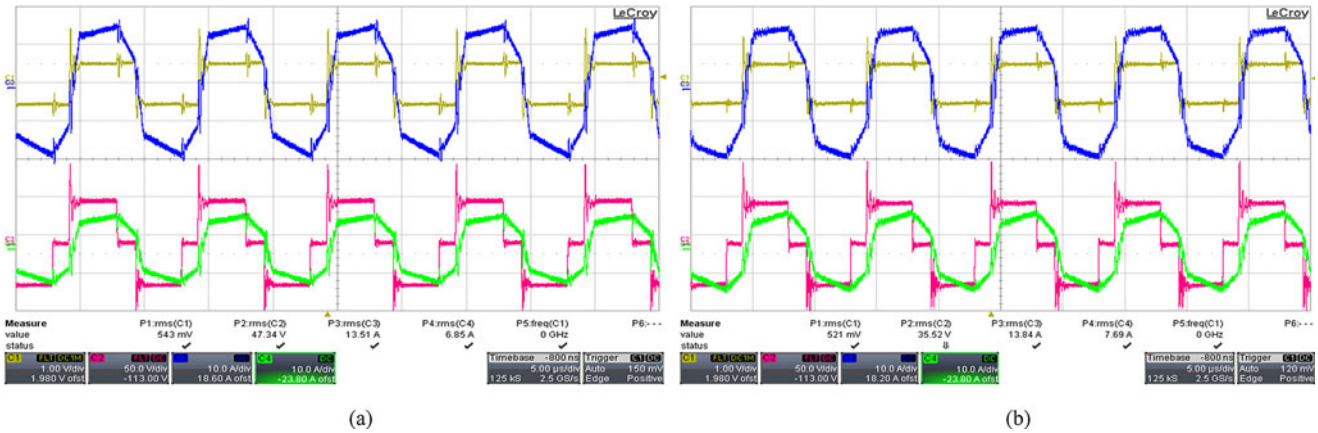

Fig. 10. (a) Waveforms of the discrete converter and (b) PIM converter, both are working under the duty-cycle control at 30-V input voltage, 600-W output power. CH1: V_{AN} (50 V/div); CH2: V_{AB} (50 V/div); CH3: $i_{T\,1}$ (10 A/div); CH4: $i_{T\,2}$ (10 A/div).

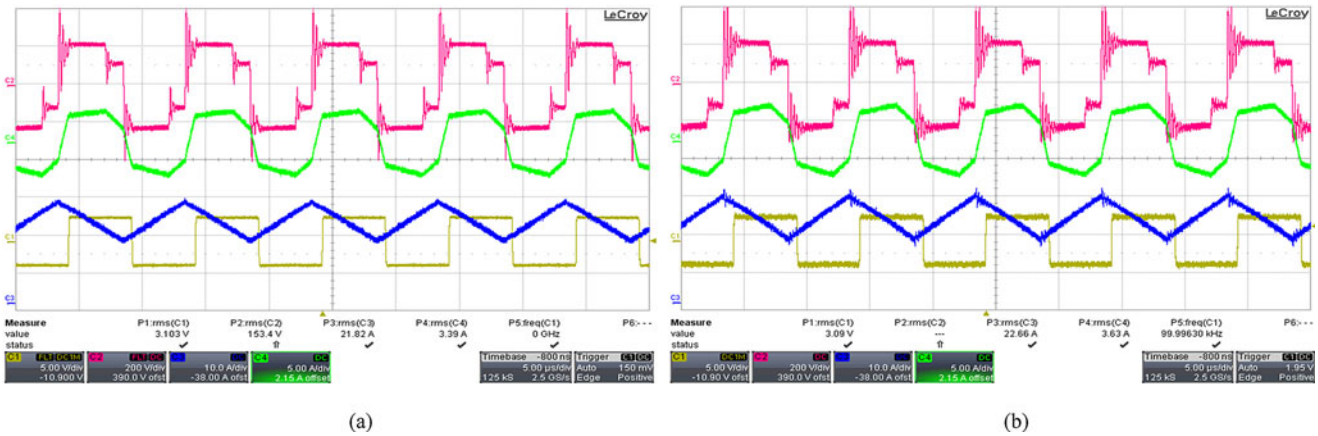

Fig. 11. (a) Waveforms of the discrete converter and (b) PIM converter, both are working under the duty-cycle control at 30-V input voltage, 600-W output power. CH1: V_{CO} (250 V/div); CH2: V_{MO} (200 V/div); CH3: $i_{L\,1}$ (10 A/div); CH4: $i_{L\,2}$ (5 A/div).

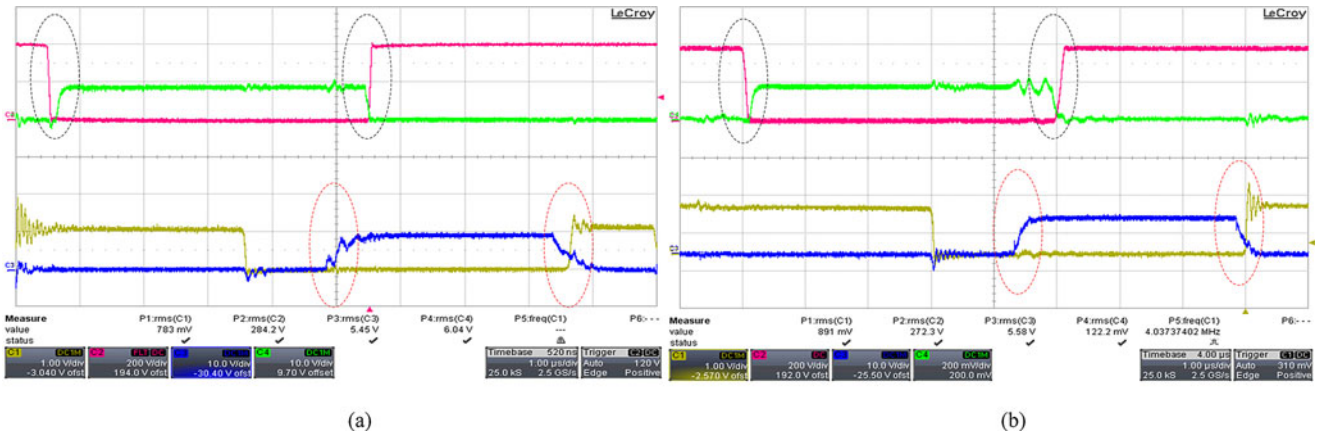

Fig. 12. ZVS waveforms of S_4 and S_6 for (a) discrete converter and (b) PIM converter, both are working under the duty-cycle control at 30-V input voltage, 600-W output power. CH1: V_{DS4} (50 V/div); CH2: V_{DS6} (200 V/div); CH3: $\mathrm{V_{GS4}}$ (10 V/div); CH4: V_{GS6} (10 V/div).

demonstrate the ZVS waveforms. In fact, zero-voltage turn on for all of MOSFETs in the circuit can be achieved at this operating point. The waveforms illustrate that the PIM module is fully functional and electromagnetically equivalent to the discrete magnetics.

High stability (<10 ppm) 0.1% shunt resistors and Agilent 34410A high precision multimeters are used for all efficiency measurements. Current sense signals are shielded and fitted with common mode filters. The comparison of efficiency curves between the discrete converter and the integrated

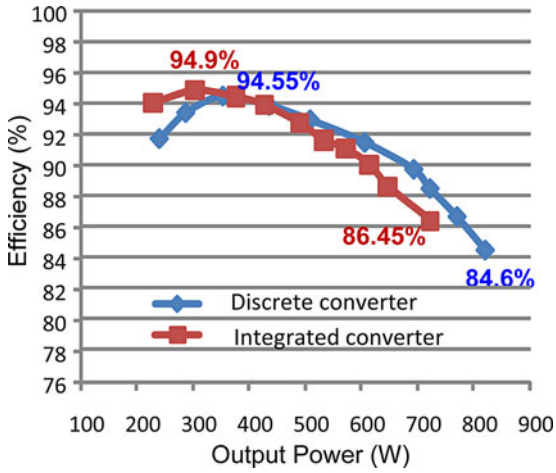

Fig. 13. Efficiency comparison between the discrete converter and the integrated converter under duty-cycle control (35%) at 30-V input voltage and 400-V output voltage.

converter is shown in Fig. 13. The integrated converter has higher efficiency at light load than the discrete converter. This is due to the fact that the core loss dominates in the total power loss at light load. Oppositely, the winding loss dominates in the total power loss at heavy load. Therefore, a higher efficiency in the discrete converter can be seen. The results coincide with the aforementioned analysis and the table breakdown.

VI. Conclusion

A new integrated magnetics approach has been proposed in this study. Two transformers and one inductor are integrated into E-I-E core geometry to reduce the total volume of the converter, core loss, and cost without compromising any electrical performance. The principle of the flux distribution in the core has been analyzed. Many advantages and disadvantages of the PIM module are included in this paper. Detail magnetics design consideration of the PIM module including primary turns factor, magnetic reluctance model, saturation problem, and winding arrangement has been investigated in depth. Two converters with discrete magnetics and integrated magnetics (PIM module) have been built to demonstrate that the PIM module is fully functional and electromagnetically equivalent. The loss evaluation has illustrated that there is a core loss reduction in the PIM design. Furthermore, almost half the size of the discrete converter can be achieved in the integrated converter with the PIM module.

References

[1] P. Xu, M. Ye, P. Wong, and F. C. Lee, "Design of 48 V voltage regulator modules with a novel integrated magnetics," *IEEE Trans. Power Electron.*, vol. 17, no. 6, pp. 990–998, 2002.

[2] J. Sun, K. F. Webb, and V. Mehrotra, "Integrated magnetics for current-doubler rectifiers," *IEEE Trans. Power Electron.*, vol. 19, no. 3, pp. 582–590, May 2004.

[3] J. Sun and V. Mehrotra, "Orthogonal winding structures and design for planar integrated magnetics," *IEEE Trans. Ind. Electron.*, vol. 55, no. 3, pp. 1463–1469, Mar. 2008.

[4] W. Chen, G. Hua, D. Sable, and F. C. Lee, "Design of high efficiency, low profile, low voltage converter with integrated magnetics," in *Proc. IEEE Appl. Power Electron. Conf. Expo.*, 1997, pp. 911–917.

[5] P. Xu, Q. Wu, P. Wong, and F.C. Lee, "A novel integrated current doubler rectifier," *Proc. IEEE Appl. Power Electron. Conf. Expo.,* 2000, pp. 735–740.

[6] R. Chen, J. T. Strydom, and J. D. van Wyk, "Design of planar integrated passive module for zero-voltage-switched asymmetrical half-bridge PWM converter," *IEEE Trans. Ind. Appl.*, vol. 39, no. 36, pp. 1648–1655, Nov./Dec. 2003.

[7] P. A. J. van Rensburg, J. D. van Wyk, and J. A. Ferreira, "Design, prototyping and assessment of a 3 kW integrated LCT component for development in various resonant converters," *IET Power Electron.*, vol. 2, no. 5, pp. 535–544, 2009.

[8] J. T. Strydom, J. A. Ferreira, J. D. van Wyk, I. W. Hofsajer, and E. Waffenschmidt, "Power electronic subassemblies with increased functionality based on planar sub-components," *Proc. IEEE Power Electron. Spec. Conf.,* 2000, pp. 1273–1278.

[9] M. J. Prieto, A. M. Pernía, J. M. Lopera, J. Á. Martínez, and F. Nuño, "Turn-coupling in thick-film integrated magnetic components for power converters," *IEEE Trans. Compon. Packag. Technol.*, vol. 31, no. 4, pp. 837–848, Dec. 2008.

[10] E. de Jong, J. Ferreira, and P. Bauer, "Toward the next level of PCB usage in power electronic converters," *IEEE Trans. Power Electron.*, vol. 23, no. 6, pp. 3153–3163, Nov. 2008.

[11] C. Quinn, K. Rinne, T. O'Donnell, M. Duffy, and C. O. Mathuna, "A review of planar magnetic techniques and technologies," in *Proc. IEEE Appl. Power Electron. Conf. Expo.,* 2001, pp. 1175–1183

[12] C. Buccella, C. Cecati, and F. de Monte, "A coupled electrothermal model for planar transformer temperature distribution computation," *IEEE Trans. Ind. Electron.*, vol. 55, no. 10, pp. 3583–3590, Oct. 2008.

[13] L-P. Wong, Y-S. Lee, M. H. L. Chow, and D. K-W Cheng, "A four-phase forward converter using an integrated transformer," *IEEE Trans. Ind. Electron.*, vol. 55, no. 2, pp. 817–831, Mar. 2008.

[14] S.-Y. Lee, A. G. Pfaelzer, and J. D. van Wyk, "Comparison of different designs of a 42-V/14-V dc/dc converter regarding losses and thermal aspects," *IEEE Trans. Ind. Appl.*, vol. 43, no. 2, pp. 520–530, Mar. 2007.

[15] P.-L. Wong, Q.-Q. Wu, P. Xu, B. Yang, and F. C. Lee, "Investigating coupling inductors in the interleaving QSW VRM," *Proc. IEEE Appl. Power Electron. Conf. Expo.,* 2000, pp. 973–978.

[16] H. Kosai, S. McNeal, B. Jordan, J. Scofield, B. Ray, and Z. Turgut, "Coupled inductor characterization for a high performance interleaved boost converter," *IEEE Trans. Magn.*, vol. 45, no. 10, pp. 4812–4815, Oct. 2009.

[17] L. Yan and B. Lehman, "An integrated magnetic isolated two-inductor boost converter: Analysis, design and experimentation," *IEEE Trans. Power Electron.*, vol. 20, no. 2, pp. 332–342, Mar. 2005.

[18] Z.-W. Ouyang, O. C. Thomsen, and M. A. E. Andersen, "New geometry integrated inductors in two-channel interleaved bidirectional converter," *Proc. IEEE Ind. Electron. Soc. Conf.,* 2010, pp. 582–586.

[19] A. Payman, S. Pierfederici, and F. M. Tabar, "Energy management in a fuel cell/supercapacitor multisource/multiload electrical hybrid system," *IEEE Trans. Power Electron*, vol. 24, no. 12, pp. 2681–2691, 2009.

[20] W.-S. Liu, J.-F. Chen, T.-J. Liang, R.-L. Lin, and C.-H. Liu, "Analysis, design, and control of bidirectional cascaded configuration for a fuel cell hybrid power system," *IEEE Trans. Power Electron.*, vol. 25, no. 6, pp. 1565–1575, Jun. 2010.

[21] M. Nymand, R. Tranberg, M. E. Madsen, U. K. Madawala, and M. A. E. Andersen, "What is the best converter for low voltage fuel cell applications-A buck or boost," in *Proc. IEEE Ind. Electron. Soc. Conf.,* 2009, pp. 959–964

[22] Z. Zhang, O. C. Thomsen, and M. A. E. Andersen, "Wide input voltage range bidirectional DC-DC converter for fuel cell and supercapacitor in UPS system," in *Proc. IEEE Power Electron. Drive Syst.,*2009 , pp. 706–711

[23] D. Xu, C. Zhao, and H. Feng, "A PWM plus phase-shift control bidirectional DC–DC converter," *IEEE Trans. Power Electron.*, vol. 19, no. 3, pp. 666–675, May 2004.

[24] J. Wang, F. Z. Peng, J. Anderson, A. Joesph, and R. Buffenbarger, "Low cost fuel cell converter system for residential power generation," *IEEE Trans. Power Electron.*, no. 5, pp. 1315–1322, Sep. 2004.

[25] Y. Jang and M. M. Jovanović, "A new PWM ZVS full-bridge converter," *IEEE Trans. Power Electron.*, vol. 22, no. 3, pp. 987–994, May 2007.

[26] D. Liu and H. Li, "A ZVS bi-directional DC–DC converter for multiple energy storage elements," *IEEE Trans. Power Electron.*, vol. 21, no. 5, pp. 1513–1517, Sep. 2006.

[27] H. Tao, A. Kotsopoulos, J. L. Duarte, and M. A. M. Hendrix, "Transformer-coupled multiport ZVS bidirectional DC–DC converter with wide input

range," *IEEE Trans. Power Electron.*, vol. 23, no. 2, pp. 771–781, Mar. 2008.
[28] Z.-W. Ouyang, Z. Zhang, O. C. Thomsen, M. A. E. Andersen, O. Poulsen, and T. Björklund, "Planar integrated magnetics design in wide input range dc-dc converter for fuel cell application," in *Proc. IEEE Energy Convers. Congr. Expo.,* 2010, pp. 4611–4618
[29] G. Sen, Z.-W. Ouyang, O. C. Thomsen, and M. A. E. Andersen, "A high efficient integrated planar transformer for primary-parallel isolated boost converters," *Proc. IEEE Energy Convers. Congr. Expo.,* 2010, pp. 4605–4610.
[30] Z.-W. Ouyang, G. Sen, O. C. Thomsen, and M. A. E. Andersen, "Fully integrated planar magnetics for primary-parallel isolated boost converter," in *Proc. IEEE Appl. Power Electron. Conf. Expo.*, 2011.
[31] K. Venkatachalam, C. R. Sullivan, T. Abdallah, and H. Tacca, "Accurate prediction of ferrite cores loss with nonsinusoidal waveforms using only Steinmetz parameters," in *Proc. IEEE Workshop Comput. Power Electron.,* Jun 3–4, 2002, pp. 36–41
[32] J. Ferreira, "Improved analytical modeling of conductive losses in magnetic components," *IEEE Trans. Power Electron.*, vol. 9, pp. 127–131, Jan. 1994.
[33] W. G. Hurley, E. Gath, and J. G. Breslin, "Optimizing the AC resistance of multilayer transformer windings with arbitrary current waveforms," *IEEE Trans. Power Electron.*, vol. 15, no. 2, pp. 369–376, Mar. 2008.
[34] X. Nan and C. R. Sullivan, "An improved calculation of proximity-effect loss in high-frequency windings of round conductors," in *Proc. IEEE Power Electron. Spec. Conf.,* 2003, pp. 853–860
[35] Z.-W. Ouyang, O. C. Thomsen, and M. A. E. Andersen, "Optimal design and tradeoffs analysis for planar transformer in high power dc-dc converters," in *Proc. Int. Power Electr. Conf. (IPEC)*, Jun. 21–24, 2010, pp. 3166–3173.
[36] Z.-W. Ouyang, O. C. Thomsen, and M. A. E. Andersen, "The analysis and comparison of leakage inductance in different winding arrangements for planar transformer," in *Proc. IEEE Power Electron. Drive Syst.,* 2009, pp. 1143–1148

Ziwei Ouyang (S'07) received the B.S. degree from the Naval University of Engineering, Wuhan, China, in 2004, and the M.S degree from the Tianjin University of Technology, Tianjin, China, in 2007, both in electrical engineering. He is currently working toward the Ph.D. degree in power electronics from the Technical University of Denmark, Kongens Lyngby, Denmark.

His current research interests include magnetics design, modeling and integration in power supplies, dc/dc converters, and digital control in high-power reversible converters.

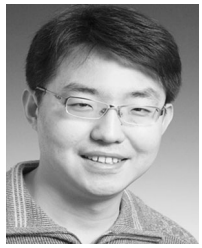

Zhe Zhang (S'07–M'11) received the B.S. and M.S. degrees in electrical engineering from Yanshan University, Qinhuangdao, China, in 2002 and 2005, respectively, and the Ph.D. degree from the Technical University of Denmark, Kongens Lyngby, Denmark, in 2010.

From 2005 to 2007, he was an Assistant Professor with Yanshan University. From June 2010 to August 2010, he was with University of California, Irvine, as a Visiting Scholar. He is currently in the Department of Electrical Engineering, Technical University of Denmark, as a Postdoctoral Researcher. His current interests include dc/dc converters, inverters for fuel cell-powered uninterruptible power supplies, and hybrid electric vehicles.

Dr. Zhang is a recipient of the 2009 Chinese Government Award for Outstanding Students Abroad in 2010.

Ole C. Thomsen (M'06) received the B.S.E.E. degree in electronics from the Engineering Academy of Denmark (DIA), Kongens Lyngby, Denmark, in 1970.

From 1970 to 1976, he was with Skandinavisk Teleindustri A/S as a RF R&D Engineer. From 1976 to 1980, he was with Christian Rovsing A/S as a Power Electronic Project Manager in the Space Department. In 1980, he was a Founder of Powerlab A/S, where he was engaged with R&D and Manufacturing of professional power electronic, and was here until 2004 as a General Manager. Since 2005, he has been with the Technical University of Denmark where he is currently an Associate Professor. His main research interests include switch-mode power supplies, power factor correction, and EMC.

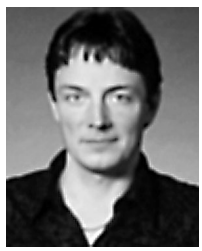

Michael A. E. Andersen (M'88) received the M.Sc.E.E. and Ph.D. degrees in power electronics from the Technical University of Denmark, Kongens Lyngby, Denmark, in 1987 and 1990, respectively.

He is currently a Professor of power electronics with the Technical University of Denmark, where he is the Deputy Director of the Department of Electrical Engineering as well as the Head of the Danish Ph.D. Research School in Electrical Energy Systems "EnergyLabDK." He is the author and coauthor of more than 90 papers. His current research interests include switch-mode power supplies, piezoelectric transformers, power factor correction, and switch-mode audio power amplifiers.

Appendix B.4

[B.4] Z. Ouyang, G. Sen, O. C. Thomsen and M. A. E. Andersen, "Analysis and design of fully integrated planar magnetics for primary-parallel isolated boost converter," *IEEE Transactions on Industrial Electronics*, 2011. (Accepted, 11-1386-TIE)

Analysis and Design of Fully Integrated Planar Magnetics for Primary-Parallel Isolated Boost Converter

***Abstract*—A high efficient planar integrated magnetics (PIM) design approach for primary-parallel isolated boost converters is presented. All magnetic components in the converter including two input inductors and two transformers with primary-parallel and secondary-series windings are integrated into an E-I-E core geometry, reducing the total ferrite volume and core loss. The transformer windings are symmetrically distributed into the outer legs of E-cores and the inductor windings are wound on the center legs of E-cores with air gaps. Therefore, the inductor and the transformer can be operated independently. Due to the low reluctance path provided by the shared I-core, the two input inductors can be integrated independently, and also the two transformers can be partially coupled each other. Detailed characteristics of the integrated structure have been studied in this paper. AC losses in the windings and the leakage inductance of the transformer are kept low by interleaving the primary and secondary turns of the transformers substantially. Because of the combination of inductors and transformers, maximum output power capability of the fully integrated module needs to be investigated. Winding loss, core loss and switching loss of MOSFETs are analyzed in-depth in this work as well. To verify the validity of the design approach, a 2-kW prototype converter with two primary power stages is implemented for a fuel cell fed traction applications with 20-50 V input and 400-V output. An efficiency of 95.9% can be achieved during 1.5-kW nominal operating conditions. Experimental comparisons between the PIM module and three separated cases have illustrated the PIM module has advantages of lower footprint and higher efficiencies.**

***Index Terms*— Core loss, dc-dc converter, fuel cell, inductor, isolated boost, planar integrated magnetics (PIM), transformer and winding loss.**

I. INTRODUCTION

DISTRIBUTED generation systems, back-up systems or traction systems based on fuel cells or batteries, requires high-power high-gain dc-dc converters to boost the low source voltage (20-50 V) to a higher dc-link voltage (350-400 V). For safety or EMC reasons, transformer isolation is often required or preferred. As power levels increase, input currents quickly reach levels where paralleling of primary switches become necessary. Since transistors are often operated close to their maximum drain current rating, direct paralleling of MOSFETs may require screening and parameter matching of on-resistance, gain and/or threshold voltages. Slowing switching speed by increasing gate impedance or addition of source inductance may also be required. A new, simple and low cost method to extend power level in isolated boost converters by paralleling of critical high-ac-current circuit parts is presented in [1]. It is found that the ac-current loop from the primary switches to the transformer primary windings is a particularly critical area with respect to scaling of power level. This requires extremely low leakage inductance of transformers and stray inductance of the circuit layout in order to achieve high efficiency. With traditional magnetics components, this extreme requirements result a high cost in magnetics components and an impossibility of mass production, although 98.2% peak efficiency can be achieved in this converter. Moreover, the size of magnetics components also limits its application in practice.

In order to satisfy the requirements of modern power electronics application, magnetics integration with planar core has proven to be an effective means of reducing the converter size and cost, while increasing the converter efficiency. Planar magnetics have unique advantages in terms of increased power density, better cooling capability, modularity and manufacturing simplicity as well as easy implementation of interleaved windings, which make them attractive for high current dc-dc power converter applications [2]-[13]. In recent years, most efforts in integrated magnetics (IM) focus on the current-doubler rectifier due to its suitability for low-output-voltage and high-output-current applications. Unlike conventional magnetic integration focusing only on core integration, both core and winding integration can be realized in the current-doubler rectifier design, causing lower conduction loss and core loss. As a result, lower overall cost, size as well as higher efficiency can be obtained by the IM design for the current-doubler circuit [2]–[6] and the dual-inductor isolated boost converter as well [14]. A 1-kW module with 300~400-V input voltage and 48-V output voltage asymmetrical half-bridge PWM converter employing an integrated L–L–C–T module is constructed in [7]. Detailed suggestions are given on how a generic, integrated LCT component could be used to implement various resonant converter topologies by merely reconfiguring the external terminals of the integrated components [8]-[9]. An integrated transformer consisted of four step-down transformers wound on a single magnetic core for an interleaved four-phase forward converter has been proposed in [15]. Coupled inductors greatly reduce the steady-state inductor current ripples without sacrificing the transient response as shown in [16]-[19]. A full procedure to generate 2D Finite Element Analysis (FEA) based model for integrated magnetics is presented in [20].

The converter in [1] is a typical application of distributed magnetics. Distributed magnetics functionally split a large magnetic element into small magnetic element which is an efficient way to reduce ac resistance and leakage inductance compared to a large single magnetic component [21]. Over 40% of the effective winding resistance and 20% leakage inductance reduction can be achieved by matrix transformers [22], making it very attractive for high current applications. However, increased numbers of components in the distributed magnetics increases the size of the power converters and reduces the power efficiency in the light load due to higher core loss. Therefore, integration of distributed magnetics becomes promising. In this paper, a new approach to integrate the distributed magnetics components for the primary-parallel isolated boost converter is presented. All magnetic components in the converter including the two input inductors and two transformers with primary-parallel and secondary-series connected windings are integrated into an E-I-E core geometry, reducing the total ferrite volume and core loss. The transformer windings are symmetrically distributed into the outer legs of E-cores and the inductor windings are wound on the

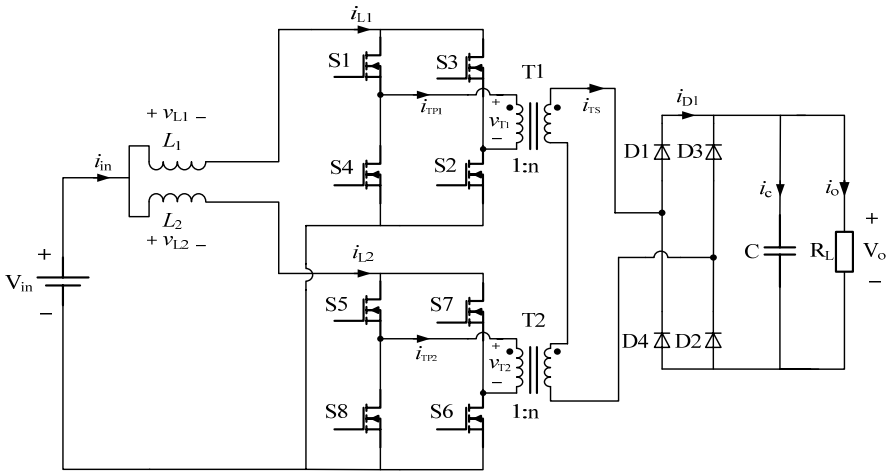

Fig. 1. Primary-parallel isolated boost converter.

center legs of E-cores with air gaps. Detail characteristics of the integrated structure are presented in Section III. Due to the integration of inductors and transformers, maximum output power capability of the integrated module has to be considered to avoid flux saturation in the core. Core loss estimation for the PIM structure has been investigated in-depth and an effect of core loss under dc bias operation has been considered as well. AC losses in the windings and leakage inductance of the transformers are kept low by interleaving the primary and secondary turns of the transformers. A detailed power loss analysis is given in section V. To verify the validity of the design approach, a 2-kW prototype converter with two primary power stages is implemented for fuel cell fed traction applications with 20~50-V input and 400-V output. An efficiency of 95.9% can be achieved during 1.5-kW nominal operating conditions. Experimental comparisons are presented in section VI show the advantages of low profile and high efficiency for the PIM module. In addition, the proposed PIM approach can solve the start-up problem of the boost converter without adding external Flyback winding [23].

II. Primary-Parallel Isolated Boost Converter

Boost derived topologies are preferred in fuel cell applications due to their low input current ripple [24]. Fig.1 shows a primary-parallel isolated boost derived topology suitable for handling high input currents for fuel cell applications. Series connection of transformer secondary windings ensures current sharing during energy transfer cycle when power is transferred to output. In this topology, primary power stages share the same control signals with same phase switching sequence for the corresponding switches which allows a simpler control. Output rectification unit as well as input and output filters are common to both of the primary stages. The paralleling method splits the critical primary high-ac-current-loop into two smaller loops. Each of the smaller loops only needs to switch half of the input current thereby achieving much faster current switching and thus higher conversion efficiency. Since the two transformers T_1 and T_2 share input current and power level, a higher turns ratio transformer in the conventional full-bridge isolated boost converter can be replaced by two individual transformers with lower turns ratio which allows a simpler design and manufacturing of the transformers.

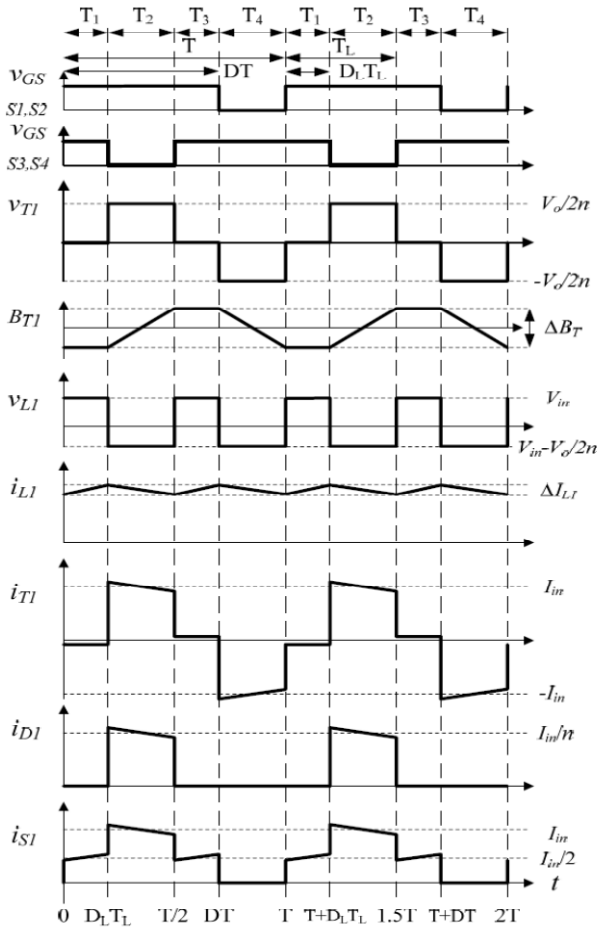

Since the two primary stages operate synchronously utilizing the same control signals, a single stage is analyzed as follows. Fig.2 shows basic waveforms of the primary-parallel isolated boost converter. Primary switches, S_1~S_4, are hard switched and operated in pairs, S_1~S_2 and S_3~S_4 respectively. Driving signals are 180˚ phase shifted. Switch transistor duty cycle, D, is above 50% to ensure switch overlap and thus a continuous current path for the boost inductor current. Basic converter operation can be divided into four stages [24].

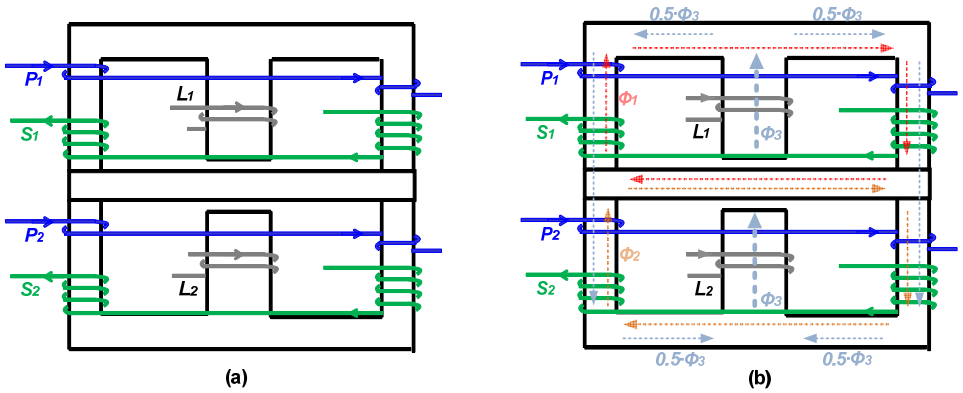

Fig. 3. Proposed E-I-E integrated magnetic structure (a) and its instantaneous flux distribution (b).

1) Stage 1 (T_1): All switches, S_1~S_4, are on and the inductor is charged. All rectifier diodes, D_1~D_4, are off and current in the transformer secondary winding is zero;

2) Stage 2 (T_2): The first energy transfer period, T_2, starts when switches, S_3 and S_4, are turned off. Inductor energy discharges with its current flowing through primary switch, S_1~S_2, and transformer, T_1 primary. The current in the secondary side flows through the rectifier diodes, D_1~D_2, and the output capacitor, C.

3) Stage 3 (T_3): Works the same as *stage 1*, all switches are turned on, the inductor is charged and the inductor current, i_{L1}, increases linearly;

4) Stage 4 (T_4): The second energy transfer cycle, T_4, starts when switches, S_1 and S_2, are turned off. Inductor energy discharges with its current flowing through primary switches, S_3~S_4, transformer, T_1 primary. The current in the secondary side flows through the rectifier diodes, D_3 and D_4, and the output capacitor, C.

III. Modeling of Integrated Magnetics

Two separated transformers and one boost inductor are integrated into an E-I-E core geometry for hybrid dc-dc converter in [25]. In this study, an additional inductor is added into a combined E-I-E core geometry where two independent transformers, T_1 and T_2, and two boost inductors, L_1 and L_2, are integrated. Fig.3 shows the proposed integrated magnetics structure. The windings of each transformer are symmetrically distributed into the outer legs of the two E-cores. L_1 and L_2 are wound on the center legs of E-cores with air gaps. The middle I-core provides a low reluctance return path where a complete flux cancellation can be achieved since the two transformers, T_1 and T_2, operate with in-phase currents utilizing the same control signals. In fact, the shared I-core could be removed where E-I-E geometry becomes E-E geometry since zero flux is in the shared I-core. However, the two inductors, L_1 and L_2 will be fully direct coupled if the shared I-core is removed. This results in a huge spike of inductor current at commutation point if there is any small mismatch in two primary stages [26]. Accordingly, the effect of the shared I-core is to decouple the two inductors. The flux generated by the transformer windings circulate only through the outer legs of the E-cores, which does not affect the inductor's behavior. As shown in Fig.3 (b), flux Φ_3 (include dc component) generated by the two input inductor windings goes through the two E-cores, and no dc flux exists in the shared I-core due to the cancellation. As seen in Fig.3, at a certain time period, half of Φ_3 increases the total flux in the right leg together with Φ_1 and Φ_2 and the other half of Φ_3 decreases it in the left side. A reverse situation will occur during the next time period. As a result, Φ_3 will not affect transformer's behavior. Hereby, the transformers and the inductors are not coupled electro-magnetically although the windings are wound in the same core. The flux waveforms in each leg are presented in Fig.9.

Fig.4 shows an equivalent magnetic reluctance model of the PIM module where R_1 is the reluctance of the outer leg of E-core, R_2 is the reluctance of I-core and R_C represents the reluctance of the center leg of E-core. R_C is much bigger than R_1 and R_2 due to the air gaps in the center legs. Since the transformers and the inductors are not coupled electromagnetically, the equivalent magnetic model can be divided into two parts as shown in the bottom of Fig.4. The left figure represents the magnetic model associated with T_1 and T_2. The flux Φ_1 and Φ_2 does not flow in the center legs of the E-core. The flux Φ_1 is identical to the flux Φ_2 due to two transformers operate with in-phase currents utilizing the same control signals. Therefore, the flux Φ_1 and Φ_2 in the shared I-core are fully cancelled. The right figure represents the magnetic model of the two inductors, L_1 and L_2.

With the assumption that the leakage flux through the air and the fringing effect are negligible, equations (1) ~ (3) can be derived according to the magnetic model,

$$N_1 \cdot i_{m1} = \Phi_1 \cdot (2R_1 + R_2) + (\Phi_1 - \Phi_2) \cdot R_2 \tag{1}$$

$$N_2 \cdot i_{m2} = \Phi_2 \cdot (2R_1 + R_2) + (\Phi_2 - \Phi_1) \cdot R_2 \tag{2}$$

$$2 \cdot N_L \cdot i_L = 2 \cdot \Phi_3 \cdot R_c + 0.5 \cdot \Phi_3 \cdot (2R_1 + R_2) \tag{3}$$

where N_1 and N_2 are the number of primary turns for the transformers T_1 and T_2 respectively. N_L is the number of turns for the inductors L_1 or L_2. The rate of change on Φ_1 and Φ_2 are the same over the entire period. Based on the Faraday's law, magnetizing inductances can be obtained,

$$L_{m1} = \frac{N_1^2}{2R_1 + R_2} \tag{4}$$

$$L_{m2} = \frac{N_2^2}{2R_1 + R_2} \tag{5}$$

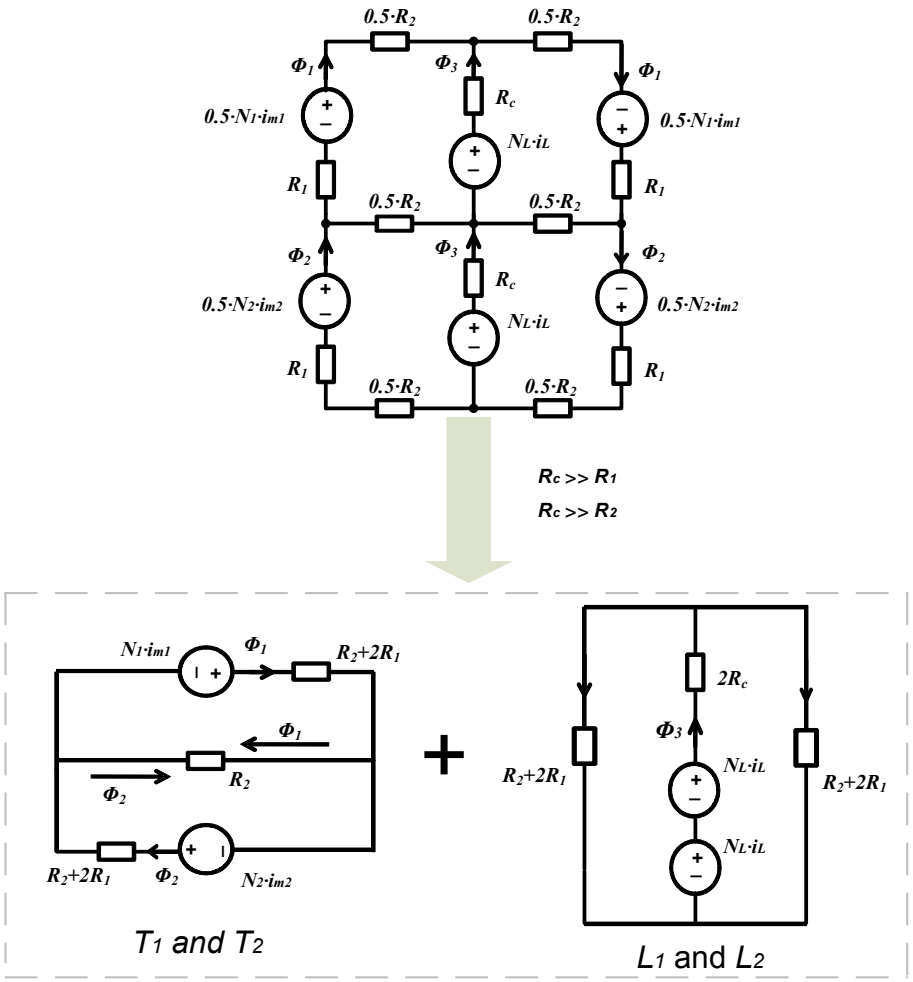

Fig. 4. Magnetic reluctance model of the PIM structure.

$$L_1 = L_2 = \frac{2 \cdot N_L^2}{2 \cdot R_c + R_1 + 0.5 \cdot R_2} \tag{6}$$

For a single separated transformer with the same winding arrangement at the outer leg, the magnetizing inductance is equal to, $L_m = N^2 / 2(R_1+R_2)$, where N is the number of primary turns for the single transformer. It is important to note that the integrated transformers have higher magnetizing inductances than the single case when both T_1 and T_2 have same current excitation. This is due to the fact that the mutual inductance between the two transformers T_1 and T_2 increases the magnetizing inductance. The coupling effect between T_1 and T_2 is shown in appendix.

IV. Magnetics Design Consideration

The advantages of this structure are highlighted in [27]. The drawback of the PIM module is to limit the maximum output power capability due to the overlapped flux. According to Faraday's law and Ampere's law, the peak flux densities of each magnetic component in the PIM module can be derived,

$$\hat{B}_T = \frac{V_{out} \cdot (1 - D)}{4 \cdot n \cdot f \cdot N \cdot A_e} \tag{7}$$

$$\hat{B}_L = \frac{\mu_0 \cdot N_L \cdot I_{pk}}{l_g} \tag{8}$$

$$\hat{B}_{Lac} = \frac{\mu_0 \cdot N_L \cdot \Delta I}{2 \cdot l_g} \tag{9}$$

where the peak current for the inductor is,

$$I_{pk} = I_{dc} + \frac{\Delta i}{2} = \frac{P_0}{\eta \cdot V_{in}} + \frac{V_{in} \cdot (D - 0.5) \cdot l_g}{2 \cdot f \cdot \mu_0 \cdot N_L^2 \cdot A_e} \tag{10}$$

$\hat{B}_T$ and $\hat{B}_L$ represent the peak flux density of each transformer (T_1 or T_2) and inductor (L_1 or L_2) respectively. $\hat{B}_{Lac}$ is the peak flux density of ac component of each inductor as shown in Fig.9. The same number of primary turns for the two transformers, $N_1=N_2=N$, is assumed. D is the switching duty cycle, n is the turns ratio of transformers, f is the switching frequency, A_e is the cross-section of the outer leg of E-core, l_g is the length of air gap in each center leg, P_o is the output power, η is the efficiency of the converter, μ_0 is the permeability of air and V_{in} represents the input voltage. In order to avoid flux saturation in the PIM module, the following equations are required,

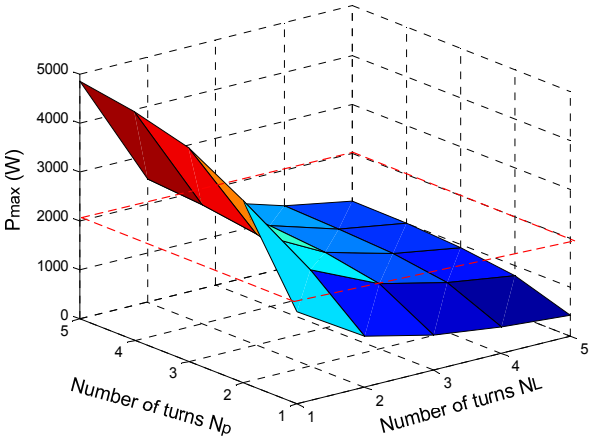

Fig. 5. 3D plot of maximum output power capability.

$$\hat{B}_T + \hat{B}_L = \frac{V_{out} \cdot (1-D)}{4 \cdot n \cdot f \cdot N \cdot A_e} + \frac{\mu_0 \cdot N_L \cdot P_0}{\eta \cdot V_{in} \cdot l_g} + \frac{V_{in} \cdot (D-0.5)}{2 \cdot f \cdot N_L \cdot A_e} \leq B_{sat} \tag{11}$$

The 3D graph in Fig.5 shows the relationship among the output power P_o, the number of turns of primary winding N_P, and the number of turns of inductor winding N_L which has been plotted based on (11) with 100 kHz switching frequency and 0.5 mm airgap. In order to design a 2-kW PIM module, the number of inductor turns, N_L, cannot exceed 3 turns. Its 2D relationship of N_P and N_L corresponding to the maximum output power capabilities is illustrated in Fig.6. The maximum output power can be enhanced by increasing the number of primary turns N or decreasing the number of inductor turns N_L. Fig.7 illustrates the fact that maximum output power capability of the PIM module is decreased by reducing the switching frequency. Of course, more energy can be stored by using large airgap, resulting in a large output power capability for the PIM module as illustrated in Fig.8. However, a large airgap results in a low inductance which causes a high current ripple in the circuit for the same number of turns and thereby reduces the efficiency. Moreover, a larger winding loss will be induced due to the fringing effect. Although the maximum output power can also be increased by using higher number of turns of primary winding N, larger winding losses and leakage inductances of the transformers T_1 and T_2 will be produced, reducing the efficiency as well. Unavoidable tradeoff in the power loss exists in the PIM design and the detailed power losses analysis will be given in section V.

V. Power Loss Analysis

A. Core Loss

Core loss separation approach [28] assumes that three fundamental effects are contributing to core losses: static hysteresis loss, eddy current loss and excess eddy current loss. The approach of loss separation has a practical disadvantage: such models are based on parameters, which are not always available and difficult to extract. The most commonly used equation that characterizes core losses is the Steinmetz equation, a curve-fitting expression of measured data under sinusoidal excitation.

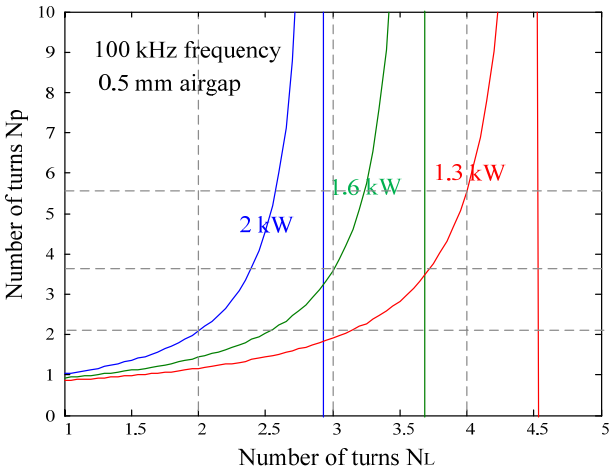

Fig. 6. Relationship of N_L and N_P under different output powers.

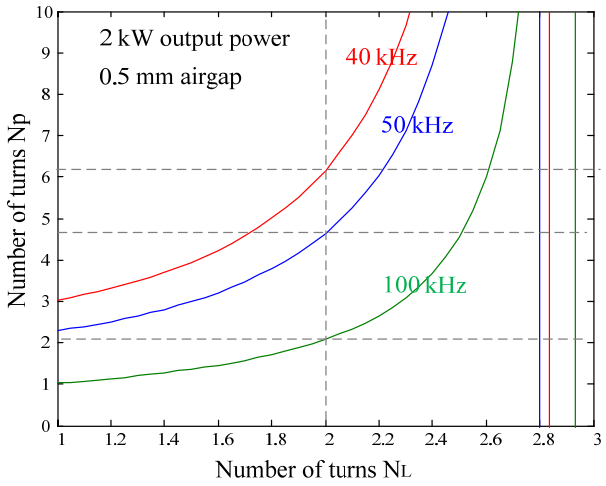

Fig. 7. Relationship of N_L and N_P under different switching frequencies.

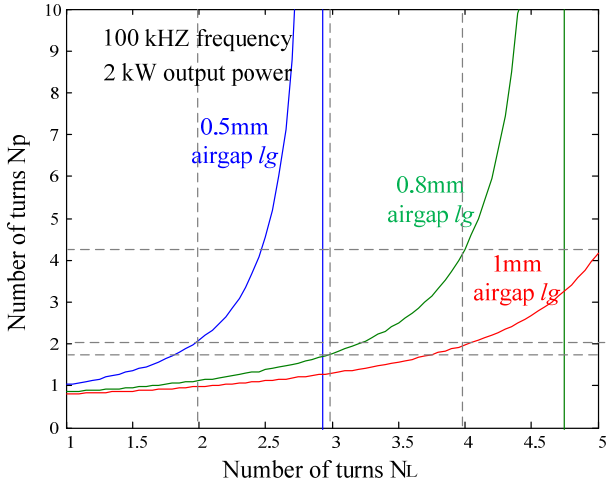

Fig. 8. Relationship of N_L and N_P under different airgaps

$$P_v = k \cdot f^{\alpha} \cdot (\frac{\Delta B}{2})^{\beta} \tag{12}$$

where k, α, β are material parameters , ΔB is peak-to-peak flux density of a sinusoidal excitation with switching frequency f, P_v is time-average core loss per unit volume. Unfortunately, the

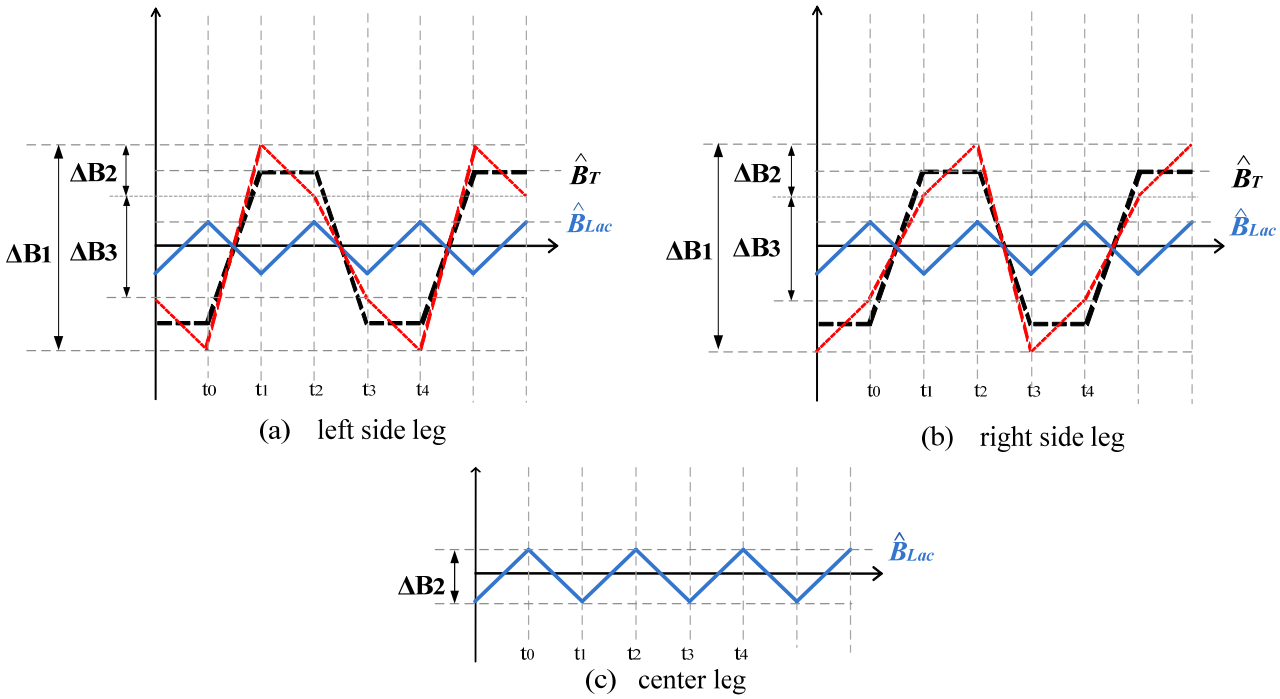

Fig. 9. Flux density waveforms in each leg of the PIM module.

Steinmetz equation is only valid for sinusoidal excitation. This is a significant drawback since in power electronics applications the core material is normally exposed to non-sinusoidal flux waveforms. Core loss due to non-sinusoidal waveforms can far exceed the loss due to sinusoidal waveforms, even if the frequencies and the peak-to-peak flux densities are identical [29]. In order to determine losses for a wider variety of waveforms, some modified expressions including modified Steinmetz expression (MSE) [30], generalized Steinmetz equation (GSE) [31], improved GSE (IGSE) [32], improved IGSE (I^2GSE) [33], natural Steinmetz extension (NSE) [34], equivalent elliptical loop (EEL) [35] and waveform coefficient Steinmetz equation (WCSE) [36] were introduced. A complete comparison among these modified empirical methods shows that the IGSE have the best loss determination with a wide variety of waveforms [29].

$$P_v = \frac{1}{T} \cdot \int_0^T k_i \cdot \left|\frac{dB(t)}{dt}\right|^{\alpha} \cdot \Delta B^{\beta-\alpha} \cdot dt \tag{13}$$

where,

$$k_i = \frac{k}{(2\pi)^{\alpha-1} \cdot \int_0^{2\pi} |\cos\theta|^{\alpha} \cdot 2^{\beta-\alpha} \cdot d\theta}$$

(13) shows the IGSE expression where k, α and β are the same parameters used in the Steinmetz equation (12). The angle θ represents the phase angle of the sinusoidal waveform. Applying a piecewise linear model (PWL) to any waveform and then combining with the IGSE, leads to an easy-to-use expression for accurate calculation of losses with any flux waveform, without requiring extra characterization of material parameters beyond the parameters of the Steinmetz equation.

It is necessary to know the flux density waveforms to estimate core loss properly using IGSE. Fig.9 shows the flux density waveforms in each leg of the PIM module.

1) In the time period t_0~t_1, the transformer flux Φ_T and the inductor flux Φ_L are adding together in the left side legs of both E-cores. On the other hand, they are cancelling in the right side legs.

2) During the time period t_1~t_2, the rate of change of Φ_T is zero, and therefore ac flux ΔB_2 in the two side legs are identical to ac flux on the inductor ΔB_L.

3) t_2~t_3, is the opposite of the period t_0~t_1 where the transformer flux Φ_T and the inductor flux Φ_L are opposing in the left side legs of both E-cores. Meanwhile, they are added in the right side legs.

4) t_3~t_4, is the same as t_1~t_2. The red dashed lines shown in Fig.9 (a) and Fig.9 (b) represent the overall flux density waveforms in the two side legs respectively. Since the flux of transformer Φ_T does not go through the center leg, the overall flux density waveform in the center leg is only dependent on the flux of inductor Φ_L.

Core loss can be calculated separately in each leg. For the applied flux waveform as illustrated in Fig.9, by using (13) together with PWL method, the following equations of core loss for each leg is obtained,

$$P_{vs} = k_i \cdot f^{\alpha} \cdot [(\Delta B_1{}^{\beta} + \Delta B_3{}^{\beta}) \cdot (1-D)^{1-\alpha} + 2 \cdot \Delta B_2{}^{\beta} \cdot (D-0.5)^{1-\alpha}] \tag{14}$$

$$P_{vc} = 4 \cdot k_i \cdot f^{\alpha} \cdot \Delta B_2{}^{\beta} \cdot (D-0.5)^{1-\alpha} \tag{15}$$

where,

$$\Delta B_1 = 2 \cdot (\hat{B}_T + \hat{B}_{Lac})$$

$$\Delta B_2 = 2 \cdot \hat{B}_{Lac}$$

$$\Delta B_3 = \Delta B_1 - \Delta B_2 = 2 \cdot (\hat{B}_T - \hat{B}_{Lac})$$

and P_{vs} is the core loss per unit volume in each side leg and P_{vc} is the core loss per unit volume in the center leg. The flux Φ_l is

TABLE I
CALCULATED RESULTS FOR CORE LOSS WITHOUT PRE-MAGNETIZATION

Input voltage	Core loss			
	Left side leg P_{CL}	Right side leg P_{CR}	Center leg P_{CC}	Total
V_{in}=30 V	5.95 W	5.95 W	0.09 W	12 W
V_{in}=45 V	13.43 W	13.43 W	0.01 W	26.87 W

identical to the flux Φ_2 due to two transformers operating with in-phase currents utilizing the same control signals. The two flux Φ_1 and Φ_2 are fully cancelled in the shared I-core where zero core loss ideally can be achieved. Table I shows the calculated results of core loss in each leg with different input voltages. The worst case for the core loss is in high input voltage where a higher peak flux is induced.

However, the aforementioned calculations are based on the IGSE formula which neglects the fact that core losses vary under dc bias conditions, i.e. the Steinmetz parameters change under dc bias condition. When a core operates under dc bias condition, the core loss still can be described using the Steinmetz equation (12) or the IGSE (13). However, the Steinmetz parameters must be adjusted according to the dc bias present. Pre-magnetization H_{DC} causes changes in the Steinmetz parameters β and k_i, but not in the parameter α. For many materials, the impact of a dc bias cannot be neglected as it may increase the core loss by a factor of more than two [37]. According to Steinmetz Pre-magnetization Graph (SPG) of the material ferrite N87 in [37], the core losses in this converter under different dc bias can be approximately estimated by multiplying the coefficient of SPG. The results are shown in Table IV and Table V respectively.

B. *Winding Loss*

Winding losses in transformers increase dramatically with high frequency due to eddy current effects. Eddy current losses, including skin effect and proximity effect losses seriously impair the performance of transformers in high-frequency power conversion applications. Both the skin effect and the proximity effect cause the current density to be non-uniformly distributed in the cross-section of the conductor, and thus cause a higher winding resistance at higher frequency. The most commonly used equation that characterizes winding losses is the Dowell's equation [38]-[40],

$$\frac{R_{ac,m}}{R_{dc,m}} = \frac{\varepsilon}{2} \cdot \left[\frac{\sinh \varepsilon + \sin \varepsilon}{\cosh \varepsilon - \cos \varepsilon} + (2m-1)^2 \cdot \frac{\sinh \varepsilon - \sin \varepsilon}{\cosh \varepsilon + \cos \varepsilon} \right] \tag{16}$$

where ε is the ratio of copper thickness h to the skin depth δ in a given frequency, and m is defined as a ratio in (17),

$$m = \frac{F(h)}{F(h) - F(0)} \tag{17}$$

where $F(0)$ and $F(h)$ are magneto motive forces (MMFs) at the limits of a layer as shown in Fig.10. The first term in (16) describes the skin effect and the second term represents the proximity effect. The proximity effect loss, in a multilayer winding, may strongly dominate over the skin effect loss depending on the winding arrangement [40]. Interleaving

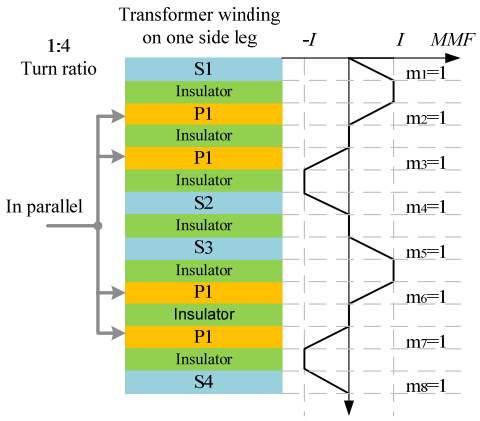

Fig. 10. Winding arrangement and MMF distribution for the transformer windings wound on one of the outer legs.

transformer windings may reduce the proximity loss significantly when the primary and secondary currents are in-phase [41]. Similarly, the leakage inductance of a transformer can also be significantly reduced [42]. Fig.10 shows the winding arrangements and MMF distributions along the vertical direction for the windings of transformer T_1 or T_2 wound on one of the outer legs. The MMF ratio m for each layer is equal to 1 which results in a lower ac resistance and leakage inductance. As seen in (16), ac resistance is not only related to MMF ratio m, but also to the ratio ε. A thinner copper can minimize the eddy current effect but a higher dc resistance will be compromised. Therefore, for a given frequency and winding arrangement, minimum ac resistance can be obtained by selection of proper copper thickness. Considering the cost of PCB and manufacturing simplicity, a 4-oz PCB copper thickness has been chosen for both primary and secondary windings for the experiment in this paper. In practice, PCB winding has a larger resistance compared to the calculation due to PCB vias and the fabrication tolerances.

It is noted that the validity of the expression (16) relies on negligible distances between consecutive turns, between adjacent layers, between the conductor edge and the magnetic core. Furthermore, the expression (16) is only valid for sinusoidal excitation waveform. Winding loss calculation for any current waveform to correct Dowell's assumptions can be found in [39]. Also [43] gives generalized correction factors to be applied to Dowell's resistance factor expression. However, these factors are usually derived from elaborated formulas and have to be determined from complicated coefficient tables.

Ferrite core has a limited saturation flux density, which requires inclusion of an airgap in the magnetic path in order to store energy for the inductors L_1 and L_2. A large airgap results in fringing flux which has two effects. First, the inductance is increased due to the effective increase in the airgap cross-sectional area, which decreases the reluctance of the gap. Second, the fringing flux induces eddy currents in the surface of nearby conductors, which causes a higher ac resistance and thereby increases the conduction loss. The fringing effect can be expressed as follows,

$$R_{ac} = F_R \cdot R_{dc} \tag{18}$$

where F_R represents the factor of fringing effect. Dowell's equation (16) does not include the fringing effect caused by the airgap. Therefore F_R in this case is much higher than the one calculated by Dowell's equation. How the fringing field affects

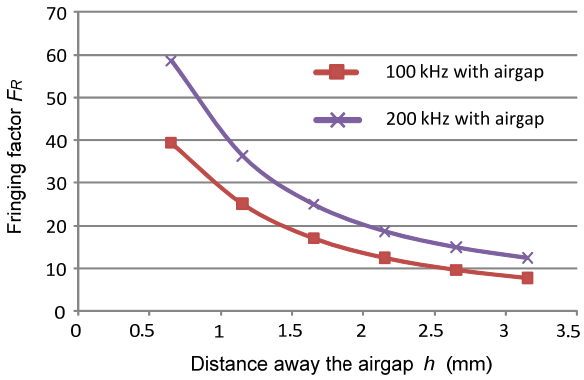

Fig. 11. Fringing factor F_R with different winding locations.

the high frequency winding loss and how to configure the windings to minimize the effect of the fringing field of the air gap have been investigated recently in [44]-[45]. The PCB windings are kept far away from the airgap in order to minimize the fringing effect in this work. Fig.11 shows FEA simulation results of the fringing effect of an airgap at different windings locations. Almost 60 times of dc resistance can be obtained when the windings are close to the airgap and with 200 kHz inductor current ripple.

C. *Switching Loss of MOSFETs*

Hard switching isolated dc-dc converters suffer increased switching loss due to leakage and stray inductances of the isolation transformer and layout, respectively. Both precise calculation and measurement of the switching losses are not straightforward due to voltage dependant parameters of the MOSFTEs like the output capacitor and time scale mismatch of MOSFET drain current and voltage waveforms. MOSFETs used in boost-type isolated dc-dc converters experience inductive switching since neither the input nor the output capacitors can directly clamp their drain-to-source voltages. This condition results in switching spikes occurring on top of the drain-to-source voltage during the turn-off process [46].

During turn-off, drain-to-source capacitance voltage of the MOSFET rises with a speed determined by the current sinking capability of the gate driver circuit in order to charge the Miller capacitance. Mostly this charging is lossless when performed by an inductive element which is the case in boost type converters. However during the turn-on process the stored energy in the output capacitor of the MOSFET is dissipated. This loss may become significant in higher voltage and frequency levels.

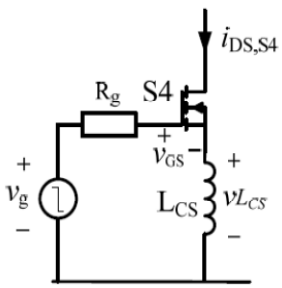

Apart from the capacitive switching loss considerations, additional factors come into play in high input current dc/dc applications. Common source inductance (Fig.12) and gate driver

TABLE II
SWITCHING LOSS PARAMETERS

Parameters	Values
Clamp voltage, V_C	84 V (at 100˚C)
Gate to source voltage at $V_{GS}(i_s)$	4.1 V
Common source inductance, L_{CS}	11.3 nH
Stay and leakage inductance, L_X	52.7 nH

voltage become the limiting factors for the MOSFET current turn off speed [47]. The negative rate of change of the drain current during turn-off induces a positive gate-to-source voltage which may keep the MOSFET in its active region together with a high drain-to-source voltage. So this extra voltage will behave as a negative feedback in the switching seep, putting an upper limit to it. A detailed analysis on two commutation types, namely voltage limited and MOSFET limited commutations, during the turn-off of MOSFET is obtained in [46]. The boundary expression determining the commutation mode is,

$$\frac{L_X}{L_{CS}} = \left(V_C - \frac{V_0}{2n}\right) \cdot \left(\frac{1}{2 \cdot V_{GS}(i_s)} + \frac{2n}{V_0}\right) \tag{19}$$

where L_X is composed of the leakage inductance and stray inductance due to the converter layout. L_{CS} is the common source inductance including the internal package inductance and the package source pin inductance. $V_{GS}(i_s)$ is the gate voltage corresponding to the drain at the start of the turn-off process. V_C is the clamp voltage which may be provided by an external clamp circuit or the avalanche voltage of the MOSFET. Table II shows the corresponding values of these parameters used in this paper. In order to have a practical value for L_{CS}, 7 *nH/cm* rule of thumb has been used. The stay and leakage inductance L_X can be found in the measurement results of Section VI. The condition in (19) can be tested for this case by inserting the parameters of Table II which results in,

$$\frac{L_X}{L_{CS}} < \left(V_C - \frac{V_0}{2n}\right) \cdot \left(\frac{1}{2 \cdot V_{GS}(i_s)} + \frac{2n}{V_0}\right).$$

This result confirms the commutation mode as MOSFET limited commutation as explained in [1]. Therefore, in this case the expression for the switching losses per full bridge is,

$$P_s = f \cdot \left[1 + \frac{V_0}{4 \cdot n \cdot V_{GS}(i_s)} \cdot L_{CS} + L_X\right] \cdot {I_{Lpeak}}^2 \tag{20}$$

VI. EXPERIMENTAL RESULTS

A. *Results of PIM module*

A 2-kW prototype has been built to verify the new integrated magnetics design approach. Input voltage is between 20-50 V and output voltage is 400 V. Primary switches are IPA028N08N3, 80-V, 2.8-mΩ power MOSFETs from Infineon. Output rectification is handled by Silicon Carbide Schottky diodes C3D10060A with 1.5-V forward voltage drop. Magnetic parameters of the PIM module are shown in Table III. One set of EELP-64 core and an additional piece of I-64 core, all composed of N87 core material. Each transformer turns ratio is 1:4 (n=4). Air gaps with 0.5-mm length are used for the energy storage

TABLE III
MAGNETIC PARAMETERS OF PIM MODULE

Parameters	Values
Number of turns in primary (N_1=N_2)	2
Turns ratio of each transformer	1:4
Number of turns for the inductors (N_{L1}=N_{L2})	2
Each air gap length (lg)	0.5 mm
Core type	EILP 64
Core material	Ferrite N87
Copper thickness mount on PCB layer	4 oz (140 µm)
Switching frequency	100 kHz

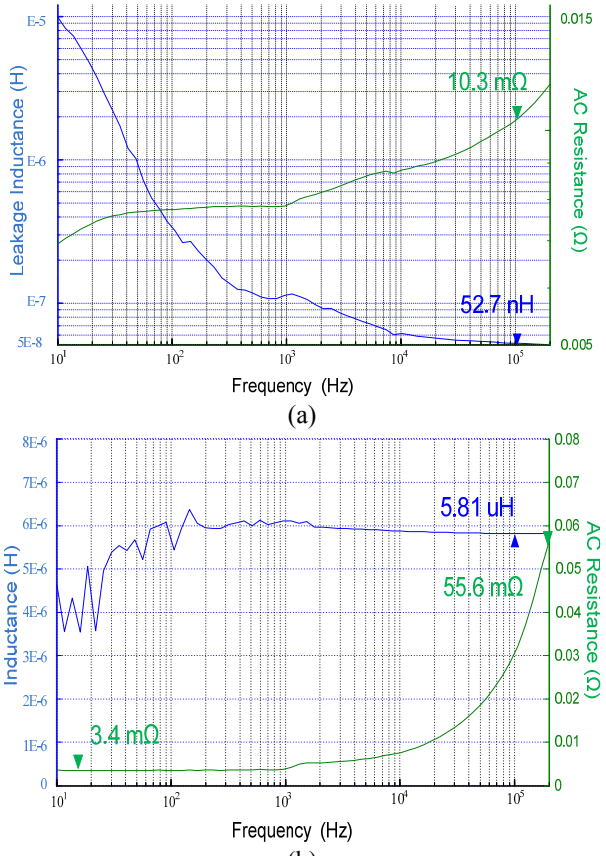

Fig. 13. Measurement results of impedance. (a) transformer T_1 or T_2. (b) Inductor L_1 or L_2.

inductors L_1 and L_2. 4-oz copper thickness is used for PCB windings. Switching frequency is 100-kHz with inductor current ripple of 200-kHz. It is note that the frequency selection is related to the optimization design.

Interleaved winding technique shown in Fig.10 is utilized to reduce the ac resistances and the leakage inductances. The measurement results for the integrated transformers and inductors are shown in Fig.13, obtained by PSM1735, impedance analyzer. The ac resistance and leakage inductance are obtained by opening secondary side and shorting both primary sides. The results in the figure have been referred to the primary side. Assuming that T_1 and T_2 have the same parameters, 52.7-nH leakage inductance and 10.3-mΩ ac resistance referred to the primary sides of each transformer can be derived. The stray

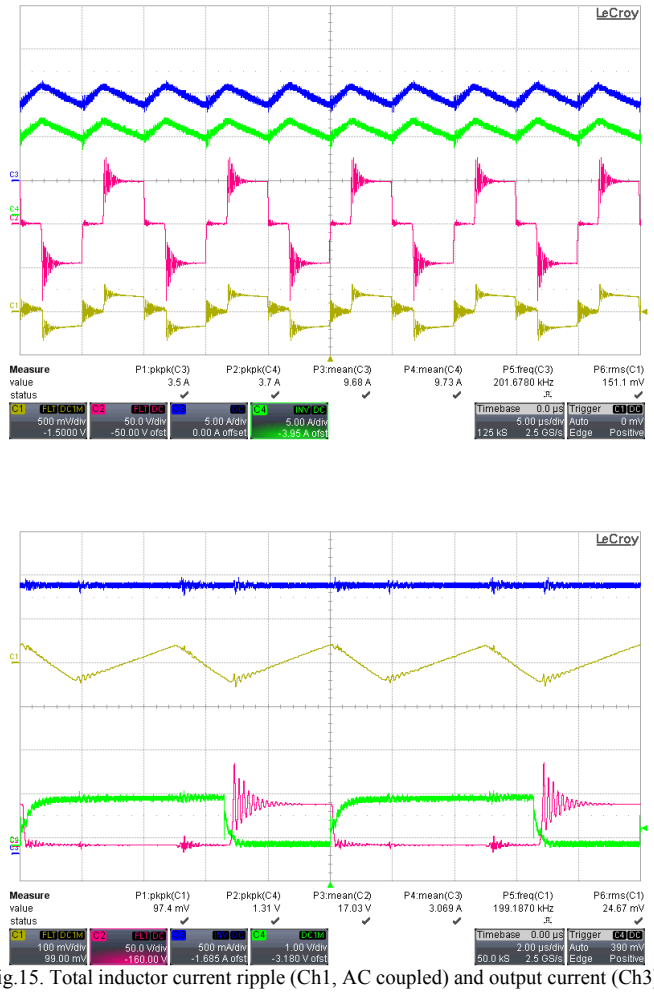

Fig.15. Total inductor current ripple (Ch1, AC coupled) and output current (Ch3), V_{DS} (Ch2) and V_{GS} (Ch4) of S_1.

parameters of the circuit are also included in the measurement results. Keeping the PCB winding far to the airgap, the fringing effect of airgap causes ac resistance of the inductors, L_1 and L_2, is 16.4 times than their dc resistances. The ac resistance of each inductor is 55.6-mΩ when the inductor current ripple works at 200-kHz. According to the above measurement results, detailed breakdown of power losses for 1.5-kW PIM module at 45-V input and 30-V input can be found in Table IV and Table V respectively. The core loss of PIM dominates over the total power loss especially for high input voltage like 45-V. The winding loss of PIM is far less than the core loss which may not an optimization case. The solution for this is to balance the core loss and winding loss by increasing the number of turns of primary. However, it is noted that the fully interleaving may not be implemented due to the PCB layer limitation; otherwise the cost of PCB manufacture will be extremely high. The switching loss dominates over the total power loss when the converter operates at low voltage input like 30-V. As seen from (20), the leakage inductance and stay inductance become very important in low voltage case. With the aforementioned solution of increased number of primary turns, the leakage inductance will be increased which allows a very high switching loss. Therefore, many tradeoffs exist in the PIM module and an optimization procedure needs to be done. However, this paper emphasis on the integration approach, the proof-concept demonstration rather than the optimization design.

IRS2110 high and low side gate drivers are used in the gate

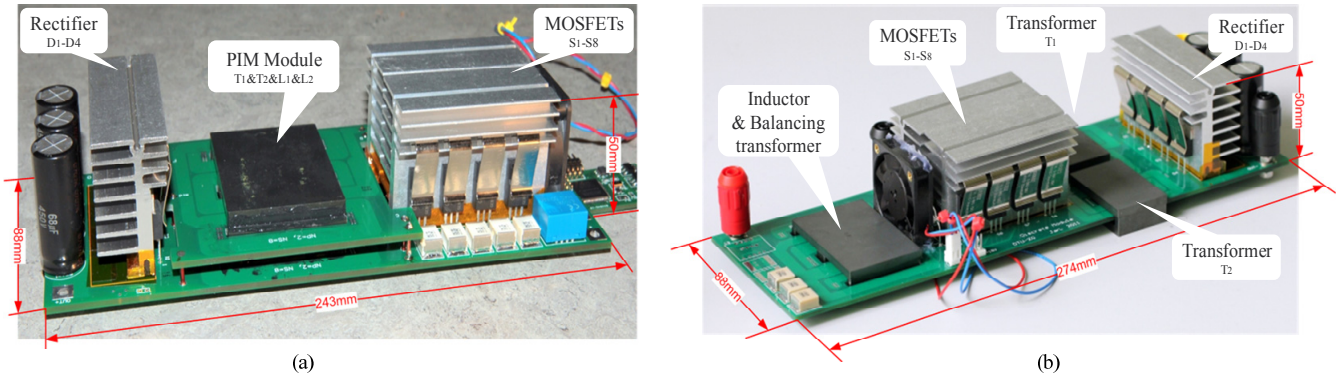

(a) (b)

Fig. 16. Photo of experimental prototype converters (a) with PIM module (b) with single inductor, integrated balancing transformers and discrete transformers.

TABLE IV

CONVERTER POWER LOSS BREAKDOWN
AT 45-V INPUT, 400-V OUTPUT AND 1.5-KW OUTPUT POWER

Components	Loss Type		Loss (W)
PIM module	Winding loss	T_1&T_2	5.2 W
		L_1&L_2	2.0 W
	Core loss		37.8 W
MOSFET 8 pcs.	Conduction		2.3 W
	Switching Loss		9.9 W
Diodes 4 pcs.	Conduction		5.9 W
	Switching Loss		1.8 W
Total loss			64.9 W

TABLE V

CONVERTER POWER LOSS BREAKDOWN
AT 30-V INPUT, 400-V OUTPUT AND 1.5-KW OUTPUT POWER

Components	Loss Type		Loss (W)
PIM module	Winding loss	T_1&T_2	7.9 W
		L_1&L_2	5.3 W
	Core loss		22 W
MOSFET 8 pcs.	Conduction		4.6 W
	Switching Loss		22 W
Diodes 4 pcs.	Conduction		7.9 W
	Switching Loss		2.3 W
Total loss			67.7 W

driver circuit together with ISO722C capacitive digital isolators for control signal protection. The control signals are produced by TMS28027 DSP. Fig.16-(a) shows the experimental prototype employing the proposed PIM module. Output is filtered by several 1-uF SMD capacitors in parallel placed very close to the rectifiers for minimizing the ac loop. When the converter operates at 100-kHz, 30-V input, 400-V output and 1.5-kW output power, the current waveforms of inductors (Ch3&Ch4), the voltage (Ch2) and the current (Ch1) of transformer T_1 are presented in Fig.14. Observe that the two currents are identical. Removing oscilloscope offset, causes current traces to fully coincide. Also the total inductor current ripple (Ch1, AC coupled) and output current (Ch3), V_{DS} (Ch2) and V_{GS} (Ch4) of S_1 are shown in Fig.15 respectively.

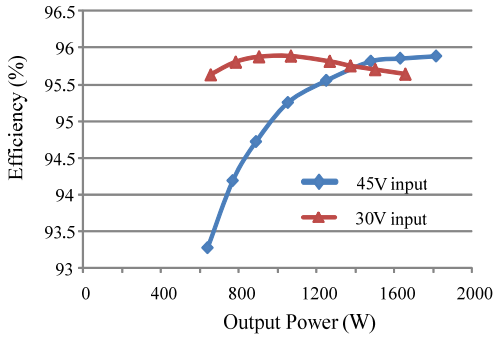

Fig. 17. Measured converter efficiency for PIM dc-dc converter.

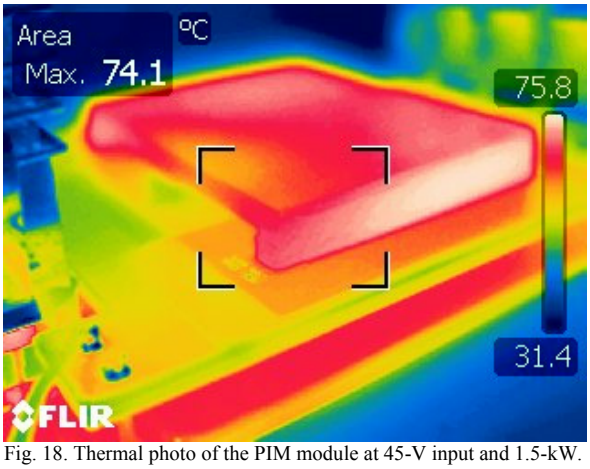

Fig. 18. Thermal photo of the PIM module at 45-V input and 1.5-kW.

High stability (< 10 ppm) 0.1 % shunt resistors are used for high precision of the efficiency measurements. Agilent 34410A high precision multimeters are used for all measurements. Current sense signals are shielded and fitted with common mode filters. Efficiency curves of the converter employing the PIM module when the output voltage is 400-V are shown in Fig.17. Maximum efficiency of 95.9% has been observed with 45-V input voltage, 400-V output voltage and 1.8-kW output power. And the same maximum efficiency can be observed at 30-V input voltage, 400-V output voltage and 1-kW. In low output

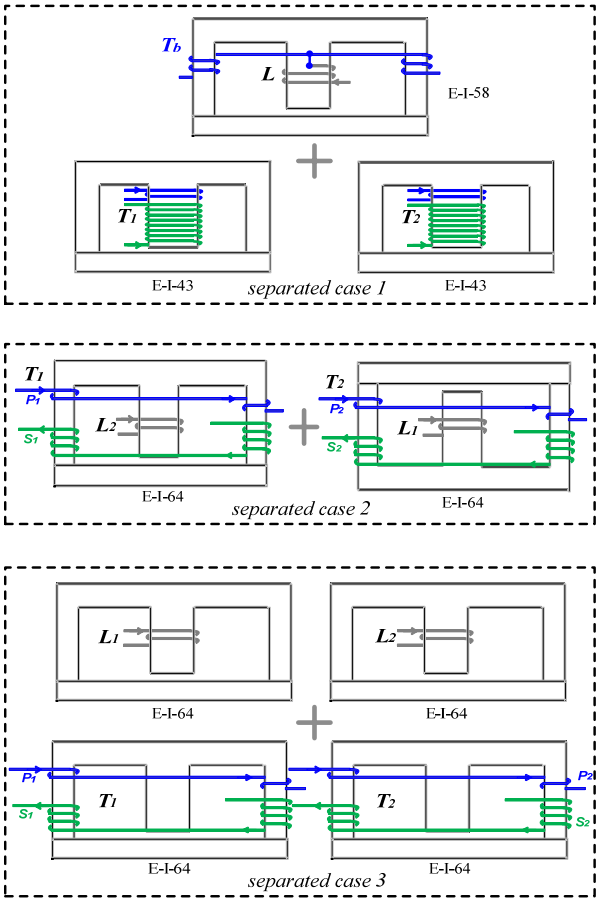

Fig. 19. Separated cases for experimental comparisons.

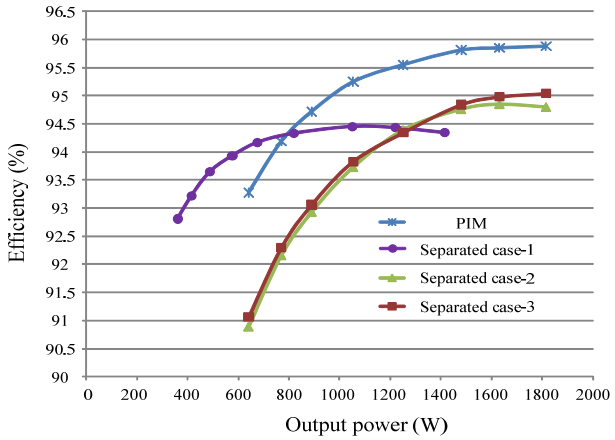

Fig. 20. Efficiency comparison at 45-V input and 400-V output.

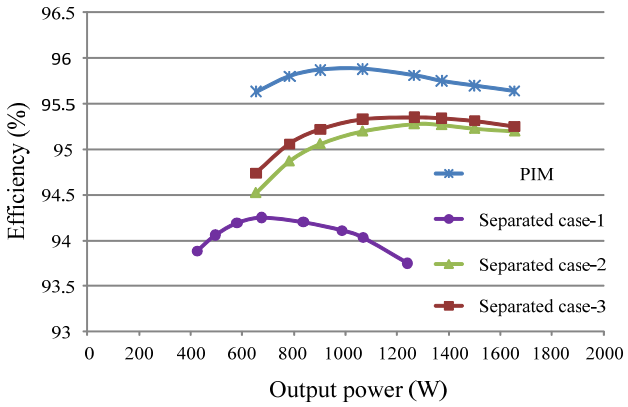

Fig. 21. Efficiency comparison at 30-V input and 400-V output.

power, the efficiency of 30-V input is much higher than that of 45-V input this is due to the fact that the low number of primary turns in this case causes the core loss of PIM dominating over the total power loss which has been mentioned in the previous. With increased output power, the switching loss becomes a crucial part in total power loss. Therefore, a lower efficiency at 30-V input can be observed. Fig. 18 shows a thermal photo of PIM module at 45-V and 1.5-kW in which is the worst case for the core loss. Notice that a forced air flow from fan is used for cooling down the converter. As shown in the photo, the heat mostly concentrates on the side legs rather than the center leg. This is coincident with the analysis of core loss in section V.

B. Comparison

In order to demonstrate the advantages of PIM such as low profile and high efficiency, a comparison between the PIM and three different separated cases has been done. In order to make a fair comparison, all switching devices, gate drivers, and capacitors are kept the same. The prototype of separated case-1 is shown in Fig.16-(b) which is consisted of single inductor with integrated balancing transformers and two discrete transformers. The detailed principle about this structure can be found in [26]. In separated case-1, two turns single inductor are wound in EILP-58 core with 0.5-mm airgap length and two turns of integrated balancing transformer are wound in each side leg. The two discrete transformers are both employing EILP-43 cores with two turns in primary sides and 8 turns in secondary sides. N87 core material is used for all cores in the separated case-1. And full interleaved winding arrangement is also used in this case. The separated case-2 is partially using integrated technology shown in Fig.19. The PCB winding and core size are kept the same with PIM module. Two E-I cores have been separated by adding a single I-core on the basis of PIM module. A single inductor and a single transformer are still integrated into the E-I core. A complete separation has been implemented in the separated case-3, consisting of four discrete magnetic components, L_1, L_2, T_1 *and* T_2. And the windings of transformer still keep the same arrangements with PIM module shown in Fig.19. The two inductors and two transformers are using the same core geometry EILP-64. Obviously, the PIM module has the smallest footprint and fewest numbers of components compared to the other separated cases. Fig.20 and Fig.21 show the efficiency comparisons among the four cases at 45-V input and 30-V input respectively. Regarding to the power losses of the separate case-2 and case-3, the only difference with PIM case is to have higher core loss. This is because the flux is cancelled in the shared I-core in PIM case, causing a lower core loss. Winding layouts are not changed and thus the other power losses are kept the same with PIM case. From the efficiency curves, the case-2 and case-3 almost have the same core loss at 45-V input and the PIM has 1% improvement at 1.5-kW output power. When the input voltage is 30-V, the efficiency of the separated case-3 is slightly higher than that of the case-2. The PIM case has almost 0.5% improvement at 1.5-kW output power. Regarding to the separated case-1, some design parameters including the number of turns of integrated balancing transformers, the winding widths, the winding lengths, the winding arrangements and the core geometries are different with the PIM case. Therefore, the difference in power loss between the PIM case

TABLE VI

POWER LOSS BREAKDOWN OF SEPARATED CASE-1 CONVERTER AT 45-V INPUT, 400-V OUTPUT AND 1.5-KW OUTPUT POWER

Components	Loss Type		Loss (W)
PIM module	Winding loss	T_1&T_2	14.8 W
		L_1&T_b	8.2 W
	Core loss		28.5 W
MOSFET 8 pcs.	Conduction		6.4 W
	Switching Loss		17.8 W
Diodes 4 pcs.	Conduction		7.4 W
	Switching Loss		3.7 W
Total loss			86.8W

and the case-1 is not only the core loss, but also the winding loss and the switching loss. The power loss breakdown for separated case-1 is shown in Table VI. From the efficiency figures, the separated case-1 has lower efficiencies than the PIM case at nominal output power. Notice that the comparison between the PIM case and separated case-1 is not fair since the two cases are both not optimized. And the efficiency of separated case-1 might be improved by changing winding widths and winding arrangements and enhancing the value of inductor. Larger core geometries could also be used for the efficiency improvement. However, the power density (larger core geometries) and the cost (more PCB layers for higher inductance) will be lost if the aforementioned methods are used.

VII. Conclusion

This work presents a new integrated magnetics approach to combine all magnetic components of the primary-parallel isolated boost converter into an E-I-E core structure. Since the design approach allows the transformers and inductors are electromagnetically uncoupled, it can be extended into many other isolated dc-dc topologies. The design approach provides a low footprint, low cost and high efficiency. Also, the integrated magnetics with planar components are made from pre-formed assemblies, thus the assembly process itself has only a few stages. This simplification of assembly allows the PIM to be manufactured with very high repeatability and with increased accuracy. The drawback of the PIM module is to limit the maximum the output power capability due to the overlapped flux. The detailed limitation of power capability has been presented and analyzed. Power loss analysis of the converter has been investigated in-depth. Test results from a 2-kW experimental prototype verify that converter employing the PIM module is fully functional and electromagnetically equivalent. An efficiency of 95.9% can be achieved during 1.5-kW nominal operating conditions. Experimental comparisons between the PIM module and three separated cases have illustrated the PIM module has advantages of lower footprint and higher efficiencies.

APPENDIX

In this appendix it is shown that the two transformers T_1 and T_2 have a partial coupling effect. The equivalent magnetic reluctance model between T_1 and T_2 is shown in the bottom of Fig.4.

$$N_1 \cdot i_{m1} = \Phi_1 \cdot (2R_1 + R_2) + (\Phi_1 - \Phi_2) \cdot R_2 \tag{21}$$

$$N_2 \cdot i_{m2} = \Phi_2 \cdot (2R_1 + R_2) + (\Phi_2 - \Phi_1) \cdot R_2 \tag{22}$$

Combining (21) and (22), the following equations are obtained,

$$\Phi_1 = \frac{2 \cdot N_1 \cdot (R_1 + R_2)}{\Delta} \cdot i_{m1} + \frac{N_2 \cdot R_2}{\Delta} \cdot i_{m2} \tag{23}$$

$$\Phi_2 = \frac{N_1 \cdot R_2}{\Delta} \cdot i_{m1} + \frac{2 \cdot N_2 \cdot (R_1 + R_2)}{\Delta} \cdot i_{m2} \tag{24}$$

where

$$\Delta = 4 \cdot {R_1}^2 + 8 \cdot R_1 \cdot R_2 + 3 \cdot {R_2}^2$$

Taking the partial derivative in (23) and (24),

$$N_1 \cdot \frac{d\Phi_1}{dt} = \frac{2 \cdot {N_1}^2 \cdot (R_1 + R_2)}{\Delta} \cdot \frac{di_{m1}}{dt} + \frac{N_1 \cdot N_2 \cdot R_2}{\Delta} \cdot \frac{di_{m2}}{dt} \tag{25}$$

$$N_2 \cdot \frac{d\Phi_2}{dt} = \frac{N_1 \cdot N_2 \cdot R_2}{\Delta} \cdot \frac{di_{m1}}{dt} + \frac{2 \cdot {N_2}^2 \cdot (R_1 + R_2)}{\Delta} \cdot \frac{di_{m2}}{dt} \tag{26}$$

(27) is rewritten from (25) and (26),

$$\begin{bmatrix} \lambda_1 \\ \lambda_2 \end{bmatrix} = \begin{bmatrix} \frac{2 \cdot {N_1}^2 \cdot (R_1 + R_2)}{\Delta} & \frac{N_1 \cdot N_2 \cdot R_2}{\Delta} \\ \frac{N_1 \cdot N_2 \cdot R_2}{\Delta} & \frac{2 \cdot {N_2}^2 \cdot (R_1 + R_2)}{\Delta} \end{bmatrix} \cdot \begin{bmatrix} i_{m1} \\ i_{m2} \end{bmatrix} = \begin{bmatrix} L_{11} & L_M \\ L_M & L_{22} \end{bmatrix} \cdot \begin{bmatrix} i_{m1} \\ i_{m2} \end{bmatrix} \tag{27}$$

where the flux linkages λ_1 and λ_2 are the time integrals of the transformer primary voltages, i_{m1} and i_{m2} are the individual excitation currents. L_{11} and L_{22} are their self-inductances. L_M represents mutual inductance between the two transformer windings. With assumption that leakage flux through the air is negligible, (28) ~ (30) can be obtained,

$$L_{m1} = L_{11} + L_M = \frac{{N_1}^2}{2 \cdot R_1 + R_2} \tag{28}$$

$$L_{m2} = L_{22} + L_M = \frac{{N_2}^2}{2 \cdot R_1 + R_2} \tag{29}$$

$$k = \frac{L_M}{L_{11}} = \frac{R_2}{2 \cdot (R_1 + R_2)} \tag{30}$$

The results of magnetizing inductance of transformers are the same with that in Section III. k represents the coupling coefficient between T_1 and T_2. According to the geometry of core, k=0.4 can be obtained for their coupling coefficient.

REFERENCES

[1] M. Nymand and M. A. E. Andersen, "New primary-parallel boost converter for high-power high gain applications," in *Proc. IEEE APEC*, 2009, pp. 35-39.

[2] P. Xu, M. Ye, P. Wong and F. C. Lee, "Design of 48 V voltage regulator modules with a novel integrated magnetics," *IEEE Trans. on Power Electron.*, vol.17, no.6, pp.990–998, Nov.2002.

[3] J. Sun, K. F. Webb, and V. Mehrotra, "Integrated magnetics for current-doubler rectifiers," *IEEE Trans. on Power Electron.*, vol. 19, no. 3, pp.582-590, May, 2004.

[4] J. Sun, V. Mehrotra, "Orthogonal winding structures and design for planar integrated magnetics," *IEEE Trans. on Ind. Electron.*, vol. 55, no. 3, pp.1463-1469, March, 2008.

[5] W. Chen, G. Hua, D. Sable and F. C. Lee, "Design of high efficiency, low profile, low voltage converter with integrated magnetics," *in Proc. IEEE APEC, 1997,* pp. 911-917.

[6] P. Xu, Q. Wu, P. Wong and F. C. Lee, "A novel integrated current doubler rectifier," *in Proc. IEEE APEC, 2000,* pp. 735-740.

[7] R. Chen, S. J. T., van Wyk J.D. "Design of planar integrated passive module for zero-voltage-switched asymmetrical half-bridge PWM converter," *IEEE Trans. on Ind. Appl.,* Vol. 39, no.36, pp.1648-1655, Nov.-Dec. 2003.

[8] P.A. J. van Rensburg, J.D. van Wyk and J.A. Ferreira, "Design, prototyping and assessment of a 3 kW integrated LCT component for development in various resonant converters," *IET Power Electron.,* Vol. 2, no.5, pp.535-544, 2009.

[9] J. T. Strydom, J. A. Ferreira, J. D. van Wyk, I**.** W. Hofsajer, E. Waffenschmidt, "Power electronic subassemblies with increased functionality based on planar sub-components," *in Proc. IEEE PESC, 2000,* pp. 1273-1278.

[10] M. J. Prieto, A. M. Pernía, J. M. Lopera, J. Á. Martínez, and F. Nuño, "Turn-Coupling in Thick-Film Integrated Magnetic Components for Power Converters," *IEEE Trans. on Components and Packaging Technologies*, vol.31, no.4, pp.837–848, Dec.2008.

[11] E. de Jong, J. Ferreira, P. Bauer, "Toward the next level of PCB usage in power electronic converters," *IEEE Trans. on Power Electron.*, vol.23, no.6, pp.3153–3163, Nov. 2008.

[12] C. Quinn, K. Rinne, T. O'Donnell, M. Duffy, C.O. Mathuna, "A review of planar magnetic techniques and technologies," *in Proc. IEEE APEC*, 2001, pp. 1175–1183.

[13] C. Buccella, C. Cecati and F. de Monte, "A coupled electrothermal model for planar transformer temperature distribution computation" *IEEE Trans. on Ind. Electron.,* Vol. 55, no.10, pp.3583-3590, Oct. 2008.

[14] L. Yan and B. Lehman*,* "An integrated magnetic isolated two-inductor boost converter: analysis, design and experimentation" *IEEE Trans. on Power Electron.*, vol.20, no.2, pp.332–342, March.2005.

[15] L-P. Wong, Y-S. Lee, M. H. L. Chow, and D. K-W Cheng, "A four-phase forward converter using an integrated transformer," *IEEE Trans. on Ind. Electron.*, vol. 55, no. 2, pp.817-831, March, 2008.

[16] S-Y Lee, A. G. Pfaelzer, and J. D. van Wyk, "Comparison of different designs of a 42-V/14-V dc/dc converter regarding losses and thermal aspects" *IEEE Trans. on Ind. Appl.*, vol.43, no.2, pp.520–530, Mar.2007.

[17] P-L. Wong, Q-Q. Wu, P. Xu, B. Yang and F. C. Lee, "Investigating coupling inductors in the interleaving QSW VRM," *in Proc. IEEE APEC, 2000,* pp. 973-978.

[18] H. Kosai, S. McNeal, B. Jordan, J. Scofield, B. Ray and Z. Turgut, "Coupled inductor characterization for a high performance interleaved boost converter," *IEEE Trans. on Magn.*, vol.45, no.10, pp.4812–4815, Oct.2009.

[19] Z. Ouyang, O. C. Thomsen, M. A. E. Andersen and T. Björklund, "Low Profile, Low Cost, New Geometry Integrated Inductors," *in Proc. IEEE APEC*, pp.150-156, March, 2011.

[20] R. Prieto, R. Asensi, J. A. Cobos and J. Uceda, "A full procedure to model integrated magnetics based on FEA," *in Proc. IEEE APEC*, pp. 952- 957, 2004.

[21] M. T. Zhang, M. M. Jovanovic, F.C. Lee, "Analysis, design, and evaluation of forward converter with distributed magnetics-interleaving and transformer paralleling" *in Proc. IEEE APEC*, 1995, pp.315–321.

[22] D. Reusch and F. C. Lee, "High Frequency Bus Converter with Integrated Matrix Transformers for CPU and Telecommunications Applications," *in Proc. IEEE ECCE*, 2010, pp. 2446-2450.

[23] K. L. Poulsen, Z. Ouyang and G. Sen, "Hybrid isolated-boost/flyback operation with integrated magnetics for start-up and full voltage range output of isolated boost family converters" *EP & US Patent*, 2011.

[24] M. Nymand and M. A. E. Andersen, "High-efficiency isolated boost dc–dc converter for high-power low-voltage fuel-cell applications," *IEEE Trans. on Ind. Electron.,* Vol. 56, no.2, pp.505-514, Feb. 2010.

[25] Z. Ouyang, Z. Zhang, O. C. Thomsen, M. A. E. Andersen, "Planar integrated magnetics (PIM) module in hybrid bidirectional dc-dc converter for fuel cell application," *IEEE Trans. on Power Electron.*, 2011.

[26] G. Sen, Z. Ouyang, O. C. Thomsen, M. A. E. Andersen, "Integrated current balancing transformer for primary parallel isolated boost converter," *in Proc. EPE,* 2011.

[27] Z. Ouyang, G. Sen, O. C. Thomsen, M. A. E. Andersen. "Fully integrated planar magnetics for primary-parallel isolated boost converter," *in Proc. IEEE APEC*, pp.174-181, March, 2011.

[28] W. A. Roshen, "A practical, accurate and very general core loss model for nonsinusoidal waveforms," *IEEE Trans. on Power Electron.*, vol.22, no.1, Jan. 2007.

[29] I. Villar, U. Viscarret, I. E.-Otadui, A. Rufer, "Global loss evaluation methods for nonsinusoidally fed medium-frequency power transformers," *IEEE Trans. Ind. Electron.*, vol. 56, no.10, pp.4132–4140, Oct. 2009.

[30] J. Reinert, A. Brockmeyer, R. W. A. A. De Doncker, "Calculation of losses in ferro- and ferrimagnetic materials based on the modified Steinmetz equation," *IEEE Trans. Ind. Appl.*, vol. 37, no. 4, pp. 1055–1060, Jul-Aug. 2001.

[31] J. Li, T. Abdallah, C. R. Sullivan, "Improved calculation of core loss with nonsinusoidal waveforms," in *Proc. IEEE IAS*, 2001, pp. 2203–2210.

[32] K. Venkatachalam, C. R. Sullivan, T. Abdallah, H. Tacca, "Accurate prediction of ferrite cores loss with nonsinusoidal waveforms using only Steinmetz parameters," in *Proc. IEEE Workshop Comput. Power Electron.*, 2002, pp. 36–41.

[33] C. R. Sullivan, "Computationally efficient winding loss calculation with multiple windings, arbitrary waveforms, and two-dimensional or three-dimensional field geometry" *IEEE Trans. on Power Electron.* vol. 16, no. 1, pp.142-150, 2001.

[34] A. Van den Bossche, V. C. Valchev, G. B. Georgiev, "Measurement and loss model of ferrites with non-sinusoidal waveforms," in *Proc.IEEE PESC*, 2004, pp. 4814–4818.

[35] D. Lin, P. Zhou, W. N. Fu, Z. Badics, and Z. J. Cendes, "A dynamic core loss model for soft ferromagnetic and power ferrite materials in transient finite element analysis," *IEEE Trans. on Magn.*, vol. 40, no. 2, pp.1318–1321, Mar. 2004.

[36] W. Shen, F.Wang, D. Boroyevich, and C. W. Tipton, "Loss characterization and calculation of nanocrystalline cores for high-frequency magnetics applications" *IEEE Trans. on Power Electron.*, vol.23, no.1, Jan. 2008.

[37] J. Muhlethaler, J. Biela, J. W. Kolar, and A. Ecklebe, "Core losses under dc bias condition based on Steinmetz parameters," in *Proc. of the IEEE/IEEJ International Power Electronics Conference (ECCE Asia)*,pp. 2430–2437, 2010.

[38] P. L. Dowell, "Effects of eddy currents in transformer windings," *Proc. Inst. Elect. Eng.*, vol. 113, no. 8, pp. 1387–1394, Aug. 1966.

[39] W. G. Hurley, E. Gath, J. G. Breslin, "Optimizing the AC resistance of multilayer transformer windings with arbitrary current waveforms," *IEEE Trans. on Power Electron.*, vol.15, no.2, pp.369–376, Mar. 2008.

[40] J. Ferreira, "Improved analytical modeling of conductive losses in magnetic components," *IEEE Trans. on Power Electron.*, vol. 9, no. 1, pp. 127–131, Jan. 1994.

[41] Z. Ouyang, O. C. Thomsen and M. A. E. Andersen, "Optimal analysis and improved design of planar transformer in high power dc-dc converters" *IEEE Trans. on Ind. Elec., 2011.*

[42] Z. Ouyang, O. C. Thomsen, M. A. E. Andersen, "The analysis and comparison of leakage inductance in different winding arrangements for planar transformer," *in Proc. IEEE PEDS*, 2009, pp. 1143 – 1148.

[43] X. Nan, C. R. Sullivan, "An improved calculation of proximity-effect loss in high-frequency windings of round conductors," *in Proc. IEEE PESC*, 2003, pp.853–860.

[44] W. A. Roshen, "High-frequency fringing fields loss in thick rectangular and round wire windings," *IEEE Trans. on Magn.*, vol. 44, no. 10, pp.2396–2401, Oct. 2008.

[45] Peter Wallmeier, "Improved analytical modeling of conductive losses in gapped high-frequency inductors," *IEEE Trans. on Ind. Appl.*, vol.37, no.4, pp.1045–1054, July.2001.

[46] M. Nymand, "High Efficiency Power Converter for Low Voltage High Power Applications", PhD dissertation. 2010.

[47] S. Havanur, "Quasi-clamped inductive switching behaviour of power MOSFETs," in *Proc. IEEE PESC 2008,* Rhodes, Greece, pp. 4349-4354.

Appendix B.5

[B.5] K. L.-Poulsen, Z. Ouyang, G. Sen and M. A. E. Andersen, “A new method for start-up of isolated boost converters using magnetic- and winding-integration,” *in Proc. IEEE APEC*, Orlando, Florida, U.S.A, Feb., 2012. (Accepted)

A New Method for Start-up of Isolated Boost Converters Using Magnetic- and Winding-Integration

ABSTRACT

A new solution to the start-up and low output voltage operation of isolated boost family converters is presented. By the use of integrated magnetics and winding integration, the transformer secondary winding is re-used during start-up as a flyback winding coupled to the boost inductor. The traditional added flyback winding coupled to the boost inductor is thus eliminated from the circuit, bringing substantial cost savings, increased efficiency and simplified design. Each subinterval of the converter operation is described through electrical and magnetic circuit diagrams, and the concept is extended to other isolated boost family topologies. Test results using a 600W planar magnetics prototype demonstrate how the converter output voltage is gradually increased, and measurement results show that the efficiency during start-up approaches the efficiency during normal boost operation.

INTRODUCTION

Isolated boost converters have been shown to be the most efficient topology for high power, low input voltage, high output voltage applications [1]-[5]. Suitable applications include distributed generation systems, backup systems, fuel cell converters, electric vehicle applications and avionic applications. However, a disadvantage of the topology is that the boost characteristic sets a lower limit for the output voltage, which introduces in-rush current during start-up from zero output voltage, as well as during fault situations such as output short circuit.

Fig. 1 shows a common solution to the start-up problem [6],[7]. A flyback winding is arranged on the boost inductor, such that the converter may operate as a flyback converter during start-up with the associated buck-boost voltage modulation factor allowing control of the output voltage all the way down to zero volts. During normal boost operation, the flyback winding is completely inactive, but occupies

part of the winding window of the boost inductor, leaving less copper area for the boost inductor, which in turn causes a drop in efficiency. Being a power transferring magnetic component, the flyback winding is a relatively expensive circuit element and complicates the assembly of the boost inductor.

Fig. 2 and Fig. 3 show the new circuit topology, where the magnetic integration of the boost inductor with the transformer allows the boost inductor to couple to the secondary winding during start-up, such that the secondary winding acts as flyback winding.

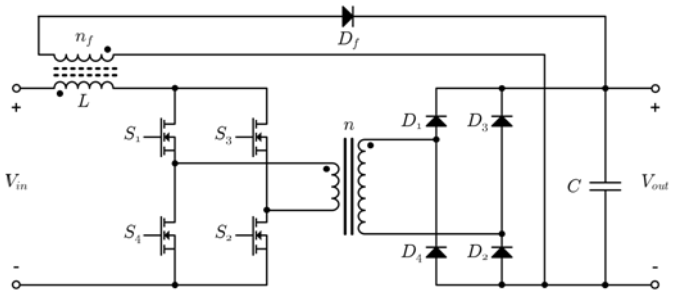

Fig. 1: Isolated full-bridge boost converter with traditional start-up method using added external flyback winding and diode.

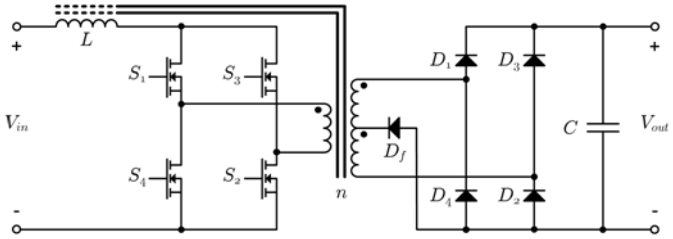

Fig. 2: Electrical circuit diagram of new start-up method.

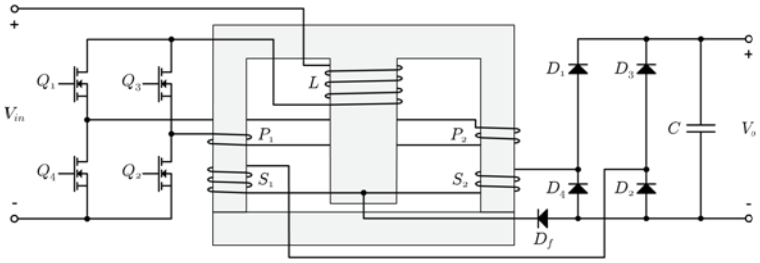

Fig. 3: Electrical and magnetic circuit diagram of new start-up method using EI core with center leg air gap.

PRINCIPLE OF OPERATION

Figure 4-7 explain the principle of operation as applied to the basic full-bridge isolated boost topology. Each subinterval of operation is shown with an electric circuit diagram on the left and a magnetic core diagram on the right. Relevant voltage polarities are marked with +/- signs, and current directions are marked with arrows while inactive elements are dimmed.

The core diagram includes the flux rate, $\frac{d\Phi}{dt} = \Phi'$, induced by the inductor, as well as the flux rate induced by the transformer. The detailed subinterval analysis will be included in final paper.

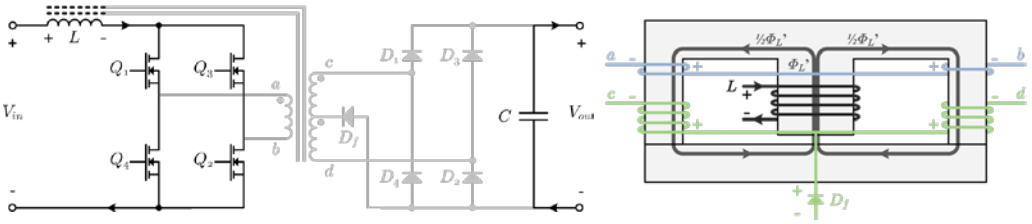

Fig. 4: Boost mode, charging subinterval. All switches are on, inductor current is increasing. Core diagram shows that inductor flux rate is decoupled from transformer.

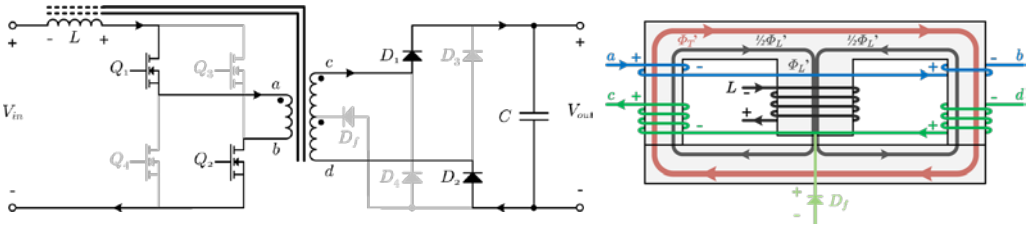

Fig. 5: Boost mode, discharge subinterval. Two diagonal switches are on, inductor current is decreased by transferring energy through the transformer. It is noted that D_f is reverse biased.

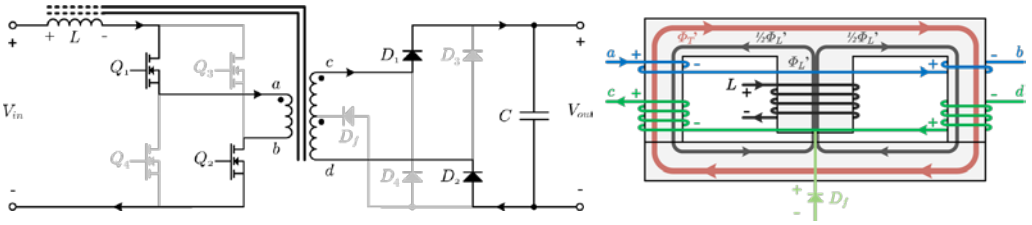

Fig. 6: Start-up mode, charging subinterval. Two diagonal switches are on, charging the inductor while also transferring energy through the transformer, as described in the literature. (7)

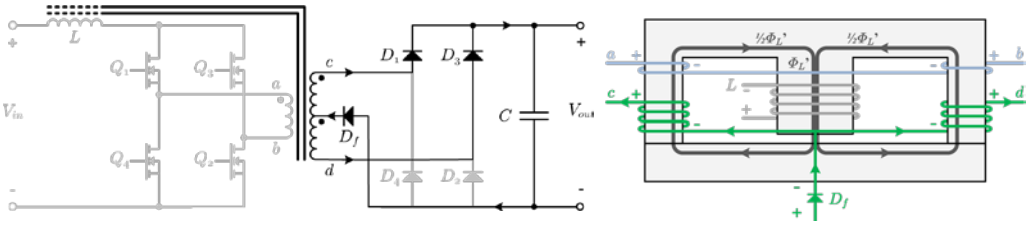

Fig. 7: Start-up mode, flyback discharge subinterval. All switches are turned off. The drop in inductor current causes a reverse in the associated flux rate, which couples to the secondary transformer windings. From the polarity of the induced voltages, it is evident that this allows D_f to be forward biased, such that the energy stored in the air gap can be discharged to the converter output.

EXTENSION TO OTHER ISOLATED BOOST FAMILY TOPOLOGIES

The concept can readily be applied to numerous isolated boost derived topologies, such as flyback-current-fed push-pull [8], dual inductor [9], and parallel primary isolated boost [3]. It can also be applied to various rectification circuits, including voltage doubler and center tap rectifier. Fig. 8 shows the principle applied to an isolated boost converter with a center tap rectifier. In this case, the diode D_f is no longer required, and the start-up functionality is gained "for free" using only the specified integrated

magnetic structure, which may be beneficial in itself by reducing magnetic component count and increasing efficiency.[10]

Fig. 9 shows the principle applied to the parallel primary topology, which has been shown to be an efficient way of scaling converter design for higher power.[3],[4] Additionally, the shown implementation features a shared center leg for flux cancellation, resulting in increased efficiency [11]. It is noted that only a single flyback diode is required, regardless of the degree of paralleling.

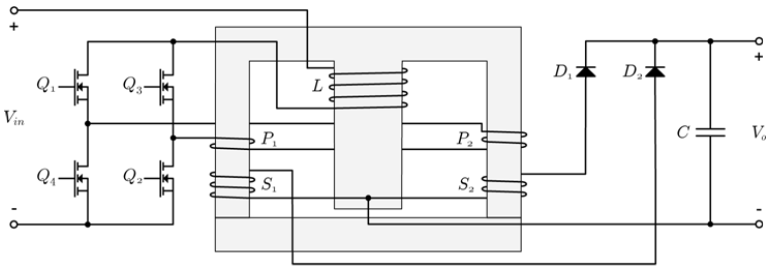

Fig. 8: New start-up method applied to isolated boost with center tap rectification circuit, where a flyback diode is not required.

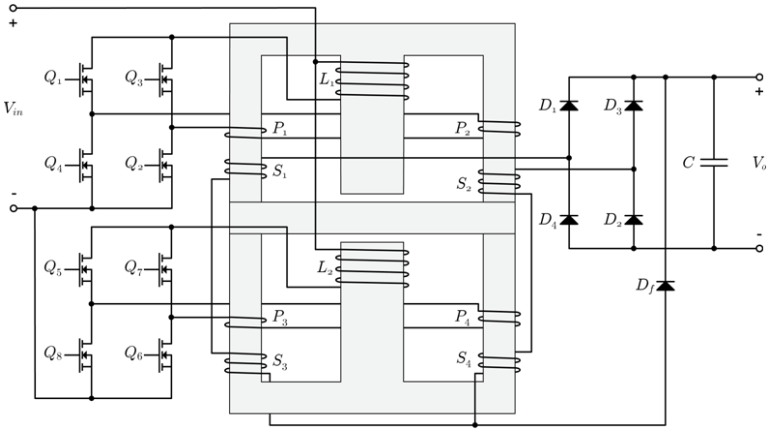

Fig. 9: New start-up method applied to parallel primary isolated boost topology.

PRELIMINARY EXPERIMENTAL RESULTS

Two prototypes have been constructed. Prototype #1 is a 600W basic isolated boost topology. Fig. 10 shows a linear sweep of duty cycle over 4 seconds and the resulting output voltage with a 68 ohm load, thus demonstrating the start-up functionality. The measurement results are compared with a simulation using a simplified gyrator-capacitor model [12], which will be included in the final paper.

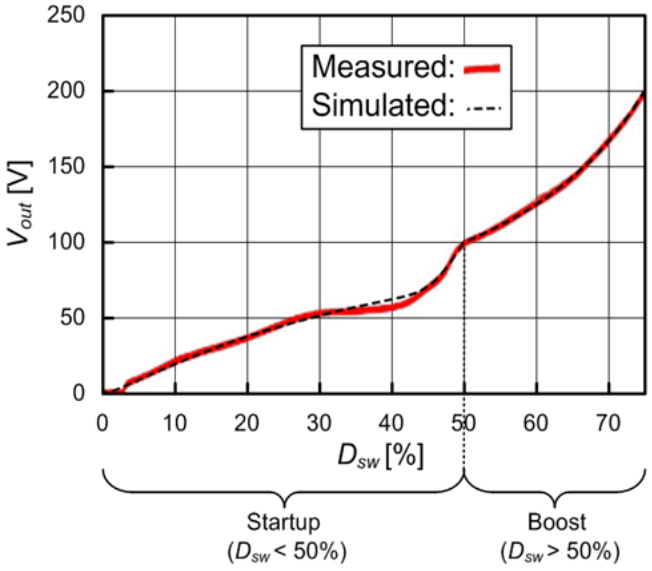

Fig. 10: Prototype #1: Experimental and simulation results from basic isolated boost topology, showing a smooth increase of output voltage as a function of duty cycle.

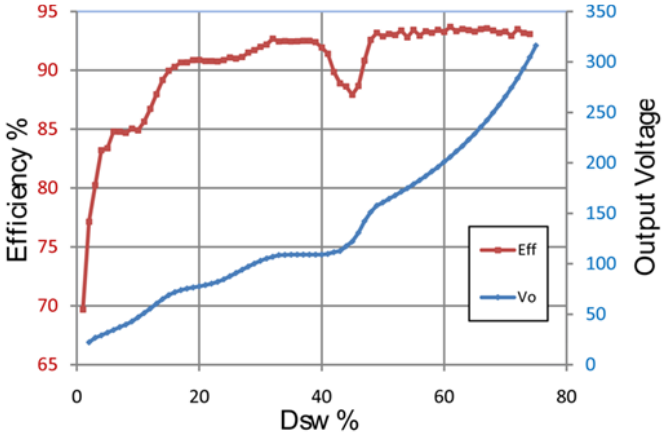

Fig. 11: Prototype #2: Efficiency measurements of parallel primary prototype, showing efficiency and output voltage as a function of duty cycle, with a fixed load of 250 ohm.

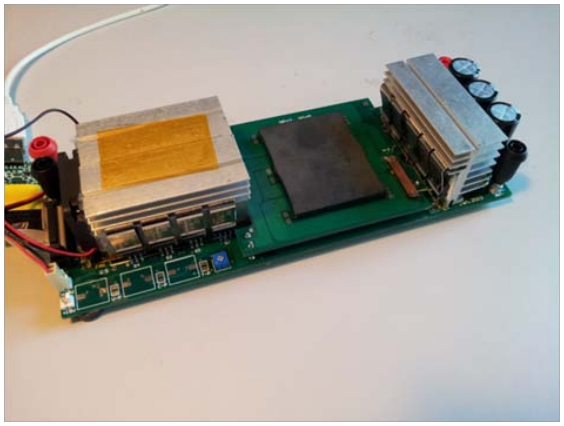

Fig. 12: Prototype #2: Parallel primary prototype converter with fully integrated planar magnetics.

Prototype #2 implements the parallel primary topology shown in Fig. 9. Fig. 11 shows the converter efficiency as a function of duty cycle, with a 250 ohm load. The high efficiency during start-up demonstrates the suitability of the topology for broad output voltage range applications, such as for producing a rectified sine as part of a line-frequency-commutated current-source inverter [13], or for broad input voltage range applications, such as for power factor correction. [8]

As seen on Fig. 11, the efficiency drops 2-4% near 50% duty cycle. This is due to leakage inductance between inductor and secondary, caused by the fact that the boost inductor and secondary windings are not interleaved in the preliminary prototype. The final prototypes will include improved interleaving, and the issue will be described further in the final paper.

CONCLUSIONS and FUTURE WORK

The presented, patent pending [14] start-up method effectively addresses the start-up issue of isolated boost converters, potentially paving the way for increased industry adoption of this highly promising topology family, which so far has been limited by the start-up issue.

The final paper will include further optimized prototypes for various topologies and power levels, including extensive analysis of efficiency and component stress during start-up, as well as in-depth analysis of the effect and minimization of inductor-to-secondary leakage inductance.

REFERENCES

[1] M. Nymand, R. Tranberg, M. E. Madsen, U. K. Madawala and M. A. E. Andersen. "What is the best converter for low voltage fuel cell applications- a buck or boost ?" in *Proc. IEEE Ind. Electron. Soc. Conf.,* 2009, pp. 962–970.

[2] M. Nymand, M. A. E. Andersen, "High-Efficiency Isolated Boost DC–DC Converter for High-Power Low-Voltage Fuel-Cell Applications." *IEEE Trans. on Ind. Electronics*, vol. 57, no. 2, 2010, pp. 505-514.

[3] M. Nymand, M. A.E. Andersen. "New primary-parallel boost converter for high-power high-gain applications." *in Proc. IEEE Appl. Power Electron. Conf. Expo.,* 2009. pp. 35-39.

[4] M. Nymand and M. A.E. Andersen. "A new very-high-efficiency R4 converter for high-power fuel cell applications", *in Proc. Int. Conf. on Power Electronics and Drive Systems*, 2009, pp. 997-1001.

[5] G. K. Andersen, C. Klumpner, S. Kjær, and F. Blaabjerg, "A new power converter for fuel cells with high system efficiency," *Int. J. Electron.*, vol. 90, no. 11/12, 2003, pp. 737–750.

[6] J. J. Albrecht, "Boost-buck push-pull converter for very wide input range single stage power conversion." *in Proc. IEEE Appl. Power Electron. Conf. Expo.,* 1995. pp. 303-308.

[7] L. Zhu, K. Wang, F. C. Lee, J-S. Lai. "New start-up schemes for isolated full-bridge boost converters." *IEEE Trans. on Power Electron.*, vol. 18, 2003. pp. 946-951.

[8] Torrico Bascope, G.V.; Barbi, I. "Isolated flyback-current-fed push-pull converter for power factor correction.", in *Proc. Power Elec. Spec. Conf.*, vol. 2, 1996, 1184 – 1190.

[9] De Aragao Filho, W.C.P.; Barbi, I.; "A comparison between two current-fed push-pull DC-DC converters - analysis, design and experimentation." *in Proc. Telecom. Energy Conf.*, 1996, pp. 313 – 320.

[10] Z. Ouyang, Z. Zhang, O. C. Thomsen, M. A. E. Andersen, O. Poulsen, T. Björklund. "Planar Integrated Magnetics Design in Wide Input Range DC-DC Converter for Fuel Cell Application.", *In Proc. IEEE Energy Conversion Congress and Exposition.* 2010, pp. 4611 – 4618.

[11] Z. Ouyang, G. Sen, O. C. Thomsen, M. A. E. Andersen and T. Björklund. "Fully integrated planar magnetics for primary-parallel isolated boost converter." *in Proc. IEEE Appl. Power Electron. Conf. Expo.,* 2011. pp. 174-181.

[12] David C. Hamill, "Lumped Equivalent Circuits of Magnetic Components: The Gyrator-Capacitor Approach", *IEEE Trans. on Power Electron.*, vol. 8, no. 2, 1993. pp. 97-103.

[13] S.B.Kjaer, J. K. Pedersen, F. Blaabjerg. "A review of single-phase grid-connected inverters for photovoltaic modules." *IEEE Trans. on Ind. Appl.*, vol. 41, no. 5, 2005. pp. 1292-1306.

[14] Inventors: K. Lindberg-Poulsen, Z. Ouyang, G. Sen, EU and US Application date: 7th July 2011.

Appendix B.6

[B.6] G. Sen, Z. Ouyang, O. C. Thomsen, M. A. E. Andersen and M. Lars. “Integrated current balancing transformer for primary parallel isolated boost converter,” *in Proc. IEEE EPE (ECCE Europe),* Birmingham, U.K, Sept. 2011.

Integrated Current Balancing Transformer for Primary Parallel Isolated Boost Converter

Gokhan Sen[1], Ziwei Ouyang[1], Ole C. Thomsen[1], Michael A. E. Andersen[1] and Lars Møller[2]
[1]TECHNICAL UNIVERSITY OF DENMARK
Ørsteds Plads, 349
Kgs. Lyngby, Denmark
Tel.: +45 / 4525 5639
Fax: +45 / 4588 6111
E-Mail: gs@elektro.dtu.dk
URL: http://www.elektro.dtu.dk

[2]H2LOGIC A/S

Keywords

«DC power supply», «integrated passive components», «passive components»

Abstract

A simple, PCB compatible integrated solution is proposed for the current balancing requirement of the primary parallel isolated boost converter (PPIBC). Input inductor and the current balancing transformer are merged into the same core, which reduces the number of components allowing a cheaper and more compact solution. Gyrator-Capacitor modeling technique has been used, providing an easy way for understanding integrated magnetic structures. Proposed idea has been verified by simulation and experimental results.

Introduction

Planar magnetics have unique advantages in terms of increased power density, better cooling capability, modularity and manufacturing simplicity [1], [5]-[9]. Recently, PPIBC has been proposed as an attractive, high efficient solution for high input current, step up DC/DC applications [4] and integrated planar technology has been successfully applied to this topology [2]. In this paper, a new approach in implementing the input inductor and the current balancing transformer of PPIBC in the same core is presented.

Primary Parallel Isolated Boost Converter

Fig. 1 shows PPIBC topology suitable for handling high input currents for fuel cell applications. The dc current is forced to be equal in both primary stages by the series secondary connection of the two transformers. Primary switches share the same control signals with the same phase switching sequence which allows a simple control. Output rectification unit as well as input and output filters are common to both primary stages. Details of this topology and basic waveforms are presented in [4].

The input inductor in Fig. 1 serves as an energy storage element for both primary power stages. As long as switches S1, S2, S3, S4 and S5, S6, S7, S8 work in the same pattern (Fig. 2a), the inductor current will be shared equally by the two full bridges. In case of a mismatch in switching, the current sharing transformer (effectively an inverse coupled inductor) in series with the input inductor shows high impedance in the differential path which limits the rate of change of the differential current (Fig. 2b). This will force the ac components of the currents in the two branches to be equal depending on the inductor value in the differential path. The simulation results in Fig.3 show the current balancing transformer suppressing the ac differences in the currents in each branch.

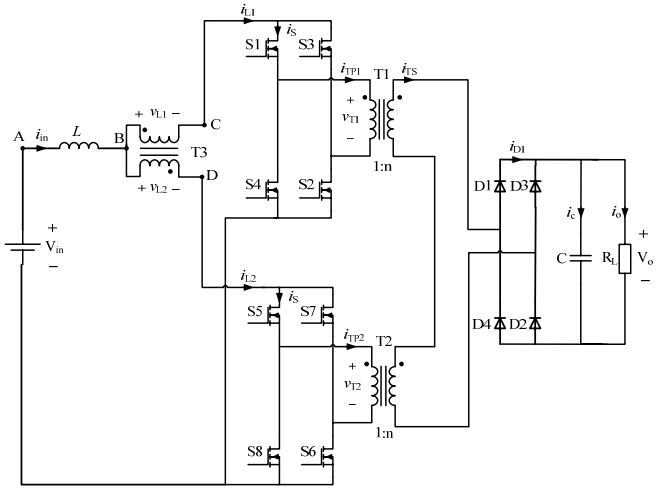

Fig. 1: Primary parallel isolated boost converter with current balancing transformer

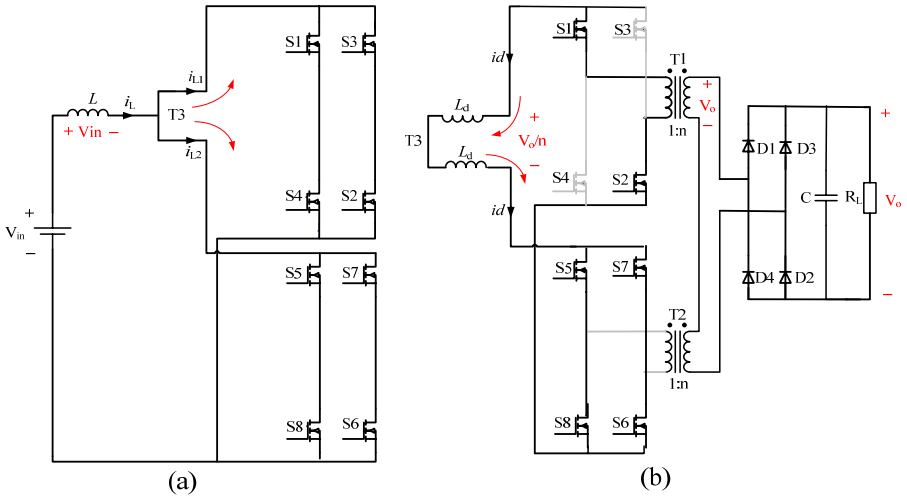

Fig. 2: (a) Forward current path during boosting (b) differential current path during gate signal mismatch

In [4], the current balancing transformer is implemented as a planar based discrete component. However, considering the small mismatch times of the switches due to the propagation delays of the ICs and parasitic elements in the gate drive circuitry, the planar core of the discrete current balancing transformer is not being used during most of the switching period. This results in an inefficient use of the core. Therefore the idea of sharing a core with another magnetic element can be proposed.

Proposed Integrated Current Balancing Transformer

The proposed integrated structure is shown in Fig.4. Both center leg and outer legs of the core are being used. Corresponding circuit model is shown in Fig. 5. Additional windings on the outer legs are reverse coupled on the forward path and direct coupled in the differential path. The magnetic reluctance model is shown in Fig.4b, where N_t and N_L are the number of turns of the winding in the outer leg and the center leg respectively. R_c is the reluctance of the outer leg of the core and R_g represents the reluctance of the center leg. R_g is much bigger than R_c due to the air gap of the center leg. The flux equations using superposition principle can be obtained as,

$$0.5 \cdot N_t \cdot i - \Phi_1 \cdot R_c = N_L \cdot i - \Phi_2 \cdot R_g \;\&\; \Phi_2 = \Phi_1 + \Phi_3 \;\&\; \Phi_1 = \Phi_3 \qquad (1)$$

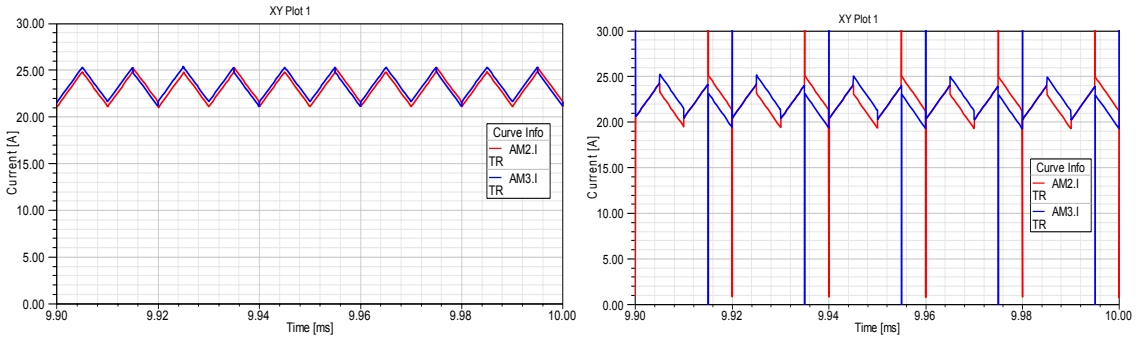

(a) Current balancing transformer used (b) No current balancing mechanism used

Fig. 3: Simulation results for currents flowing into each full bridge in Fig. 1.

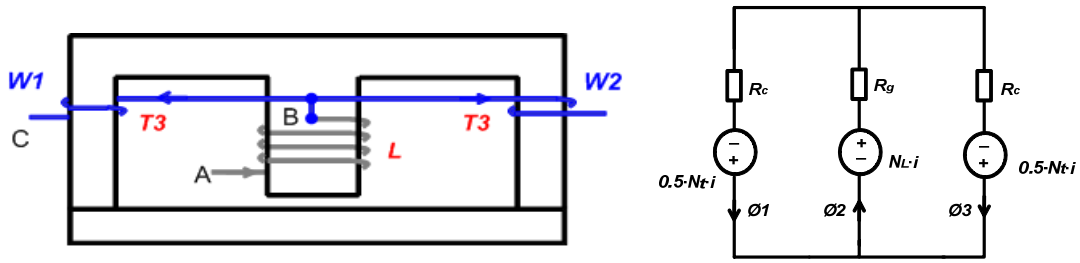

(a) Proposed integration structure (b) Magnetic reluctance model

Fig. 4: Physical placement of the windings and basic modeling

According to Faraday's law, inductances corresponding to each leg can be obtained as,

$$L = \frac{N_L \cdot (N_t + N_L)}{R_g + R_c/2} \;\&\; L_c = L_{c1} = L_{c2} = \frac{N_t \cdot (N_t + N_L)}{R_g + R_c/2} \;\&\; L_d = \frac{(2N_t)^2}{2R_c} \tag{2}$$

The integrated solution has the advantage of eliminating the extra core for the current balancing transformer T3, reducing the cost and the volume of the converter. As shown in Fig. 5, additional inductances (L_{c1} and L_{c2}) are appearing in the forward path due to the direct coupling between L and T3 which reduces the input inductor current ripple. Differential inductances (Ld) in T3 depend on the reluctance of the outer loop of the core in Fig. 4a which does not contain any air gap. This low reluctance path allows for having low number of turns for a certain inductance in the outer leg.

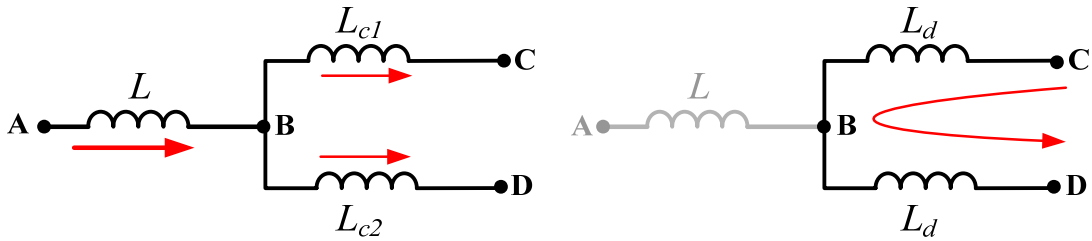

Fig. 5: Circuit models of the integrated structure in (a) forward and (b) differential path

G-C Modeling and FEA Simulation

Gyrator-Capacitor (G-C) modeling technique has been used in the literature especially for integrated magnetic design [10]-[12]. It is a simple and intuitive method which uses capacitance, representing the magnetic core permeance. This approach is compatible with the energy storing capability of a magnetic core, which can not be represented by the reluctance model. Fig. 6 shows the G-C model of the proposed integrated magnetic structure. The model consists of two parts: 1) magnetic part represented with electrical circuit elements (black), 2) electrical part composed of center leg and side leg windings (red).

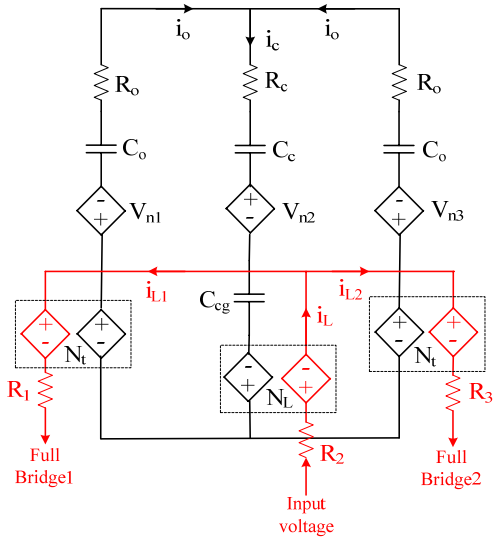

Fig. 6: (a) G-C model of the proposed integrated structure

The coupling points between the electrical and magnetic parts of the model are the current controlled voltage source pairs inside the dashed frames on each leg. The currents i_L, i_{L1} and i_{L2} in the windings are converted into MMFs represented as voltages in the magnetic circuit. The currents i_o and i_c flowing in the magnetic circuit represent the respective flux rates on the core legs which are converted into voltage drops on the windings depending on the number of turns (N_L and N_t). Capacitances C_o and C_c represent the permeances of the outer and center legs where the air gap permeance in the center leg is represented by C_{cg}. Resistances R_1, R_2 and R_3 are the winding resistances. Core loss in each leg can also be represented by the resistances R_o and R_c. Saturation of the core has been represented by the voltage controlled voltage sources V_{N1}, V_{N2} and V_{N3} for each leg. Details of model parameter calculations can be obtained from [10]-[11]. In order to verify the operation of the proposed integrated magnetic structure, the model in Fig. 6 has been simulated. The simulation results with and without outer leg windings are shown in Fig. 7. In Fig.7a center leg has four turns and each outer leg has two turns. On the other hand, Fig. 7b has six turns only in the center leg. The increase in the ripple current in Fig. 7a compared to Fig. 7b is the result of smaller number of turns in the center leg. Since the two outer leg inductances are in parallel in the forward path, effective inductance is reduced. This can be counted as a disadvantage of the method considering the same amount of copper and window area.

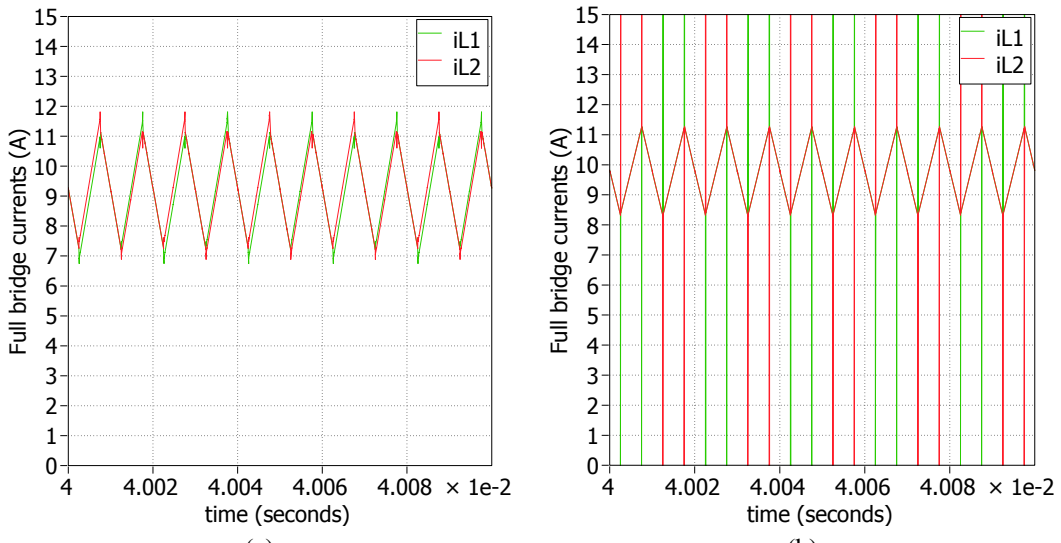

Fig. 7: Simulation of the G-C model: full bridge currents (a) with and (b) without outer leg windings

In order to see the details of the flux distribution in the core, FEA simulations have been carried out. Fig. 8 shows the results for two different cases of winding arrangement. The result in Fig. 8a has been obtained using the configuration in Fig. 4a, where the outer leg windings are reverse coupled with respect to each other, which results in a direct coupling with the winding in the center leg. Fig. 8b shows the case where the outer leg windings are direct coupled, which is included here to investigate as a possible mistake during the winding process. The unbalance of flux distribution and saturation are clearly observed in the latter case. This can be understood by considering the magnetic circuit in Fig. 4b. Here, if one of the outer leg MMF source polarities is reversed, a much bigger amount of flux is produced due to the low reluctance non-gapped outer path. It should be noted that the scales in Fig. 8a and Fig. 8b are not kept the same due to the relatively big difference in flux in both cases.

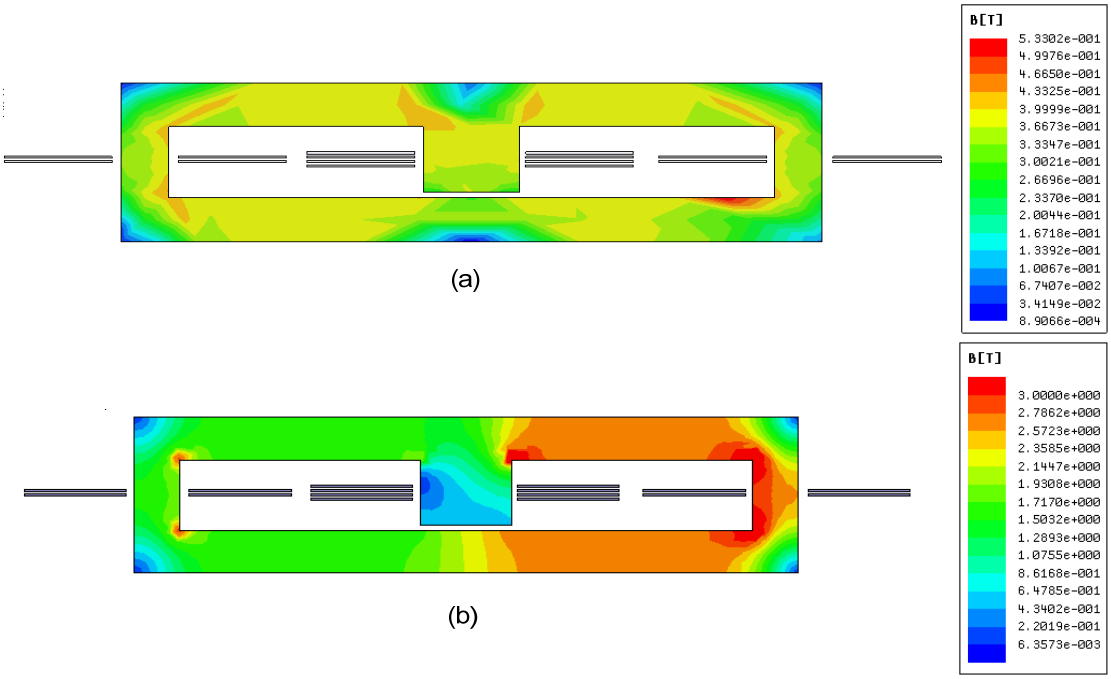

Fig. 8: Finite element analysis of the integrated structure a) with proper coupling of the outer leg windings (b) uneven flux distribution and saturation due to wrong coupling

Experimental Results

A 1kW converter with the integrated current balancing transformer has been built to verify the validity of the proposed idea of integration. Input voltage is between 20-50 V and output voltage is 170-200 V. Primary switches are IPA028N08N3, 80-V, 2.8-mΩ power MOSFETs from Infineon. Output rectification is handled by V30200C Schottky diodes with 0.65-V forward voltage drop. IRS2110 high and low side gate drivers are used in the gate driver circuit together with ISO722C capacitive digital isolators for control signal protection. The control signals are produced by a Texas Instruments TMS320F28027 DSP. Output is filtered by two 10-uF capacitors placed very close to the rectifiers for minimizing the ac loop. Converter waveforms are presented in Fig.9. In Fig. 9a, a small deviation occurs between the currents at the mismatch instants where Fig. 9b shows the clear unbalance with very high rate of change of the currents at the mismatch instants.

A picture of the experimental setup is given in Fig. 10. The integrated current balancing transformer is implemented with ELP58 cores with N87 material. The details of the windings can be seen in Fig. 11. Maximum efficiency of 96% has been observed with 40-V input voltage, 180-V output voltage and 800-W output power.

 ISBN: 9789075815153

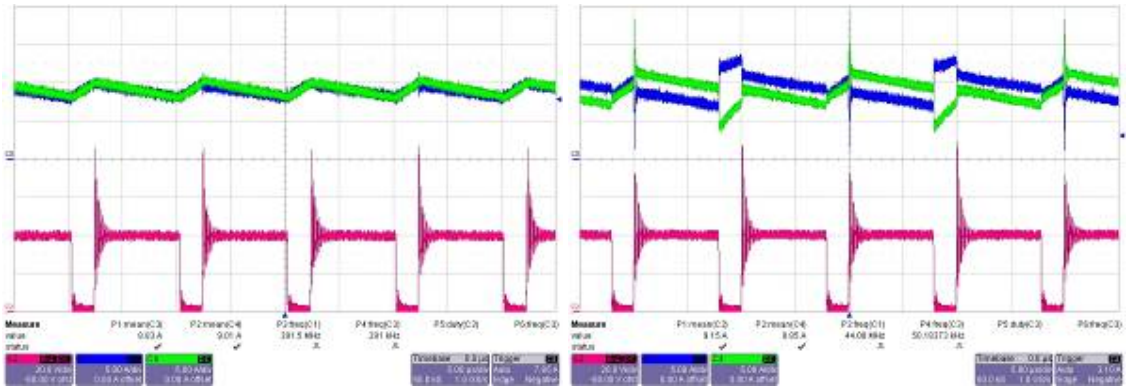

(a) (b)

Fig. 9: Experimental results for currents going into each full bridge in Fig. 1. (a) with and (b) without current balancing transformer

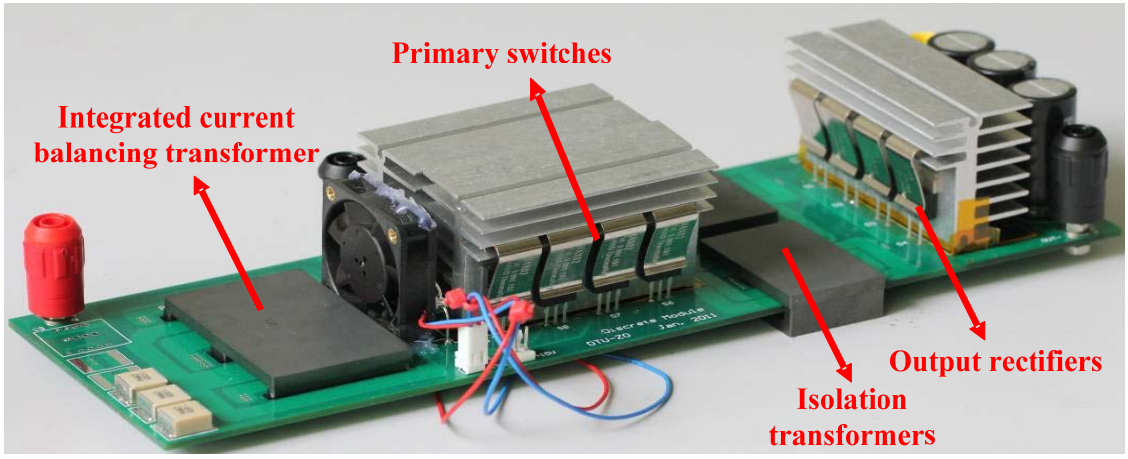

Fig. 10: Experimental prototype of PPIBC with integrated current balancing transformer

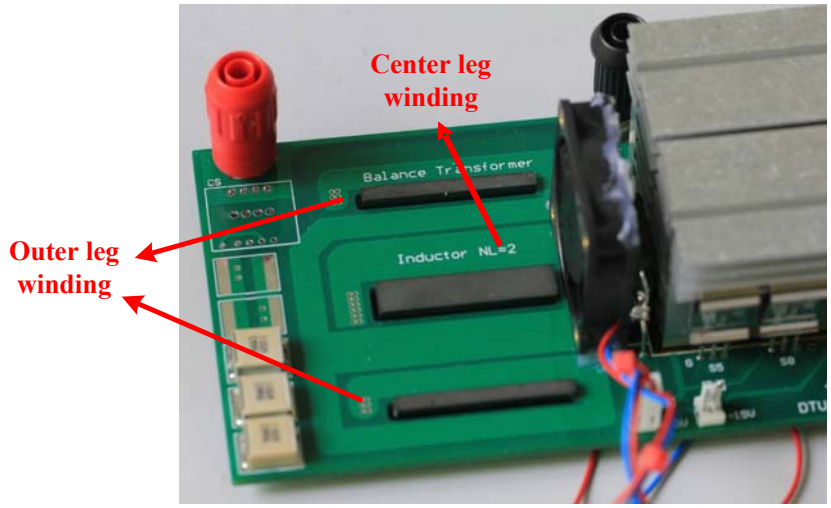

Fig. 11: Detailed view of the PCB tracks

Conclusion

This work presents a new approach in implementation of the current balancing transformer for primary parallel isolated boost converter. Instead of using a separate core the current balancing transformer is implemented in the same core with the input inductor. This reduces the number of components and the number of terminations in the converter. The extra windings in the side legs of the integrated core provide additional inductance in the forward path as well as in the differential path. The new integrated design approach provides a high power density and higher efficiency alternative to the discrete design.

References

[1] Z. Ouyang, Z. Zhang, O. C. Thomsen, M. A. E. Andersen. "Planar Integrated Magnetics (PIM) Module in Hybrid Bidirectional DC-DC Converter for Fuel Cell Application" IEEE Transactions on Power Electronics, 2011.

[2] G. Sen, Z. Ouyang, O. C. Thomsen, M. A. E. Andersen, "A high efficient integrated planar transformer for primary-parallel isolated boost converters," in Proc. IEEE ECCE, 2010.

[3] M. Nymand and M. A. E. Andersen, "High-efficiency isolated boost dc–dc converter for high-power low-voltage fuel-cell applications," IEEE Trans. on Ind. Electron., Vol. 56, no.2, pp.505-514, Feb. 2010.

[4] M. Nymand and M. A. E. Andersen, "New primary-parallel boost converter for high-power high-gain applications" in Proc. IEEE APEC 2009, pp. 35-39.

[5] R. Chen, S. J. T., van Wyk J.D. "Design of planar integrated passive module for zero-voltage-switched asymmetrical half-bridge PWM converter," IEEE Trans. on Ind. Appl., Vol. 39, no.36, pp.1648-1655, Nov.-Dec. 2003.

[6] P. Xu, M. Ye, P. Wong and F. C. Lee, "Design of 48 V voltage regulator modules with a novel integrated magnetics," IEEE Trans. on Power Electron., vol.17, no.6, pp.990–998, Nov.2002.

[7] J. Sun, V. Mehrotra. "Orthogonal winding structures and design for planar integrated magnetics," IEEE Trans. on Ind. Electron., vol. 55, no. 3, pp.1463-1469, March, 2008

[8] W. Chen, G. Hua, D. Sable and F. C. Lee, "Design of high efficiency, low profile, low voltage converter with integrated magnetics," in Proc. IEEE APEC, 1997, pp. 911-917.

[9] P. Xu, Q. Wu, P. Wong and F. C. Lee, "A novel integrated current doubler rectifier," in Proc. IEEE APEC, 2000, pp. 735-740.

[10] D. C. Hamill, "Lumped equivalent circuits of magnetic components: the gyrator-capacitor approach," IEEE Trans. Power Electron., vol. 8, no. 2, pp. 97-103, Apr. 1993.

[11] D. C. Hamil, "Gyrator-capacitor modeling: a better way of understanding magnetic components," in Proc. IEEE APEC'94 Conf., 1994, pp. 326-332.

[12] M. E. Eaton, "Adding flux paths to SPICE's analytical capability improves the ease and accuracy of simulating power circuits," in Proc. IEEE APEC'98 Conf., 1998, pp. 386-392.

Appendix B.7

[B.7] Z. Ouyang, O. C. Thomsen, M. A. E. Andersen and T. Björklund. “Low profile, low cost, new geometry integrated inductors,” *in Proc. IEEE APEC*, pp.150-156, Fort Worth, TX, U.S.A, March, 2011.

Low Profile, Low Cost, New Geometry Integrated Inductors

Ziwei Ouyang[1], Ole C. Thomsen[1], Michael A. E. Andersen[1], and Thomas Björklund[2]

1. Department of Electrical Engineering,
Technical University of Denmark,
Kgs. Lyngby, 2800, Denmark, zo@elektro.dtu.dk

2. Flux A/S - Europe
Asnæs, 4550, Denmark

***Abstract*- A new geometry of integrated inductors with low profile and low cost is presented in this paper. The new geometry integrates two inductors by stacking three I-cores. The middle I-core provides a shared low reluctance flux path. The air gaps are formed by separating the I-cores using copper foil windings with well-defined thickness. Many advantages and disadvantages are described in-depth. In this work, inverse coupling and direct coupling in the new geometry have been analyzed. Coupling characteristic caused by a special gradual saturation behavior has been presented. And thus variable inductors caused by the special saturation behavior are formed. The new integrated inductors make it possible to build low-profile, low-cost, flexibility DC/DC converters, and it can be extensively designed for the low-voltage and high-current required by the modern digital applications. Experiment results obtained from a two-phase interleaved bidirectional DC/DC converter with 48-V input, 12-V and 30-A output, demonstrates the characteristic of new geometry and difference between inverse coupling and direct coupling.**

INTRODUCTION

In order to satisfy the requirements of modern power electronics application, magnetics integration with planar core has proven to be an effective means of reducing DC/DC converter size and cost and increasing converter efficiency [1]-[4]. Planar E-I cores were usually chosen for magnetics integration to improve thermal behavior and reduce profile as well as easy mass production attached with PCB windings [5]-[8].

To achieve a low profile, low cost and flexible magnetic module, a new geometry of integrated inductors is proposed. The new geometry integrates two inductors by stacking three I-cores. Air gaps are constructed by separating the I-cores using copper foil windings with well-defined thickness. The middle I-core provides a shared flux path with a low reluctance. Non-uniform flux distribution in the core causes a special gradual saturation behavior. This saturation firstly occurs at center point of the I-core, and then the saturated area gradually extends to the end with increasing current. Accordingly, a variable inductor can be implemented without complex and expensive manufacture techniques. A typical application for variable inductor is presented in paper [9]. The detail model analysis is involved in Section II. Furthermore, the special gradual saturation behavior causes a coupling characteristic to the new geometry inductors which are presented in Section III. Many advantages such as low cost, low profile, excellent thermal performance, low interwinding capacitance and flexibility are described in Section IV. And also a disadvantage of higher eddy current effect is described in-depth as well.

A 48V-12V 30A two-phase interleaved bidirectional DC/DC converter employing the new geometry integrated inductors has been built. In low-voltage, high-current applications, interleaving has been an attractive technique to achieve high output current, zero output current ripple, fast transient response [10]-[12]. Fig.1 shows a 48V-12V bidirectional DC/DC converter with two channels interleaved technique. Bidirectional power flows for the 48V-12V buck converter and the 12V-48V boost converter are obtained. Inverse coupling and direct coupling structures of the new geometry integrated inductors have been compared to demonstrate the characteristic of new geometry. For the inverse coupling, core loss can be reduced due to AC flux cancellation effect occurs in the middle I-core. However, DC flux will be added over there which promotes an earlier special saturation behavior than the direct coupling. Simulation and experimental results can be obtained from Section V.

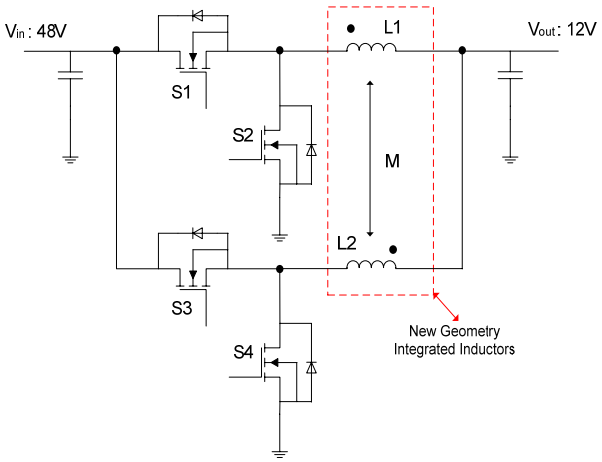

Fig. 1. 48V-12V bidirectional two-channel interleaved DC-DC converter

MODELING OF NEW GEOMETRY

A 3D modeling construction of the new geometry is shown in Fig.2. The module is implemented by three stacked I-cores. Air gaps are constructed by separating the I-cores using copper foil windings with well-defined thickness. The windings are wound in the top I-core and the bottom I-core separately with helical-wound structure, and the middle I-core

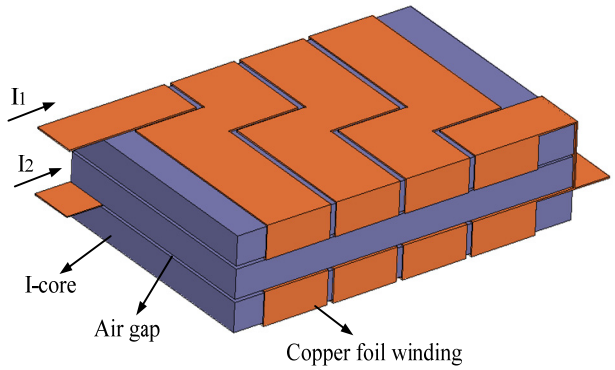

Fig. 2. 3D modeling construction of the new geometry.

provides a shared flux path with low reluctance. The helical-wound structures can dissipate heat quickly with the windings located external to the core and directly exposed to the ambient environment or a heat sink [13].

A 2D section of the inductor along YZ axis and corresponding equivalent magnetic reluctance model are shown in Fig. 3. R_a and R_c represent the reluctances of free air space and the cores respectively. Flux Φ_1 and Φ_2 generated by the two windings are uncoupled this is due to the reluctance of air gap is much higher than that of the middle I-core. Hence the coupling coefficient between L_1 and L_2 is almost zero. AC flux ripple cancellation effect can be obtained in the middle I-core if inverse coupling is used as shown in Fig.3 since the two phase currents are shifting 180°, meanwhile their DC components are added over there. Therefore, the integrated module with inverse connection features a lower core loss.

The flux distribution in this geometry is not as uniform as

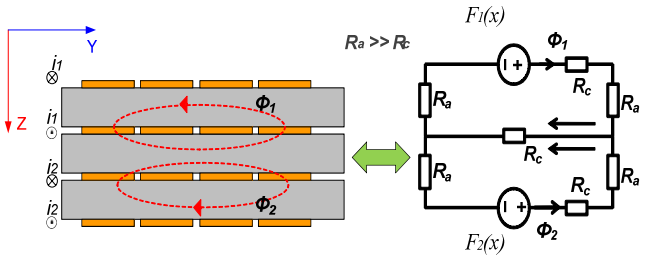

Fig. 3. 2D section and its equivalent magnetic model of the new geometry.

traditional geometry inductor. In Fig.4, a simple experiment based on Faraday's law verifies that the flux throughout air gap, $\Phi_g(x)$, situated in the horizontal element, Δx, almost moves in linear along the horizontal direction (surface of the cores). With assumption that leakage flux through the environmental air is negligible, the flux, $\Phi_g(x)$, in the element, Δx, (assuming $R_a >> R_c$) can be simply expressed by,

$$\Phi_g(x) = \frac{F(x)}{2 \cdot R_a} = \frac{N \cdot I \cdot 2x}{b} \cdot \frac{\mu_0 \cdot w \cdot \Delta x}{2 l_g} \tag{1}$$

where N is the number of turns wound in the I-core, b is the length of the core, w is the width of the core and l_g is the length of the air gap as shown in Fig.5. μ_0 represents the

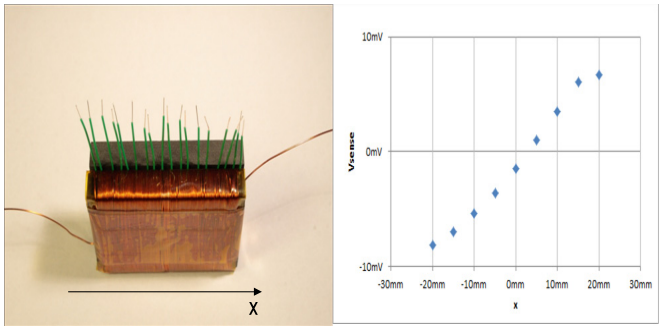

Fig. 4. A simple experiment to reflect a flux distribution characteristic.

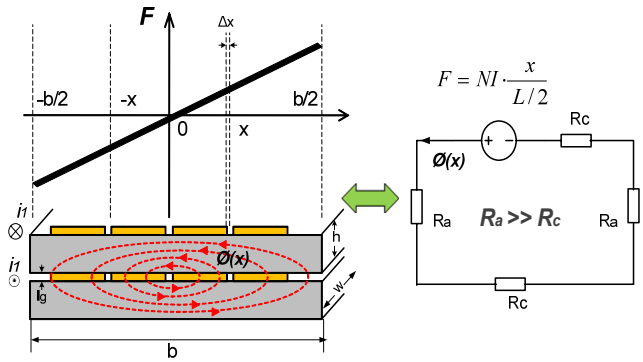

Fig. 5. An oval-shaped flux distribution associating with different magnetic strengths in the new geometry.

permeability of free air. The flux density, $B_g(x)$, stored in the air gap is,

$$B_g(x) = \frac{\Phi_g(x)}{w \cdot \Delta x} = \frac{\mu_0 \cdot N \cdot I \cdot x}{b \cdot l_g} \tag{2}$$

The total flux in the core is found, by performing the integration (2) with $x=b/2$,

$$\Phi_c(x) = \int_x^{\frac{b}{2}} B_g(x) \cdot w \cdot dx = \frac{\mu_0 \cdot N \cdot I \cdot w}{2 \cdot b \cdot l_g} \cdot \left(\frac{b^2}{4} - x^2\right) \tag{3}$$

According to Faraday's law and Ampere's law, the inductance of the element associated with the flux, $\Phi_g(x)$, can be derived,

$$dL = \frac{N^2(x)}{2 \cdot R_a} = \frac{4 \cdot N^2 \cdot x^2}{b^2} \cdot \frac{\mu_0 \cdot w \cdot \Delta x}{2 \cdot l_g} \tag{4}$$

The overall inductance is obtained by integrating (4) from $x=0$ to $x=b/2$.

$$L_t = \int_0^{\frac{b}{2}} \frac{4 \cdot N^2 \cdot x^2}{b^2} \cdot \frac{\mu_0 \cdot w}{2 l_g} \cdot dx = \frac{\mu_0 \cdot N^2 \cdot w \cdot b}{12 \cdot l_g} \tag{5}$$

Fig.6 shows a plot of (3). As can be seen, a maximal flux in the core occurs at $x=0$. Accordingly, a special gradual saturation behavior and a variable inductor can be created. The saturation firstly occurs at center point of the I-core, and

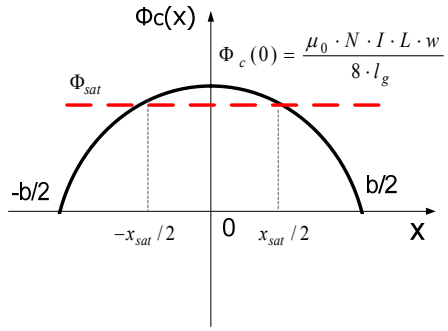

Fig. 6. Flux distribution in the core along horizontal direction.

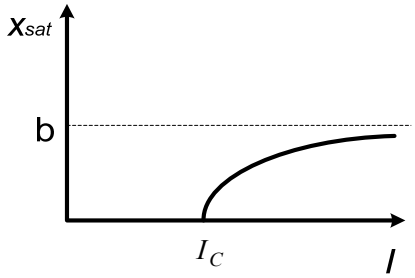

$$I_C = \frac{8 \cdot B_{sat} \cdot h \cdot l_g}{\mu_0 \cdot N \cdot b}$$

Fig. 7. The relationship between the saturated area and the current.

then the saturated area gradually extends to the end of the I-core with increasing current. The relationship between the saturated area and the current can be obtained from,

$$x_{sat} = 0; \quad when\ I \le \frac{8 \cdot B_{sat} \cdot h \cdot l_g}{\mu_0 \cdot N \cdot b} \tag{6}$$

$$x_{sat} = 2 \cdot \sqrt{\frac{b^2}{4} - \frac{2 \cdot B_{sat} \cdot b \cdot l_g}{\mu_0 \cdot N \cdot I}}; \quad when\ I > \frac{8 \cdot B_{sat} \cdot h \cdot l_g}{\mu_0 \cdot N \cdot b} \tag{7}$$

where B_{sat} is the saturation flux density of the core material and h is the height of the I-core. At low currents there is no saturation. With the special saturation behavior being activated, the overall inductance is decreased due to an increased reluctance in the flux path. Therefore, a variable inductor whose inductance varies with current is produced.

$$L_{sat} = \int_0^{\frac{b}{2}} \frac{N^2(x)}{2 \cdot (R_a + R_{sat})} \cdot dx \tag{8}$$

where,

$$R_{sat} = \frac{x_{sat}}{\mu_0 \cdot w \cdot h}$$

The gradual saturation behavior might be utilized in some application such as active power factor correction (PFC) etc. The paper [9] has demonstrated that a variable inductor with sloped air-gap (SAG), whereby the inductance falls off with increasing current, is suitable for power factor correction, providing adequate harmonic reduction, and can save considerable space (up to 65%) and cost over a conventional inductor as employed in passive power factor correction. However, the SAG variable inductor needs to provide a complex manufacturing. The proposed integrated inductors may contribute a fully functional and electromagnetically equivalent to the SAG variable inductor applied in PFC converters without complexity and expensive manufacture.

COUPLING CHARACTERISTIC

In conventional coupled E-I integrated inductors, the relative even flux distribution appears in the core. When saturation occurs in the center leg due to overlapping of the DC flux, the entire center leg will suddenly become a very low permeability material (high reluctance). Accordingly, an undesired strong coupling emphasizes on the two inductors where increased current ripples and slow transient response can be obtained for the interleaved converters due to the equivalent inductances are reduced. To show the coupling effect in the interleaved DC/DC converter, the following equivalent inductances can be derived from the analysis of coupled inductors circuit [10] and [12].

$$L_{stage1} = \frac{L^2 - M^2}{L + (\frac{D}{D'}) \cdot M} \tag{9}$$

$$L_{stage\ 2,4} = L + M \tag{10}$$

$$L_{stage3} = \frac{L^2 - M^2}{L + (\frac{D'}{D}) \cdot M} \tag{11}$$

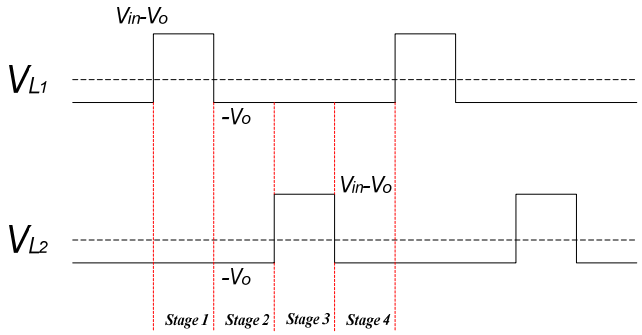

Fig. 8. Voltage waveforms across on the two inductors for the buck mode of interleaved DC/DC converter.

where D is duty-cycle ratio and $D'=1-D$, L is self-inductance and M is mutual inductance between L_1 and L_2. For the inverse coupling, M is negative. Coupling coefficient is defined as $\alpha=M/L$. Fig.9 shows the normalized steady state equivalent inductance, L_{stage1}, in different coupling coefficient, α, under inverse coupling. The design should be required in the region of $L_{stage1}>L$, where the steady state conduction loss can be reduced. The region shrinks as the duty cycle, D, decreases. Fig.10 shows steady-state current waveforms for coupling inductors. It is obvious that direct coupling causes a higher current ripple for the interleaving converter. However, inverse coupling contributes a lower current ripple.

Unlike the conventional coupled E-I integration, the new

geometry has a special gradual saturation behavior in the middle I-core due to a non-uniform flux distribution. With an oval-shaped flux distribution as shown in Fig. 5, the magnetic strength decreases alone a parabola line from center of the core to its end as shown in Fig.6. The saturation firstly occurs at center point of the middle I-core, and then the saturated area gradually extends to the end with increasing current. Accordingly, a variable coupling coefficient α can be implemented by a controlled output current.

$$\alpha = \frac{M}{L} = \frac{R_{sat}}{2 \cdot R_a + R_{sat}} = \frac{b \cdot x_{sat}}{4 \cdot l_g \cdot h + b \cdot x_{sat}} \tag{12}$$

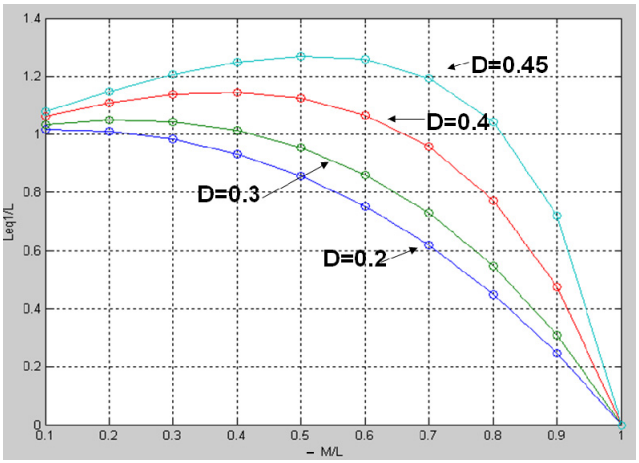

Fig. 9. Normalized equivalent inductance of different coupling effects.

With increasing current, coupling coefficient, α, increases. In terms of the same self-inductances, L, as a comparative prerequisite condition, a proper coupling coefficient α can reduce inductor current ripple and improve transient response. However, lower self-inductances are obtained in this case when saturation occurs in the middle I-core due to an increased reluctance in the flux path. Therefore, the special saturation behavior in the new geometry may have negative effect for current ripple but it may handle higher output current and faster transient response.

ADVANTAGES AND DISADVANTAGES

In term of the new geometry module, comparing with traditional E-I integrated inductors, some advantages can be concluded as follows,

(1) Low cost. The grinding process for air gaps can be eliminated because the copper foil windings with well-defined thickness can be used instead, which is a cost-effective way to produce inductors. Furthermore, I-core is much cheaper than E-core in the market.

(2) High current capability. More energy can be stored in the new geometry due to there are two symmetrical segments air gaps with the same length involved in the closed flux path. Also the air gaps have wide cross-section. Furthermore, the special gradual saturation behavior may handle more output current.

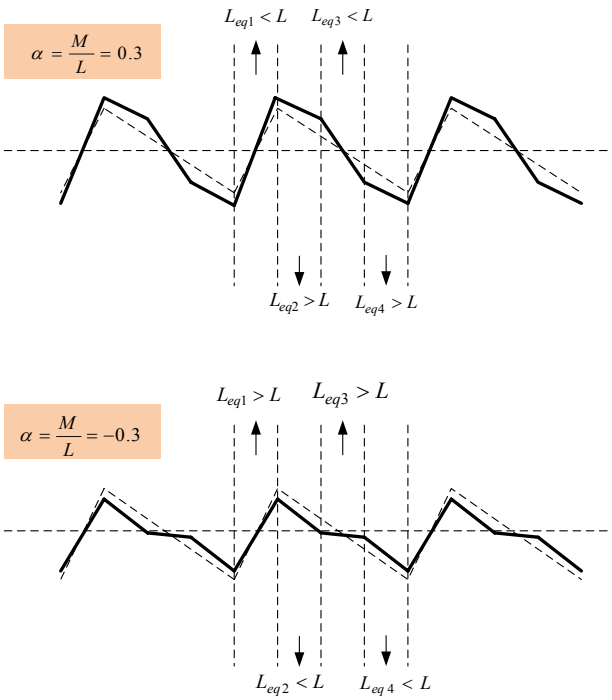

Fig. 10. Steady-state current waveforms for coupling inductors.

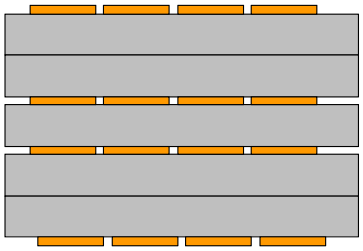

Fig. 11. Flexibility in the new geometry.

(3) Low profile. The new geometry provides a very low height for the converter, and thus increases the power density of the converters.

(4) Excellent thermal performance. The helical-wound structures can dissipate heat quickly with the windings located external to the core and directly exposed to the ambient environment or a heat sink.

(5) Low interwinding capacitances. The turn-to-turn capacitance is very low due to very small overlapping surface area in two conductive plates [15].

(6) Flexibility. It is very easy and convenient to increase the cross-section by stacking additional I-cores as shown in Fig.11, This results in many advantages such as higher inductance, low core loss, high current capability .etc.

A significant drawback of this structure is that a higher eddy current effect is induced in the conductors and thus causes a higher winding conduction loss. This is due to the fact that the windings are situated in the gaps where an external flux is approximated as purely vertical directed to the surface of the conductors. Since the external flux is tangential to the vertical edges of the conductors, a current must flow toward to the edges in order to exclude the magnetic field from the inside of conductor. The cross-sectional area of its

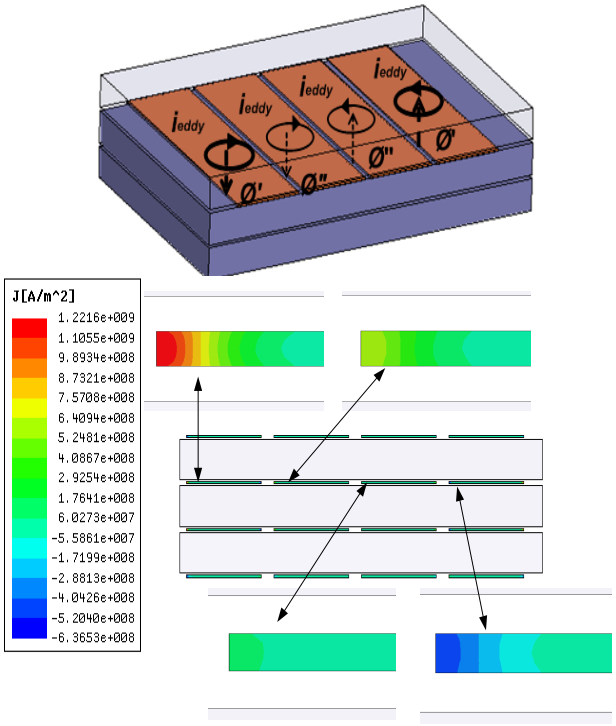

Fig. 12. High eddy current effect caused by perpendicular flux to the horizontal windings.

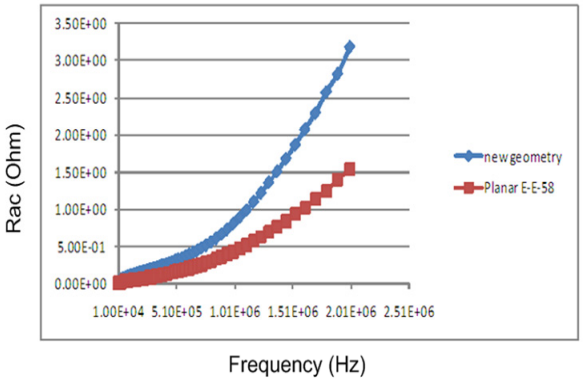

Unit (mohm)	DC	50 kHz	200 kHz	500 kHz	1MHz
New geometry	2.5	79.9	161	318	815
Planar E-E-58	2.5	31.8	66.2	163	433

Fig. 13. Measurement comparison on ac resistances.

ac current distribution in the conductor is therefore proportional to δ^2 (δ is skin depth), so the effective ac resistance is much higher than dc resistance [4], [19]. Fig.12 shows a current density distribution in the conductors. A comparison on measured ac resistance between the new geometry inductor and standard inductor with planar core is shown in Fig.13, obtained by PSM1735, impedance analyzer. The ac resistance in new geometry is almost two times as high as that of standard inductor. A reduction to ac resistance can be obtained by using narrow copper tracks. The width of track close to the skin depth might be the best choice for the ac resistance, but a high dc resistance is compromised. Hereby, an auxiliary winding solution [20] to balance the ac resistance and dc resistance is recommend, where the auxiliary winding is optimally designed with lower ac resistance to carry the ac current while the main winding with low dc resistance is designed for the large dc current.

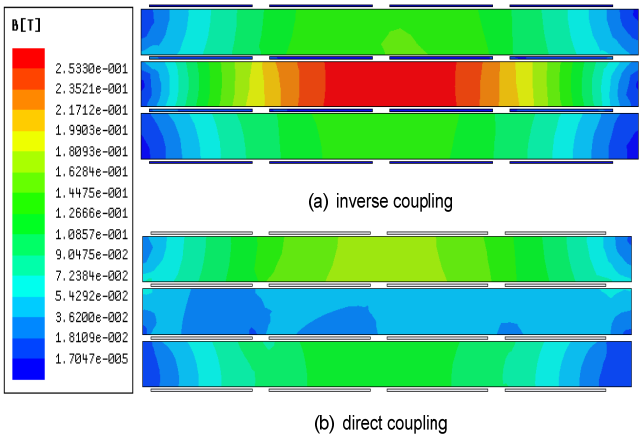

Fig. 14. Instantaneous flux distribution in the new geometry based on FEA simulation.

Simulation and Experiment Results

A 2D FEA simulation is built in order to verify previous analysis of the flux distribution and the gradual saturation behavior. Fig.14 shows instantaneous flux distributions in the core under the inverse coupling and the direct coupling respectively. For the inverse coupling, flux density in the middle I-core is higher than that in the side I-cores due to dc flux are added over there. It can be seen that the strongest magnetic field occurs at center point of the middle I-core where the saturation behavior firstly occurs at. And ac flux components are not able to be recognized in the figure. However, simulation animation within a period shows the flux in the middle I-core is stable (there is almost no flux variation), which means that ac flux are cancelled over there. Oppositely, dc flux cancellation effect occurs in the middle I-core for the direct coupling, and ac flux are added over there.

An experimental converter employing the new geometry inductors has been built in order to demonstrate the characteristic. The converter is designed to operate with an input voltage 48-V, an output voltage 12-V, and a rated output power 400-W. The switching MOSFETs S1 and S3 are implemented by Vishay SUM90N08-7M6P. The rectifiers MOSFETs S2 and S4 are realized by Vishay SUM90N08-4M8P. 200-kHz is chosen as the operating frequency. For simplification, a 132-ns dead time is used for S2 and S4 instead of synchronous rectifier. Of course it will increase the

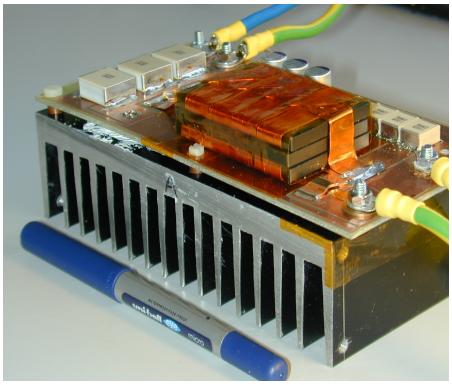

Fig. 15. Converter prototype employing the new geometry.

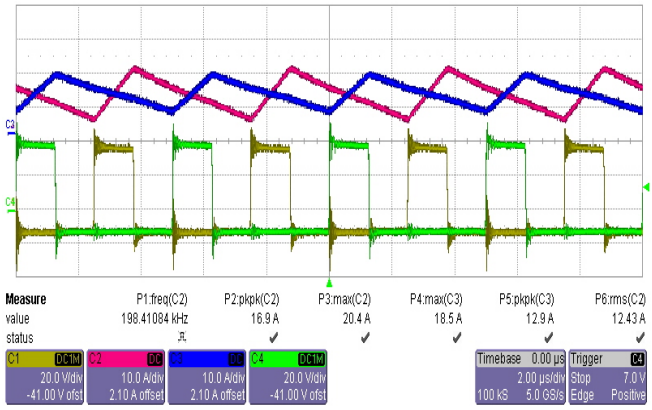

Fig. 16. The waveforms in the inverse connection when output is 25A.

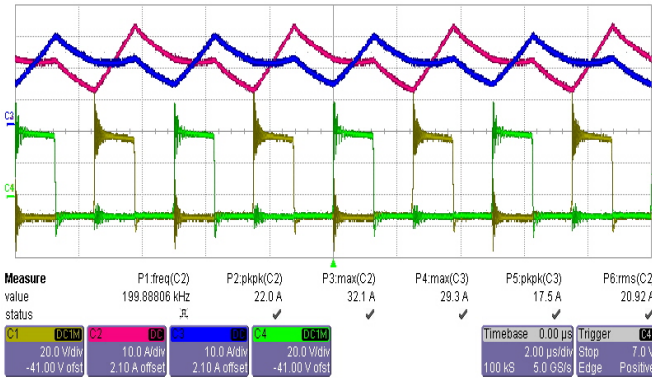

Fig. 17. The waveforms in the inverse connection when output is 40A.

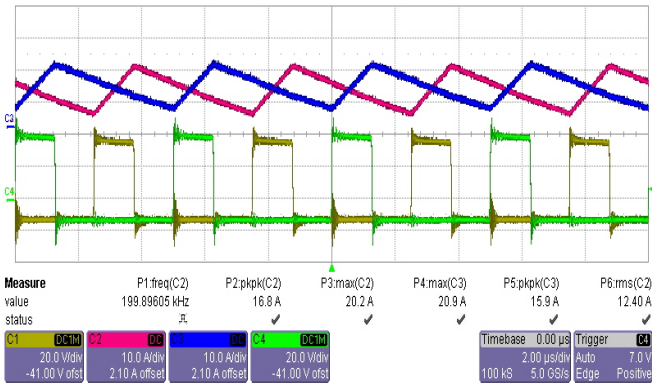

Fig. 18. The waveforms in the direct connection when output is 25A.

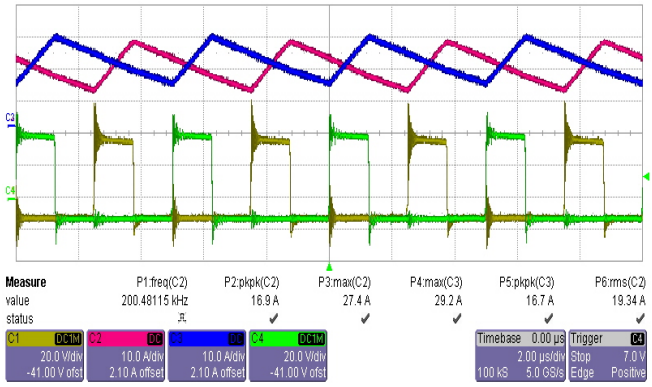

Fig. 19. The waveforms in the direct connection when output is 40A.

body-diode conduction loss and the reverse-recover loss. The new geometry inductors use ILP 58 cores with 3F3 material. 4 turns are wound both in the top I-core and in the bottom I-core. 0.2-mm copper thickness is used to handle a high output

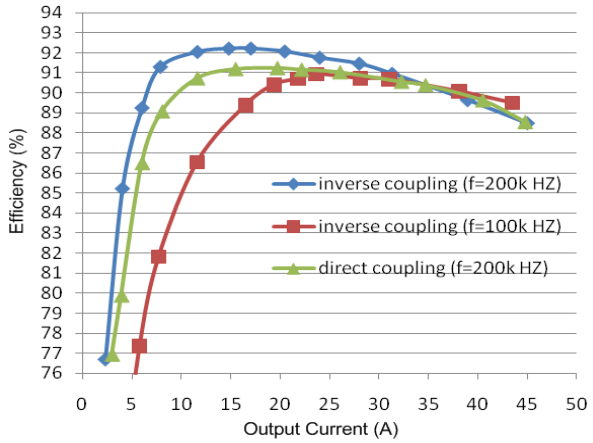

Fig. 20. Comparative efficiencies in the converter.

current and construct air gaps together with 0.1-mm Kapton tapes. 4-uH self-inductances can be obtained for each of inductors.

Fig.15 shows a prototype of the converter employing the new geometry. Fig. 16-19 shows the plots of the currents on the two inductors (Ch2 and Ch3), and the voltages across on the two inductors (Ch1 and Ch4). The duty cycle D is 25% and the two channels with interleaving technique are controlled by shifting 180° gate signal. Fig.16 shows the waveforms for the inverse coupling when output current is 25-A. There is a little unbalance on the current waveforms (Ch2 and Ch3) because of uneven air gaps on the two inductances caused by handcraft (uneven surface of copper foil, but it could be overcome by careful manufacture or balancing transformer). Fig.17 shows the waveforms for the inverse coupling when output current is 40-A. As seen from the current waveforms, the two inductors have been coupled due to the gradual saturation behavior in the middle I-core. The peak to peak currents are increased from 16.9-A to 22-A due to lower self–inductances caused by the saturation behavior. Two variable inductors are therefore formed. The equivalent inductances, L_{stage2} and L_{stage4}, are lower than self-inductance L, and the equivalent inductances, L_{stage1} and L_{stage3}, may be higher than self-inductance L depending on the coupling coefficient α as seen (9) ~ (11). Notice that the current waveforms goes down nonlinearly in both stage 2 and in stage 4 since coupling coefficient α varies with the output current. However, the current waveforms in stage 1 seem to be increased linearly due to L_{stage1} slightly vary with the output current. A higher equivalent inductance, L_{stage3}, causes the current waveform with a slight slope in stage 3. Fig.18 and Fig.19 show the waveforms under 25-A output current and 40-A output current respectively, both for the direct coupling. No saturation behavior occurs in the middle I-core due to dc flux are cancelled over there. Therefore the current waveforms still keep the same as uncoupled status.

High stability (< 10 ppm) 0.1 % shunt resistors are used for high precision of the efficiency measurements. Agilent 34410A high precision multimeters are used for all measurements. Current sense signals are shielded and fitted with common mode filters. The efficiency results are shown in Fig. 20. Comparing with the direct coupling, a higher efficiency can be achieved in the inverse coupling when the output current is below 35-A because of flux cancellation in

the middle I-core which features a lower core loss. However, when the output current is above 35-A, a higher current ripple caused by the saturation behavior in the inverse coupling reduces the overall efficiency. The overall efficiency of 100-kHz is much lower than that of 200-kHz in the light load this is because of the fact that the core loss mainly dominates over the total power loss in the light load. A higher frequency causes a lower current ripple which contributed a lower core loss. Oppositely, winding loss strongly dominates over the total power loss in the heavy load. So the efficiency curves get to close.

CONCLUSION

This work proposes a new geometry integrated inductor. It can handle high current without grinding air gaps. And many advantages such as low cost, low profile, excellent thermal performance, low interwinding capacitance and flexibility have been described in this paper. And also a disadvantage of higher eddy current effect in this geometry has been presented. A coupling characteristic in the new geometry caused by a special gradual saturation behavior has been analyzed. Although the saturated behavior may have negative in power efficiency, it may handle more current as well as variable inductors might be utilized in some other applications.

REFERENCES

[1] H. Kosai, S. McNeal, B. Jordan, J. Scofield, B. Ray, and Z. Turgut, "Coupled inductor characterization for a high performance interleaved boost converter," *IEEE Trans. on Magn.*, vol. 45, no.10, pp.4812–4815, Oct, 2009.

[2] P. Xu, M. Ye, P-L. Wong, and F. C. Lee, "Design of 48 V voltage regulator modules with a novel integrated magnetics," *IEEE Trans. on Power Electron.,* vol.17, no.6, pp.990–998, Nov.2002.

[3] W. Chen, F. C. Lee, X. Zhou and P. Xu, "Integrated planar inductor scheme for multi-module interleaved quasi-square-wave (QSW) DC/DC converter," *in Proc. IEEE PESC, 1999,* pp. 759-763.

[4] J. Sun, V. Mehrotra. "Orthogonal Winding Structures and Design for Planar Integrated Magnetics" *IEEE Trans. on Ind. Electron.*, vol. 55, no. 3, pp.1463-1469, March, 2008.

[5] W. Chen, Y.-P. Yan, Y.-Q. Hu, Q. Lu, "Model and design of PCB parallel winding for planar transformer," *IEEE Trans. on Magn.*, vol. 39, no. 5, pp.3202–3204, Sept. 2003.

[6] E. de Jong, J. Ferreira, P. Bauer, "Toward the next level of PCB usage in power electronic converters," *IEEE Trans. on Power Electron.*, vol.23, no.6, pp.3153–3163, Nov. 2008.

[7] C. Quinn, K. Rinne, T. O'Donnell, M. Duffy, C.O. Mathuna, "A review of planar magnetic techniques and technologies," *in Proc. IEEE APEC*, 2001, pp. 1175–1183.

[8] C. Buccella, C. Cecati and F. de Monte, "A coupled electrothermal model for planar transformer temperature distribution computation" *IEEE Trans. on Ind. Electron.,* Vol. 55, no.10, pp.3583-3590, Oct. 2008.

[9] W. H. Wölfle and W. G. Hurley, "Quasi-Active power factor correction with a variable inductive filter: theory, design and practice," *IEEE Trans. on Power Electron.*, vol.18, no.1, pp.248–255, Jan. 2003.

[10] P-L. Wong, Q. Wu, P. Xu, B. Yang, F. C. Lee, "Investigating coupling inductors in the interleaving QSW VRM," *in Proc. IEEE APEC, 2000, pp. 973-978*.

[11] P-W. Lee, Y-S. Lee, D. K. W. Cheng, X-C. Liu; , "Steady-state analysis of an interleaved boost converter with coupled inductors," *IEEE Trans. on Ind. Electron.*, vol.47, no.4, pp.787-795, Aug 2000.

[12] S-Y. Lee, A. G. Pfaelzer, and J. D. van Wyk, "Comparison of different designs of a 42-V/14V DC/DC converter regarding losses and thermal aspects," *IEEE Trans. on Ind. Appl.*, vol. 43, no.2, pp.520–530, Mar, 2007.

[13] F. Wong and J. Lu, "High frequency planar transformer with helical winding structure," *IEEE Trans. on Magn.*, vol. 36, no.5, pp.3524–3526, Sept, 2000.

[14] W. G. Hurley and M. C. Duffy, "Calculation of self- and mutual impedances in planar sandwich inductors," *IEEE Trans. on Magnetics*, vol.33, no.3, pp. 2282- 2290, May, 1997.

[15] Z-W. Ouyang, O. C. Thomsen, M. A. E. Andersen, "Optimal analysis and improved design for planar transformer in high power dc-dc converters," *IEEE Trans. on Ind. Electron.*, 2010. (in press)

[16] Søren Petersen. "Improved geometry of integrated magnetics for the hybridge topology" *in Proc. ESA, May, 2002,* pp. 241-246.

[17] Z-W. Ouyang, O. C. Thomsen, M. A. E. Andersen, "New geometry integrated inductors in two-channel interleaved bidirectional converter," *in Proc. IEEE IECON, 2010*. pp. 582-586.

[18] C. Collins, M. Duffy. "Distributed (Parallel) inductor design for VRM applications" *IEEE Trans. on Magn.*, vol. 41, no.10, pp.4000–4002, Oct, 2005.

[19] X. Mao, W. Chen, Y. Li. "Winding loss mechanism analysis and design for new structure high-frequency gapped inductor," *IEEE Trans. on Magn.*, vol.41, no.10, pp. 4036- 4038, Oct. 2005

[20] M. Nymand, U. K. Madawala, M. A. E. Andersen, B. Carsten, O. S. Seiersen, "Reducing ac winding losses in high-current high-power inductors," in *Proc. IEEE IECON*, 2009, pp. 774-778.

[21] A.D. Podoltsev, I. N. Kucheryavaya, B. B. Lebedev. "Analysis of effective resistance and eddy-current losses in multiturn winding of high-frequency magnetic components," *IEEE Trans. on Magnetics*, vol.39, no.1, pp. 539- 548, Jan, 2003.

[22] Z-W. Ouyang, O. C. Thomsen, M. A. E. Andersen, "Low Profile, Low Cost, New Geometry Integrated Inductors" *in Proc. IEEE APEC, 2011*.

Appendix B.8

[B.8] Z. Ouyang, M. Acanski, J. Popovic-Gerber, J. A. Ferreira, O. C. Thomsen and M. A. E. Andersen. “Design consideration of ultra-thin coupled inductors for photovoltaic application,” in *Proc. IEEE CIPS,* Nuremberg, Germany, March, 2012. (Accepted)

Design Consideration of Ultra-thin Coupled Inductors for Photovoltaic Application

Z. Ouyang*, M. Acanski**, J. Popović**, J. A. Ferreira**, O. C. Thomsen* and M. A. E. Andersen*

*Electrical Engineering, Technical University of Denmark, Kgs.Lyngby, Denmark

** Electrical Power Processing, Delft University of Technology, Delft, The Netherlands

***Abstract*—Ultra-thin power converters with flexible PCB integrated magnetic components are highly demanded in future photovoltaic (PV) application, resulting in a higher power density. In this paper, a 1.5-mm thickness integrated coupled inductor with sandwich core structure is under investigation. Several important design issues for the sandwich core structure including self-inductance, leakage inductance, eddy current effect and core loss are analyzed in-depth in this work. In order to reduce the high frequency eddy current effect in sandwich core structure, section III initiates a discussion with adjustable core structures and winding arrangements such as closed core structure, hollow type structure and meander winding. The tradeoffs among them are presented. Accordingly, an ultra-thin coupled inductor is designed and employed in a 100-W high step-up dc-dc converter to demonstrate the design approach and theoretical analysis.**

***Index Terms*— integrated magnetics, ultra-thin, sandwich core structure, coupled inductor.**

I. INTRODUCTION

WITH an increasing worldwide interest in sustainable energy production and use, there is renewed focus on the power electronic converter interface for dc energy sources. Ultra-thin power converters with flexible PCB integrated magnetic components are highly demanded in future photovoltaic module integrated converter (PV-MIC) which are mounted behind the PV panel, resulting in a higher power density. Since the PV cell provides a low dc voltage, a high step-up dc-dc converter is required in order to interface with 400-V dc bus. Therefore, high voltage ratio elements like transformers and coupled inductors become necessary in the PV application. A high step-up boost converter with coupled inductors is chosen for this design as shown in Fig.1 where a low leakage inductance is required to minimize the switching loss of MOSFET. Hereby, magnetic components using ultra-thin integrated technology become a challenge in this work.

Due to the attractive advantage of low size, PCB integrated magnetics technology has been rapidly developed in recent years. In [1], a 4.7-μH PCB integrated inductor with dc current handling of up to 500-mA was designed and employed in a 1.5-W buck converter with overall 1.3-mm thickness. The embedded passive integrated circuit (emPIC) was discussed in [2] and a 60-W series resonant offline converter with integrated capacitors and an ultra thin, PCB integrated transformer was designed and manufactured with standard PCB manufacturing processes.

This paper highlights a design consideration for a 1.5-mm thickness integrated coupled inductor with sandwich core structure. Since the core plates are close together, the winding area acts as an airgap and thus lead to a non-uniform flux distribution, which is not considered in standard analytical approaches for the traditional magnetic structure. How self-inductance and leakage inductance relevant to the core geometry and the core material needs to be investigated. Eddy current significantly affects the winding loss at high frequency due to external flux penetrated to the conductors cause the current moving towards the edges of conductor. The traditional analytical approach for the core loss is not in valid due to a non-uniform flux distribution in the core plates. In order to reduce the high frequency eddy current effect in the sandwich core structure, Section III initiates a discussion with adjustable core structures and winding arrangements such as closed core structure, hollow type structure and meander winding. The tradeoffs among them are presented. Accordingly, an ultra-thin coupled inductor is designed in Section IV and employed in a 100-W high step-up dc-dc converter to demonstrate the design approach and theoretical analysis.

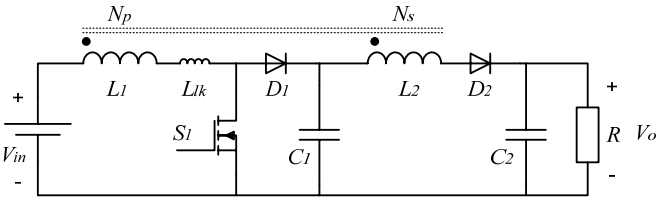

Fig. 1. High step-up boost dc-dc converter with coupled inductors.

II. DESIGN CONSIDERATION FOR SANDWICH MAGNETICS

A. Self- inductances and leakage inductance

In recent, coreless PCB transformers make attraction in some applications due to its inherent low profile property [3], [4]. However, it also exposes many drawbacks such as low inductance and significant EMI radiation issues. It is well known that the addition of magnetics core plates to either side of planar winding structures provides enhancement of inductance values, and reduction of EMI problem. Since the core plates are close together, the winding area acts as an airgap and thus as a high reluctance path for the magnetic flux. This leads to a non-uniform flux distribution, which is not considered in standard analytical approach. The cases of filament conductors (small width-to-height ratio) in non-conducting magnetic media have been treated in the past [5], [6], leading to inductance models by current images. The formulas presented in these papers may not

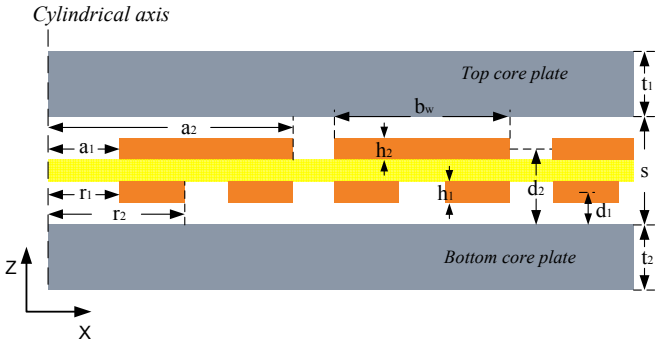

Fig. 2. Cross-section of the sandwich coupled inductor along 2-D RZ plane.

be well suited for the wide track (high width-to-height ratio) due to its non-uniform current density has not been considered. Hurley *et al.* [7], in an excellent work, presents a precise impedance formula with consideration of non-uniform current distribution and lossy magnetic media.

Fig.2 shows a cross-section of the sandwich coupled inductor along 2-D X-Z plane. For an N_p turns spiral primary winding, the total self-inductance of the primary winding is the summation of each mutual inductance pairs between two concentric winding tracks, M_{ij}, where both i and j are from 1 to N_p. The self-inductance of the primary winding is given by (1). The same approach to obtain the total self-inductance for N_s turns spiral secondary winding is given by (2).

$$L_p = \sum_{j=1}^{N_p} \sum_{i=1}^{N_p} M_{ij} \tag{1}$$

$$L_s = \sum_{j=1}^{N_s} \sum_{i=1}^{N_s} M_{ij} \tag{2}$$

The mutual-inductance is the sum of mutual magnetic coupling pairs between the primary and the secondary windings and thus it is given by (3),

$$M_{ps} = \sum_{j=1}^{N_s} \sum_{i=1}^{N_p} M_{ij} \tag{3}$$

In general, the terminal equations of a two-winding coupled inductor can be written,

$$\begin{bmatrix} v_p(t) \\ v_s(t) \end{bmatrix} = \begin{bmatrix} L_p & M_{ps} \\ M_{ps} & L_s \end{bmatrix} \cdot \begin{bmatrix} i_p(t) \\ i_s(t) \end{bmatrix} \tag{4}$$

The leakage inductance referred to the primary side is given by,

$$L_{lkp} = L_p - \sqrt{\frac{L_p}{L_s}} \cdot M_{ps} \tag{5}$$

Derivation of mutual inductance, M_{ij}, in planar sandwich structure has been reported by Hurly [7],

$$Z = \frac{j\omega \cdot \mu_0 \cdot \pi}{h_1 \cdot h_2 \cdot \ln(\frac{r_2}{r_1}) \cdot \ln(\frac{a_2}{a_1})} \int_0^{\infty} S(kr_2, kr_1) \cdot S(ka_2, ka_1) \cdot \left[f(\lambda) + g(\lambda) + e^{-2 \cdot k \cdot |d_2 - d_1|} \right] \cdot Q(kh_1, kh_2) \cdot dk \,. \tag{6}$$

where

$$S(kr_2, kr_1) = \frac{J_0(kr_2) - J_0(kr_1)}{k};$$

$$S(ka_2, ka_1) = \frac{J_0(ka_2) - J_0(ka_1)}{k};$$

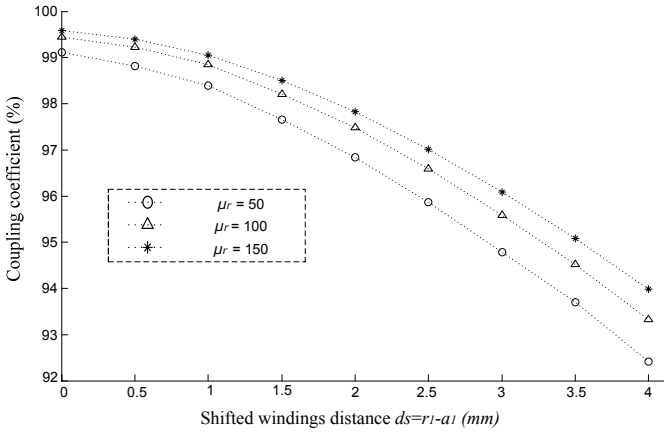

Fig. 3. FEA plotted function of coupling coefficient and shifted winding distance between the primary and the secondary.

$$f(\lambda) = \frac{\lambda(t_1) \cdot e^{-k(d_1 + d_2)} + \lambda(t_2) \cdot e^{-k(d'_1 + d'_2)}}{1 - \lambda(t_1) \cdot \lambda(t_2) \cdot e^{-2ks}};$$

$$g(\lambda) = \frac{2 \cdot \lambda(t_1) \cdot \lambda(t_2) \cdot e^{-2k \cdot s} \cdot \cosh\left[k \cdot (d_2 - d_1)\right]}{1 - \lambda(t_1) \cdot \lambda(t_2) \cdot e^{-2k \cdot s}};$$

$$\lambda(t) = \frac{\phi(k) \cdot (1 - e^{-2\eta t})}{1 - \phi^2(k) \cdot e^{-2\eta t}};$$

$$\phi(k) = \frac{\mu_r - \frac{\eta}{k}}{\mu_r + \frac{\eta}{k}};$$

$$\eta = \sqrt{k^2 + j \cdot w \cdot \mu_r \cdot \mu_0 \cdot \sigma};$$

$$Q(kh_1, kh_2) = \begin{cases} \frac{2}{k^2}(\cosh k\frac{h_1 + h_2}{2} - \cosh k\frac{h_1 - h_2}{2}), \\ \qquad when \quad z > \frac{h_1 + h_2}{2} \\ \frac{2}{k}(h - \frac{e^{-kh} - 1}{k}), \; when z = 0, h_1 - h_2 = h \end{cases};$$

ω	*angular frequency (rad/s)*
μ_0	*permeability of airgap;*
μ_r	*relative permeability of core plate;*
σ	*electrical conductivity of core plate;*
s	*core plates separation in sandwich structure;*
t	*core plate thickness;*
h_1, h_2	*coil thicknesses in axial direction;*
d_1, d_2	*distance of coil centers to core plate;*
d_1', d_2'	*s-d_1, s-d_2;*
r_1, r_2	*inter and outer radius of j^{th} circular track;*
a_1, a_2	*inter and outer radius of i^{th} circular track;*
$J_0(x)$	*first kind Bessel function of order zero;*

Equations (1) to (6) indicate that self-inductance and leakage inductance relevant to the geometry of sandwich structure including the winding thicknesses, the substrate separation, the winding width, the inner and outer radius of winding track and the distance of winding center to core plates. In addition, the number of turns and relative permeability of core material also strongly influence the inductive parameters. We have studied the FEA results for the self-inductance and leakage inductance of primary winding in the sandwich structure. The spiral winding used for this study has the following geometrical parameters: 5-turns for the primary winding and 25-turns for the secondary

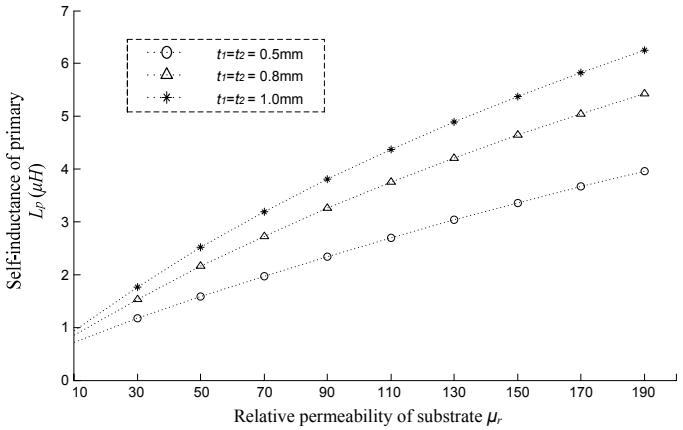

Fig. 4. FEA plotted function of self-inductance of primary and core permeability (<200).

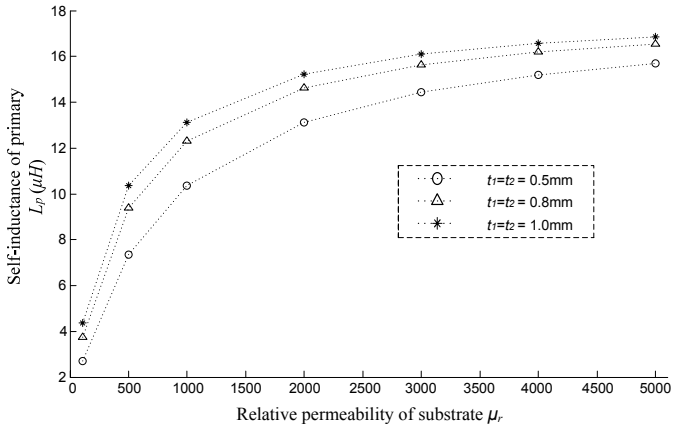

Fig. 5. FEA plotted function of self-inductance of primary and core permeability (>500).

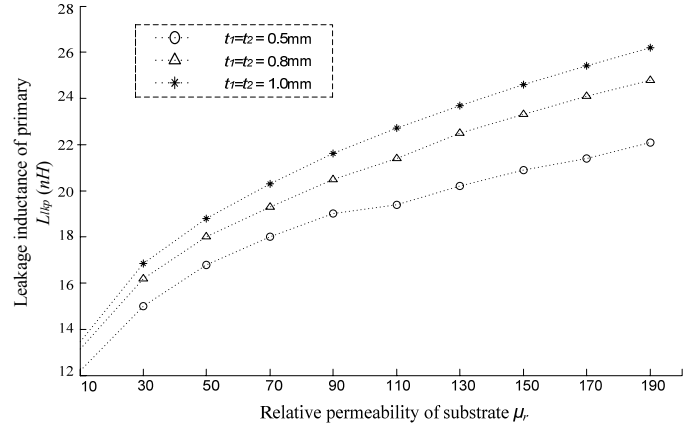

Fig. 6. FEA plotted function of leakage inductance of primary and core permeability.

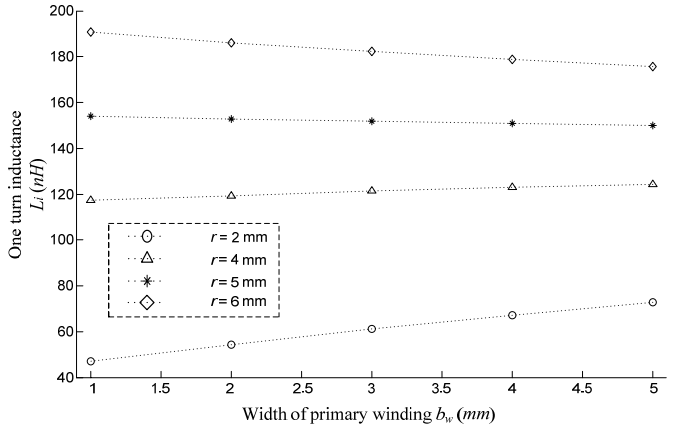

Fig. 7. FEA plotted function of one-turn inductance and winding width under different inner radius.

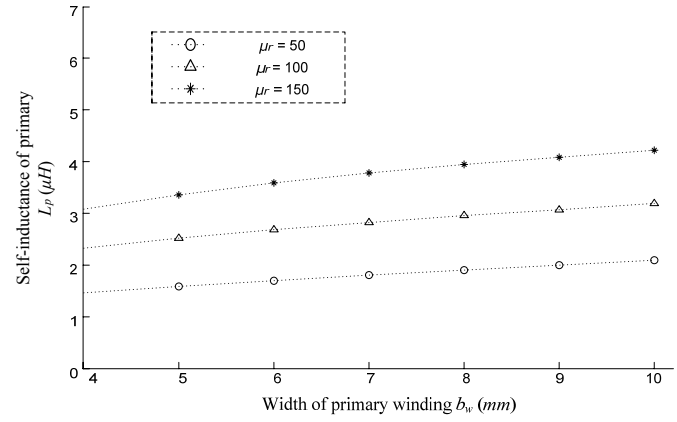

Fig. 8. FEA plotted function of self-inductance of primary and winding width under different core permeability.

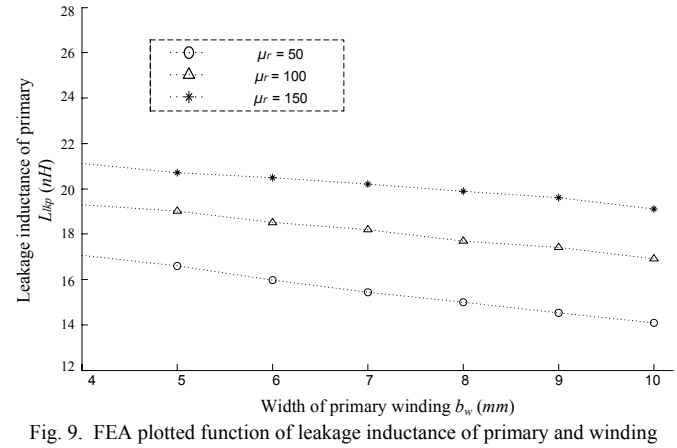

Fig. 9. FEA plotted function of leakage inductance of primary and winding width under different core permeability.

winding, both are with 2-oz copper thickness; the insulation thickness between the two windings is 0.1-mm; the clearance between each turn is 0.5-mm; the innermost radius is also 0.5-mm. Core plate separation s is used as gap length due to the sandwich structure which is kept 0.32-mm. Fig.3 shows a relationship between coupling coefficient and shifted windings distance d_s=r_1-a_1. In order to feature a lower leakage inductance, all secondary windings should be completely covered by the primary windings without any shift so that there is no portion of the secondary windings exposed to the clearance as shown in Fig.2. The width of each primary winding is 5-mm. Hereby, 0.6-mm track width is chosen for the secondary winding. In Fig.4 and Fig.5, self-inductance of the primary is plotted as a function of relative permeability μ_r of the core plates. Core plate thickness t is varied as a parameter. As seen from Fig.4, the increased permeability and thickness of magnetic plates can significantly enhance the value of self-inductance. The rate of change becomes smaller and smaller when the relative permeability μ_r is above 1000 as shown in Fig.5. It is noted that ferrite material with high permeability is very brittle and very difficult to manufacture for extremely thin (< 1 mm) core plate. This will be discussed in detailed in the section of core material. In Fig.6, the

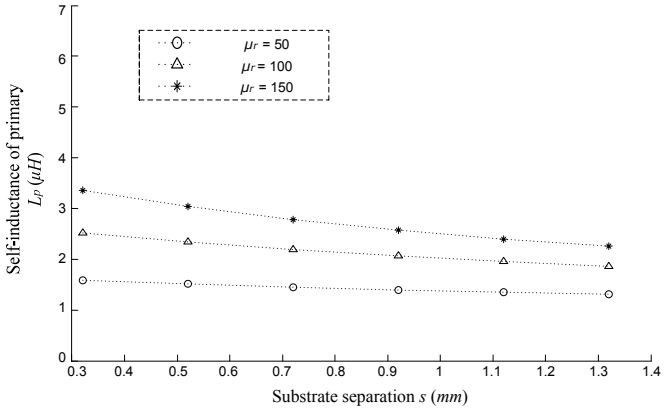

Fig. 10. FEA plotted function of self-inductance of primary and substrate separation under different core permeability.

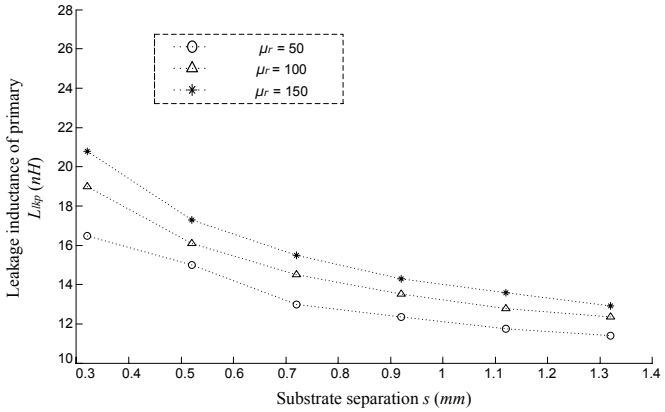

Fig. 11. FEA plotted function of leakage inductance of primary and substrate separation under different core permeability.

primary leakage inductance is plotted as a function of core permeability μ_r for different core plate thicknesses t. The leakage inductance L_{lkp} is increased with a higher permeability. However, the increased leakage inductance does not mean a worse coupling effect. In fact, a better coupling effect is performed when the high permeability is used because more flux concentration in the core plates instead of radiation to the air. Fig.7 plots a function of one turn inductance and the winding width b_w under different inner radius r. The relative permeability is set by 100 and the core plate thickness is 0.5-mm. The inductance can be enhanced by increasing the winding width when the inner radius r is small. The enhancement becomes slight when the inner radius r is increased. Up to 5-mm inner radius, there is almost no inductance enhancement whereas a reduction starts up. Therefore, it is not correct to simply describe that the inductance is proportional to the winding width or the inner radius. A reasonable relationship can be obtained in equation (6). For the spiral turns, a function of the primary self-inductance and the winding width is plotted in Fig.8 where the other parameters are the same as aforementioned. And its leakage inductances are plotted in Fig.9 where the relative permeability μ_r is used as varied. Apparently, wider tracks cause higher self-inductances and lower leakage inductances where a better coupling effect is performed. However, wider tracks cause a higher ac resistance at high frequency which will be presented in the next subsection. In addition, core plate separation s is used as gap length in this sandwich structure. Like the conventional transformers, the inductance is reduced with increased gap

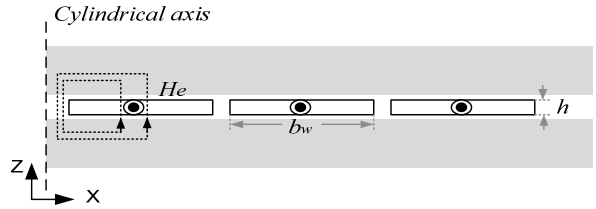

Fig. 12. External flux penetrated to the horizontal surface of conductors.

length. Fig.10 illustrates the planar sandwich structures feature the same behaviors as the conventional structures. And Fig.11 allows that a lower leakage inductance can be obtained when the core separation is high.

B. Eddy current effect

As frequency increases, the current density becomes non-uniform due to the formation of eddy currents. The eddy current effect occurs when a conductor is subjected to time-varying magnetic fields and is governed by Faraday's law. Eddy currents reduce the net current flow in the conductor and effectively decrease the cross-section of conductor, hence increase the ac resistance. The distribution of eddy currents depends on the geometry of the conductor and its orientation with respect to the impinging time-varying magnetic field. In the conventional transformer without airgap, ac resistance of the winding normally performs a low value due to no external flux affects its current distribution. The magnetic field generated by a layer or multilayer solenoid is neglected outside the region enclosed by the layers as it is small. The magnetic field inside the region has only a component in z direction and contributes skin effect loss and proximity effect loss which is usually calculated by Dowell equation [8] and its improved formations [9], [10]. The proximity effect loss, in a multilayer winding, may strongly dominate over the skin effect loss depending on the winding arrangement. The thickness of conductor h is usually chosen around the skin depth in order to minimize the eddy current effect. The inductor winding, however, shows a much higher ac resistance than the transformer winding due to the fringing flux effect caused by the airgap.

Regarding to the planar sandwich structure, the conductors between the two core plates form an airgap and all flux flow throughout the conductors. Since the gap is very thin along the vertical direction, H_e in the gap is approximated as purely z directed as shown in Fig.12. Since H_e is tangential to the left vertical edge of the innermost conductor, a current must flow toward to that edges in order to exclude the magnetic field from the inside of conductor. The cross-sectional area of its ac current distribution in the conductor is therefore proportional to δ^2 (δ is skin depth), so the effective resistance is much higher than dc resistance. Furthermore, large circulating currents in each turn crowd into these vertical edges cause a high dissipation as well [11]. Fig.13 shows a FEA simulation result for eddy current effect in the planar sandwich structure. When the relative permeability μ_r=50 is used for the core material, the ac resistance is 25 times than the dc resistance at 1-MHz frequency. With increased core permeability, this effect will be strongly activated. As seen in the result, the ratio of ac resistance to dc resistance reaches 65 at 1-MHz frequency when the relative permeability μ_r is 150. To obtain the power dissipated per square meter in the Y-Z plane, the following is given,

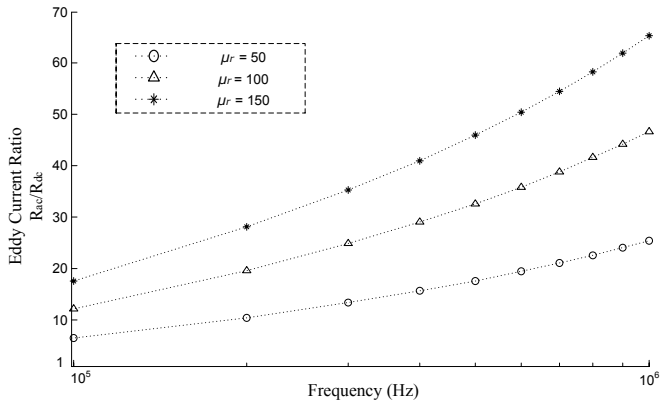

Fig. 13. FEA results of eddy current effect at 1-MHz for planar sandwich coupled inductor.

$$P(x) = \frac{1}{2 \cdot \sigma} \cdot \int_0^b J_y(x) \cdot J_y^*(x) \cdot dx \tag{7}$$

The current density $J_y(x)$ inside the conductor can be obtained by using FEA simulation. And then substitute the FEA results into (7) to get the power loss. On the other hand, the current density can be calculated based on Maxwell's equations, the followings are obtained,

$$J_y(x) = J_1 \cdot e^{kx} + J_2 \cdot e^{-kx} \tag{8}$$

$$H_z(x) = -\frac{\partial J_y / \partial x}{k^2} \tag{9}$$

The expressions for J_1 and J_2 can be obtained from $H_z(0)$, $H_z(b)$ and (9).

A reduction to ac resistance can be obtained by using a narrow winding foil. The width of winding close to the skin depth might be the best choice for the ac resistance, but a high dc resistance is compromised. Therefore, the choice of the winding width is very dependent on the application of power converters.

C. Material and core loss

In well-known, ferrite core features a lower core loss. However, ferrite is very brittle and difficult to implement an ultra sheet. Normally, the thickness of ferrite core is more than 1-mm. In order to avoid breaking, a highly flexible and shock resistant soft magnetic sheet material FPC (ferrite polymer compounds) consisting of ferrite powder in a polymer matrix is usually used. The relative permeability of FPC material is typically low and ranges from 10 to 20. In addition, it is not compatible to a PCB integration process as it performs a low resistivity and thus neighbored vias through this material need additional insulation, meanwhile its operating temperature is not well suitable for PCB lamination [3]. Further materials with different compounds are developed to increase the relative permeability and the resistivity like IRJ08 from TDK consisting of ferrite powder and resin. Another material class is high permeability iron foil like μ-metal, amorphous iron or nanocrystalline iron. These materials exhibit an extremely high permeability of μ_r > 10000 and a high saturation flux density of more than 1-T. Therefore, they can be used as ultra thin foils with thickness in the range of 20-μm to 100-μm. However, this kind of iron foil typically has higher core loss.

The most commonly used equation that characterizes core losses is the Steinmetz equation, a curve-fitting expression of measured data under sinusoidal excitation,

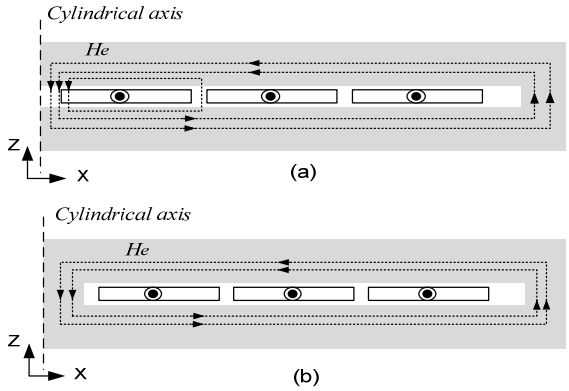

Fig. 14. Closed core structure (a) edge filled (b) fully closed.

$$P_v = k \cdot f^{\alpha} \cdot (\Delta B / 2)^{\beta} \tag{10}$$

where k, α, β are material parameters , ΔB is peak-to-peak flux density of a sinusoidal excitation with switching frequency f, P_v is time-average core loss per unit volume. Unfortunately, the Steinmetz equation is only valid for sinusoidal excitation. This is a significant drawback since in power electronics applications the core material is normally exposed to non-sinusoidal flux waveforms. Core loss due to non-sinusoidal waveforms can far exceed the loss due to sinusoidal waveforms, even if the frequencies and the peak-to-peak flux densities are identical [12]. In order to determine losses for a wider variety of waveforms, improved IGSE [13] are usually used.

$$P_v = \frac{1}{T} \int_0^T k_i \cdot \left| \frac{dB(t)}{dt} \right|^{\alpha} \cdot (\Delta B)^{\beta - \alpha} \cdot dt$$

$$k_i = \frac{k}{(2\pi)^{\alpha - 1} \cdot \int_0^{2\pi} \left| \cos\theta \right|^{\alpha} \cdot 2^{\beta - \alpha} \cdot d\theta} \tag{11}$$

Eq. (11) shows the IGSE expression where k, α and β are the same parameters used in the Steinmetz equation (10). The angle θ represents the phase angle of the sinusoidal waveform. Applying a piecewise linear model (PWL) to any waveform and then combining with the IGSE, leads to an easy-to-use expression for accurate calculation of losses with any flux waveform, without requiring extra characterization of material parameters beyond the parameters of the Steinmetz equation. However, since a non-uniform flux density is produced in the planar sandwich structure, the core loss therefore will be re-written as follows,

$$P_c = 4 \cdot t_1 \cdot b_c \cdot \frac{1}{T} \cdot \int_0^l \int_0^T k_i \cdot \left| \frac{dB(t,x)}{dt} \right|^{\alpha} \cdot (\Delta B)^{\beta - \alpha} \cdot dt \cdot dx \tag{12}$$

where t_1 represents the core plate thickness, b_c is the width of core plate and l is half length of the core plate.

III. Discussions

A. Closed core structure

A comparison between closed core structure and gapped core structure is presented in [1] and it is shown that closed core structure provides a higher inductance. This is due to the fact that the closed core structure rearranges the magnetic reluctance model which enables most of the flux to concentrate in the core plate and the windings are fully enclosed by the centralized flux. Fig.14 shows the examples of closed core structure with edge filled and fully closed. The edge filled is that only the edge of

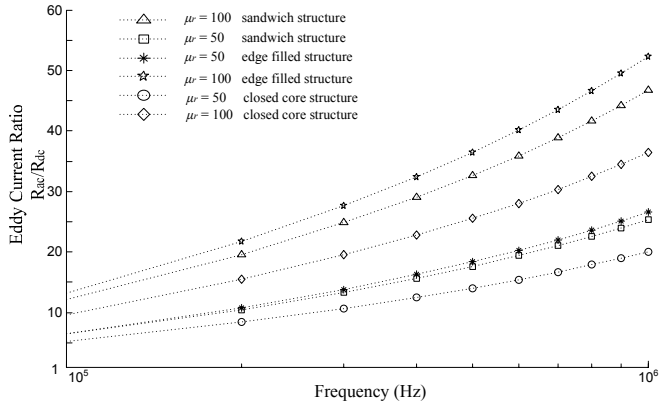

Fig. 15. A comparison of FEA results of eddy current effect at 1-MHz for different closed core structures.

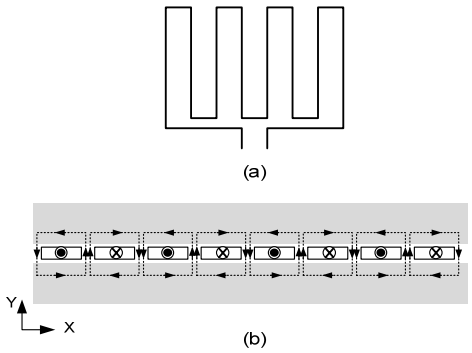

Fig. 16. (a) meander type winding (b) flux distribution in meander type winding with planar sandwich core structure.

core plate is filled by magnetic material and the fully closed is filled by magnetic material in both edge and center of the core plate. Both methods can improve the inductance value. However, there is significant difference in the eddy current effect for high frequency winding loss. The edge filled case makes the right vertical flux of closed path concentrate on the filled magnetic material. Therefore, more current flows toward to the left vertical edge of conductor and thus increase the ac resistance. For the fully closed case, most of vertical flux flow in both filled magnetic material rather than penetrating on the horizontal surface of conductors where a lower ac resistance can be obtained. Fig.15 shows a comparison of eddy current effect at 1-MHz for the different core structures. The fully closed core structure has a significant reduction on the ac resistance. However, the saturation problem has to be consideration when the fully closed core structure is used especially in the coupled inductor design due to dc energy needs to be stored.

B. Meander type winding

Meander type winding is shown in Fig.16. As seen in this figure, the direction of the flux changes alternately with the pitch of meander coil where the path of each flux is restricted. Thus, a lower inductance is provided compared to the spiral coil. However, a lower high frequency effect in the winding resistance is obtained for the meander type coil. A comparison between spiral type coil and meander type coil is shown in [14]. The further reduction to the eddy current effect is shown with special winding arrangements such as mesh coil [15] and helical winding structure.

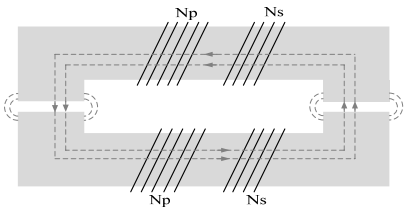

Fig. 17. Hollow type core structure.

C. Hollow type core

Due to a rectangle is cut out from the center of the core shown in Fig.17, "hollow type core" is therefore named. In fact, the hollow type core performs the same character with the traditional U-core. The flux generated by the windings flow in horizontal direction and vertical direction of the core which are called easy direction and hard direction respectively in [16]. This is due to the fact that a higher core loss dissipates in the hard direction and a lower core loss in easy direction. The hollow type winding has a lower fringing effect in ac resistance since the windings can be arranged far away to the airgaps. Therefore, the hollow type provides the lowest winding loss compared to the other ultra-thin structures. However, it is not easy to implement PCB winding tracks due to additional vias needs to be used. If the converters operate with a high current, there is insufficient space to arrange wider winding tracks side by side.

IV. EXPERIMENT

A 100-W high step-up boost dc-dc converter employed an ultra-thin sandwich coupled inductor with spiral windings is built to demonstrate the design approach and theoretical analysis. Input voltage is between 8-17 V, and output voltage is 400 V. The switching frequency is 1-MHz. The detailed experimental results will be included in the final paper.

V. CONCLUSION AND FUTURE WORK

Detailed design considerations of ultra-thin coupled inductor including self-inductance, leakage inductance, eddy current effect and core loss are presented. Several alternative core structures have been discussed to illuminate their advantages and disadvantages. A 100-W high step-up boost dc-dc converter with overall 1.5-mm thickness has been built and detailed experimental results will be included in the final paper.

REFERENCES

[1] M. Ludwig, M. Duffy, T. O'Donnell, P. McCloskey and S. C. Mathuna, "PCB integrated inductors for low power dc-dc converter," *IEEE Trans. on Power Electron.*, vol.18, no.4, pp.937–945, July.2003.

[2] E. Waffenschmidt, B. Ackermann and J. A. Ferreira, "Design method and material technologies for passives in printed circuit board embedded circuits," *IEEE Trans. on Power Electron.*, vol.20, no.3, pp.576–584, May, 2005.

[3] S. C. Tang, S. Y. Hui, and H. S. Chung, "Characterization of coreless printed circuit board (PCB) transformers," *IEEE Trans. on Power Electron.*, vol. 15, no. 6, pp.1257-1282, Nov. 2000.

[4] S. Y. Hui, H. S. Chung and S. C. Tang, "Coreless PCB-based transformers for power MOSFETs/IGBT's gate drive circuits," *IEEE Trans. on Power Electron.*, vol. 14, pp.422-430, May, 1999.

[5] W. A. Roshen, "Effect of finite thickness of magnetic substrate on planar inductors," *IEEE Trans. on Mag.*, vol.26, no.1, pp. 270-275, Jan. 1990.

[6] W. A. Roshen, "Analysis of planar sandwich inductors by current images," *IEEE Trans. on Mag.*, vol.26, no.5, pp. 2880-2887, Spet. 1990.

[7] W. G. Hurley and M. C. Duffy, "Calculation of self- and mutual impedances in planar sandwich inductors," *IEEE Trans. on Mag.*, vol. 33, no.3, pp.2282-2290, May. 1997.
[8] P. L. Dowell, "Effects of eddy currents in transformer windings," *Proc. Inst. Elect. Eng.*, vol. 113, no. 8, pp. 1387–1394, Aug. 1966.
[9] J. Vandelac and P. D. Ziogas, "A novel approach for minimizing high-frequency transformer copper losses," *IEEE Trans. on Power Electron.*, vol. 3, no.3, pp.266-277, July, 1988.
[10] J. Ferreira, "Improved analytical modeling of conductive losses in magnetic components," *IEEE Trans. on Power Electron.*, vol. 9, no. 1, pp. 127–131, Jan. 1994.
[11] A. F. Goldberg, J. G. Kassakian and M. F. Schlecht, "Issues related to 1-10 MHz transformer design," *IEEE Trans. on Power Electron.*, vol. 4, no. 1, pp. 113–123, Jan. 1989.
[12] I. Villar, U. Viscarret, I. E. Otadui and A. Rufer, "Global loss evaluation methods for nonsinusoidally fed medium-frequency power transformers," *IEEE Trans. Ind. Electron.*, vol. 56, no.10, pp.4132–4140, Oct. 2009.
[13] C. R. Sullivan, "Computationally efficient winding loss calculation with multiple windings, arbitrary waveforms, and two-dimensional or three-dimensional field geometry" *IEEE Trans. on Power Electron.* vol. 16, no.1, pp.142-150, 2001.
[14] K. Kawabe, H. Koyama and K. Shirae, "Planar inductor," *IEEE Trans. on Mag.*, vol. 20, no.5, pp.1804-1806, Sept. 1984.
[15] I. Sasada, T. Yamaguchi and K. Harada, "Methods for loss reduction in planar inductors," in *Proc. IEEE PESC*, pp. 1409–1415. July, 1992.
[16] C. Marxgut, J. Muhlethaler, F. Krismer and J. W. Kolar, "Multi-objective optimization of ultra-flat magnetic components with a PCB-integrated core," in *Proc. IEEE ICPE & ECCE*, pp. 460–467. 2011.

Appendix B.9

[B.9] Z. Ouyang, Z. Zhang, M. A. E. Andersen and O. C. Thomsen, "Four quadrants integrated transformers for dual-input isolated dc-dc converters," *IEEE Transactions on Power Electronics Letter*, 2011. (Accepted, TPEL-Letter-2011-10-0082)

Four Quadrants Integrated Transformers for Dual-input Isolated DC-DC Converters

Ziwei Ouyang, Zhe Zhang, Michael A. E. Andersen and Ole C. Thomsen, *IEEE members*

Electrical Engineering Department, Technical University of Denmark, Kgs. Lyngby, Denmark

***Abstract*—A common limitation of some known multiple-input dc-dc converters has been addressed in the literatures. In order to overcome this limitation, a new concept for decoupling the primary windings in the integrated multiple-winding transformers based on 3-dimensional (3D) space orthogonal flux is proposed in this letter. And thus a new geometry core and relative winding arrangements are proposed in accordance with the orthogonal flux decoupling technology. Due to the four secondary windings are arranged in a quadratic pattern at the base core plate with the two perpendicular primary windings, a name of "four quadrants integrated transformers" (FQIT) is therefore given to the proposed construction. Since the two primary windings are uncoupled, the FQIT allows the two input power stages to transfer the energy into the output load simultaneously or at any time-multiplexing scheme, which can optimize the utilization of input sources, simplify the system structure and reduce the overall cost, so they are attractive for the hybrid renewable power system. Section III initiates a discussion for the advantages of the FQIT. In order to verify the feasibility of the FQIT in multiple-input converter, a dual-input isolated boost dc-dc converter with the FQIT is designed and tested. The results have excellently demonstrated that the two input power stages can be operated independently and the correctness of all the analysis in the letter.**

***Index Terms*— decoupling, dc-dc, integrated transformer, multiple-input converter (MIC), phase shift.**

I. Introduction

MULTIPLE-INPUT converters (MICs) have been proposed as a cost-effective and flexible way to interface various sources such as solar array, wind turbine, fuel cell, and commercial ac line, to get a regulated output voltage, and in some cases, energy-storage devices, with a load [1-4]. A common limitation of some known MICs is that only one input power source is allowed to transfer the power energy to the output at a time to prevent power coupling effect. Recently, in order to overcome this limitation, it has been proposed to use multiple-winding transformers based on flux additivity technology with phase-shifted PWM control [5]. This technology can transfer power from two or multiple different input voltage sources to the output load simultaneously meanwhile reverse blocking diodes are required at the input power stage sides. The reverse blocking diodes are needed to prevent a reverse power flow from one of the input voltage sources to another input voltage source through the coupled primary sides of the transformer as well as body diodes of semiconductor switches of the input power stages. Without these reverse blocking diodes, different input sources coupled to the multiple-input power converter cannot deliver power to the load simultaneously. Furthermore, this technology cannot be applied in the buck type isolated MICs unless the input voltages are strictly limited according to the turns ratio of multiple primary windings. Otherwise, an undesirable voltage difference stresses on one of the input power stages, causing an extremely high current on the semiconductors and thus damages the circuit. In addition, some other prior art approaches nowadays to overcome this limitation result in a large number of power switches and complicated control schemes [6], [7].

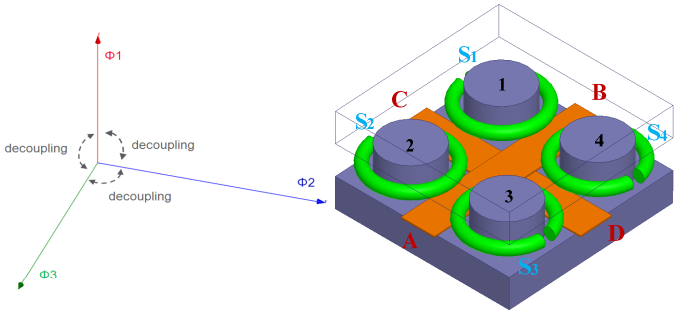

(a) (b)

Fig.1. (a) 3D space orthogonal flux decoupling; (b) proposed integrated transformer with four quadrants structure.

The main reason for the problem in the MICs is the multiple primary windings are coupled. Consequently, it would be advantages to provide an integrated transformer with uncoupled primary windings for use in the MICs to allow multiple input power sources to be operated independently without compromising any functions of the power converter or required complex control or protection circuitry to be added to the input power stages. However, current decoupling approaches applied to traditional core geometries such as E-I or E-E rely on a shared lower reluctance path or flux cancellation mechanisms that have been mentioned before. In practical, both approaches applied to the traditional cores will cause lower magnetizing inductances, higher winding loss and EMI problem [8], [9], [10]. Hereby, this letter proposes a new flux decoupling concept for the multiple-winding transformers used in the MICs. As shown in Fig. 1-(a), the new flux decoupling concept is based on 3-dimensional (3D) space orthogonal flux decoupling wherein the three flux paths extend substantially orthogonally to each other within the shared magnetically permeable core. This requires a sort of non-traditional core geometries to carry out the orthogonal flux paths, shown in Fig. 1-(b). Since this letter focuses on a new idea and its specific contributions rather than a detailed circuit analysis for its applicable topologies, the construction of this letter is accordingly organized as follows: Section II briefly presents the principle of the proposed integrated transformer for use in the MICs. Section III initiates a discussion of the advantages of the proposed transformer. In order to verify the feasibility of the proposed transformer and the correctness of its analysis, an experimental

Manuscript submitted 2th Oct. 2011. This work has been filed as EU&US patent and is supported by Flux A/S.
The corresponding author Ziwei Ouyang, Ph.D student, is with the Department of Electrical Engineering, Technical University of Denmark, 2800 Kongens Lyngby, Denmark (e-mail: zo@elektro.dtu.dk).

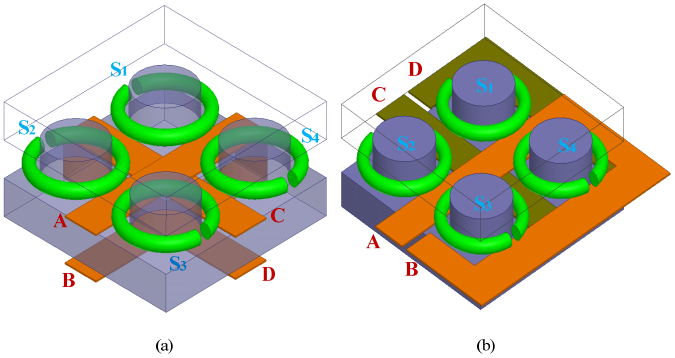

Fig.2. Alternative arrangements for plurality turns of primary windings.

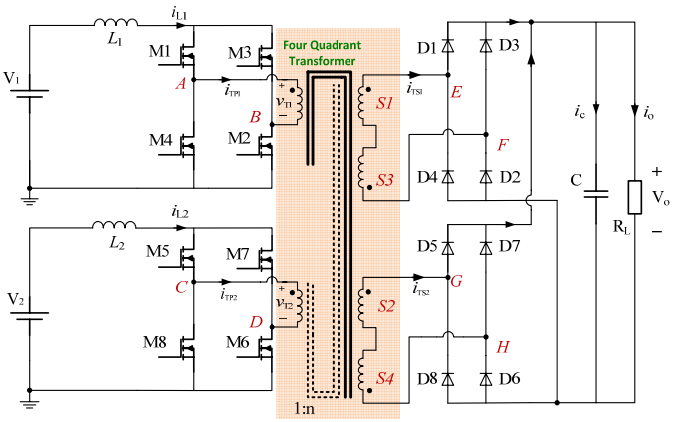

Fig.3. Dual-input isolated boost dc-dc converter with four quadrant integrated transformer.

dual-input isolated boost dc-dc converter employed with the proposed integrated transformer has been built. The experimental results are shown in Section IV.

II. Operational Principle of Four Quadrants Integrated Transformer

As shown in Fig. 1-(b), the magnetically permeable core comprises of a base rectangular core plate with four legs situated at respective corners, and a top rectangular core plates. In order to clearly illustrate the winding arrangements, a transparent top core plate is drawn in Fig. 1-(b). The first primary winding *AB* and the second primary winding *CD* are orthogonally arranged as a cross-shaped layout in-between the four legs. The flux generated from winding *AB* is substantially orthogonal to the flux generated from winding *CD* in the base and top core plates, and thus the uncoupled primary windings are constructed. The four legs provide a shared magnetic flux path to the two primary windings where the four secondary windings, S_1, S_2, S_3 and S_4, are wound in each respectively. Therefore, the two primary windings are both coupled with the four secondary windings. A name of "four quadrants integrated transformer" (FQIT) is given to the proposed integrated transformer since the four legs with enclosed secondary windings are arranged in a quadratic pattern at the base core plate with the two perpendicular primary windings. The plurality turns of primary windings can be arranged as shown in Fig. 2 (a) and (b).

This transformer can be used in many different topologies employing the multiple-winding transformers. In order to describe a basic principle of the FQIT, a dual-input isolated boost dc-dc converter is given in Fig. 3 as an example. In the secondary side, the windings wound in the diagonal legs, $S_1$and S_3, S_2 and S_4

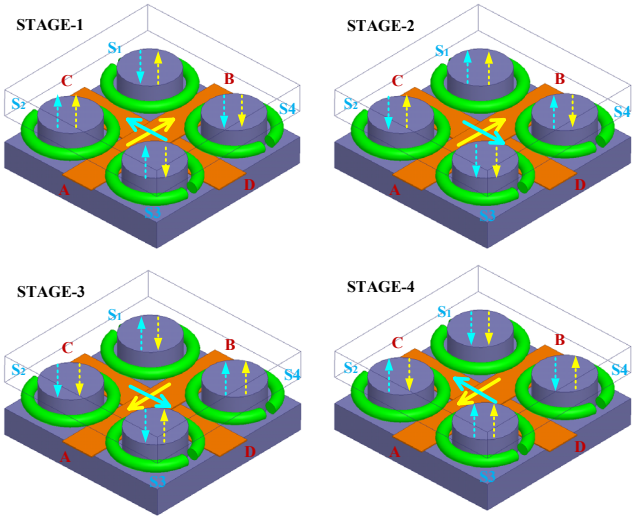

Fig.4. Four stages of flux directions through the legs.

are connected in series with a reverse coupled winding direction. The respective series-wound are electrically coupled to their individual rectifiers and then in parallel connected to the output load.

The direction and amplitude of the magnetic fluxes in the legs are dependent of the magnetizing currents of the primary windings. Accordingly, the four stages of the magnetic fluxes through the legs in accordance with the magnetizing current states have been depicted in Fig. 4. The directions for the magnetizing currents of the primary windings, i_{T1} and i_{T2}, are indicated by solid arrows. The corresponding magnetic fluxes through the four legs induced by the two currents are indicated by the dash arrows respectively. Due to the full-bridge boost converter, the duty cycle must be operated above 50% to ensure switch overlap and thus a continuous current path for the boost inductor current. Accordingly, typical primary voltage waveforms V_{T1} and V_{T2} with zero voltage platforms are produced as depicted in Fig. 5 and a 75% duty cycle is given as an example.

1) *STAGE-1 (t_0—t_1)* the magnetizing current, i_{T1}, is positive and the magnetizing current, i_{T2}, is negative. This currents state is characterized by the indicated direction shown in Fig. 4-(a). Using the right hand rule, the current i_{T1} leads to the magnetic fluxes in the leg 1 and leg 2 flowing along the same direction indicated by the yellow dash arrows. This is a consequence of the leg 1 and the leg 2 being arranged on the same side of the primary winding *AB*. Furthermore, the current i_{T1} also leads to the magnetic fluxes in the leg 3 and leg 4 flowing along the same direction. The magnetic fluxes induced by the current i_{T1} leads to oppositely directed fluxes in the leg 1 and leg 2 relative to the leg 3 and leg 4 which is a consequence of the geometry of the closed magnetic flux loop. Likewise, the current i_{T2} leads to the same flux directions in the leg 1 and leg 4 indicated by the blue dash arrows. The opposite flux direction relative to the flux direction in the leg 1 and leg 4 are induced in the leg 2 and leg 3 by the current i_{T2}. Hereby, a flux cancellation can be observed in the leg 1 and leg 3, meanwhile an overlapped flux occurs in the leg 2 and leg 4.

2) *STAGE-2 (t_1—t_2)* the magnetizing currents, i_{T1} and i_{T2}, are both positive. This currents state is characterized by the indicated direction shown in Fig. 4-(b). The magnetic fluxes induced by the current i_{T1} through all four legs keep the same directions with those produced in the stage-1 since the direction of the current i_{T1} is not changed. However, as the direction of the current i_{T2} is

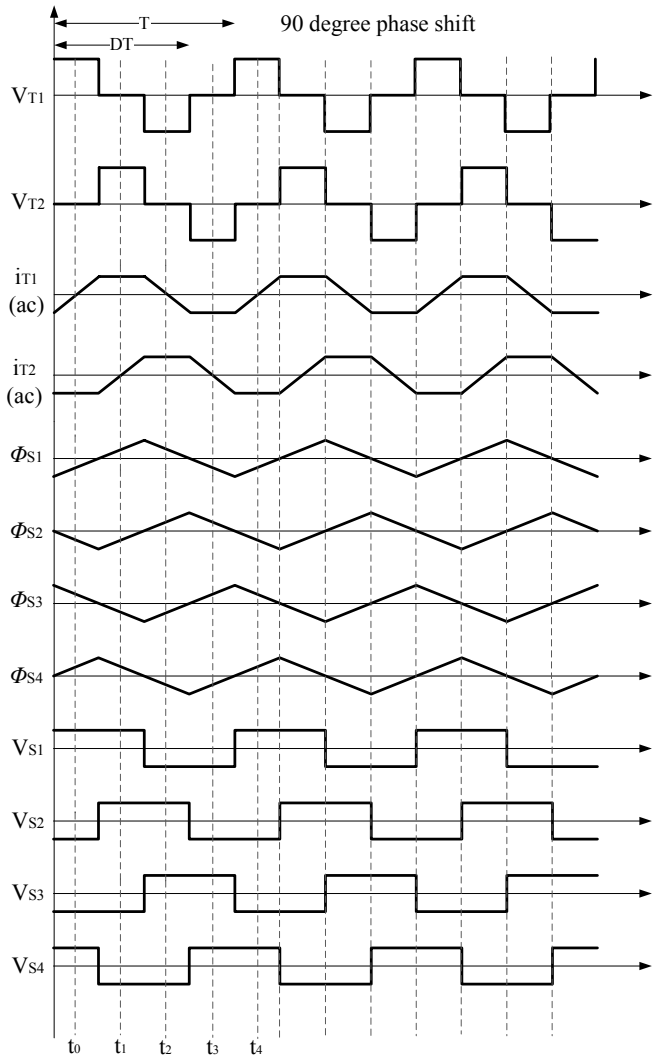

Fig.5. Timing diagram and basic waveforms for the four quadrants integrated transformer.

changed, the directions of the induced magnetic fluxes indicated by the blue dash arrows are accordingly changed. Hereby, a flux cancellation can be observed in the leg 2 and leg 4, meanwhile an overlapped flux occurs in the leg 1 and leg 3.

3) STAGE 3 (t_2—t_3) the magnetizing current, i_{T1}, becomes negative and the magnetizing current, i_{T2}, still keeps positive. This currents state is characterized by the indicated direction shown in Fig. 4-(c). All magnetic fluxes induced by the currents i_{T1} and i_{T2} are reversed relative to those induced in the stage-1.

4) STAGE 4 (t_3—t_4) the magnetizing currents, i_{T1} and i_{T2}, are both negative. This currents state is characterized by the indicated direction shown in Fig. 4-(d). All magnetic fluxes induced by the currents i_{T1} and i_{T2} are reversed relative to those induced in the stage-2.

Overall, a cancelled flux and an overlapped flux can be always observed in the each pair of diagonal legs respectively. Since there is a 90˚ degree between the two excitation currents and 75% duty cycle, the triangular flux waveforms through each leg can be plotted in Fig. 5 where Φ_{S1}, Φ_{S2}, Φ_{S3} and Φ_{S4} represent the overall flux through each secondary winding S_1, S_2, S_3 and S_4 respectively. This implies that square voltages with 50% duty cycle are produced in each secondary winding as symbols V_{S1}, V_{S2}, V_{S3} and V_{S4} in Fig. 5.

For the different phase shift angle between the two input power stages, the induced voltage waveforms on each secondary winding can be obtained by using the aforementioned analytical approach. As shown in Fig.6, not only the shapes but also the amplitudes of the voltages are changed. The maximum output voltage for the dual-input isolated boost dc-dc converter is achieved in the cases of 0˚ and 180˚ phase shift. The minimum voltage is obtained in the case of 90˚ phase shift and the case of 45˚ phase shift causes an output voltage in between. In fact, this characteristic of the flux cancellation and adding in each pair of diagonal legs effectively changes turns ratio of the transformer. Accordingly, the output voltage can be controlled by the phase shift angle. The function of voltage gain in the converter cannot simply described by the duty cycle and turns ratio since the phase shift angle has to be considered. The detailed function relationship of voltage gain specified to this converter will be analyzed in the future continued publication.

III. Discussion of Advantages

A. Independent operation

Since the two primary windings *AB* and *CD* are uncoupled, the two input power stages have the common ground and can be operated independently where the two input power sources are allowed to transfer the energy into the output simultaneously or at any time-multiplexing scheme. Meanwhile, the two power stages can be operated in different input voltage levels due to its independent operation. These advantages enable an operational reliability for the dual-input converter when any faults occur in one of the input power stages. Furthermore, the FQIT can be applied in any type of topologies associated with multiple inputs. Currently, these features cannot be implemented efficiently by using the traditional multiple-winding transformers with the flux additive.

B. Cost-effective, low size and high efficiency

Unlike a conventional multiple-input converter, the FQIT features minimized number of magnetic components without adding extra auxiliary circuit and switches. Hereby, this is a cost-effective way to implement the dual-input converter. Certainly, a lower size for the converter can be obtained as well. Furthermore, the flux cancellation occurring in the magnetic core may cause a lower core loss compared to the solutions with the discrete magnetic components, and thus a higher efficiency may be achieved.

C. Wide range input/output voltages

The output voltage is not only controlled by the duty cycle of PWM signal but also controlled by the phase shift angle between the two input power stages. If a combination of duty cycle control and phase shift control is used in the dual-input converter, a wider range of input or output voltages accordingly can be achieved.

D. Waveforms characteristics

50% duty cycle square waveforms without zero voltage platforms are induced on each secondary winding when the phase shift angle is 90°. Ideally, zero voltage ripple can be achieved in the load without any output capacitor. In addition, the current stress on the semiconductors of secondary side can be significantly reduced since the multi-level voltage waveforms are induced when the phase shift angle is 45°.

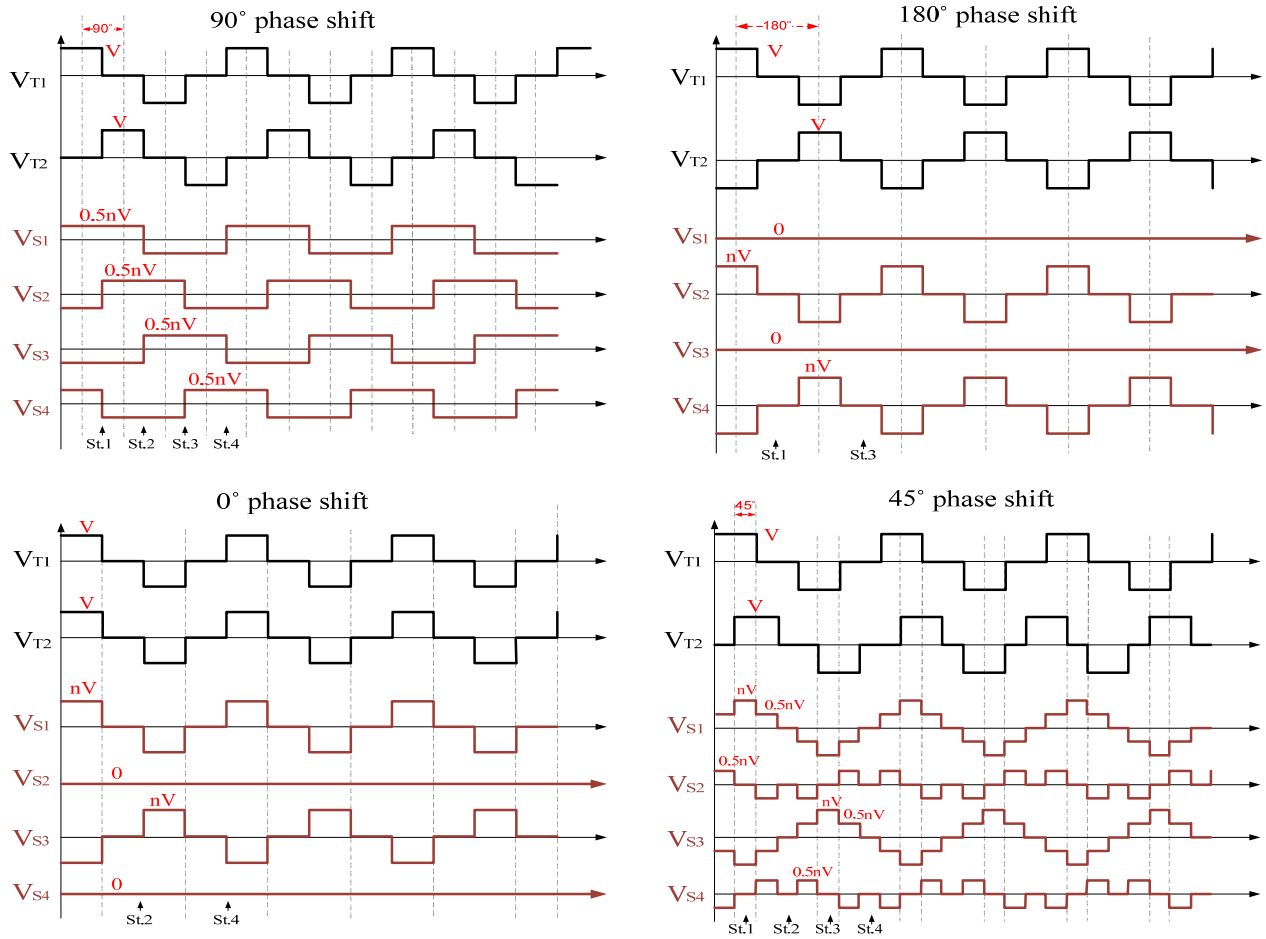

Fig.6. Induced secondary voltages in each leg for different phase shift angles between two input power stages.

The different output voltage waveforms are induced in the secondary windings as the different phase shift angle between the two input power stages, which may extensively derive some improved configurations for specific application.

IV. Experimental Verification

In order to verify the correctness of the above analysis, a proof-concept experimental prototype with the proposed FQIT has been built. Fig. 7 shows the photo of the experimental prototype and the dimension of the employed FQIT is shown in Fig. 8. Mn-Zn ferrite is used as the material of magnetically permeable core. For simplification, one turn copper foil is used in the both primary sides and four turns are used in each secondary winding which are implemented by the PCB winding. The switching frequency is operated at 100-kHz. The experimental results have excellently demonstrated that the two input power stages can be operated independently. Two terminal voltages of the primary windings, V_{AB} and V_{CD} (CH3&CH4), and two terminal voltages of the series-secondary windings, V_{EF} and V_{GH} (CH1&CH2), are presented in Fig. 9. The two input dc voltages are both 12.5-V and the duty cycle are kept 75%. The output voltage can be adjusted by shifting the phase angle between the two power stages. Maximum 200-V output voltage is obtained when the phase angle is 0˚ or 180˚. Minimum 100-V output voltage is obtained when the phase angle is 90˚, and around 141-V output voltage is obtained when the phase angle is 45˚. As seen in these plots, the experiment results have demonstrated the correctness of the analysis in Section II.

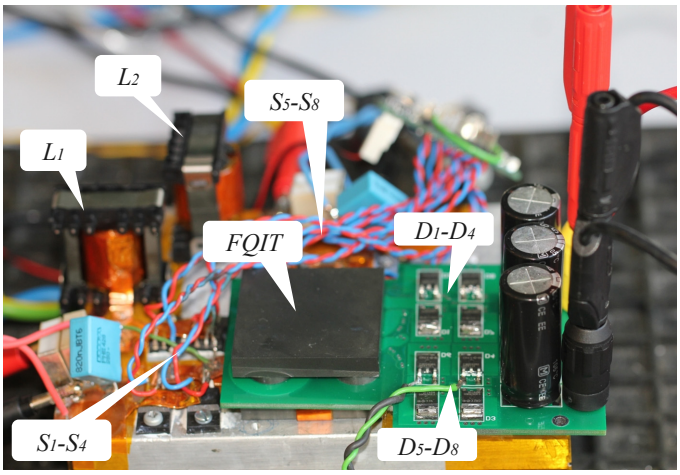

Fig.7. Photo of experimental prototype with the FQIT.

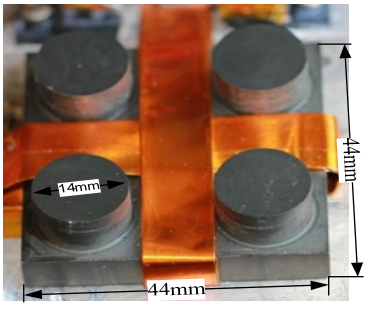

Fig.8. Dimension of the FQIT.

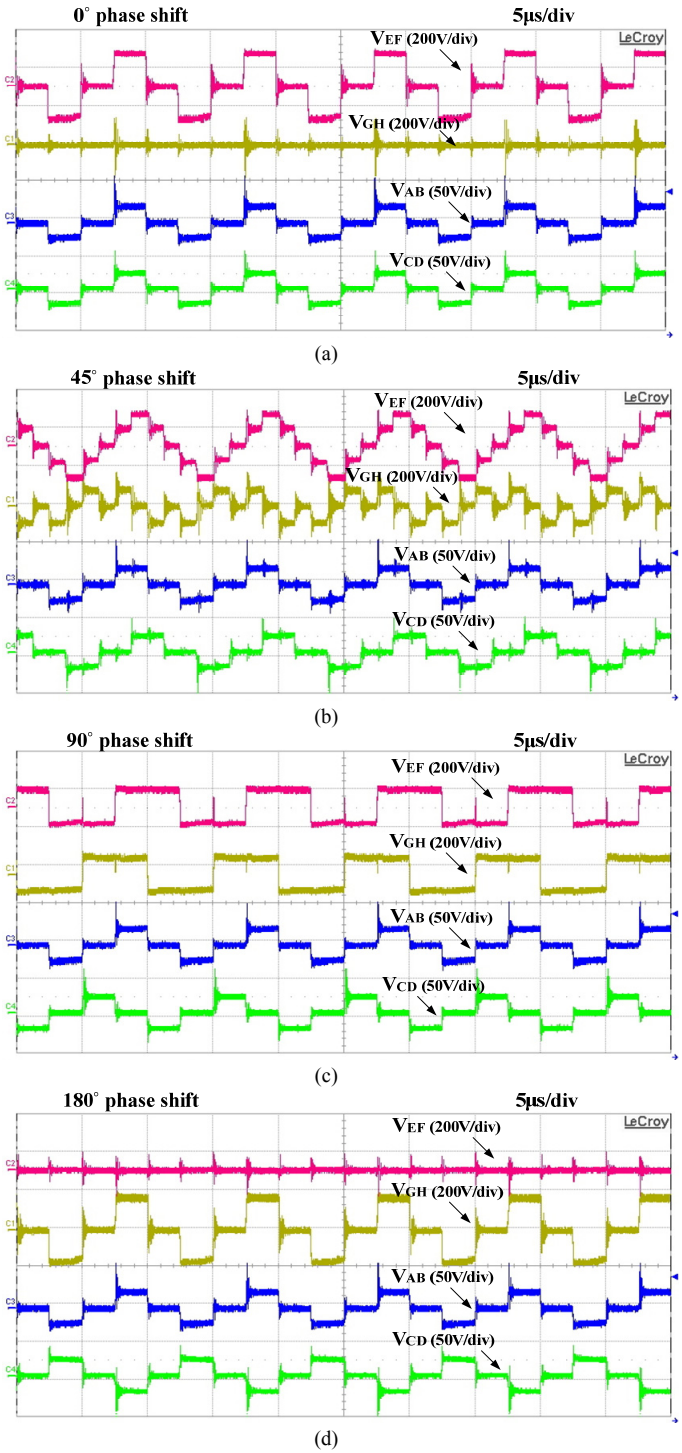

Fig.9. Experimental waveforms for different phase shift angles.

V. Conclusion

This letter proposes a new concept for decoupling the primary windings in the integrated multiple-winding transformers based on 3-dimensional (3D) space orthogonal flux decoupling. Only 2D orthogonal flux path is utilized in the proposed four quadrants integrated transformer and an applicable geometry of 3D orthogonal flux decoupling can be found in [11]. The proposed FQIT allows the two input power stages to transfer the energy into the output simultaneously or at any time-multiplexing scheme. This enables a solution to the limitation of the traditional multiple-input converters. Many advantages of the FQIT such as cost-effective, low size and high efficiency have been discussed. In addition, wider range input/output voltages may be achieved since the phase shift between the two input power stages can be used to control the output voltage. This letter gives an applicable example of isolated boost dc-dc converter for the proposed FQIT. From the authors' points of view, the interesting waveforms induced on the secondary windings with the phase shift control may arouse some improved topologies development for specific application in future works.

References

[1] Y-C. Liu, Y-M. Chen, "A systematic approach to synthesizing multi-input dc–dc converters," *IEEE Trans. on Power Electron.*, vol.24, no.1, pp.116-127, Jan. 2009

[2] K. Kobayashi, H. Matsuo, and Y. Sekine, "Novel solar-cell power supply system using a multiple-input DC–DC converter," *IEEE Trans. on Ind. Electron.*, vol. 53, no. 1, pp. 281–286, Feb. 2006.

[3] H. Matsuo, T. Shigemizu, F. Kurokawa, N. Watanabe, "Characteristics of the multiple-input dc-dc converter," *IEEE Trans. on Ind. Electron.*, vol.51, no.3, pp. 625- 631, June 2004

[4] K. P. Yalamanchili, M. Ferdowsi, "Review of multiple input dc-dc converters for electric and hybrid vehicles," in *Proc. IEEE Vehicle Power and Propulsion Conference*, pp. 160- 163, 7-9 Sept. 2005

[5] Y-M. Chen, Y-C. Liu and F-Y. Wu, "Multi-input dc/dc converter based on the multiwinding transformer for renewable energy applications" *IEEE Transactions on Ind. Appl.*, vol.38, no.4, pp. 1096- 1104, July 2002.

[6] J. Ruan, F. Liu, X. Ruan, D. Yang, Y. Li and K. Jin, "Isolated multiple-input dc/dc converter using alternative pulsating source as building cells," in *Proc. IEEE IPEC,* pp.1463-1470, 2010.

[7] H-J. Chiu, H-M. Huang, L-W. Lin and M-H. Tseng, "A multiple-input dc/dc converter for renewable energy systems," in *Proc. IEEE ICIT*, pp.1304-1308, Dec. 2005.

[8] S.S. Ochi and E.H. Wittenbreder, "Integrated multi-transformer" US patent, US20090230776A1.

[9] L. Yan, D. Qu and L. B, "Integrated magnetic full wave converter with flexible output inductor," *IEEE Trans. on Power Electron.,* vol.18, no.2, pp. 670- 678, Mar 2003.

[10] D. Cheng, L-P. Wong, and Y-S. Lee, "Design, modeling, and analysis of integrated magnetics for power converters," in *Proc. IEEE PESC*, pp:320-325, 2000.

[11] Z. Ouyang, M. A. E. Andersen and Z. Zhang, "Four quadrants transformers" US&EU patent, 2011, P1099US00 (pending).

Appendix B.10

[B.10] K. L.-Poulsen, Z. Ouyang and G. Sen, “An isolated boost flyback power converter,” *EU & US Patent*, US application no. 61505205, and EU application no. EP11172997.6, 2011 (pending).

NIXON PEABODY LLP
Customer No. 70001

PATENT
059244-5PL01

U.S. PROVISIONAL PATENT APPLICATION

FOR

AN ISOLATED BOOST FLYBACK POWER CONVERTER

BY

KRISTIAN LINDBERG-POULSEN

ZIWEI OUYANG

AND

GÖKAN SEN

AN ISOLATED BOOST FLYBACK POWER CONVERTER

COPYRIGHT

FIELD OF THE PRESENT DISCLOSURE

[0002] The present invention relates to an isolated boost power converter comprising a boost inductor being wound around a first leg of a magnetically permeable multi-legged core. The boost inductor is electrically coupled between an input terminal of the boost converter and a transistor driver to be alternatingly charged and discharged with magnetic energy. A first and second series connected secondary transformer windings with a center-tap arranged in-between are wound around separate legs of the magnetically permeable multi-legged core. In a first discharge state, the magnetic energy of the boost inductor is discharged by directing a discharge current from the boost inductor through a primary transformer winding and in a second discharge state, the magnetic energy of the boost inductor is discharged by discharging a magnetic flux through the first and second secondary transformer windings. In this manner, the secondary transformer windings can replace the traditional separate flyback winding used for start-up purposes of isolated boost power converters.

BACKGROUND

[0003] Isolated boost power converters are generally accepted as a highly efficient converter topology or architecture for high power converters with low input voltage and high output voltage. Isolated boost power converters are very useful for DC-DC voltage conversion in a diverse range of applications such as fuel cell converters, electric vehicles applications and avionic applications. However, a disadvantage of prior art isolated boost power converters is the need for a so-called flyback winding during a start-up phase or state of the power converter. During start-up, a duty cycle of a Pulse Width Modulated (PWM) control signal applied to a driver circuit must be ramped-up slowly to avoid excessive in-rush currents. During ramp-up of

the duty cycle, it starts at a value much less than 0.5 which means that the driver circuit is placed in an open or cut-off state during a cycle of the PWM control signal without any low impedance path to a positive or negative input voltage terminal or rail. This situation leads to excessive voltage spikes across the boost inductor(s) which spikes may exceed the rated break-down voltage of semiconductor devices, such as MOS transistors, of the driver circuit so as to destroy these. This problem has previously been addressed by adding a flyback winding and a flyback diode to the isolated power converter providing a discharge path for energy stored in the boost inductor. However, the addition of a flyback winding has numerous drawbacks as the flyback winding is a separate power transferring element that is relatively costly, adds to size and increases component count of the boost power converter.

SUMMARY

[0004] A first aspect of the invention relates to an isolated boost power converter comprising a magnetically permeable multi-legged core. An input terminal is adapted for receipt of an input voltage, V_{in}. A boost inductor is wound around a first leg of the magnetically permeable multi-legged core where the boost inductor is electrically coupled between the input terminal and a driver to be alternatingly charged and discharged with magnetic energy. The driver has a driver output coupled to a primary transformer winding wound around a second leg of the magnetically permeable transformer core and the driver is configured to generate a primary voltage to the primary transformer winding in accordance with a driver control signal. First and second series connected secondary transformer windings with a center-tap arranged in-between are wound around separate legs of the magnetically permeable multi-legged core and a rectification circuit is coupled to respective outputs of the first and second secondary transformer windings to provide a rectified converter output voltage, V_{out}. In a first discharge state, the magnetic energy stored in the boost inductor is discharged by directing a discharge current from the boost inductor through the primary transformer winding. In a second discharge state, the magnetic energy stored in the boost inductor is discharged by discharging a magnetic flux through the first and second secondary transformer windings.

[0005] The ability provided by the present isolated boost power converter to discharge magnetic energy stored in the boost inductor through the first and second secondary transformer windings provides a novel solution to start-up of isolated boost power converters/DC-DC

converters allowing these to operate below 50% duty cycle, D, of a Pulse Width Modulated (PWM) driver control signal. Consequently, the output voltage range at V_{out} can be extended down to zero without use of the traditional separate flyback winding as the first and second secondary transformer windings provide the functionality of the separate flyback winding of prior art boost power converters. The omission of the traditional separate flyback winding leads to a significant simplification of electric and magnetic circuit design, reduces component count, improves reliability, reduces the price and size of the power converter and decreases manufacturing costs. Furthermore, power conversion efficiency during start-up, and generally operation below 50% duty cycle of the PWM driver control signal, is improved without affecting normal boost operation because copper material is not wasted on the traditional flyback winding. It is also noticeable that secondary transformer winding normally is designed for low winding resistance such that the flyback winding functionality requires no modification of an existing secondary transformer winding. The normal low resistance of existing secondary transformer windings also means that its use as flyback winding in accordance with the present invention can increase power efficiency compared with the traditional separate flyback winding. Furthermore, the second discharge state also allows stored magnetic energy in the boost inductor to be discharged or dissipated during error states of the isolated boost converter which e.g. may arise in case of switching errors in the driver or an output short circuit condition.

[0006] The skilled person will understand that the term “isolated” does not imply that the input and output sides of the present isolated boost power converter necessarily are galvanically isolated by the magnetically permeable multi-legged core even though they may be so in some embodiments of the invention. Respective negative terminals or rails of the rectified output voltage V_{out} and the input voltage V_{in} may be electrically coupled to each other, for example through a shared GND connection such that a galvanic connection is established between the input/primary and output/secondary sides of the isolated boost power converter.

[0007] According to a preferred embodiment, during the second discharge state the first and second secondary transformer windings are coupled in parallel from the center-tap arranged between first and second series connected secondary transformer windings to the rectified converter output voltage, V_{out}. This allows discharge current to be directed to the rectified converter output voltage by both half-windings so as to minimize conductive losses in the

secondary transformer winding. The magnetic flux flowing through the first and second secondary transformer windings, generated by the magnetic energy stored in the boost inductor, is converted to respective discharge currents flowing through the first and second secondary half windings SW_1 and SW_2. Thereby, power or energy is transferred to the rectified converter output voltage so as to control the latter when the output voltage is below a minimum voltage required for normal boost mode operation.

[0008] The present isolated boost converter is preferably configured such that the second discharge state is automatically entered when the driver enters a non-conducting or OFF-state for example when a duty cycle of a pulse width modulated driver control signal is less than 0.5. The driver may for example enter the non-conducting state when all transistors of the driver simultaneously are in non-conducting states. The driver may comprise a half-bridge or an H-bridge with two or four MOS transistors, respectively. The H-bridge or full-bridge transistor driver may have first and second complementary driver outputs coupled to respective ends of the primary transformer winding. When all transistors of the half-bridge or full-bridge transistor driver are placed in non-conducting states by the pulse width modulated driver control signal, a voltage across the driver rapidly rises to a destructive level due the continued effort of the boost inductor to transmit current towards the driver. This undesired rise of boost inductor voltage takes place during start-up of the isolated boost converter where the duty cycle D of the pulse width modulated driver control signal must be initialized to a value below 0.5, preferably close to zero, to avoid large in-rush currents. However, the automatic entry into the second discharge state provided by this embodiment eliminates the generation of destructive boost inductor voltage spikes by discharging the magnetic energy stored in the boost inductor as the discharge currents running through the first and second secondary transformer windings. The automatic entry of the second discharge state may be caused by a reverse in a flux rate through the boost inductor due to a sudden decrease of boost inductor current.

[0009] In accordance with a preferred embodiment of the invention, the boost converter is configured to change between the first and second discharge states by selectively coupling and decoupling the boost inductor from the secondary transformer windings such that:

- during the first discharge state, magnetically decoupling the boost inductor from the first and second secondary transformer windings to deliver the magnetic energy to the primary transformer winding;

- during the second discharge state, magnetically coupling the boost inductor to the first and second secondary transformer windings through a shared flux path in the magnetically permeable multi-legged core. The shared flux path may comprise two separate shared flux paths such that a first shared flux path runs between the boost inductor and the first secondary transformer winding and a second shared flux path runs between the boost inductor and the second secondary transformer winding. The number of windings of the first and second secondary transformer windings is preferably substantially identical to allow effective decupling between the boost inductor and the first and second secondary transformer windings in the first discharge state.

[0010] As previously mentioned the first and second secondary transformer windings are preferably configured to discharge the magnetic energy stored in the boost inductor by supplying a discharge current to the rectified converter output voltage, V_{out}, so as to transfer energy to the output. In this scheme the first and second secondary transformer windings act as a flyback winding.

[0011] According to an advantageous embodiment of the invention, the magnetically permeable multi-legged core comprises:

- a center leg, having an air gap arranged therein,
- a first outer leg and a second outer leg; The boost inductor is magnetically coupled to the center leg to store the magnetic energy therein and the first and second secondary transformer windings are wound around the first and second outer legs, respectively. This topology of the magnetically permeable multi-legged core may comprise a conventional EI core. The air gap is well-suited for storage of the magnetic energy due to its high reluctance or low magnetic permeability and preferably has a height between 0.1 mm and 10 mm. In one embodiment, the boost inductor is wound around the center leg while in other embodiments windings of the boost inductor is split into two series connected half-windings wound around respective ones of the first and second outer legs. In the latter embodiment, the boost inductor is magnetically coupled to the air gap by a suitable magnetically permeable structure of the magnetically permeable multi-legged core.

[0012] In yet another embodiment of the invention which comprises the center leg with the air gap and the first and second outer legs, the primary transformer winding comprises first and second series connected half-windings wound around the first and second outer legs, respectively, of the magnetically permeable multi-legged core. In this embodiment, the first half-winding of the primary transformer winding and the first secondary transformer winding are both

wound around the first outer leg of the magnetically permeable multi-legged core. Likewise, the second half-winding of the primary transformer winding and the second secondary transformer winding are both wound around the second outer leg of the magnetically permeable multi-legged core.

[0013] The skilled person will understand that the present isolated boost power converter may comprise many different types of primary side circuit topologies in addition to the previously mentioned half-bridge and full-bridge drivers. In one embodiment, the primary side comprises a first boost inductor and a second boost inductor such that the first boost inductor is coupled between the input terminal and a first transistor driver output. The first transistor driver output is coupled to a first end or first winding output of the primary transformer winding. The second boost inductor is coupled between the input terminal and a second transistor driver output. The second transistor driver output is coupled to a second end or second winding output of the primary transformer winding. The first and second transistor driver outputs may comprise respective drain or collector terminals of a MOS or bipolar transistor. The use of at least two boost inductors is advantageous because this reduces driver component count such as reducing the number of switch transistors.

[0014] In another embodiment, the boost inductor comprises a first half-winding and a second half-winding of the primary transformer winding to provide an integrally formed boost inductor and primary winding which is advantageous because of improved copper utilization. In this embodiment, the magnetic energy stored in the boost inductor is directly transferred to the first and second secondary transformer windings by a magnetic flux through the magnetically permeable multi-legged core. In the above-discussed embodiments with separate primary transformer winding and boost inductor, magnetic energy is initially stored in the boost inductor and subsequently released or discharged, during the first discharge state, as discharge current flowing through the primary transformer winding to induce a primary side voltage therein.

[0015] In a number of embodiments of the isolated boost power converter a rectifying element is electrically coupled to the center-tap to conduct a discharge current, during the second discharge state, from the first and second secondary transformer windings to the rectified converter output voltage, V_{out}. The discharge current is induced by the magnetic flux generated by the boost inductor flowing through the first and second secondary transformer windings. The rectifying element is preferably electrically coupled to a supply rail, such as ground, a negative

supply rail or a positive supply rail, of the secondary side of the isolated boost power converter. The rectifying element may be required if the rectification circuit comprises a full-bridge rectifier or a voltage doubler because during the first discharge state, the center-tap voltage is different from both the rectified converter output voltage and a negative rectified converter output voltage.

[0016] Alternatively, the rectification circuit may comprise a center-tapped rectifier in accordance with a preferred embodiment of the invention where a rectifying element coupled in series with the center-tap can be avoided. According to this embodiment, the center-tap is electrically connected to a negative rectified converter output voltage or the rectified converter output voltage, V_{out},

- the respective outputs of the first and second secondary transformer windings are coupled to the opposite output voltage to the one electrically coupled to the center-tap through first and second rectifying elements. Each of the first and second rectifying elements preferably comprises a semiconductor diode.

[0017] As previously mentioned, the rectification circuit may comprise a voltage multiplier for example a voltage doubler circuit to increase the level of the rectified converter output voltage, V_{out}. The skilled person will understand that the rectifying element and/or the rectification circuit each may comprise one or more semiconductor diode(s), diode-coupled transistor(s) or synchronously controlled transistor switch(es). Each of the semiconductor diodes may comprise a MOS diode, a bipolar diode, a Schottky diode or any combination thereof.

[0018] According to one advantageous embodiment or variant of the invention discussed above with the center leg surrounded by the first and second outer legs, the isolated boost power converter comprises:

- a second magnetically permeable multi-legged core and a second boost inductor magnetically coupled to a center leg of the second magnetically permeable multi-legged core to store magnetic energy therein. The second boost inductor being electrically coupled between the input terminal and a second driver to be alternatingly charged and discharged with magnetic energy. The second driver having a second driver output coupled to a second primary transformer winding wound around a first outer leg and a second outer leg of the second magnetically permeable transformer core. The second driver is configured to generate a second primary voltage to the

second primary transformer winding in accordance with the driver control signal. The boost power converter further comprises first and second secondary transformer windings wound around the first outer leg and the second outer leg, respectively, of the second magnetically permeable multi-legged core. The first secondary transformer winding of the second magnetically permeable multi-legged core is coupled in series between the rectification circuit and the output of the first secondary transformer winding of the first magnetically permeable multi-legged core. The second secondary transformer winding of the second magnetically permeable multi-legged core is coupled in series between the rectification circuit and the output of the second secondary transformer winding of the magnetically permeable multi-legged core, or first magnetically permeable multi-legged core, such that:

- in the first discharge state, the respective magnetic energies stored in the first and second boost inductors are discharged by directing respective discharge currents from the respective boost inductors through the respective primary transformer windings,
- in the second discharge state, the respective magnetic energies stored in the respective boost inductors are discharged by discharging respective magnetic fluxes through the respective first and second secondary transformer windings.

[0019] According to the latter embodiment of the invention, the first and second secondary transformer windings of the first magnetically permeable multi-legged core are electrically coupled to the rectification circuit in an indirect manner through the respective ones of the first and second secondary transformer windings of the second magnetically permeable multi-legged core. The first and second secondary transformer windings are therefore coupled in series such that the rectified converter output voltage, V_{out} is doubled in a symmetrical architecture or topology of transformer windings on the first and second magnetically permeable multi-legged cores. The first and second magnetically permeable multi-legged cores may be provided as separate parts, for example arranged in abutment or proximate to each other, or as an integrally formed element which has a common magnetically permeable structure or leg. In a preferred embodiment, the first and second magnetically permeable multi-legged cores share a common magnetic flux path extending through a shared magnetically permeable leg. In the latter embodiment, the first and second magnetically permeable multi-legged cores may advantageously be configured to provide magnetic flux cancellation or suppression in the shared magnetically permeable leg. This saves magnetic material such that material costs and size of the

isolated boost power converter is reduced. The above-discussed embodiments of the present invention based on the first and second magnetically permeable multi-legged cores possess numerous favourable characteristics: These embodiments are readily scalable by the addition of further magnetically permeable multi-legged cores, associated primary side and secondary side transformer windings and drivers. This property means that isolated boost power converters can readily be adapted to a whole range of applications with varying power capacity. Thus, saving design time, reducing design risk and reducing manufacturing costs etc. In addition, the current rating of each semiconductor switch of the first and second drivers can be halved for a given current handling capacity due to the split of input current between the first, second and possibly further drivers.

[0020] The driver control signal may comprise a PWM signal having an adjustable duty cycle, D. The adjustable duty cycle may be used to set a desired or target DC level of the rectified converter output voltage, V_{out}. The duty cycle is preferably set to a value between 0.5 and 1.0 after exiting from a start-up state or mode, i.e. during normal boost mode operation of the isolated boost converter. The duty cycle, D, may be set or controlled in connection with a closed loop control scheme for controlling any of the state variables of the isolated power converter, such as the boost inductor current or the rectified converter output voltage, $V_{out.}$

[0021] Another aspect of the invention relates to a method of generating a rectified converter output voltage, V_{out}, from an input voltage, V_{in}, by an isolated boost power converter according to any of the preceding claims. The method comprises steps of:

- generating a pulse width modulated driver control signal,
- supplying the pulse width modulated driver control signal to the driver,
- gradually increasing a duty cycle, D, of the pulse width modulated driver control signal from below 0.5, preferably below 0.1, to a value above 0.5, preferably between 0.55 and 0.99,
- adjusting the duty cycle, D, to a desired value to reach a desired or target AC voltage waveform or DC voltage level at the rectified converter output voltage, $V_{out.}$. As previously explained, before the isolated boost converter reaches its normal operating state, a start-up mode or state is required. During the start-up phase or mode of the isolated boost power converter the duty cycle of the Pulse Width Modulated (PWM) driver control signal applied to the driver must be ramped-up slowly to avoid excessive in-rush currents. During ramp-up of the duty cycle, it

preferably starts at a value much less than 0.5 which means that the driver is placed in an open or cut-off state during a certain time interval of a cycle of the PWM signal. The open state of the driver means the driver lacks a low resistive path to the input voltage or a negative input voltage rail such as ground, GND. However, thanks to the ability of the first and second secondary transformer windings to discharge the magnetic flux stored in the boost inductor, the present isolated boost power converter can enter and exit the start-up mode so as to establish an initial output voltage as V_{out} without any need for a separate flyback winding or other auxiliary start-up circuit.

BRIEF DESCRIPTION OF THE DRAWINGS

[0022] A preferred embodiment of the invention will be described in more detail in connection with the appended drawings, in which:

[0023] Figs. 1a) and 1b) illustrate schematically an electrical circuit diagram and a magnetic circuit diagram, respectively, of an isolated boost power converter in accordance with a first embodiment of the invention,

[0024] Figs. 2a) and 2b) illustrate schematically an electrical circuit diagram and a magnetic circuit diagram, respectively, of the isolated boost power converter in accordance with the first embodiment of the invention during a charging subinterval of boost mode operation,

[0025] Figs. 3a) and 3b) illustrate schematically an electrical circuit diagram and a magnetic circuit diagram, respectively, of the isolated boost power converter in accordance with the first embodiment of the invention during a first discharge state of the boost mode operation,

[0026] Figs. 4a) and 4b) illustrate schematically an electrical circuit diagram and a magnetic circuit diagram, respectively, of the isolated boost power converter in accordance with the first embodiment of the invention during a charging subinterval of a start-up mode.

[0027] Figs. 5a) and 5b) illustrate schematically an electrical circuit diagram and a magnetic circuit diagram, respectively, of the isolated boost power converter in accordance with the first embodiment of the invention during a second discharge state of the start-up mode wherein magnetic energy stored in a boost inductor is discharged by discharging a magnetic flux through secondary transformer windings,

[0028] Fig. 6a) is an electrical circuit diagram of an isolated boost power converter with integration of a boost inductor and primary transformer windings in accordance with a second embodiment of the invention,

[0029] Fig. 6b) is an electrical circuit diagram of an isolated boost power converter with a center-tapped rectification circuit in accordance with a third embodiment of the invention,

[0030] Fig. 7 is an electrical circuit diagram of an isolated boost power converter with an integrally formed dual core topology in accordance with a fourth embodiment of the invention; and

[0031] Fig. 8 is a graph depicting measurement data from an experimental isolated boost power converter in accordance with the first embodiment of the invention.

DETAILED DESCRIPTION

[0032] The embodiments described in detail below are particularly well-suited for power converters providing DC voltage amplification or step-up. However, the skilled person will understand that power converter in accordance with the present invention are highly useful for other types of applications both in step-up and step down voltage converting applications.

[0033] Fig. 1a) illustrates schematically an electrical circuit diagram of an isolated boost power converter 100 in accordance with a first embodiment of the present invention. The isolated boost power converter 100 comprises a magnetically permeable multi-legged core in form of the three legged EI core 102. The three legged EI core 102 comprises a center leg 134 surrounded by a first outer leg 132 and a second outer leg 136 in a mirror-symmetrical layout or structure about a central vertical axis extending through the center leg 134. The center leg 134 comprises an air gap 138 which allows magnetic energy of a boost inductor, L_{boost}, to be stored therein. The isolated boost power converter 100 comprises an input terminal 104 for receipt of an input voltage, Vin, which for example may be a DC voltage between 5 Volt and 100 Volt. The boost inductor, L_{boost}, is arranged or wound around a first leg of the three legged EI core 102 and electrically coupled between the input terminal 104 and a transistor driver 106 to be alternatingly charged and discharged with magnetic energy through the transistor driver 106. The primary and secondary windings are both split into two half-windings distributed between the first and second EI core legs so that the flux from the boost inductor, L_{boost}, is decoupled from

the transformer function in normal boost operation. The transformer winding outputs or ports are marked a; b; c and d in both the electrical circuit diagram of Fig. 1a) and the magnetic diagram of Fig. 1b). The transistor driver 106 comprises four NMOS transistors $S_1 - S_4$ coupled as a full-bridge or H-bridge such that a first driver output, at a shared junction or node in-between the NMOS transistors S_1 and S_4, is electrically coupled to the first winding output, a, of a primary transformer winding or primary side transformer winding PW_{1-2}. A second driver output, at a shared junction or node in-between NMOS transistors S_2 and S_3, is electrically coupled to the second winding output, b, of the primary transformer winding PW_{1-2}. The primary transformer winding PW_{1-2} is split as mentioned above so as to comprise two series connected half-windings PW_1 and PW_2 (refer to Fig. 1b)) wound around the first and second outer legs, 132, 136, respectively, of the EI core 102.

[0034] The transistor driver 106 consequently generates a primary voltage across the primary winding 110 in accordance with a driver control signal, such as a pulse width modulated control signal, adapted to individually control the switching of the NMOS transistors S_1 - S_4, which each are switched between conducting and non-conducting states, i.e. On or Off. The isolated boost power converter 100 comprises first and second series connected secondary transformer windings, SW_1 and SW_2, respectively, having a center-tap or midpoint 116 arranged in-between them. The first and second series connected secondary transformer windings, SW_1 and SW_2, respectively, are wound around the first outer leg 132 and the second outer leg 136, respectively, i.e. separate legs of the EI core 102 such that the second secondary transformer winding SW_2 is arranged on the same outer leg 136 as the half-winding PW_2 of the primary transformer winding and the first secondary transformer winding SW_1 is arranged on the same outer leg 132 as the half-winding PW_1 of the primary transformer winding. A voltage transfer ratio between the primary and secondary sides of the transformer function provided by the EI core 102 is set by a turns ratio, *n*, between a number of secondary side transformer windings relative to a number of primary side transformer windings. In the present embodiment, this turns ratio, *n*, equals the

number of secondary transformer windings of SW_1 and SW_2 combined divided by the number of primary transformer windings of PW_1 and PW_2 combined. The turns ratio, *n*, may naturally vary with requirements of a particular application, in particular whether the boost converter is intended to function as a step-up or step-down converter. The turns ratio, *n*, is preferably set to value between 0.25 and 100 such as between 1.0 and 64. The integration on the common or shared EI core 102 of the boost inductor, L_{boost}, the primary transformer winding PW_{1-2} and the first and second series connected secondary transformer windings, SW_1 and SW_2 is often referred to as ”integrated magnetics” in the art.

[0035] A rectification circuit 118 is electrically coupled to respective outputs of the first and second secondary windings to provide a rectified converter output voltage, V_{out}, between rectified converter output voltage, V_{out}, 119 and a negative rectified converter output voltage 121. A supply capacitor C or C_{out} is coupled between these converter output voltages or rails to suppress ripple voltages at the output of the rectification circuit 118 and provide an energy reservoir stabilising the output voltage, V_{out}. In the depicted isolated boost power converter 100, the input side or primary side and secondary side are galvanically isolated by the EI core 102. However, the skilled person will understand that the negative terminals or rails of the output voltage V_{out} and the input voltage may be electrically coupled to each other, for example through a shared GND connection without compromising the desired boost inductor discharge functionality of the first and second secondary transformer windings of the present isolated boost power converter 100. A rectifying element in form of a semiconductor diode, D_f, is coupled between the center-tap 116 and the negative rectified converter output voltage 121 to facilitate a flow of discharge current through the first and second secondary transformer windings, SW_1 and SW_2, respectively. The discharge current subsequently flows through the rectification circuit 118 and to the output terminal or node 119 providing the rectified converter output voltage, V_{out}, so as to transfer energy to the output, facilitating start-up of the power converter 100 as explained in further detail below.

[0036] The transfer characteristic of the isolated boost converter is set by a duty cycle, D, of the Pulse Width Modulated (PWM) driver control signal, during normal boost operation according to:

$$\frac{V_{out}}{V_{in}} = \frac{n}{2(1-D)} \Leftrightarrow V_{out} \geq \frac{nV_{in}}{2}$$

(Equation 1) wherein:

V_{out} = rectified DC output voltage of the boost converter,

V_{in} = the DC input voltage to the boost converter;

D = a duty cycle of the PWM control signal at each transistor input of the driver and defined as: T_{on}/T_{period} of a single PWM period;

n = transformer turns ratio set by the number of secondary transformer windings divided by the number of primary transformer windings.

[0037] When $V_{out} \leq \frac{nV_{in}}{2}$, the isolated boost converter may be in the start-up phase and the duty cycle, D, of the Pulse Width Modulated (PWM) driver control signal below 0.5.

[0038] Fig. 2a) illustrates schematically an electrical circuit diagram 100 of the isolated boost power converter during a first subinterval or state boost mode operation. Circuit elements that are not carrying current have been dimmed to clarify the operation during the first state. Generally, when the duty cycle of the driver control signal, D, exceeds 0.5, the isolated boost power converter 100 operates as a normal isolated boost converter. The boost mode operation can be divided into two subintervals: The first state or boosting subinterval where all the NMOS transistors S_1-S_4 are in placed in respective conducting states or on states. A second state of the boost mode operation is an energy transfer subinterval where two of the NMOS transistors, either S_1-S_2 or S_3-S_4 , are in conduction states simultaneously as illustrated on Fig. 3a) and Fig. 4a). In the latter state or subinterval boost inductor current is allowed to flow through the primary transformer winding $PW_{1\text{-}2}$ such that energy or power is transferred through the EI core 102 to the rectified output voltage. The positive direction of any currents is indicated by arrows on electrical conductors or wires and relevant voltage polarities indicated by +/- signs. Fig. 2b) shows the magnetic diagram, including flux rate induced by the boost inductor winding: $d\Phi/dt = \Phi_{L'}$, shown by fat dotted lines 112a and 112b. The rising current in L_{boost} corresponds to a

positive voltage drop of the input voltage, $V_{in.}$ The DC flux is excluded from the analysis and the illustrated drawing as this is only relevant for magnetic saturation and power loss considerations of the EI core 102. The induced magnetic flux Φ_L, splits evenly between the first and second outer legs 132, 136, respectively, inducing voltage drops on the transformer windings with polarities indicated by the indicated +/- signs at respective winding outputs a, b, c and d following from the right hand rule. The polarities across the two series connected primary side half-windings PW_1, PW_2 are opposite, and the voltages cancel and likewise for induced voltages across the two series connected secondary side half-windings SW1 and SW2, so it can be concluded that the boost inductor L_{boost} or L is not coupled to the transformer function of the EI core 102 during this state or subinterval. Furthermore, it is also evident that D_f is reverse biased in the illustrated subinterval of boost mode operation.

[0039] Fig 3a) illustrates schematically the electrical circuit diagram of the isolated boost power converter 100 during a first discharge state, or transformer energy transfer subinterval, of the boost mode. Circuit elements that are not carrying current have been dimmed to clarify the operation in this state. During the illustrated energy transfer subinterval, the two series connected primary side half-windings PW_1, PW_2 or primary winding PW_{1-2} of the EI core based transformer is connected in series with the boost inductor, such that the magnetic energy stored in the boost inductor is discharged by a discharge current flowing through the primary transformer winding such that energy is transferred to the rectified output voltage. The current direction through the primary winding PW_{1-2} is alternated for every other subinterval, such that either NMOS transistors S_1; S_2 and rectifying diodes D_1 and D_2 or NMOS transistors S_3, S_4 and rectifying diodes D_3 and D_4 are conducting . Fig.3a) shows the subinterval where the NMOS transistors S_1, S_2 and rectifying diodes D_1 and D_2 are conducting.

[0040] Fig. 3b) shows the magnetic diagram, including a flux rate, $d\Phi/dt = \Phi_L$', induced by the boost inductor L_{boost}. A first flux path associated with the boost inductor extends around the center leg 134, the first outer leg 132 and the air gap 138 as illustrated symbolically by fat dotted line 112a. Likewise, a second flux path extending around the center leg 134, the second outer leg

132 and the air gap 138 is illustrated symbolically by fat dotted line 112b. The flux rate induced by the primary winding $PW_{1-2,}$ $d\Phi_T/dt = \Phi_T'$, is shown by an outer fat dotted line 114 illustrating how the flux circulates clockwise around an outer closed path or loop 114 around the outer periphery of the EI core 102 including the first and second outer legs 132, 136, respectively. As seen in Fig.3b), the flux rate Φ_T' flows in a low reluctance outer path of the EI core 102 avoiding to travel across the air gap 138 due to its high reluctance or low magnetic permeability. Using the right hand rule and the depicted voltage polarity on the two half-windings PW_1, PW_2 of the primary winding, it can be seen that these two flux rates are in the same direction along the outer flux path depicted by the fat dotted line 114. In the same manner, it is evident that the flux rate Φ_T' couples to the secondary side half-windings SW_1 and SW_2 such that induced current flows from winding output d to the winding output c, forward biasing the rectifying diodes D1 and D2. From this it follows that output voltage at the mid-point 116 between the secondary side half-windings is positive with approximately one-half of the rectified converter output voltage, V_{out}, such that D_f is reverse biased.

[0041] When instead NMOS transistors S_3, S_4 and rectifying diodes D_3 and D_4 are conducting, a corresponding analysis applies due to symmetry. In the latter case, all transformer winding voltages and currents are reversed, which still results in D_f being reverse biased by one-half of V_{out}. It is also worthwhile to notice that in both cases, the flux rate induced by the boost inductor, L, is not coupling to the primary and secondary transformer windings PW_{1-2}, and $SW_{1,}$ SW_2, respectively, of the EI core 102 such that the boost inductor is magnetically decoupled from the transformer operation. Furthermore, the current in the boost inductor, L, is falling, seen as a negative voltage drop across the boost inductor in both Figs. 3a) and b).

[0042] Figs. 4a) and b) show schematically an electrical circuit diagram and a magnetic circuit diagram, respectively, during a charging subinterval of a start-up mode. The input voltage, Vin is charging the boost inductor while also transferring energy to the rectified output voltage through the transformer operation of the EI core 102 of the isolated boost power converter 100. This charging subinterval can be viewed as a hybrid boost and energy transfer subinterval. The MOS transistors S_1, S_2 of the driver 106 and rectifying diodes D_1 and D_2 are

conducting. The operation is identical to the second subinterval discussed above in connection with Figs. 3a) and 3b) except current in the boost inductor, L, or L_{boost} is increasing as indicated by the reversed polarity of the voltage across the boost inductor. The term "hybrid" indicates that the boost inductor, L, and the primary transformer winding, PW_{1-2}, are both active such that magnetic energy is loaded into the boost inductor, L, at the same time as energy is transferred to the rectified output voltage through the transformer operation between the primary and secondary windings PW_{1-2}, and SW_1, SW_2, respectively, of the EI core 102. Consequently, during the first discharge state, the flux rate Φ_L, induced by the boost inductor, L, is decoupled from the secondary transformer windings SW_1, SW_2 of the EI core 102 such that the boost inductor is substantially magnetically decoupled from the transformer operation.

[0043] Figs. 5a) and 5b) illustrate schematically an electrical circuit diagram and a magnetic circuit diagram, respectively, the isolated boost power converter 100 during a second discharge state. Magnetic energy stored in a boost inductor, L, is discharged by discharging a magnetic flux through secondary transformer windings SW_1, SW_2. Circuit elements that are not carrying current have been dimmed to clarify the operation during the second discharge state of start-up mode.

[0044] During the second discharge state, which can be viewed as a second subinterval of the start-up mode, the magnetic energy stored in the boost inductor, L, is discharged by circulating the stored magnetic flux through the first and second secondary transformer windings SW_1, SW_2. When all the NMOS transistors S_1 - S_4 of the driver circuit 106 are turned off, i.e. non-conducting, the boost inductor current commutates to the first and second secondary transformer windings SW_1, SW_2 through the flyback diode D_f, as shown in Fig. 5a) by a magnetic coupling 108 as symbolically indicated on Fig. 5a). A shared magnetic flux path comprising the first and second flux paths 112a, 112b (refer to Fig. 5b)) extending around the first and second outer legs, 132, 136, respectively, magnetically coupling the boost inductor, L, to the first and second secondary transformer windings SW_1, SW_2. The cutoff or non-conducting state of the NMOS transistors of the driver leads to a suddenly dropping boost inductor current which results in a reverse in the respective rates of fluxes $½\Phi_L$, at the first and second flux paths 112a, 112b

whereby the voltage polarity across the boost inductor is reversed (compared to Fig. 4b)). This flux rate reversal of $\frac{1}{2}\Phi_L$, induces a voltage drop across each of the secondary side half-windings SW_1 and SW_2. There is a positive voltage drop from secondary winding output c to D_f as well as from secondary winding output d to rectifying diode D_f. Consequently, a discharge current, I_d, can now travel from secondary winding output c through D_1 and into the load resistance R_L continuing back through D_f. Similarly, a discharge current can travel from secondary winding output d through D_3 into R_L and back through D_f. In effect, during the second discharge state of the start-up mode, the two secondary half windings SW_1 and SW_2 are working or coupled electrically in parallel from the center-tap 116 to the rectified output voltage V_{out} through respective rectifying diodes D_1 and D_2 so as to jointly discharge the magnetic energy in the boost inductor. This magnetic energy is largely stored in the air gap 138. As illustrated, the magnetic energy stored in the boost inductor is converted to discharge currents flowing through the first and second secondary half windings SW_1 and SW_2 to the rectified converter output voltage, V_{out} through the shared magnetic flux path 112a, 112b. Consequently, the the boost inductor, L, is magnetically coupled to the first and second secondary transformer windings SW_1 and SW_2. In effect, transferring energy to the rectified output voltage during the start-up mode and allowing a gradual transition towards a state of normal boost mode operation for the isolated boost power converter 100.

[0045] Fig. 6a) is an electrical circuit diagram of an isolated boost power converter 600 in accordance with a second embodiment of the invention. The isolated boost power converter 600 is similar to the previously described isolated boost converter 100 except for the reversal of the polarity of the rectifying diode D_f and an accompanying reversal of a winding orientation of the boost inductor L_{boost} relative to the winding orientation depicted on Fig. 1b). Like features have been marked with corresponding numerals to assist the comparison. The skilled person will notice that this configuration of the rectifying diode D_f works similarly to the above-described

configuration, in that when the primary transformer winding is inactive, a decreasing flux in the center leg will cause D_f to be forward biased in either case.

[0046] Fig. 6b) is an electrical circuit diagram 640 of an isolated boost power converter with a center-tapped rectification circuit 648 in accordance with a third embodiment of the invention. The transistor based full-bridge driver 606, the primary and secondary windings PW_1, PW_2 and SW_1, SW_2, respectively, and the EI core 102 itself are preferably all identical to the same features of the above-discussed first embodiment of the present isolated power converter. However, in the present embodiment, the rectification circuit only comprises two rectifying diodes D_1 and D_2 coupled from a first winding output of the first half-winding SW_1 and second winding output of the second half-winding SW_2, respectively, to a rectified converter output voltage, V_{out}, at positive and negative output nodes 619, 621, respectively. However, as a center-tap voltage at node 616 arranged in-between the first and second secondary transformer half-winding SW_1, SW_2 is always held at the negative rectified converter output voltage on output node 621, which may be ground level GND, there is not any need to add a rectifying diode D_f in series with the center-tap 616 like in the previously discussed embodiments.

[0047] Fig. 7 is an electrical circuit diagram of an isolated boost power converter 700 with a dual core topology comprising an integrally formed multi-legged EI core 702a, 702b in accordance with a fourth embodiment of the invention. The isolated boost power converter 700 comprises an integrally formed magnetically permeable multi-legged core in form of a first three legged EI core 702a and a second three legged EI core 702b that share a common "I" leg 740 such that the entire magnetically permeable multi-legged core is a unitary structure. The structure of the integral magnetically permeable multi-legged core 702a, 702b is mirror symmetrical about a horizontal symmetry axis 750. Each of the EI cores 702a, 702b comprises a center leg 734a, 734b, respectively, surrounded by a first outer leg 732a,b and a second outer leg 736a,b in a mirror-symmetrical layout or structure about a central vertical axis extending through a middle of the center legs 734a, 734b.

[0048] Each of the center legs 734a, 734b comprises an air gap 738a, 738b which allows magnetic energy of an associated boost inductor, L_{boosta}, and L_{boostb}, respectively, to be stored

therein. The isolated boost power converter 700 comprises an input terminal 104 for receipt of an input voltage, V_{in}, which for example may be a DC voltage between 5 Volt and 100 Volt. The first and second boost inductors, L_{boosta}, and L_{boostb}, are both coupled to the input voltage at terminal 704. A first H-bridge transistor driver 706a is coupled to the first boost inductor, L_{boosta}, and a second H-bridge transistor driver 706b is coupled to the second boost inductors, L_{boostb}. Each of the first and second three legged EI cores 702a, 702b have associated primary and second transformer windings, PW_{1a} , PW_{2a} and SW_{1a}, SW_{2a} and PW_{1b} , PW_{2b} and SW_{1b}, SW_{2b}, respectively, in a topology similar to the topology discussed above in detail in connection with the first embodiment of the invention. However, only the center-tap 716 in-between the first and second series connected secondary transformer windings, SW_{1a} and $SW_{2a,}$ respectively, is coupled to a rectifying element in form of semiconductor diode D_f. The first and second series connected secondary transformer windings, $SW_{1b,}$ SW_{2b} of the second EI core 702b are not connected to a center-tap but each half-winding output is coupled in series with the corresponding secondary half-winding of the first EI core 702a. The isolated boost power converter 700 comprises a shared single rectification circuit 719 coupled to respective winding outputs of the first and second secondary windings SW_{1b} and SW_{2b}. The rectification circuit 719 is configured as a full-wave rectifier comprising four rectifying diodes D_1 - D_4 to produce a rectified converter output voltage V_{out} between positive and negative output voltage terminals or nodes 719, 721, respectively.

[0049] It is accordingly evident that the first and second primary transformer windings PW_{1-2a} and PW_{1-2b} are both coupled to separate drivers 706a and 706b, respectively, while the pair of first secondary transformer windings SW_{1a} and SW_{1b} are coupled in series between the center tap 716 and the rectification circuit 718 and the pair of second secondary transformer windings SW_{2a} and SW_{2b} likewise are coupled in series between the center tap 716 and the rectification circuit 718. This topology has the beneficial effect that voltage amplification, i.e. the ratio between the input voltage V_{in} and the rectified converter output voltage V_{out}, is doubled

compared to the topology disclosed on Figs. 1-5 due to the series connected pairs of first and second secondary windings. In addition, the shared "I" leg 740 provides further magnetics integration so as to reduce material costs, decrease size and increase efficiency due to flux cancellation in the shared "I" leg 740.

[0050] Furthermore, the first and second series connected secondary transformer windings, $SW_{1a,}$ SW_{2a} are configured to discharge magnetic energy stored in the first boost inductor, L_{boosta}, in a manner similar to one used in the above-mentioned first embodiment of the invention by a shared magnetic flux path comprising a first magnetic flux path extending through the first center leg 734a, and the first outer leg 732a and a second magnetic flux path extending through the first center leg 734a, and the second outer leg 736a. Likewise, the first and second series connected secondary transformer windings, $SW_{1b,}$ SW_{2b} of the upper EI core 702b are configured to discharge magnetic energy stored in the second boost inductor, L_{boostb}, through a shared magnetic flux path in the upper EI core 702b.

[0051] Fig. 8 is a graph 800 depicting measurement data from an experimental isolated boost power converter in accordance with the above-described first embodiment of the invention. The experimental isolated boost power converter had the following key data:

Windings on $L_{boost} = 2$

primary transformer windings, $PW_{1-2} = 2$

secondary transformer windings, $SW_1 + SW_2 = 8$

DC input voltage, $V_{in} = 25$ Volt

Load resistance, $R_L = 68.2$ ohm

Core type: ELP64 available from manufacturer EPCOS AG.

Core material: N87

Air gap height (at center leg) = 0.5 mm.

[0052] The graph data were acquired by maintaining V_{in} at 25 Volt and sweeping a duty cycle, D, of a Pulse Width Modulated (PWM) driver control signal from 0 to 0.75 and then back to 0 over a time period of 4 seconds. The time variable is indicated along the x-axis 805. The corresponding duty cycle, D, is indicated on the right-hand vertical scale 803 and the measured

rectified converter output voltage, V_{out}, indicated on the left-hand vertical scale in Volts. The substantially linear correlation between the duty cycle and the rectified converter output voltage, V_{out}, is evident, and is for D>0.5 in accordance with equation (1) above. It is also noticeable that the rectified converter output voltage, $V_{out,}$ is continuous across the boundaries at D = 0.5 between start-up mode operation and normal boost mode operation. For D = 0.75, the following electrical data were measured, input current (at V_{in}) = 27.94 A, V_{out} = 205.11 Volt, output current = 3.006 A.

[0053] Hence, the present measurement data confirms the capability of the present experimental isolated boost power converter to start-up (D<0.5) and proceed to normal boost operation (D>0.5) in a well-behaved manner without any need for a separate flyback winding or other dedicated start-up circuitry.

CLAIMS

1. An isolated boost power converter comprising:

- a magnetically permeable multi-legged core,

- an input terminal for receipt of an input voltage, Vin,

- a boost inductor being wound around a first leg of the magnetically permeable multi-legged core,

- the boost inductor being electrically coupled between the input terminal and a driver to be alternatingly charged and discharged with magnetic energy,

- the driver having a driver output coupled to a primary transformer winding wound around a second leg of the magnetically permeable transformer core,

- the driver being configured to generate a primary voltage to the primary transformer winding in accordance with a driver control signal,

- first and second series connected secondary transformer windings with a center-tap arranged in-between and wound around separate legs of the magnetically permeable multi-legged core,

- a rectification circuit electrically coupled to respective outputs of the first and second secondary transformer windings to provide a rectified converter output voltage, Vout; wherein

- in a first discharge state, the magnetic energy stored in the boost inductor is discharged by directing a discharge current from the boost inductor through the primary transformer winding,

- in a second discharge state, the magnetic energy stored in the boost inductor is discharged by discharging a magnetic flux through the first and second secondary transformer windings.

2. An isolated boost power converter according to claim 1, wherein the first and second secondary transformer windings are coupled in parallel from the center-tap between first and

second series connected secondary transformer windings to the rectified converter output voltage, V_{out}.

3. An isolated boost power converter according to claim 1 or 2, wherein the second discharge state is automatically entered when the driver enters a non-conducting or off-state such as when a duty cycle of a pulse width modulated driver control signal is less than 0.5.

4. An isolated boost power converter according to any of the preceding claims, wherein the boost converter is configured to:

- during the first discharge state, magnetically decoupling the boost inductor from the first and second secondary transformer windings to deliver the magnetic energy to the primary transformer winding;
- during the second discharge state, magnetically coupling the boost inductor to the first and second secondary transformer windings through a shared flux path in the magnetically permeable multi-legged core.

5. An isolated boost power converter according to any of the preceding claims, wherein the first and second secondary transformer windings are configured to discharge the magnetic energy stored in the boost inductor by supplying a discharge current to the rectified converter output voltage, V_{out}, so as to transfer energy to the output - Whereby the first and second secondary transformer windings act as flyback windings.

6. An isolated boost power converter according to any of the preceding claims, wherein the magnetically permeable multi-legged core comprises:

- a center leg, having an air gap arranged therein,
- a first outer leg and a second outer leg;
- wherein the boost inductor is magnetically coupled to the center leg to store the magnetic energy therein and the first and second secondary transformer windings being wound around the first and second outer legs, respectively.

7. An isolated boost power converter according to claim 6, wherein the boost inductor is wound around the center leg.

8. An isolated boost power converter according to claim 6 or 7, wherein the air gap of the center leg has a height between 0.1 mm and 1.0 mm.

9. An isolated boost power converter according to any of claims 6-8, wherein the primary transformer winding comprises first and second series connected half-windings wound around the first and second outer legs, respectively, of the magnetically permeable multi-legged core.

10. An isolated boost power converter according to any of the preceding claims, wherein the driver comprises a full-bridge transistor driver having a first and second complementary driver outputs coupled to respective ends of the primary transformer winding.

11. An isolated boost power converter according to any of claims 1-9, comprising a first boost inductor and a second boost inductor;

- the first boost inductor being coupled between the input terminal and a first transistor driver output coupled to a first end of the primary transformer winding,
- the second boost inductor being coupled between the input terminal and a second transistor driver output coupled to a second end of the primary transformer winding.

12. An isolated boost power converter according to any of claims 1-9, wherein the boost inductor comprises a first half-winding and a second half-winding of the primary transformer winding to provide an integrally formed boost inductor and primary winding.

13. An isolated boost power converter according to any of the preceding claims, further comprising a rectifying element electrically coupled to the center-tap to conduct a discharge

current, during the second discharge state, from the first and second secondary transformer windings to the rectified converter output voltage, V_{out}.

14. An isolated boost power converter according to any of claims 1-12, wherein the rectification circuit comprises a center-tapped rectifier wherein:

- the center-tap is electrically connected to a negative rectified converter output voltage or the rectified converter output voltage, V_{out},
- the respective outputs of the first and second secondary transformer windings are coupled to the opposite output voltage to the one electrically coupled to the center-tap through first and second rectifying elements.

15. An isolated boost power converter according to any of the preceding claims, wherein the rectification circuit comprises a voltage doubler circuit.

16. An isolated boost power converter according to claim 13, wherein the rectifying element and/or the rectification circuit comprises one or more semiconductor diode(s), diode-coupled transistor(s), synchronously controlled transistor switch(es).

17. An isolated boost power converter according to claim 9, further comprising:

- a second magnetically permeable multi-legged core,
- a second boost inductor magnetically coupled to a center leg of the second magnetically permeable multi-legged core to store magnetic energy therein,
- the second boost inductor being electrically coupled between the input terminal and a second driver to be alternatingly charged and discharged with magnetic energy,
- the second driver having a second driver output coupled to a second primary transformer winding wound around a first outer leg and a second outer leg of the second magnetically permeable transformer core,
- the second driver being configured to generate a second primary voltage to the second primary transformer winding in accordance with the driver control signal,

- first and second secondary transformer windings wound around the first outer leg and the second outer leg, respectively, of the second magnetically permeable multi-legged core, wherein:

- the first secondary transformer winding of the second magnetically permeable multi-legged core is coupled in series between the rectification circuit and the output of the first secondary transformer winding of the magnetically permeable multi-legged core; and

- the second secondary transformer winding of the second magnetically permeable multi-legged core is coupled in series between the rectification circuit and the output of the second secondary transformer winding of the magnetically permeable multi-legged core such that:.

- in the first discharge state, the respective magnetic energies stored in the first and second boost inductors are discharged by directing respective discharge currents from the respective boost inductors through the respective primary transformer windings,

- in the second discharge state, the respective magnetic energies stored in the respective boost inductors are discharged by discharging respective magnetic fluxes through the respective first and second secondary transformer windings.

18. An isolated boost power converter according to claim 17, wherein the first and second magnetically permeable multi-legged cores share a common magnetic flux path extending through a shared magnetically permeable leg.

19. An isolated boost power converter according to claim 18, wherein the first and second magnetically permeable multi-legged cores are configured to provide magnetic flux cancellation or suppression in the common magnetically permeable leg.

20. An isolated boost power converter according to any of the preceding claims, wherein the driver control signal comprises a pulse width modulated signal having an adjustable duty cycle, D.

21. A method of generating a rectified converter output voltage, V_{out} from an input voltage, V_{in}, by an isolated boost power converter according to any of the preceding claims, comprising steps of:

- generating a pulse width modulated driver control signal,
- supplying the pulse width modulated driver control signal to the driver,
- gradually increasing a duty cycle, D, of the pulse width modulated driver control signal from below 0.5, preferably below 0.1, to a value above 0.5, preferably between 0.55 and 0.99,
- adjusting the duty cycle, D, to a desired value to reach a desired or target AC or DC voltage at the rectified converter output voltage, V_{out}.

ABSTRACT

The present invention relates to an isolated boost power converter comprising a boost inductor being wound around a first leg of a magnetically permeable multi-legged core. The boost inductor is electrically coupled between an input terminal of the boost converter and a transistor driver to be alternatingly charged and discharged with magnetic energy. A first and second series connected secondary transformer windings with a center-tap arranged in-between are wound around separate legs of the magnetically permeable multi-legged core. In a first discharge state, the magnetic energy of the boost inductor is discharged by directing a discharge current from the boost inductor through a primary transformer winding and in a second discharge state, the magnetic energy of the boost inductor is discharged by discharging a magnetic flux through the first and second secondary transformer windings. In this manner, the secondary transformer windings can replace the traditional separate flyback winding used for start-up purposes of isolated boost power converters.

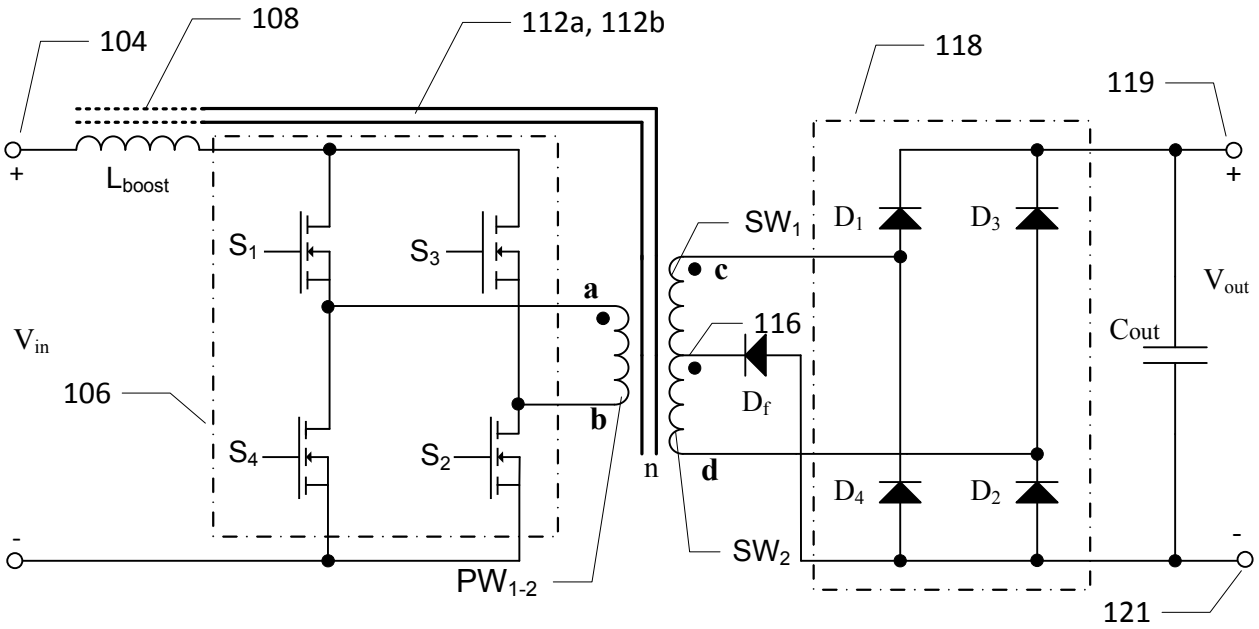
104
108
112a, 112b
118
119
+
L_{boost}
S_1
S_3
SW_1
D_1
D_3
+
a
c
V_{out}
V_{in}
116
Cout
106
D_f
b
S_4
S_2
n
d
D_4
D_2
-
SW_2
-
PW_{1-2}
121

a)

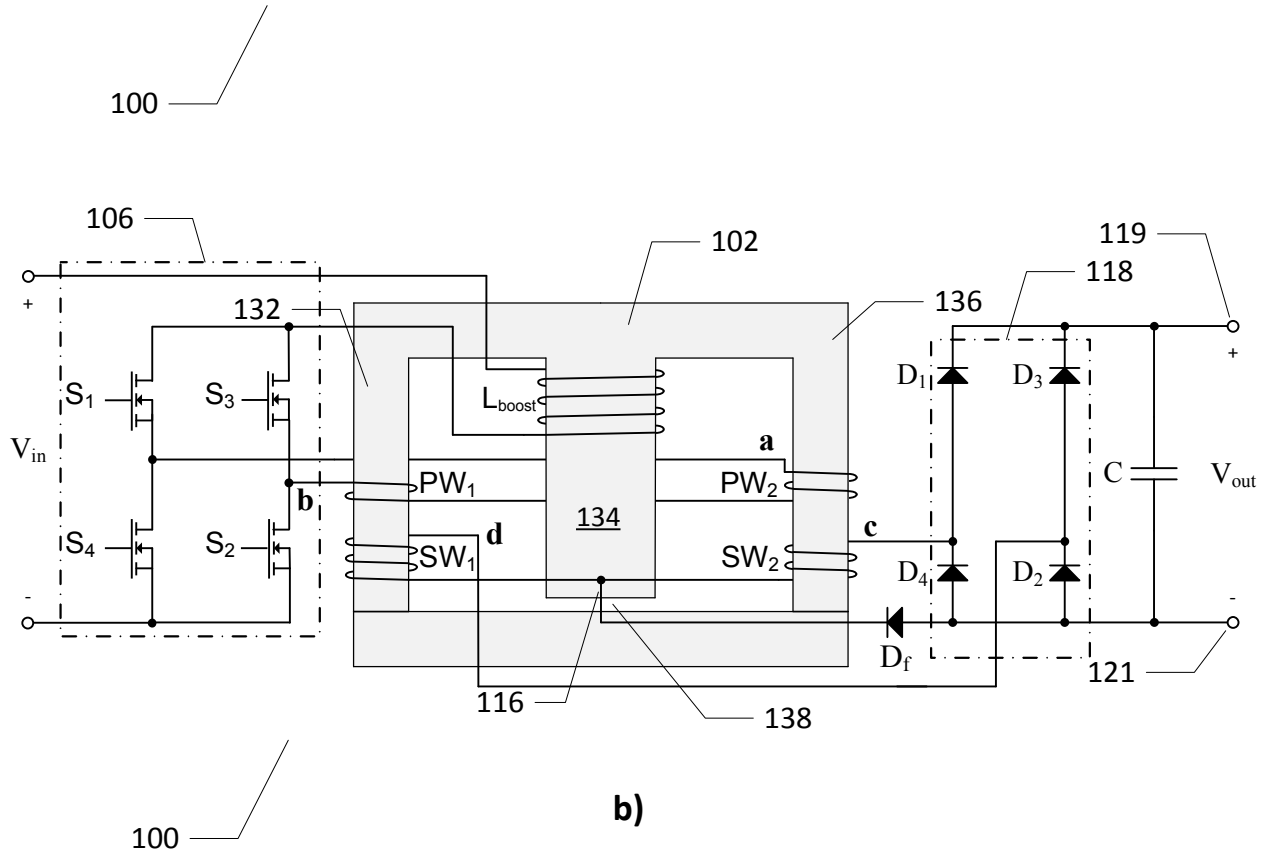
100
106
102
119
118
+
132
136
S_1
S_3
L_{boost}
D_1
D_3
+
a
V_{in}
PW_1
PW_2
C
V_{out}
b
134
S_4
S_2
d
SW_1
c
SW_2
D_4
D_2
-
D_f
-
116
138
121
100

b)

Fig. 1

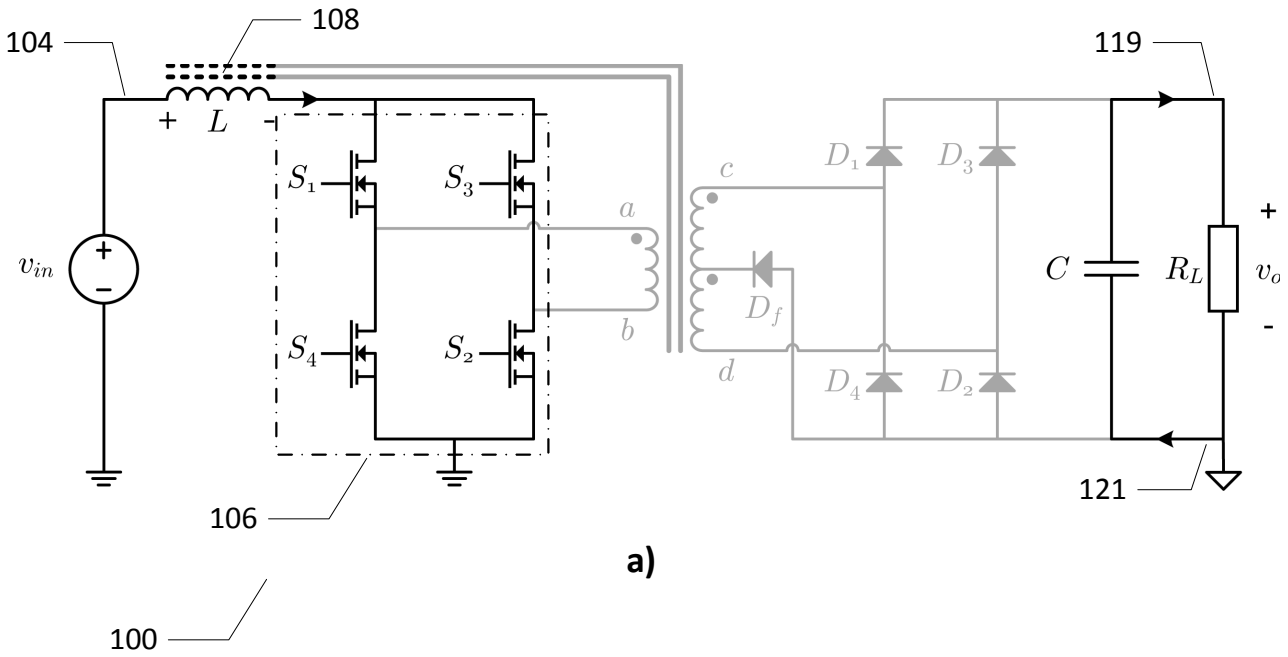
104
108
119
L
S_1
S_3
S_4
S_2
a
b
c
d
D_1
D_3
D_4
D_2
D_f
v_{in}
C
R_L
v_o
106
121
100
a)

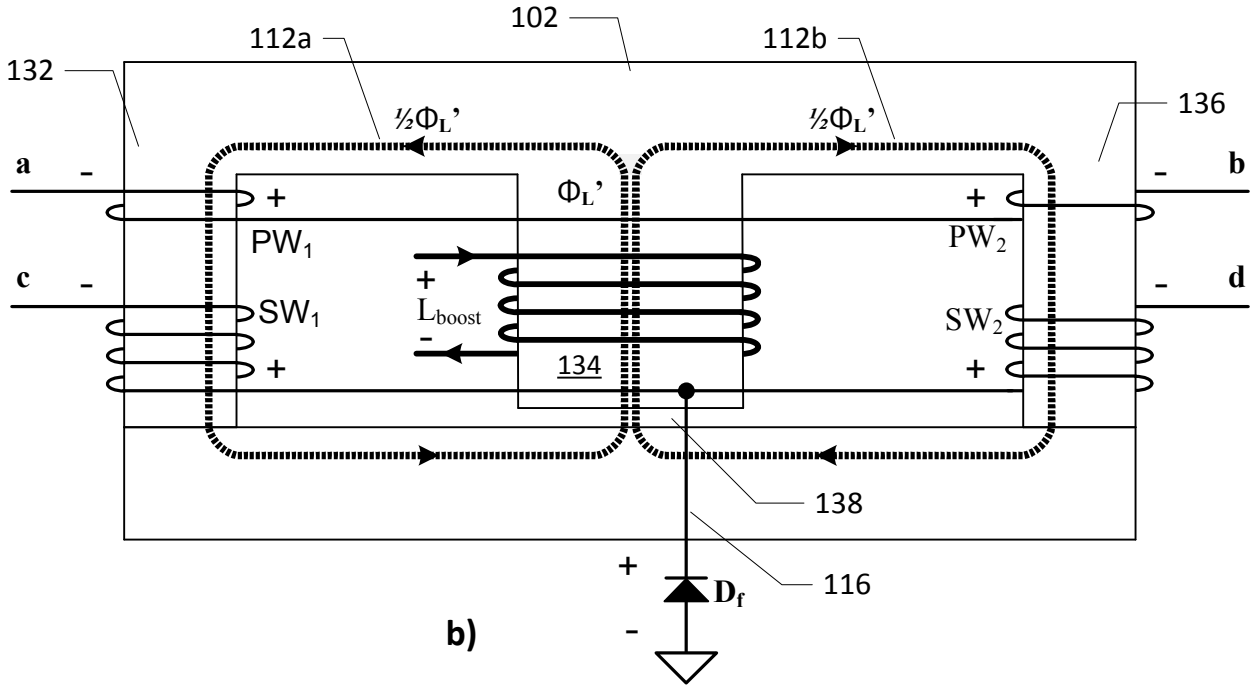
102
112a
112b
132
136
½Φ_L'
½Φ_L'
a
b
c
d
Φ_L'
PW_1
PW_2
SW_1
SW_2
L_boost
134
138
116
D_f
b)

Fig. 2

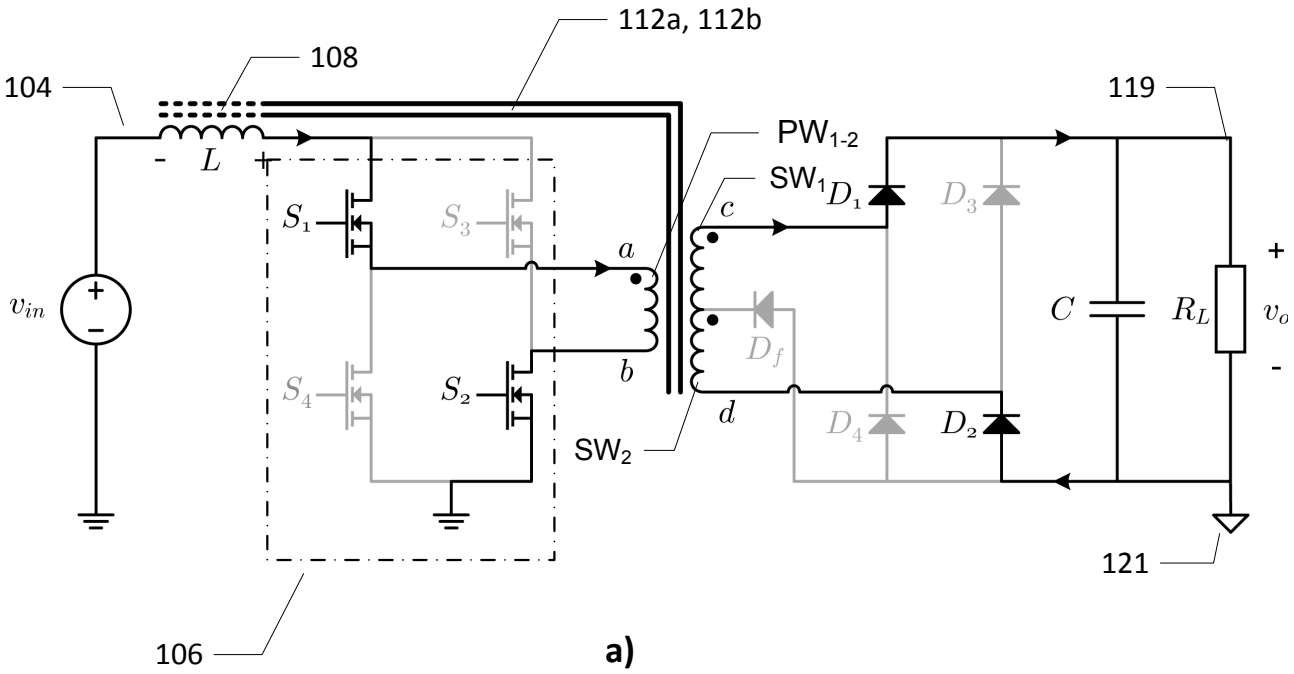
112a, 112b
108
104
119
PW1-2
SW1
L
S1
S3
a
c
D1
D3
vin
C
RL
vo
Df
b
S4
S2
d
D4
D2
SW2
121
106

a)

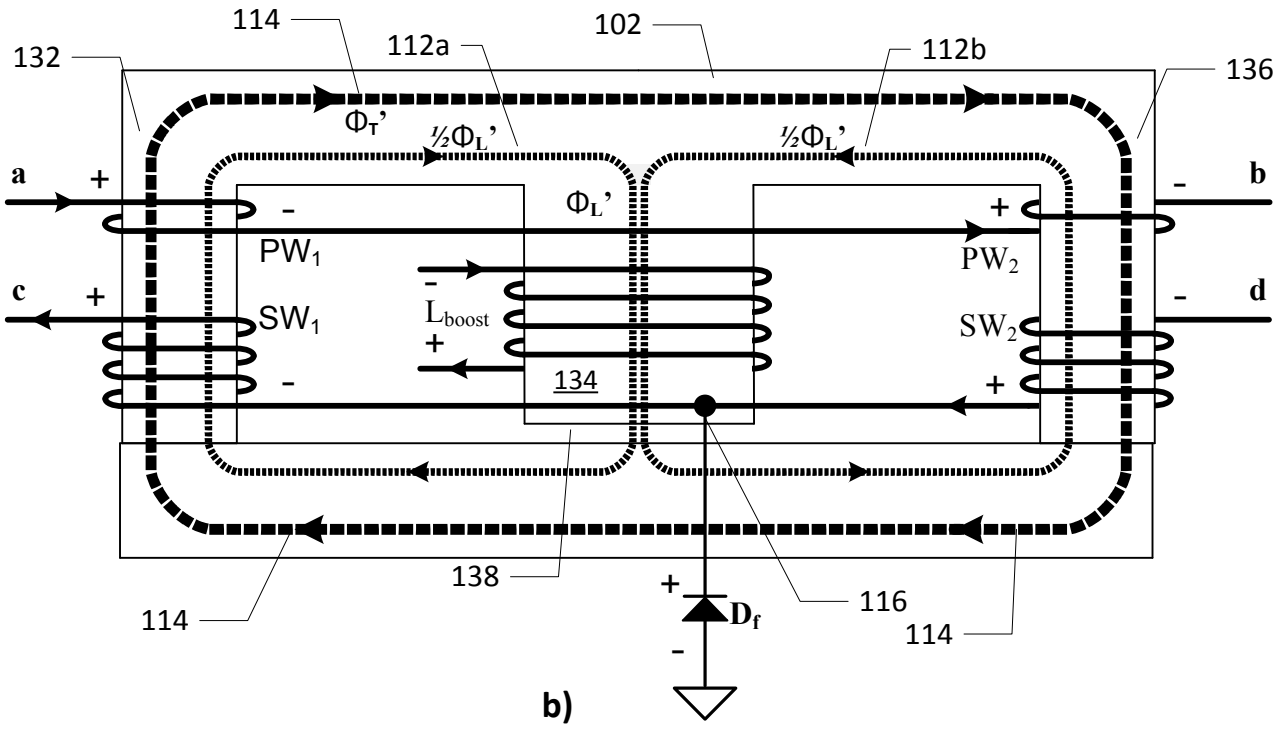
114
102
132
112a
112b
136
Φτ'
½ΦL'
½ΦL'
a
b
ΦL'
PW1
PW2
c
d
SW1
Lboost
SW2
134
138
116
114
114
Df

b)

Fig. 3

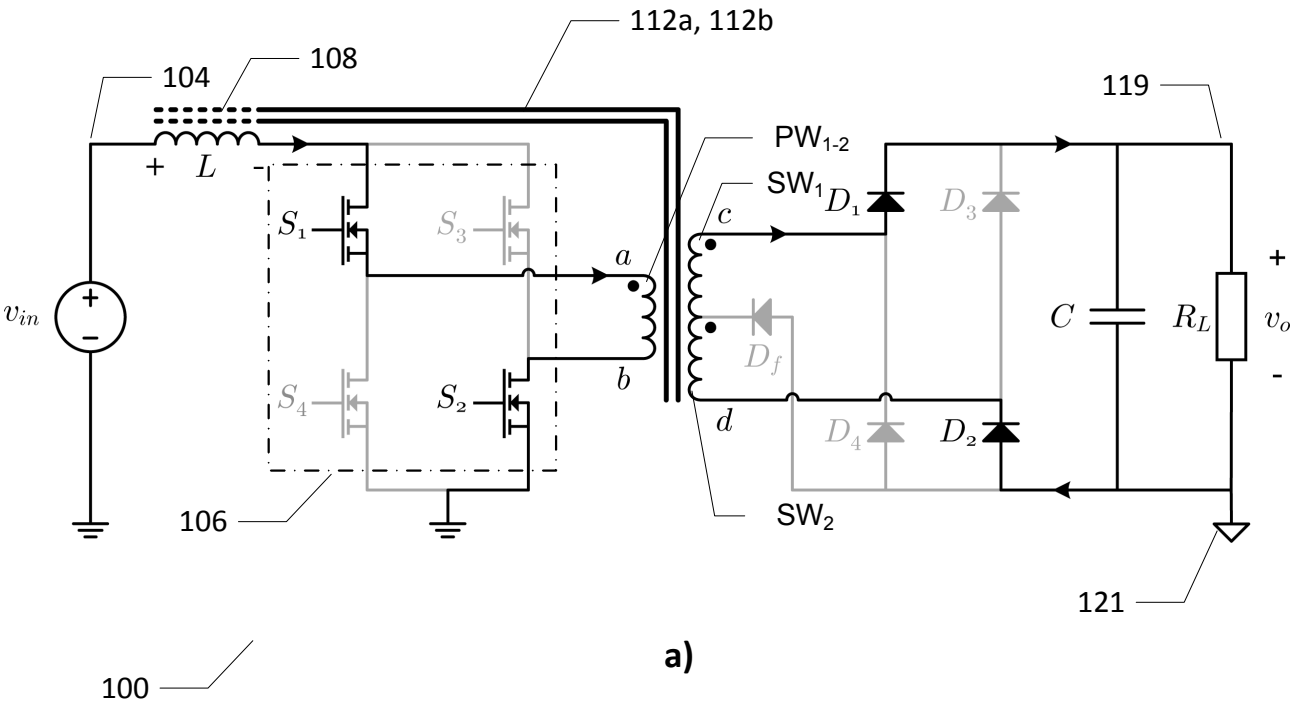
112a, 112b
104
108
119
PW1-2
SW1
L
S_1
S_3
S_4
S_2
a
b
c
d
D_1
D_3
D_f
D_4
D_2
v_{in}
C
R_L
v_o
106
SW2
121
100

a)

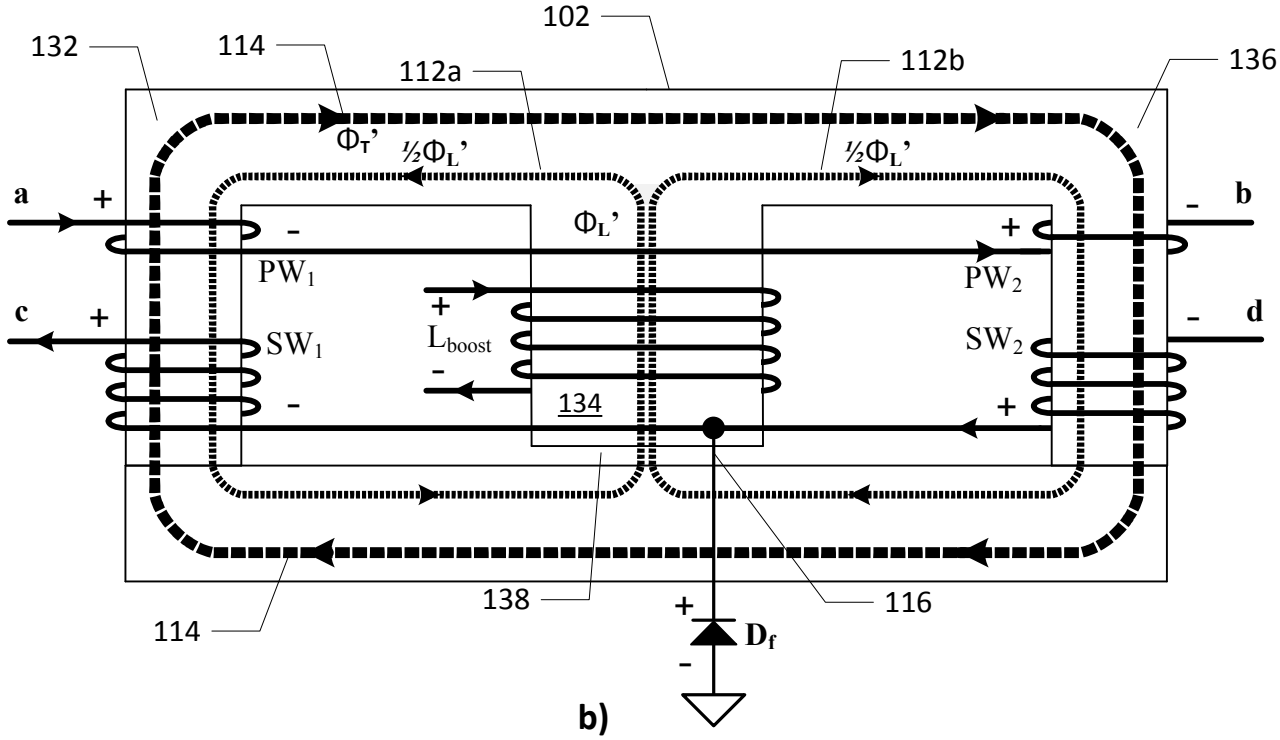
102
132
114
112a
112b
136
Φτ'
½ΦL'
½ΦL'
ΦL'
a
b
c
d
PW1
PW2
SW1
SW2
Lboost
134
138
116
114
Df

b)

Fig. 4

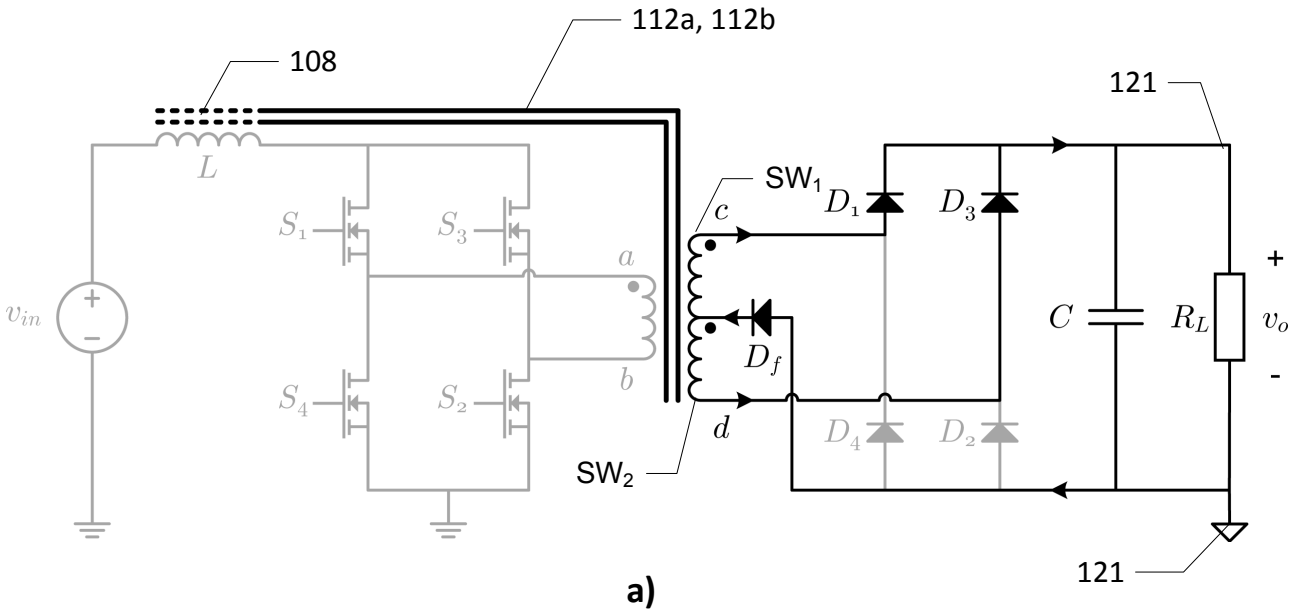
112a, 112b
108
121
L
SW1
D1
D3
c
S1
S3
a
+
vin
−
C
RL
vo
-
Df
b
S4
S2
d
D4
D2
SW2
121

a)

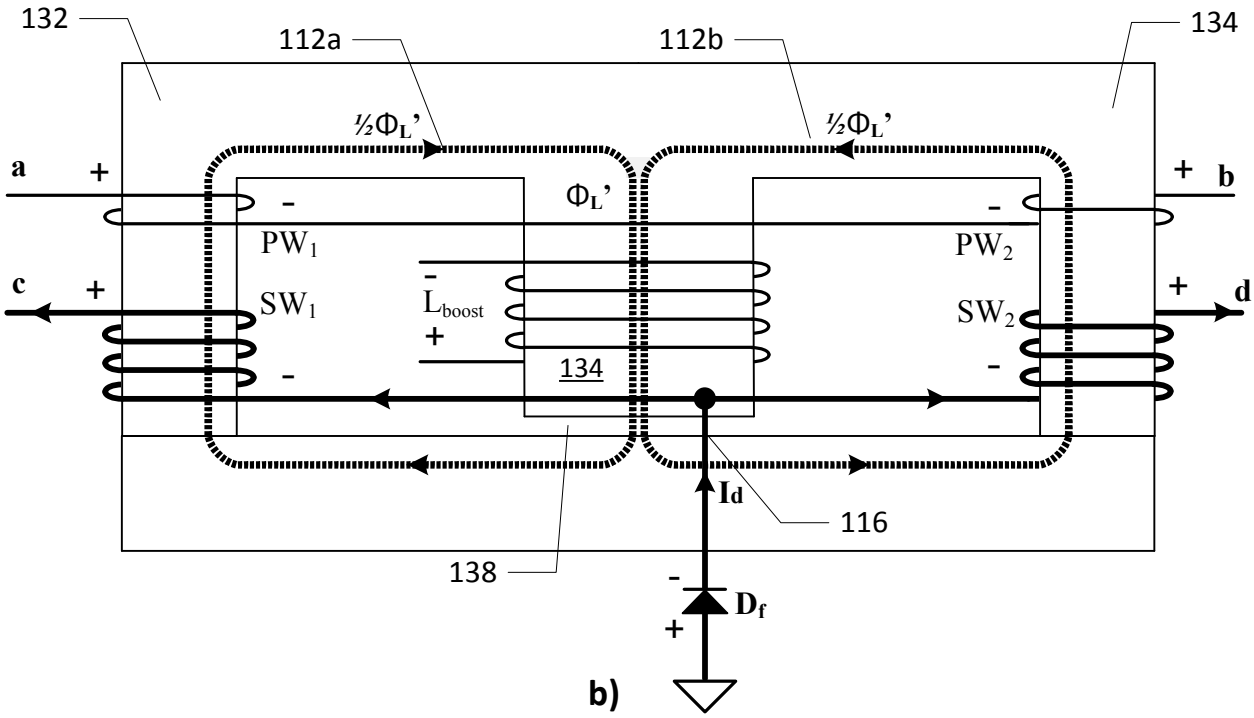
132
112a
112b
134
½ΦL'
½ΦL'
a
+
+
b
-
ΦL'
PW1
-
PW2
c
+
SW1
-
Lboost
+
SW2
+
d
134
-
-
Id
116
138
-
Df
+

b)

Fig. 5

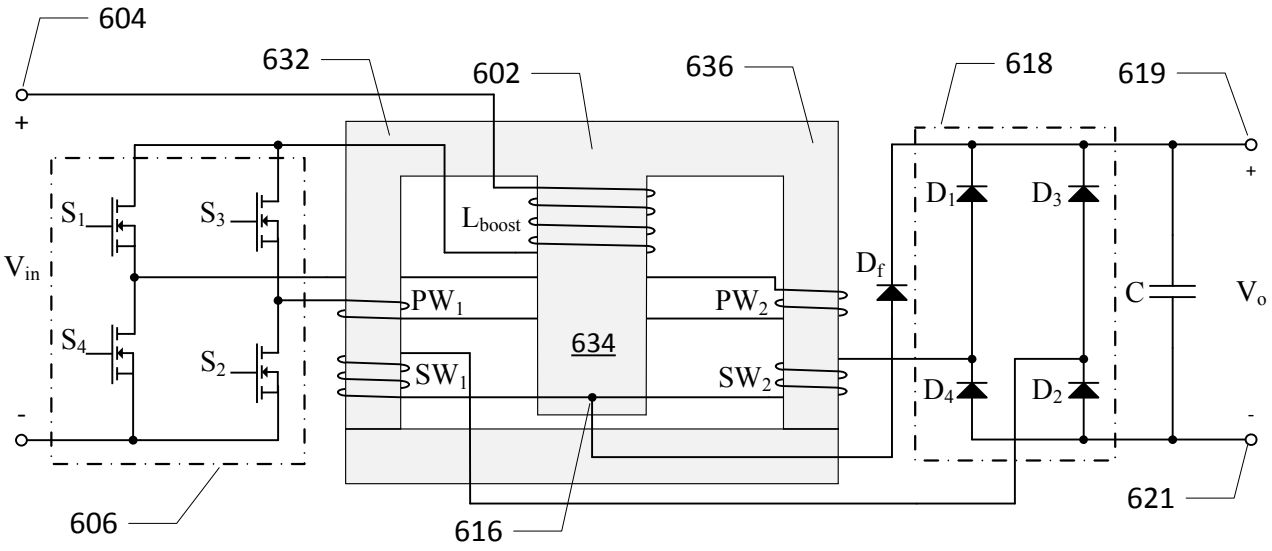
604
632
602
636
618
619
+
V_{in}
S_1
S_3
S_4
S_2
-
L_{boost}
PW_1
PW_2
SW_1
SW_2
634
D_f
D_1
D_3
D_4
D_2
C
V_o
606
616
621

a)

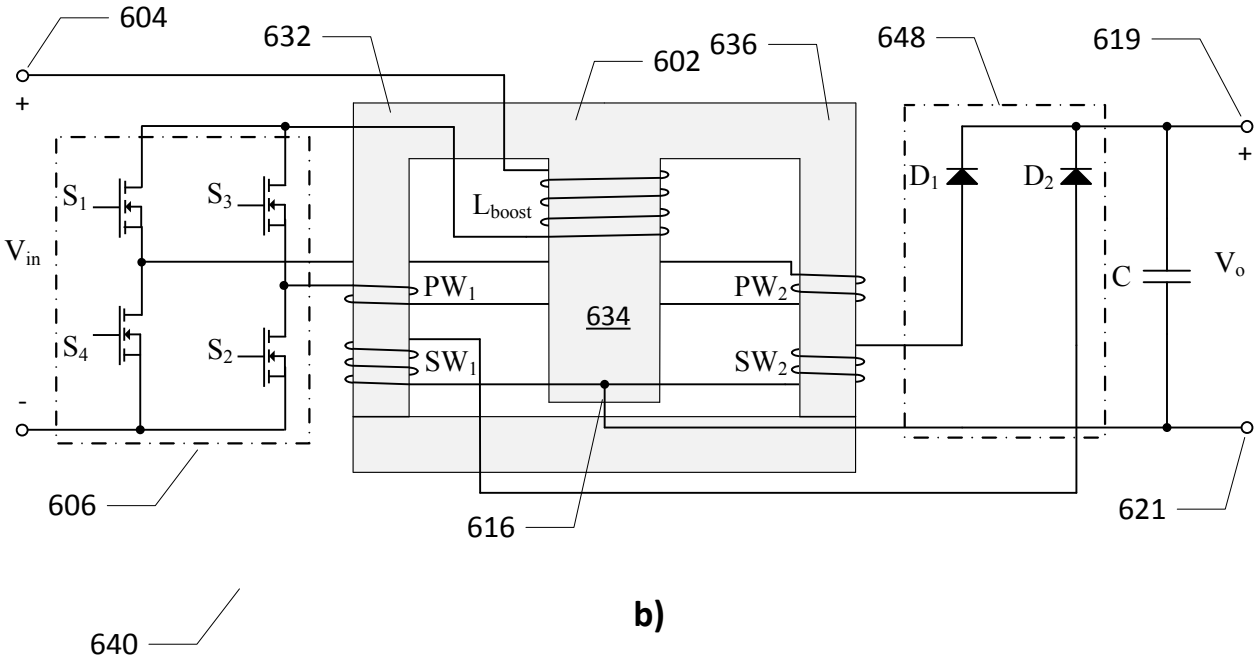
604
632
602
636
648
619
+
V_{in}
S_1
S_3
S_4
S_2
-
L_{boost}
PW_1
PW_2
SW_1
SW_2
634
D_1
D_2
C
V_o
606
616
621
640

b)

Fig. 6

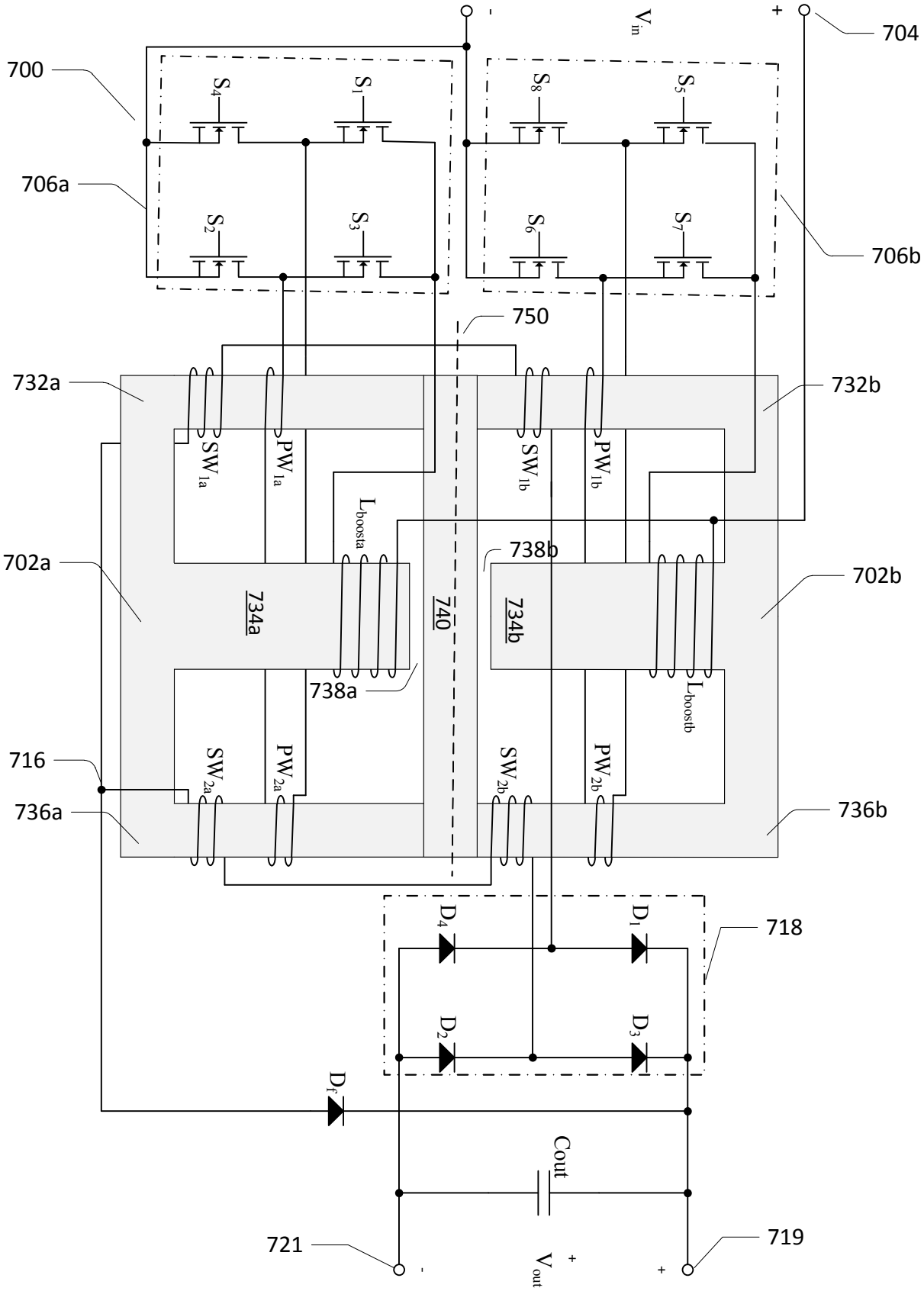
700
704
706a
706b
750
732a
732b
702a
702b
738b
738a
716
736a
736b
718
721
719
V_{in}
V_{out}
S_1
S_2
S_3
S_4
S_5
S_6
S_7
S_8
SW_{1a}
PW_{1a}
SW_{1b}
PW_{1b}
L_{boosta}
L_{boostb}
SW_{2a}
PW_{2a}
SW_{2b}
PW_{2b}
734a
734b
740
D_1
D_2
D_3
D_4
D_f
Cout

Fig. 7

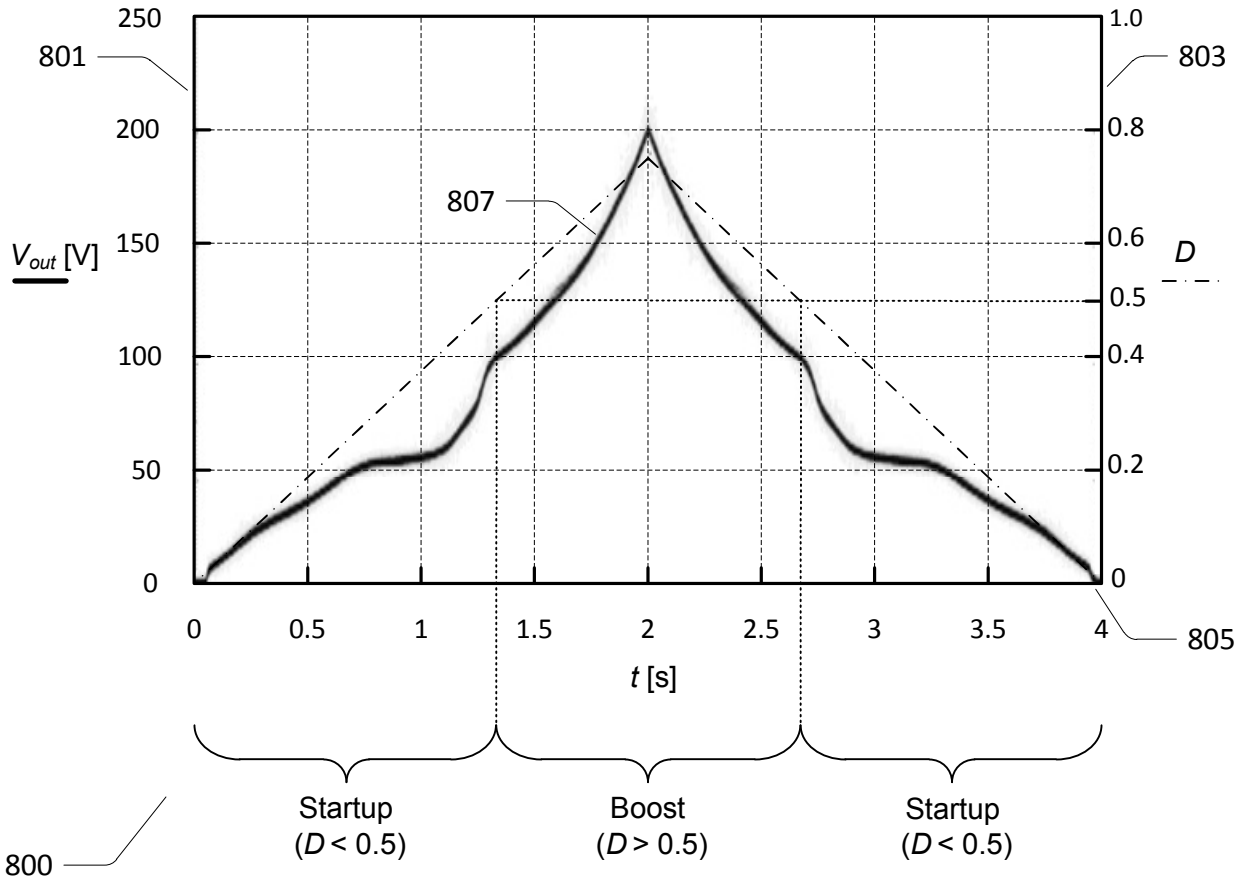
250
200
150
100
50
0
801
V_{out} [V]
807
1.0
0.8
0.6
0.5
0.4
0.2
0
803
D
805
0
0.5
1
1.5
2
2.5
3
3.5
4
t [s]
800
Startup
(D < 0.5)
Boost
(D > 0.5)
Startup
(D < 0.5)

Fig. 8

Appendix B.11

[B.11] Z. Ouyang, M. A. E. Andersen and Z. Zhang, “An integrated magnetics component,” *EU & US Patent*, US application no. 61534202, and EU application no. EP11181106.3, 2011 (pending).

NIXON PEABODY LLP
Customer No. 70001

PATENT
059244-7PL01

U.S. PROVISIONAL PATENT APPLICATION

FOR

AN INTEGRATED MAGNETICS COMPONENT

BY

ZIWEI OUYANG

MICHAEL A. E. ANDERSEN

and

ZHE ZHANG

AN INTEGRATED MAGNETICS COMPONENT

COPYRIGHT

FIELD OF THE PRESENT DISCLOSURE

[0002] The present invention relates to an integrated magnetics component comprising a magnetically permeable core comprising a base member extending in a horizontal plane and first, second, third and fourth legs protruding substantially perpendicularly from the base member. First, second, third and fourth output inductor windings are wound around the first, second, third and fourth legs, respectively. A first input inductor winding of the integrated magnetics component has a first coil axis and extends in-between the first, second, third and fourth legs to induce a first magnetic flux through a first flux path of the magnetically permeable core. A second input inductor winding of the integrated magnetics component has a second coil axis extending substantially perpendicularly to the first coil axis to induce a second magnetic flux through a second flux path of the magnetically permeable core extending substantially orthogonally to the first flux path. Another aspect of the invention relates to a multiple-input isolated power converter comprising the integrated magnetics component.

BACKGROUND

[0003] In order to combine power generated from two or more input voltage or energy sources to get a DC output voltage, different circuit topologies of multi-input power converters have been proposed in recent years [1-4]. The input voltage or energy sources may for example comprise clean energy sources such as solar arrays, wind turbines, fuel cells and commercial ac power lines.

[0004] A common limitation of some known multiple-input power converters is that only one input power source is allowed to transfer power or energy to the output at a time to prevent power coupling effect. Recently, in order to overcome this limitation, it has been proposed to use multiple-input winding transformers based on flux additivity technology with phase-shifted

PWM control. While this technology can transfer power from two or multiple different input voltage sources to the DC output and its associated load individually or simultaneously [5], reverse blocking diodes are required at the input drivers of the multi-input power converter. The reverse blocking diodes are needed to prevent a reverse power flow from one of the input voltage sources to another input voltage source through the coupled primary side of the transformer and through body diodes of semiconductor switches of the input drivers. Without these reverse-blocking diodes, different input sources coupled to the multi-input power converter cannot deliver power to the load simultaneously. Some prior art approaches to overcome the problems associated with the coupling between the transformer input windings have relied on a shared low reluctance path or utilized flux cancellation mechanisms to decouple the input windings of a transformer [6]. In addition, higher current stress in low side MOSFETs of the input driver can be imposed due to a clamped voltage of the mutually coupled input inductor windings which causes a higher power loss.

[0005] Consequently, it would be advantageous to provide an integrated magnetics component with uncoupled input inductor windings for use in multiple-input power converters and other applications to allow multiple input power sources to be operated independently without compromising any functions of the power converter or require complex control or protection circuitry to be added to the input drivers.

SUMMARY

[0006] A first aspect of the invention relates to an integrated magnetics component comprising: a magnetically permeable core comprising a base member and a top member, the base member extending in a horizontal or first plane and comprises first, second, third and fourth legs protruding substantially perpendicularly from the base member. The top member is attached to opposite ends of the first, second, third and fourth legs relative to the base member. The integrated magnetics component additionally comprises first, second, third and fourth output inductor windings wound around the first, second, third and fourth legs, respectively. The integrated magnetics component also comprises a first input inductor winding having a first coil axis and extending in-between the first, second, third and fourth legs to induce a first magnetic flux through a first flux path of the magnetically permeable core, and a second input inductor winding having a second coil axis, extending substantially perpendicularly to the first coil axis,

to induce a second magnetic flux through a second flux path of the magnetically permeable core. The second flux path extending substantially orthogonally to the first flux path.

[0007] The present invention is accordingly based on a new flux path decoupling concept for use e.g. in multiple-input power converters such as boost converters and buck converters etc. The flux path decoupling concept is based on 2-dimensional (2D) or a 3-dimensional (3D) space orthogonal flux decoupling wherein the first and second flux paths extend substantially orthogonally to each other within the shared magnetically permeable core.

[0008] In a preferred embodiment, the magnetically permeable core comprises a new unusual geometry wherein the first, second, third and fourth legs are arranged in a substantially rectangular or quadratic pattern at the base member with the first, second, third and fourth legs situated at respective corners. In this embodiment, the first and second input inductor windings may be arranged in a cross-shaped layout with the first, second, third and fourth legs located in respective ones of four quadrant areas.

[0009] The skilled person will appreciate that a cross-sectional profile of each of the first, second, third and fourth legs may vary considerably depending on a particular application. The cross-sectional profile may e.g. be circular, elliptical, rectangular, pentagon, hexagon, heptagon, octagon etc. The shape of each of the first, second, third and fourth output inductor windings may be adapted to conform to anyone of these cross-sectional profiles of the legs so as to fit tightly around the leg in question. Furthermore, each of the first, second, third and fourth output inductor windings may comprise a single inductor winding or a plurality of full inductor windings.

[0010] In one embodiment, the first coil axis and the second coil axis both extend in, or parallelly with, the horizontal plane. In one such embodiment, the first and second input inductor windings are arranged proximate to each other for example in abutment such that the first and second input inductor windings are abutted and overlapped in a central region of the base member.

[0011] In other embodiments, the first and second input inductor windings are vertically off-set (i.e. off-set in the direction in which the first, second, third and fourth legs protrude) such that the first or second input inductor winding is arranged in abutment with, or fastened to, the base member while the other input inductor winding is raised a certain distance above the base member towards the top member.

[0012] Each of the first and second input inductor windings may comprise a flat strip of electrically conductive material such as copper or aluminum and preferably comprises an electrical insulation layer. The flat strips of electrically conductive material may be arranged in abutment with the base member or in abutment with the top member. If the base member comprises an essentially flat upper surface, the flat strips of electrically conductive material may be fastened to the flat upper surface of the base member. The flat strips of electrically conductive material may be formed as straight strips forming respective half-windings extending orthogonally in the horizontal plane.

[0013] In another embodiment, each of the flat strips of electrically conductive material may be U-shaped with a pair of substantially parallel winding legs extending in or parellelly to the horizontal plane and a bridging portion or neck connecting the two winding legs both mechanically and electrically. In both cases, the first and second input inductor windings may be attached to the base member by gluing or similar processes.

[0014] According to an advantageous embodiment of the invention, the integrated magnetics component comprises a third input inductor winding having a third coil axis and extending between a diagonal pair of the first, second, third and fourth legs to induce a third magnetic flux through a third flux path of the magnetically permeable core; wherein the third flux path extends substantially orthogonally to the first flux path and substantially orthogonally to the second flux path in the magnetically permeable core. This embodiment is capable of supporting a three-input power converters capable of transferring power from three different input voltage sources to the DC output voltage individually or simultaneously. The fact that the third flux path extends substantially orthogonally to both the first and second flux paths provides a 3-dimensional (3D) space orthogonal flux decoupling wherein the first, second and third flux paths extend substantially orthogonally to each other within the shared magnetically permeable core.

[0015] In one embodiment, the top member comprises fifth, sixth, 7^{th} and 8^{th} legs extending parallelly to the horizontal plane. This is preferably achieved by placing a through-going aperture of appropriate dimensions in the top member leaving 4 vertices that form respective ones of the fifth, sixth, 7^{th} and 8^{th} legs. In one such embodiment, the magnetically permeable core comprises a hollow cubic structure wherein the first, second, third, fourth, fifth, sixth, 7^{th} and 8^{th} legs form respective vertices of the hollow cubic structure. In this embodiment, the base member may also comprise a central aperture.

[0016] In a preferred embodiment, the first, second, third and fourth legs are arranged at respective positions of the base member such that fi**r**st and second substantially orthogonally extending valleys or trenches are formed at a surface of the base member. The first and second input inductor windings are projecting through the first trench and the second trench, respectively. Bottom surfaces of the first and second trenches may be essentially plane and arranged in the horizontal plane such that each of the trenches are delimited by the first, second, third and fourth legs.

[0017] The base member may comprise an essentially flat rectangular plate with the first, second, third and fourth legs arranged at respective corners of the base member.

[0018] The top member may comprise an essentially flat rectangular plate arranged substantially parallelly to the flat rectangular base plate to contact and terminate the first, second, third and fourth legs at respective corners of the top member. The latter embodiment provides a magnetically permeable core with a regular cubic shape. In other embodiments, the base member may have a shape of a flat circular, elliptical, pentagon, hexagon, heptagon, octagon etc. structure wherein the first, second, third and fourth legs are arranged at respective circumferential edges of the structure.

[0019] The first input inductor winding preferably comprises first and second electrical terminals arranged at opposite ends of the first winding and the second input inductor winding preferably also comprises first and second electrical terminals arranged at opposite ends of the second winding. The first input inductor winding may comprise a single straight electrical conductor, such as a flat strip of electrically conductive material as discussed above and the second input inductor winding may also comprise a single straight electrical conductor. The first and second electrical terminals serve as externally accessible inputs of the input inductor windings for electrical driver circuits such as a transistor based half-bridge or full-bridge driver to establish electrical connection to the inductor winding in question and supply a drive signal thereto.

[0020] The first input inductor winding may comprise a single or a plurality of full inductor winding(s) wound around the base member or wound around the top member; and the second input inductor winding comprise a single or a plurality of full inductor winding(s) wound around the base member or wound around the top member. The choice of the exact number of windings on each of the first and input inductor windings depends on a multitude of design considerations

of a power converter, such as a dual-input or triple-input isolated boost/buck DC-DC converter, using the integrated magnetics component. Power converter parameters like input signal switching frequency, input and output voltages, output power level and power efficiency, etc are typically relevant characteristics in determining the number of windings of each of the first and input inductor windings. However, in a number of useful embodiments, each of the first and second input inductor windings comprises between 2 and 50 individual windings and each of the first, second, third and fourth output inductor windings comprises between 2 and 50 individual windings.

[0021] In another embodiment, the first input inductor winding comprise a single or a plurality of full inductor winding(s) wound around a first pair of adjacent legs of the first, second, third and fourth legs; and the second input inductor winding comprise a single or a plurality of full inductor winding(s) wound around a second pair of adjacent legs of the first, second, third and fourth legs whereby the single or plurality of full inductor winding(s) of each of the first and second input inductor windings extend exclusively above the base member or above the top member in or parallel to the horizontal plane. In this embodiment, the first and second inductor winding possess a horizontally folded geometry or layout. The horizontally folded geometry of the first input inductor winding is wound around, or encircles, a first pair of adjacently arranged legs and the horizontally folded geometry of the second input inductor winding is wound around, or encircles, a second pair of adjacently arranged legs. A significant advantage of this embodiment is that the first and second input inductor windings can easily be integrated with standard types of stiff or flexible printed circuit boards (PCBs). Other components of the power converter can be integrated on the PCB together with the inductor windings such that effective modularization of the power converter is enabled.

[0022] According to a preferred embodiment of the invention, the first input inductor winding is configured to generate a magnetic flux in a first direction through a first pair of adjacent legs arranged on a first side of the first input inductor winding and an oppositely directed magnetic flux through a second pair of adjacent legs arranged on a second and opposite side of the first input inductor winding. In addition, the second input inductor winding is configured to generate a magnetic flux in a second direction through a first pair of adjacent legs arranged on a first side of the second input inductor winding and an oppositely directed magnetic flux through a second pair of adjacent legs arranged on a second and opposite side of the second

input inductor winding. The magnetic fluxes are inducted by flow of input currents in the first and second input inductor windings and since the current in each input inductor winding can flow in two different directions four different input current states are created. In each state, a resulting magnetic flux in each of the first, second, third and fourth leg is set by contributions from both the first magnetic flux and the second magnetic flux. This implies that an output voltage induced in each of the first, second, third and fourth output inductor windings likewise is determined by the contributions from both of the first and second input currents . This property leads to a new and highly flexible way of using phase control between first and second pulse width modulated drive signals, applied to the first and second input inductor windings, respectively, for controlling a DC output voltage of a multiple-input power converter employing the present integrated magnetics component as described below in further detail.

[0023] A second aspect of the present invention therefore relates to a multiple-input isolated power converter comprising an integrated magnetics component according to any of the above-described embodiments thereof. The multiple-input isolated power converter further comprises a first input driver electrically coupled to the first input inductor winding to supply a first drive signal thereto and a second input driver electrically coupled to the second input inductor winding to supply a second drive signal thereto. The output inductor windings of a first pair of diagonal legs are coupled electrically to a first output rectification circuit and the output inductor windings of a second pair of diagonal legs are coupled electrically to a second output rectification circuit. The first and second output rectification circuits are preferably coupled in parallel to a DC output voltage node or terminal such that input power delivered through both the first input driver and the second input driver are transferred to a common DC output voltage.

[0024] In one embodiment of the multiple-input isolated power converter, the output inductor windings of the first pair of diagonal legs are connected in series and the output inductor windings of the second pair of diagonal legs are connected in series.

[0025] The previously described 2D or 3D orthogonal flux decoupling of the first and second input inductor windings (and possibly third input inductor winding) allow these to be operated independently such that the first and second input drivers can be coupled to a common electrical potential like ground. The skilled person will understand that the present multiple-input isolated power converter can have a variety of different topologies such as a boost or a buck topology or configuration.

[0026] A third aspect of the present invention relates to a method of controlling a DC output voltage of the multiple-input isolated power converter described above, the method comprising steps of:

- generating a first a pulse width modulated drive signal having a first phase angle on the first input inductor winding,

- generating a second pulse width modulated drive signal having a second phase angle on the second input inductor winding,

- adjusting a phase angle difference between the first and second phase angles to control the DC output voltage. The method may comprise of a further step of:

- adjusting a duty cycle of the first pulse width modulated drive signal and/or a duty cycle of the second pulse width modulated drive signal to adjust the DC output voltage. The ability to control the DC output voltage either by adjusting the duty cycle, adjusting the phase angle difference or adjusting both leads to an extremely flexible way of controlling the DC output voltage with numerous benefits such as the provision of wider input and/or output voltage ranges of the multiple-input isolated power converter. Consequently, the same isolated power converter can be readily adapted to a broad variety of applications and therefore reduces the required number of variants of a given power converter topology, lowering assembly costs, component costs, stock costs etc. The flexible adaptation offered by the present multiple-input isolated power converter is particularly well-suited for power conversion in connection with clean energy sources like photovoltaic cells which often output a wide range of different voltages.

BRIEF DESCRIPTION OF THE DRAWINGS

[0027] Preferred embodiments of the invention will be described in more detail in connection with the appended drawings, in which:

[0028] Fig. 1 shows an assembled view of an integrated magnetics component in accordance with a first embodiment of the invention,

[0029] Fig. 2 shows an exploded perspective view of the integrated magnetics component in accordance with the first embodiment of the invention,

[0030] Fig. 3 illustrates schematically first and second orthogonally extending magnetic flux paths in a magnetically permeable core of the integrated magnetics component in accordance with the first embodiment of the invention,

[0031] Fig. 4 shows an exploded perspective view of an integrated magnetics component in accordance with a second embodiment of the invention,

[0032] Fig. 5 shows an assembled view of the integrated magnetics component in accordance with a third embodiment of the invention,

[0033] Fig. 6 shows an exploded perspective view of the integrated magnetics component in accordance with the third embodiment of the invention,

[0034] Figs. 7a), b), c) and d) illustrate respective magnetic flux directions through the four legs of the integrated magnetics component in accordance with the first embodiment of the invention for four different input current states,

[0035] Fig. 8 shows an assembled perspective view of an integrated magnetics component comprising three input inductor windings in accordance with a fourth embodiment of the invention,

[0036] Fig. 9 illustrates schematically first, second and third orthogonally arranged magnetic flux paths in the core of the integrated magnetics component in accordance with the fourth embodiment of the invention,

[0037] Fig. 10 shows an assembled perspective view of an integrated magnetics component comprising three input inductor windings in accordance with a fifth embodiment of the invention,

[0038] Fig. 11 is a schematic drawing of a dual-input isolated boost DC-DC converter comprising an integrated magnetics component in accordance with the first embodiment of the invention,

[0039] Fig. 12 shows two graphs depicting respective sets of simulated input and output voltage waveforms of a prototype dual-input isolated boost DC-DC converter for phase angle shifts between the first and second input voltage waveforms of 90 degrees and 0 degrees; and

[0040] Fig. 13 shows two graphs depicting respective sets of simulated input and output voltage waveforms of a prototype dual-input isolated boost DC-DC converter for phase angle shifts between the first and second input voltage waveforms of 180 degrees and 45 degrees.

DETAILED DESCRIPTION

[0041] The embodiments described in detail below are particularly well-suited for application in isolated boost power converters providing DC voltage amplification or step-up.

However, the skilled person will understand that the below described integrated magnetics component embodiments are highly useful for other types of applications such as buck type power converters and multi-coupled inductors with variable coupling coefficients.

[0042] Fig. 1 shows an assembled perspective view of an integrated magnetics component 100 in accordance with a first embodiment of the invention. The integrated magnetics component 100 comprises a magnetically permeable core 101 comprising a base member 102 and a top member 104. The base member 102 comprises a first leg 110, a second leg 112, a third leg 114 and fourth leg 116 all protruding substantially perpendicularly from the base member 102 to a lower surface of the top member such that the top member is attached to opposite ends of the first, second, third and fourth legs, 110, 112,114 and 116, respectively, relative to the base member 102. The attachment between the opposite ends of the first, second, third and fourth legs, 110, 112,114 and 116, respectively, and the top member may be provided in numerous ways such as by soldering, gluing, welding, press-fitting and the attachment mechanism preferably ensures good magnetic coupling between the top member 104 and each of the legs 110, 112,114 and 116. The integrated magnetics component 100 furthermore comprises a first output inductor winding 120, a second output inductor winding 122, a third output inductor winding 124 and a fourth output inductor winding 126 wound around the first, second, third and fourth legs, respectively. The fourth output inductor winding 126 comprises a pair of electrical terminals 130, 132 at each end of the output winding 126 and each of the first, second and third output inductor windings 120,122 and 124, respectively, comprises a similar pair of electrical terminals (not shown). Each of the first, second third and fourth output inductor windings is formed as a single full-winding in the present embodiment of the invention but the skilled person will understand that each of the output inductor windings 120,122, 124 and 126, respectively, may comprise a plurality of full windings. The integrated magnetics component 100 furthermore comprises a first input inductor winding 106 formed as a straight flat ribbon or strip of electric conductive material extending in-between the first, second, third and fourth legs, 110, 112, 114 and 116, respectively. The first input inductor winding 106 is adapted to induce a first magnetic flux through a first flux path of the magnetically permeable core when an input current flows therein in accordance with the well-know right hand rule. The generation and arrangement of the first flux path is discussed in further detail below in connection with Fig. 3 and Figs. 7a)-d). The first input inductor winding 106 is a straight half winding which is arranged along a first coil axis

142 indicated by the dotted line. Each end of the first input inductor winding 106 comprises an electrical termination or terminal (not shown) allowing electrical driver circuits such as a transistor based half-bridge or full-bridge driver to establish electrical connection to the inductor winding 106 and supply a drive signal thereto. A second input inductor winding 108 has a second coil axis as indicated by the dotted line 140 which extends substantially perpendicularly to the first coil axis 142. As the first inductor winding 106, the second inductor winding 108 is also formed as a straight flat ribbon of electric conductive material extending in-between the first, second, third and fourth legs, 110, 112,114 and 116, respectively, albeit in an orthogonal direction of the base member 102. The first inductor winding 106 and the second inductor winding 108 accordingly form a cross-shaped winding geometry arranged in abutment with or close to an upper substantially flat surface 103 of the base member with an overlap region situated substantially in a central region of the upper surface of the base member. The first and second input inductor windings may comprise material with high electrical conductivity such as copper, aluminium or various alloys etc. The first and second input inductor windings may comprise wire designs like litz wire or other special winding arrangements aimed at reducing eddy current effects at high operational frequencies of the input drive signals applied to the first and second input inductor windings. Consequently, such special winding arrangements can reduce power loss in the input and/or output inductor windings of the integrated magnetics component and improving overall power conversion efficiency of the power converter in a beneficial manner.

[0043] The first and second inductor windings are preferably coated with an electrically insulating layer to prevent short circuits between the first and second inductor windings or between each of these and the base member 102. The second input inductor winding 108 is adapted to induce a second magnetic flux through a second first flux path of the magnetically permeable core extending substantially orthogonally to the first flux path in accordance with the well-known right hand rule. The base member 102 extends in a horizontal plane in the geometry of Fig. 1 and the first coil axis 142 and the second coil axis 140 both extend in the horizontal plane. The skilled person will appreciate that the chosen designation of the top member and bottom member is arbitrary since a 180 degree rotation about the horizontal plane of the integrated magnetics component 100 would reverse the orientation of the top and bottom members without affecting the functionality of the component at all. In the depicted first

embodiment of the invention each of the top and bottom members comprises a substantially quadratic flat plate structure with the first, second, third and fourth legs arranged in a substantially quadratic pattern at respective corners of the quadratic flat plate. The flat plate structure of the top member 104 is arranged substantially parallelly to the flat plate structure of the base member 102. The skilled person will appreciate that the base member and/or the top member each may have numerous different shapes such as rectangular, square, circular, elliptical, octagon etc.

[0044] The base member 102, including the first, second, third and fourth legs, 110, 112, 114 and 116, respectively, preferably comprises a material possessing high magnetic permeability such as a soft magnetic material like Ferrite or a ferromagnetic alloy like Sheet steel, Silicon steel, Cast steel, Tungsten steel Magnet steel, cast iron, Nickel etc. The same type of materials are suitable for the top member 104 such that each of the first and second magnetic flux paths exhibits low magnetic reluctance and preferably has high magnetic saturation points as well.

[0045] The skilled person will also appreciate each of the first, second, third and fourth legs, 110, 112, 114 and 116, respectively, may have other cross-sectional profiles or shapes than the depicted circular shape such as triangular, quadratic, rectangular, elliptical, pentagon, hexagon, heptagon, octagon etc. The shape of each of the output inductor windings may be adapted to conform to these alternative cross-sectional profiles of the legs so as to fit tightly around a circumference of the leg in question.

[0046] An experimental prototype of the integrated magnetics component 100 in accordance with the present embodiment was built by the inventors with the following dimensions:

- Base plate thickness, width and depth: 7 mm, 44 mm, 44 mm.
- Length of each of the first, second, third and fourth legs = 8 mm.
- Diameter of each of the first, second, third and fourth legs = 14 mm.
- Base plate material and top member material: Mn-Zn ferrite MN80C.
- Maximum power conversion capacity between 1 kW and 2 kW depending on the specifics of the application in question such as input voltage, output voltage, switching frequency etc of a power converter.

[0047] Fig. 2 shows an exploded perspective view of the integrated magnetics component 100 in accordance with the above-described first embodiment of the invention. The base member 102 is formed as a single unitary structure comprising a substantially quadratic flat plate

structure with each of the first, second, third and fourth legs, 110, 112, 114 and 116, respectively, protruding substantially perpendicularly from the surface 103 of the flat plate. The top member 104 is also formed as a separate structure which is attached to the respective ends of the first, second, third and fourth legs, 110, 112, 114 and 116, respectively, by gluing/welding or by using adhesive tape or clamp recesses.

[0048] Fig. 3 illustrates schematically the first and second orthogonally extending magnetic flux paths, Φ1 and Φ2, respectively, associated with the first and second input inductor windings 106, 108, respectively. The first and second orthogonally extending magnetic flux paths are schematically indicated by the circles in full lines and broken lines, respectively, running through the magnetically permeable core of the integrated magnetics component 100 designed in accordance with the first embodiment of the invention. The first magnetic flux path Φ1 is generated by input current flowing through the first input inductor winding 106. The first magnetic flux path Φ1 runs in a closed path extending vertically up through the first leg 110, horizontally through the flat top plate 104 towards the fourth leg 116 and vertically down through the fourth leg 116 towards the flat plate structure of the bottom member 102 and horizontally through the flat plate structure and back to a lower surface of the first leg 110. The first magnetic flux path Φ1 furthermore extends in a similar manner through the second leg 112, the flat top plate 104, the third leg 114 and the flat plate structure of the bottom member 102 for symmetry reasons. The second magnetic flux path Φ2 is generated by input current flowing through the second input inductor 108. The first magnetic flux path Φ2 runs in a closed path extending vertically up through the first leg 110, horizontally through the flat top plate 104 towards the second leg 112, vertically down through the second leg 116 towards the flat plate structure of the bottom member 102 and horizontally through the flat plate structure and back to a lower surface of the first leg 110. The second magnetic flux path Φ2 furthermore extends in a similar manner through the third leg 114, the flat top plate 104, the fourth leg 116 and the flat plate structure of the bottom member 102 for symmetry reasons. Consequently, input current flowing through the first input inductor winding 106 generates magnetic flux in each of the first, second, third and fourth legs, 110, 112, 114 and 116 and input current flowing through the second input inductor winding 108, arranged orthogonally to the first input inductor winding, generates magnetic flux in each of the first, second, third and fourth legs, 110, 112, 114 and 116

such that a resulting flux in each leg depends on the magnitude and direction/phase of both input currents as discussed in further detail below in connection with Figs 7a)-d).

[0049] Fig. 4 shows an exploded perspective view of an integrated magnetics component 400 in accordance with a second embodiment of the invention. The reference numerals are numbered such that corresponding features of the first embodiment (Fig. 1) and the present embodiment have corresponding designations. In the integrated magnetics component 400, the first inductor winding 406 comprises a single full-turn winding formed as a flat U-shaped ribbon or strip of electrically conductive material. The flat U-shaped strip of conductive material 406 comprises a first leg or arm arranged proximate to an upper surface 403 of the base member 402 and extending in-between first, second, third and fourth legs, 410, 412, 414 and 416, respectively, which protrude from the base member 402. A second leg or arm of the flat U-shaped strip 406 is arranged below the flat quadratic structure of the base member 402. A bridging or coupling portion of the flat U-shaped strip 406 extends around an edge of the flat rectangular structure of the base member. The first input inductor winding 406 is adapted to induce a first magnetic flux through a first flux path of the magnetically permeable core in response to flow of input current therein in accordance with the well-know right hand rule in a manner similar to the one described in detail above in connection with Fig. 3. A second inductor winding 408 of similar shape and material as the first inductor winding 406 is arranged or wound around the flat quadratic structure of the base member 402 in the same manner as the first inductor winding 406, but is oriented orthogonally to the first inductor winding 406. This orthogonal arrangement leads to an orthogonal orientation of a first coil axis 442, associated with the flat U-shaped strip 406, relative to a second coil axis 440, associated with the flat U-shaped strip 408, as indicated.

[0050] The second input inductor winding 408 is adapted to induce a second magnetic flux through a second flux path of the magnetically permeable core in response to flow of input current therein in accordance with the well-know right hand rule in a manner similar to the one described in detail above in connection with Fig. 3.

[0051] The upper leg of the first inductor winding 406 and the upper leg of the second inductor winding 408 overlaps each other in a central region of the upper surface 403 of the base member 402. The main advantage of the present embodiment compared to the first embodiment is that multiple turns can be obtained on each of the first and second input inductor windings and achieve numerous advantages such as higher turns ratio of the transformer and lower core loss.

[0052] Fig. 5 is an assembled perspective view of an integrated magnetics component 500 in accordance with a third embodiment of the invention. The reference numerals are designated such that corresponding features of the first embodiment (Fig. 1) and the present embodiment correspond. The integrated magnetics component 500 comprises a base member 502 with a flat quadratic plate structure and a top member 504 which likewise has a substantially flat and quadratic plate like structure conforming to the outer contour of the base member 502. The top member 504 is firmly attached, and magnetically coupled, to opposite ends of first, second, third and fourth legs, 510, 512,514 and 516, respectively, relative to the base member 502 so as to form a coherent magnetically permeable core of the integrated magnetics component 500.

[0053] In the integrated magnetics component 500, the first inductor winding 506 comprises a single full-turn winding formed as a flat ribbon or strip of conductive material. However, instead of the U-shaped form used in the second embodiment of the invention, the present first inductor winding 506 is folded in a horizontal plane extending along the upper surface 503 of the flat quadratic structure of a base member 502. In this manner, the first input inductor winding 506 extends exclusively above the base member 502 in the horizontal plane. The horizontally folded layout or geometry of the first input inductor winding 506 is wound around, or encircles, the fourth leg 516 and the third leg 514 which are arranged adjacently at the upper surface 503 of the base member 502. The horizontally folded layout or geometry of the first input inductor winding 506 forms a single full turn winding formed as a folded flat strip of winding with electrical terminal (now shown) arranged at end sections of the input winding 506. A second input inductor winding 508 of similar shape and material as the first input inductor winding 506 is arranged on the upper surface 503 of the flat quadratic structure of the base member 502 but oriented orthogonally to the first input inductor winding 506 in the horizontal plane. The horizontally folded layout or geometry of the second input inductor winding 508 is wound around, or encircles, the second leg 512 and the third leg 514 which are arranged adjacently at the upper surface 503 of the base member 502. This orthogonal arrangement of the first and second input windings leads to an orthogonal orientation of a first coil axis 542, associated with the folded flat strip winding 506, relative to a second coil axis 540, associated with the folded flat strip winding 508, as indicated. The main advantage of the present embodiment compared to the first and second embodiment is that the first and second input inductor windings can easily be arranged or printed on a standard type of stiff or flexible printed circuit board (PCB). This is

feature supports modularization of a power converter based on the integrated magnetics component because other components of the power converter can be integrated on the PCB together with the inductor windings.

[0054] Fig. 6 is an exploded perspective view of the integrated magnetics component 500 depicted above in accordance with the third embodiment of the invention. The horizontally folded layouts or geometries of the first and second inductor winding 506, 508 are evident such that the inductor windings form respective flat folded strips of winding. Likewise, the figure depicts the orthogonal orientation in the horizontal plane of the first coil axis 542, associated with the input winding 506, relative to the second coil axis 540, associated with the second winding 508.

[0055] Fig. 7a) illustrates respective magnetic flux directions through the first, second, third and fourth legs, 110, 112, 114 and 116, respectively, of the integrated magnetics component 100 in accordance with the first embodiment of the invention in a first input current state of four different input current states. The first input current state is characterized by the indicated direction of the input current, I1, flowing through the first input conductor winding 106 and by the indicated direction of the input current, I2, flowing through the second input inductor winding 108. In the first input current state using the right hand rule, the input current I1 leads to the magnetic fluxes indicated by solid arrows 109a and 109b in the same direction in the first leg 110 and the second leg 112. This is a consequence of the first leg 110 and the second leg 112 being arranged on the same side of the input inductor winding 106. Furthermore, the input current I1 also leads to the magnetic fluxes indicated by solid arrows 109c and 109c in the same direction in the third leg 114 and the fourth leg 116. The magnetic fluxes induced by I1 accordingly lead to oppositely directed magnetic fluxes in the first and second legs relative to the third and fourth legs which is a consequence of the geometry of the closed loop formed by the first magnetic flux path Φ1 depicted on Fig. 3.

[0056] In the first input current state using the right hand rule on the indicated direction of the input current I2 flowing through the second input inductor winding 108 leads to the magnetic fluxes indicated by dotted arrows 111c and 111d in the same direction in the first leg 110 and the fourth leg 116. This is a consequence of the first leg 110 and the fourth leg 116 being arranged on the same side of the second input inductor winding 108. Furthermore, the input current I2 also leads to the magnetic fluxes indicated by dotted arrows 111b and 111a in the same direction in

the second leg 112 and the third leg 114. The magnetic fluxes induced by I2 accordingly leads to oppositely directed magnetic fluxes in the first and fourth legs relative to the second and third legs which is a consequence of the geometry of the closed loop formed by the second magnetic flux path $\Phi 2$ depicted on Fig. 3.

[0057] This analysis of the respective magnetic fluxes induced by input currents I1 and I2 reveals that a resulting magnetic flux in each of the first, second, third and fourth legs, 110, 112, 114 and 116, respectively, is set by contributions from both the first magnetic flux path $\Phi 1$ and the second magnetic flux path $\Phi 2$. This implies that an output voltage induced in each of the output inductor windings 120,122, 124 and 126 is likewise determined by the contributions from both of the first and second magnetic flux paths.

[0058] Fig. 7b) illustrates respective magnetic flux directions through the first, second, third and fourth legs, 110, 112, 114 and 116, respectively, in a second input current state. In the depicted second input current state, the direction of the second input current I2 is reversed relative to the direction of I2 in the first input current state described above. The direction of the first input current I1 is the same as in the first input current state. These directions for the first and second input current leads to the depicted directions of the magnetic fluxes induced by I1 indicated by solid arrows 109a, 109b, 109c, 109d. Likewise, the respective magnetic fluxes through the legs induced by I2 are indicated by the dotted arrows 111a, 111b, 111c, 111d. As expected, the direction of the magnetic fluxes generated by I2 has been reversed in each of the first, second, third and fourth legs 110, 112, 114 and 116 while the direction of the magnetic fluxes generated by I2 has been maintained in each of the legs.

[0059] Fig. 7c) illustrates respective magnetic flux directions through the first, second, third and fourth legs 110, 112, 114 and 116, respectively, in a third input current state. In the depicted third input current state, the direction of both the first input current I1 and the second input current I2 have been reversed relative to their respective directions in the first input current state described above under Fig. 7a). These directions for the first and second input current leads to the depicted directions of the magnetic fluxes induced by I1 indicated by solid arrows 109a, 109b, 109c, 109d. Likewise, the respective magnetic fluxes through the legs induced by I2 are indicated by the dotted arrows 111a, 111b, 111c, 111d. As expected, the directions of all the induced magnetic fluxes have been reversed (relative to the first input current state) through each

of the first, second, third and fourth legs, 110, 112, 114 and 116 due to the reversal of both input currents I1, I2.

[0060] Fig. 7d) illustrates respective magnetic flux directions through the first, second, third and fourth legs 110, 112, 114 and 116, respectively, in a fourth input current state. In the depicted fourth input current state, the direction of the first input current I1 is reversed relative to the direction of I1 in the first input current state described above in connection with Fig. 7a). These directions for the first and second input current leads to the depicted directions of the magnetic fluxes induced by I1 indicated by solid arrows 109a, 109b, 109c, 109d. Likewise, the respective magnetic fluxes through the legs induced by I2 are indicated by the dotted arrows 111a, 111b, 111c, 111d.

[0061] The above-described ability to alter the resulting magnetic flux through each of the first, second, third and fourth legs 110, 112, 114 and 116, respectively, depending on the directions or polarity of the first and second input or excitations currents flowing through the first and second input inductor windings 106, 108, respectively, leads to the possibility of producing different voltage waveforms on each of the output inductor windings 120,122, 124 and 126 by a relative shift of the voltage waveforms applied to the first and second input inductor windings 106, 108, respectively. Consequently, the output voltage of the output inductor windings 120,122, 124 and 126 can be adjusted by controlling a phase shift angle between the input voltage waveforms, and thus input currents I1 and I2, applied to the first and second input inductor windings 106, 108, respectively. This property is illustrated detail below in connection with Fig. 12 showing respective measured output voltage waveforms at each of the output inductor windings 120,122, 124 and 126 for different phase angle shifts between the first and second input voltage waveforms.

[0062] Fig. 8 shows an assembled perspective view of an integrated magnetics component 800 comprising three separate input inductor windings 806, 807, 808 in accordance with a fourth embodiment of the invention. The integrated magnetics component 800 comprises a magnetically permeable core which has a hollow cubic structure 801. The hollow cubic structure 801 comprises an integrally formed base member 802 and top member 804. The top member 804 has a centrally arranged quadratic aperture 805 leading to the formation of a fifth leg 811, a sixth leg 813, a 7^{th} leg 815 and an 8^{th} leg 817 in the top member structure. In addition, a first leg 810, a second leg 812, a third leg 814 and a fourth leg 816 are protruding vertically from the base

member 802. The first to 8th legs are formed as respective vertices of the hollow cubic structure 801. The integrated magnetics component 800 furthermore comprises a first, a second, a third and a fourth output inductor winding wound around the first leg 810, the second leg 812, the third leg 814 and the fourth leg 816, respectively. In addition, the integrated magnetics component 800 comprises a fifth output inductor winding, a sixth output inductor winding, a 7th output inductor winding and an 8th output inductor winding wound around respective ones of the fifth leg 811, the sixth leg 813, the 7th leg 815 and the 8th leg 817. The first to 8th output inductor windings are not depicted on the figure for the sake of clarity.

[0063] The first inductor winding 806 comprises a single full-turn winding formed as a flat U-shaped ribbon or strip of electrically conductive material. The flat U-shaped strip of conductive material 806 is similar to the U-shaped input inductor winding 406 described above in connection with the second embodiment of the invention in that it comprises a first winding leg or arm arranged proximate to an upper surface of the base member 802. The first leg extends in-between first, second, third and fourth legs 810, 812, 814 and 816, respectively, which protrude from the base member 802 and form vertices of the hollow quadratic core 801. A second winding leg or arm of the flat U-shaped strip 806 is arranged below the flat hollow quadratic structure of the base member 802. A bridging or coupling portion of the flat U-shaped strip 806 extends around an edge or vertices of the hollow rectangular structure of the base member. A second inductor winding 808 of similar shape, dimensions and material as the first inductor winding 806 is arranged or wound around the hollow quadratic structure of the base member 802 in the same manner as the first input inductor winding 806, but oriented orthogonally to the first inductor winding 806. A first winding leg of the second inductor winding 808 also extends in-between the first, second, third and fourth legs 810, 812, 814 and 816, respectively, such that the first winding legs of the first and second inductor windings overlap each other in a central region of the base member 802.

[0064] The integrated magnetics component 800 finally comprises a third input inductor winding 807 of similar shape, dimensions and material as the first and second input inductor winding 806, 808, respectively. The third input inductor winding is arranged or wound around the diagonally arranged second and fourth legs 812, 816, respectively, vertically off-set from the horizontal plane at the upper surface of the hollow quadratic structure of the base member 802. A first winding leg of the third inductor winding 807 also extends in-between the first, second,

third and fourth legs 810, 812, 814 and 816, respectively, but the orientation of the first winding leg is rotated 90 degrees about the horizontal plane relative to the orientation of the first and seconds inductor winding 806, 808, respectively. The third inductor winding 807 is configured to induce a third magnetic flux through a third flux path of the magnetically permeable core 801 in response to a third input current being applied thereto. This third input current leads to the formation of a third flux path which extends substantially orthogonally to a first flux path and substantially orthogonally to a second flux path in the magnetically permeable core 801 as explained in further detail below.

[0065] Fig. 9 illustrates schematically first, second and third orthogonally arranged magnetic flux paths 823, 825 and 827, respectively, in the core 801 of the integrated magnetics component 800. The first magnetic flux path indicated by broken lines 823 conducts magnetic flux generated in response to the first input current being applied to the first input inductor 806 flowing from the top to the bottom or vice versa depending on a direction of the input current through the first input inductor 806. The second magnetic flux path indicated by dotted lines 825 conducts magnetic flux generated in response to the second input current being applied to the second input inductor 808 flowing from the top to the bottom or vice versa depending on the direction of the input current through the second input inductor 808. As illustrated, the first magnetic flux path 823 is arranged substantially orthogonally to the second magnetic flux path 825. The third magnetic flux path indicated by the full lines 827 conducts magnetic flux generated in response to the third input current being applied to the third input inductor 807 flowing from a proximate to a distant vertical surface of the core 801 or vice versa depending on the direction of the input current through the third input inductor 807.

[0066] As illustrated, the third magnetic flux path 827 extends substantially orthogonally to the second magnetic flux path 825 and substantially orthogonally to the first magnetic flux path 823 leaving all magnetic flux paths orthogonal to each other. This orthogonal arrangement of the first, second and third flux paths provides 3D orthogonal flux decoupling of the first, second and third input inductor windings and allow these to be operated independently substantially without any mutual magnetic coupling taking place such that three independent input voltage sources of a multiple-input power converter can be accommodated and work in unison to supply power to a common DC output voltage.

[0067] Fig. 10 shows an assembled perspective view of an integrated magnetics component 1000 comprising three separate input inductor windings 1006, 1007, 1008 in accordance with a fifth embodiment of the invention. The integrated magnetics component 1000 comprises a magnetically permeable core 1001 which has a hollow cubic structure. The hollow cubic structure 1001 comprises an integrally formed base member 1002 and top member 1004. The arrangement of the first, second and third input inductor winding 1006, 1008, 1007, respectively, on the magnetically permeable core 1001 is similar to the arrangement disclosed and discussed in detail above in connection with the fourth embodiment of the invention. Likewise, the shape, material and dimensions of the first, second and third input inductor windings 1006, 1008, 1007, respectively, may be identical to those discussed in detail above in connection with the fourth embodiment of the invention. However, while the top member of the previous embodiment comprised a centrally arranged quadratic aperture leading to the formation of 4 additional legs, the present top member is a solid plate like structure. The skilled person will appreciate that the hollow cubic core structure 1001 of the present embodiment is capable of supporting a corresponding set of three orthogonal magnetic flux paths as the first, second and third orthogonally arranged magnetic flux paths 823, 825 and 827, respectively, of the fourth embodiment of the integrated magnetics component 800. The integrated magnetics component 1000 furthermore preferably comprises at least a first, a second, a third and a fourth output inductor winding wound around the first leg 1010, the second leg 1012, the third leg 1014 and the fourth leg 1016, respectively. These output inductor windings have been left out of the figure for the sake of clarity.

[0068] Fig. 11 is a schematic drawing of a dual-input isolated boost DC-DC converter comprising an integrated magnetics component 1100 in accordance with the first embodiment thereof. The integrated magnetics component 1100 acts as a transformer in the dual-input isolated boost DC-DC converter with the first and second input inductor windings SI1 and SI2, respectively, arranged at a primary transformer side and first, second, third and fourth output inductor windings S1-S4, respectively, arranged at a secondary transformer side. The skilled person will understand that the present integrated magnetics component 1100 could be replaced by an integrated magnetics component in accordance with any of the above-discussed second and third embodiments of the integrated magnetics component which both comprise a two-input inductor winding architecture. In the alternative, the present integrated magnetics component

1100 could be replaced by the integrated magnetics component in accordance with any of the above-discussed fourth and fifth embodiments of the integrated magnetics component despite each of these comprises a three-input inductor winding configuration. However, anyone of the three input inductor windings may be left open without any connection to an input voltage source without compromising the operation of the integrated magnetics component utilizing only the two residual input inductor windings. The turns ratio is 1: n as indicated on the figure where n may have a value between 0.1 to 100. The turns ratio being defined as the number of windings of the first input inductor winding relative to the number of windings of an output inductor winding. Consequently, each of the first, second and third input inductor windings may have less, the same or more windings than each of the output inductor windings.

[0069] The dual-input isolated boost DC-DC converter comprises a first input driver 1102 electrically coupled to the first input inductor winding SI1 to supply a first drive signal thereto and a second input driver 1104 electrically coupled to the second input inductor winding SI2 to supply a second drive signal thereto. A first output inductor winding S1 corresponding to the first winding 120 of Fig. 1 is coupled in series with a second output inductor winding S3, for example corresponding to the third output winding 124 of Fig. 1, such that S1 and S3 are wound around diagonally arranged legs of the integrated magnetics component 1100. Respective end terminals of S1 and S3 are electrically coupled to a first output rectification circuit 1110 at circuit nodes E and F, respectively. A third output inductor winding S2 corresponding to the second winding 122 of Fig. 1 is coupled in series with a fourth output inductor winding S4, for example corresponding to the fourth output winding 126 of Fig. 1, such that S2 and S4 are wound around respective diagonally arranged legs of the integrated magnetics component 1100. Respective end terminals of S2 and S4 are electrically coupled to a second output rectification circuit 1114 at circuit nodes G and H, respectively. The first and second output rectification circuits 1110, 1114, respectively, each comprises a full-wave diode rectifier. The full-wave diode rectifier of the first output rectification circuit 1110 comprises semiconductor diodes D1, D2, D3 and D4 while the full-wave diode rectifier of the second output rectification circuit 1114 comprises semiconductor diodes D5, D6, D7 and D8. The first and second output rectification circuits 1110, 1114, respectively, are coupled in parallel to a DC output voltage node at Vo. A load on the dual-input isolated boost DC-DC converter is schematically indicated by a load resistance RL. An output capacitor C is coupled across the a DC output voltage node to suppress voltage ripple in the

voltage waveforms supplied by the first and second output rectification circuits 1110, 1114, respectively, and provide a stable low-ripple DC output voltage.

[0070] The first input driver 1102 comprises an H-bridge transistor driver coupled to a first input voltage, V1, which for example may be a DC voltage between 5 Volt and 100 Volt, through a first boost inductor L1. Complementary output nodes, node A and node B respectively, of the first H-bridge transistor driver are electrically coupled to opposite ends of the first input inductor winding Si1. The second input driver 1104 comprises an H-bridge transistor driver coupled to a second input voltage, V2, which for example may be a DC voltage between 5 Volt and 100 Volt, through a second boost inductor L2. Complementary output nodes, node C and node D, of the second H-bridge transistor driver are electrically coupled to opposite ends of the second input inductor winding SI2.

[0071] As previously explained, the orthogonal arrangement of the first and second flux paths associated with the first and second input inductor windings, SI1 and SI2, respectively, within the magnetically permeable core of the integrated magnetics component 1100 provides 2-dimensional (2D) (or even 3D) orthogonal flux decoupling of the first and second input inductor windings and allow these to be operated independently such that the input voltage sources V1 and V2 can be coupled to a common electrical potential like ground as indicated on Fig. 11. The magnetic flux induced in the first input inductor winding SI1 induces substantially zero magnetic flux in the second input inductor winding SI2 since the magnetic flux generated by SI1 runs parallelly with the coil axis of SI2 in the magnetically permeable core and vice versa as explained above e.g. in connection with Fig. 3.

[0072] In Fig. 12, graph a) on the top depicts a first set of simulated input and output voltage waveforms of a prototype dual-input isolated boost DC-DC converter for phase angle shifts between the first and second input voltage waveforms of 90 degrees. The first and second input voltage waveforms are applied to respective ones of the first and second input inductor windings SI1, SI2 as first and second the PWM modulated drive signals. The duty cycle of the PWM modulated first and second drive signals was fixed at 75 %.

[0073] Graph a) depicts, for a phase shift angle of 90 degrees, the first and second drive signal waveforms, VT1 and VT2, respectively, applied to first and second input inductor windings SI1 and SI2. The respective output signal waveforms VS1 v VS2, VS3 and VS4 induced in the first, second, third and fourth output inductor winding 120, 122, 124 and 126,

respectively, are plotted below. Likewise, graph b) of Fig. 12, depicts, for a phase shift angle of 0 degree, the first and second drive signal waveforms, VT1 and VT2, respectively, applied to first and second input inductor windings SI1 and SI2. The respective output signal waveforms VS1 v VS2, VS3 and VS4 induced in the first, second, third and fourth output inductor winding 120, 122, 124 and 126, respectively, in response thereto are plotted below. Finally, graph a) and b) of Fig. 13, depicts, for phase shift angle of 180 degrees and 45 degrees, respectively, the first and second drive signal waveforms, VT1 and VT2, respectively, applied to first and second input inductor windings SI1 and SI2. The respective output signal waveforms VS1 v VS2, VS3 and VS4 induced in the first, second, third and fourth output inductor winding 120, 122, 124 and 126, respectively, in response thereto under each phase shift angle are plotted below the drive signal waveforms.

[0074] As illustrated the respective output signal waveforms VS1v, VS2, VS3 and VS4 can be adjusted by adjusting the phase shift angle between the first and second drive signal waveforms, VT1 and VT2. Maximum DC output voltage is produced when the phase shift angle is 0 or 180 degrees while minimum DC output voltage is produced for 90 degrees phase angle shift. In addition, the DC output voltage can also be controlled by adjusting the duty cycle of the PWM modulated first and second drive signal. This is contrary to traditional power converters where the DC output voltage is adjusted solely by duty cycle control of a PWM input signal.

[0075] Furthermore, a multi-level output voltage waveform is produced in each of the output signal waveforms VS1, VS2, VS3 and VS4 for a phase shift angle of 45 degrees between the first and second drive signal waveforms as illustrated on Fig. 13 b). The multi-level output voltage waveforms demonstrate an interesting potential for new topologies of multi-level power converters that could replace traditional diode clamped cascaded and capacitor clamped multi-level converter topologies. One advantage of the generated multi-level output voltage waveform is that peak current through each of the MOSFETs M1-M4 of the first input driver 1102 and each of the MOSFETs M5-M8 of second input driver 1104 is reduced. Likewise, peak currents induced in each of the first and second input inductor windings and in the output inductor windings can be significantly reduced due to the multi-level waveforms generated by the 45 degree phase shift angle setting. This feature also leads to a higher conversion efficiency of power converter.

[0076] Another advantage of the present power converter is the ability to generate pure rectangular pulse waveforms at 50 % duty cycle of the PWM modulated input signals without inducing any intermittent zero voltage levels or platforms on each of the first output inductor winding S1, second output inductor winding S3, third output inductor winding S3 and fourth output inductor winding S4. The rectangular pulse waveforms are generated when the phase shift angle between the first and second drive signal waveforms is 90 degrees and can ideally achieve zero voltage ripple at the DC output voltage even in the absence of an output filter. This requires that diagonally arranged output inductor windings on the base member are coupled in series on the secondary side of the integrated magnetic component (which acts like a transformer)

CLAIMS

1. An integrated magnetics component comprising:

- a magnetically permeable core comprising a base member and a top member, the base member extending in a horizontal plane and comprises first, second, third and fourth legs protruding substantially perpendicularly from the base member,

- the top member being attached to opposite ends of the first, second, third and fourth legs relative to the base member,

- first, second, third and fourth output inductor windings wound around the first, second, third and fourth legs, respectively,

- a first input inductor winding having a first coil axis and extending in-between the first, second, third and fourth legs to induce a first magnetic flux through a first flux path of the magnetically permeable core,

- a second input inductor winding having a second coil axis, extending substantially perpendicularly to the first coil axis, to induce a second magnetic flux through a second flux path of the magnetically permeable core extending substantially orthogonally to the first flux path.

2. An integrated magnetics component according to claim 1, wherein the first coil axis and the second coil axis both extend in, or parallelly with, the horizontal plane.

3. An integrated magnetics component according to claim 1 or 2, comprising a third input inductor winding having a third coil axis and extending between a diagonal pair of the first, second, third and fourth legs to induce a third magnetic flux through a third flux path of the magnetically permeable core;

- wherein the third flux path extends substantially orthogonally to the first flux path and substantially orthogonally to the second flux path in the magnetically permeable core.

4. An integrated magnetics component according to claim 3, wherein the top member comprises fifth, sixth, 7^{th} and 8^{th} legs extending parallelly to the horizontal plane.

5. An integrated magnetic component according to claim 4, wherein the magnetically permeable core comprises a hollow cubic structure wherein the first, second, third, fourth, fifth, sixth, 7^{th} and 8^{th} legs form respective vertices of the hollow cubic structure.

6. An integrated magnetics component according to claim 1, wherein the first, second, third and fourth legs are arranged at respective positions of the base member such that first and second substantially orthogonally extending trenches are formed at a surface of the base member; and

- the first and second input inductor windings projecting through the first trench and the second trench, respectively.

7. An integrated magnetics component according to claim 6, wherein the first and second input inductor windings are abutted and overlapped in a central region of the base member.

8. An integrated magnetics component according to any of the preceding claims, wherein the first, second, third and fourth legs are arranged in a substantially rectangular or quadratic pattern at the base member with the first, second, third and fourth legs situated at respective corners of the base member.

9. An integrated magnetics component according to any of the preceding claims, wherein the base member comprises an essentially flat rectangular plate with the first, second, third and fourth legs arranged at respective corners of the base member.

10. An integrated magnetics component according to claim 9, wherein the top member comprises an essentially flat rectangular plate arranged substantially parallelly to the flat rectangular base plate to contact and terminate the first, second, third and fourth legs at respective corners of the top member.

11. An integrated magnetics component according to any of the preceding claims, wherein

- the first input inductor winding comprises a single straight electrical conductor having first and second electrical terminals arranged at opposite ends of the conductor; and

- the second input inductor winding comprises a single straight electrical conductor having first and second electrical terminals arranged at opposite ends of the conductor.

12. An integrated magnetics component according to any of claims 1-10, wherein

- the first input inductor winding comprise a single or a plurality of full inductor winding(s) wound around the base member or wound around the top member; and

- the second input inductor winding comprise a single or a plurality of full inductor winding(s) wound around the base member or wound around the top member.

13. An integrated magnetics component according to any of claims 1-10 wherein:

- the first input inductor winding comprise a single or a plurality of full inductor winding(s) wound around a first pair of adjacent legs of the first, second, third and fourth legs; and

- the second input inductor winding comprise a single or a plurality of full inductor winding(s) wound around a second pair of adjacent legs of the first, second, third and fourth legs;

- wherein the single or plurality of full inductor winding(s) of each of the first and second input inductor windings extend exclusively above the base member or above the top member in or parallel to the horizontal plane.

14. An integrated magnetics component according to any of claims 10-13, wherein:

- the first and second input inductor windings comprise respective flat strips of electrically insulated conductor material arranged in abutment with the base member or in abutment with the top member.

15. An integrated magnetics component according to any of the preceding claims, wherein the first input inductor winding comprises first and second electrical terminals arranged at opposite ends of the first winding; and

- the second input inductor winding comprises first and second electrical terminals arranged at opposite ends of the second winding.

16. An integrated magnetics component according to any of the preceding claims, wherein each of the first, second, third and fourth output inductor windings comprises a single or a plurality of full inductor winding(s).

17. An integrated magnetics component according to any of the preceding claims, wherein

- the first input inductor winding is configured to generate a magnetic flux in a first direction through a first pair of adjacent legs arranged on a first side of the first input inductor winding and an oppositely directed magnetic flux through a second pair of adjacent legs arranged on a second and opposite side of the first input inductor winding; and

- the second input inductor winding is configured to generate a magnetic flux in a second direction through a first pair of adjacent legs arranged on a first side of the second input inductor winding and an oppositely directed magnetic flux through a second pair of adjacent legs arranged on a second and opposite side of the second input inductor winding.

18. A multiple-input isolated power converter comprising an integrated magnetics component according to any of the preceding claims and further:

- a first input driver electrically coupled to the first input inductor winding to supply a first drive signal thereto,

- a second input driver electrically coupled to the second input inductor winding to supply a second drive signal thereto,

- the output inductor windings of a first pair of diagonal legs being coupled electrically to a first output rectification circuit,

- the output inductor windings of a second pair of diagonal legs being coupled electrically to a second output rectification circuit; and

- the first and second output rectification circuits being coupled in parallel to a DC output voltage node or terminal.

19. A multi-input power isolated power converter according to claim 18, wherein the output inductor windings of the first pair of diagonal legs are connected in series and the output inductor windings of the second pair of diagonal legs are connected in series.

20. A multiple-input isolated power converter according to claim 18 or 19, wherein the first and second input drivers are electrically coupled to a common electrical potential such as ground.

21. A multiple-input isolated power converter according to any of claims 18-20, having a boost or a buck configuration.

22. A method of controlling a DC output voltage of a multi-input isolated power converter according to any of claims 18-21 comprising steps of:

- generating a first a pulse width modulated drive signal having a first phase angle on the first input inductor winding,

- generating a second pulse width modulated drive signal having a second phase angle on the second input inductor winding,

- adjusting a phase angle difference between the first and second phase angles to control the DC output voltage.

23. A method of controlling a DC output voltage of a multi-input isolated power converter according to claim 22, comprising a further step of:

- adjusting a duty cycle of the first pulse width modulated drive signal and/or a duty cycle of the second pulse width modulated drive signal to adjust the DC output voltage.

ABSTRACT

The present invention relates to an integrated magnetics component comprising a magnetically permeable core comprising a base member extending in a horizontal plane and first, second, third and fourth legs protruding substantially perpendicularly from the base member. First, second, third and fourth output inductor windings are wound around the first, second, third and fourth legs, respectively. A first input inductor winding of the integrated magnetics component has a first coil axis and extends in-between the first, second, third and fourth legs to induce a first magnetic flux through a first flux path of the magnetically permeable core. A second input inductor winding of the integrated magnetics component has a second coil axis extending substantially perpendicularly to the first coil axis to induce a second magnetic flux through a second flux path of the magnetically permeable core extending substantially orthogonally to the first flux path. Another aspect of the invention relates to a multiple-input isolated power converter comprising the integrated magnetics component.

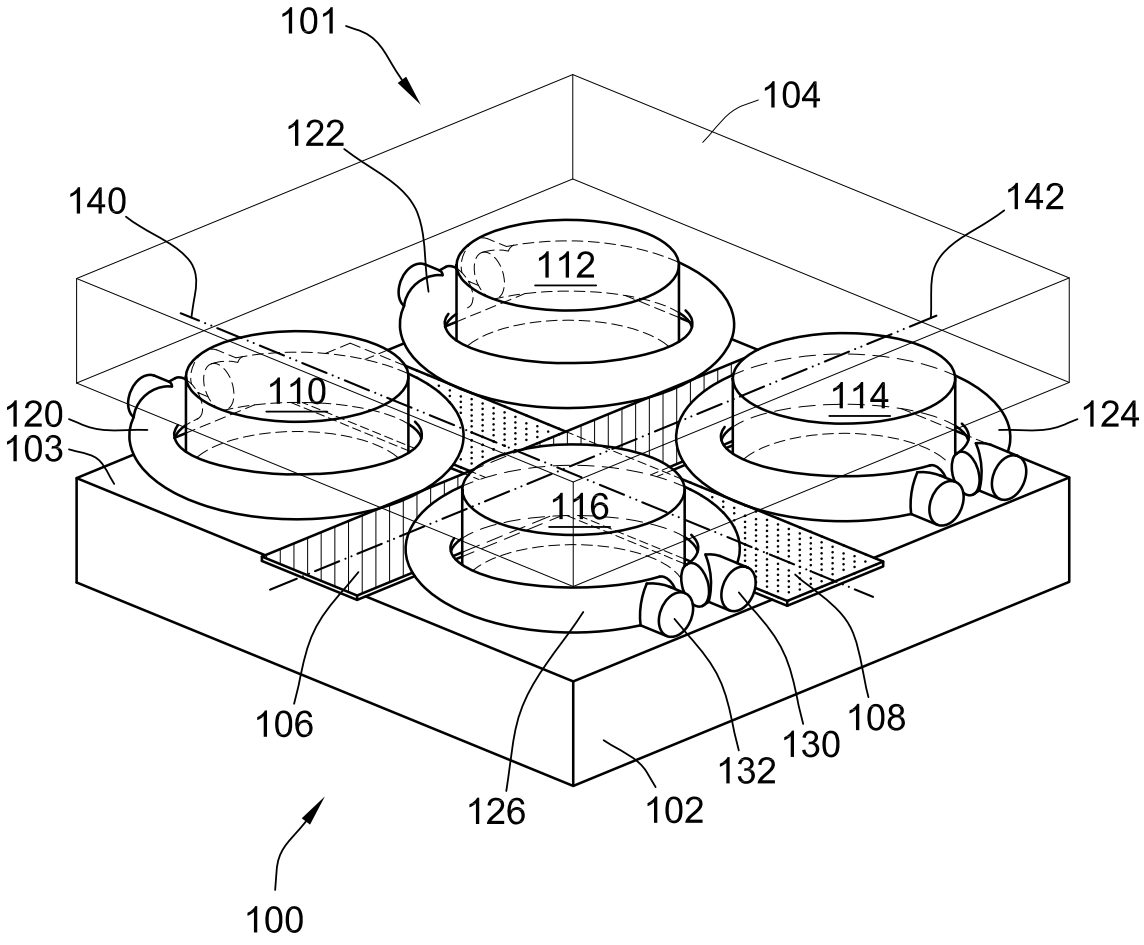
101
104
122
140
142
112
110
114
120
124
103
116
106
126
102
132
130
108
100

FIG. 1

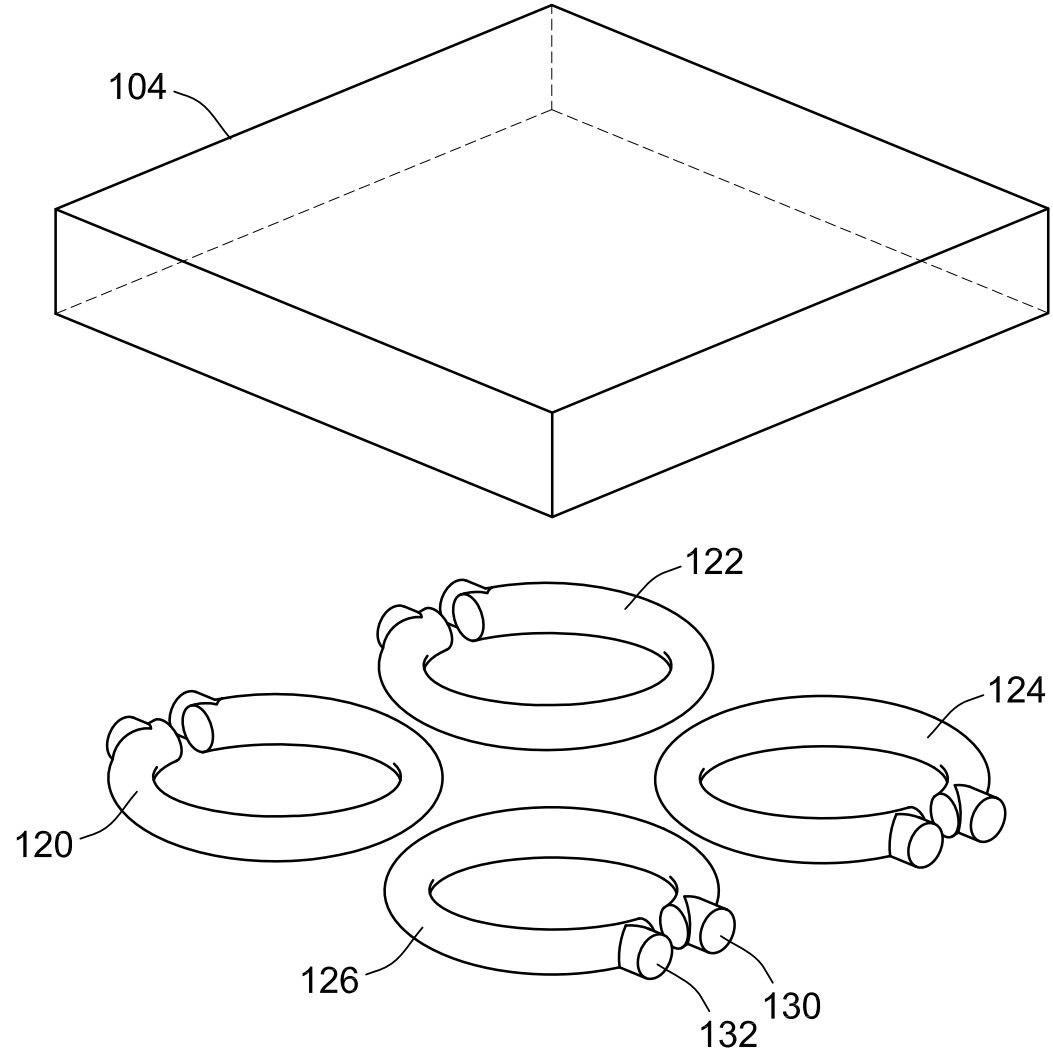
104
122
124
120
126
130
132
140
142
112
110
114
103
116
106
108
100
102

FIG. 2

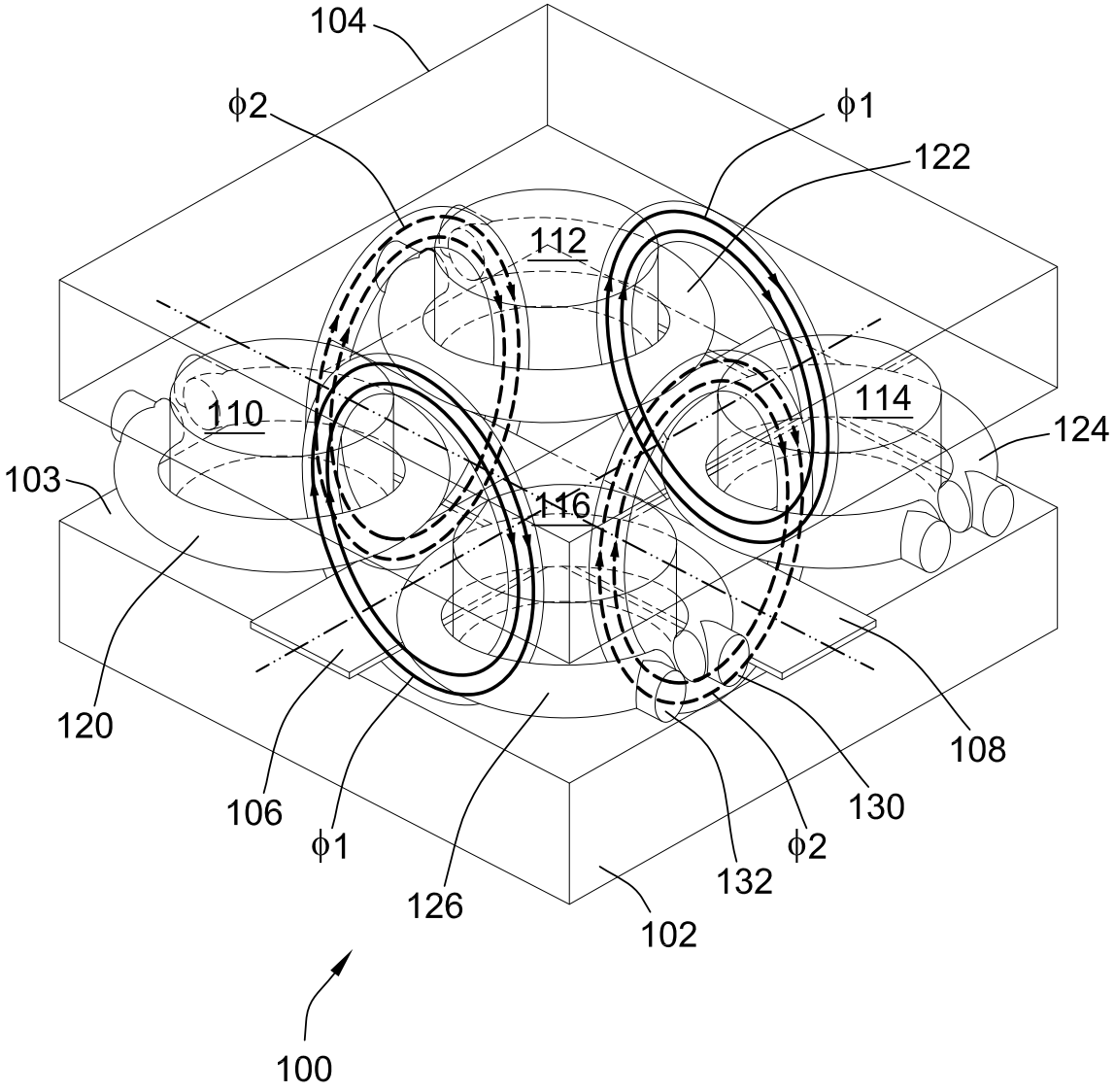
104
ϕ2
ϕ1
122
112
110
114
124
103
116
120
108
106
130
ϕ1
ϕ2
132
126
102
100

FIG. 3

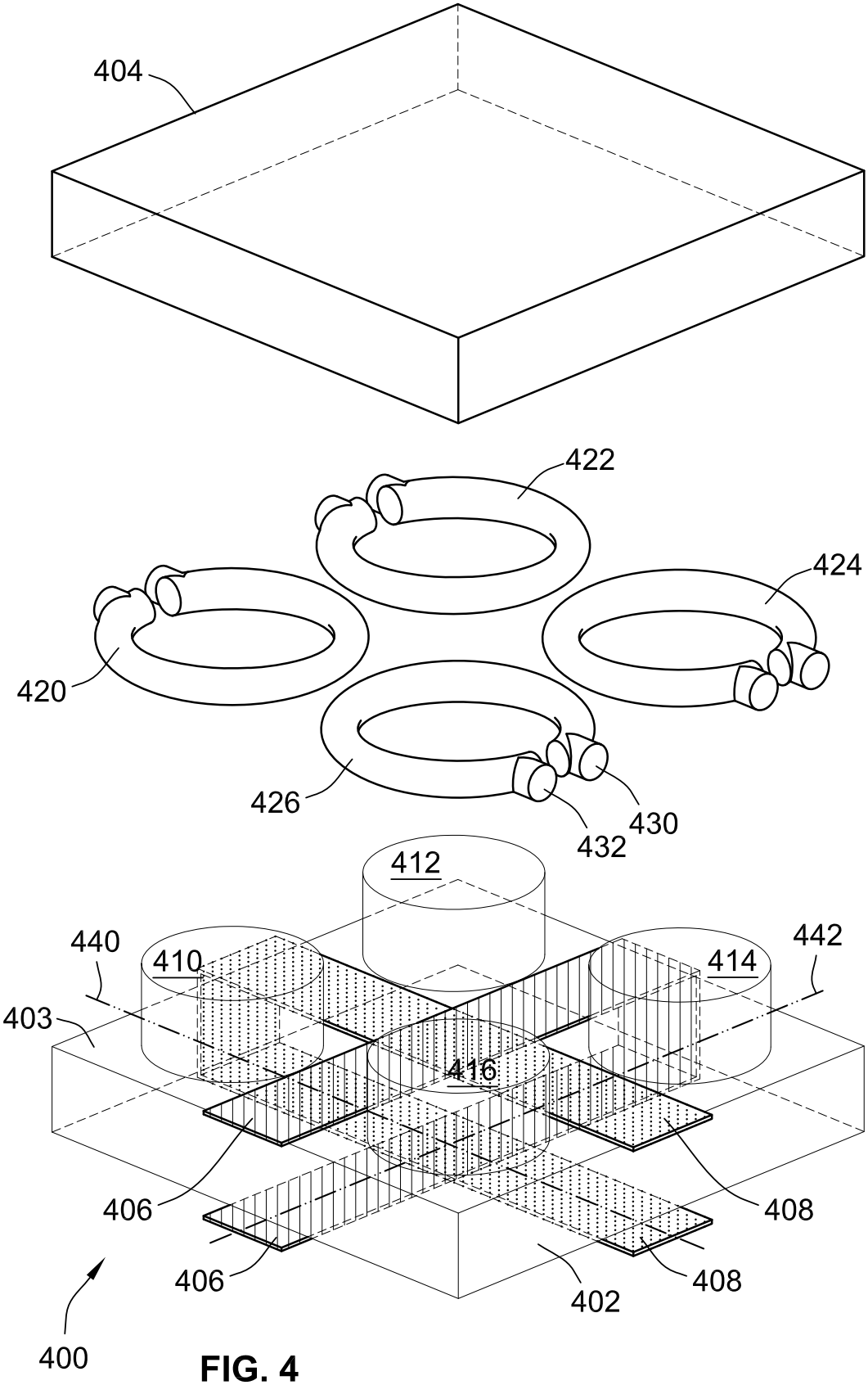
404
422
424
420
426
430
432
412
440
410
414
442
403
416
406
408
406
408
402
400

FIG. 4

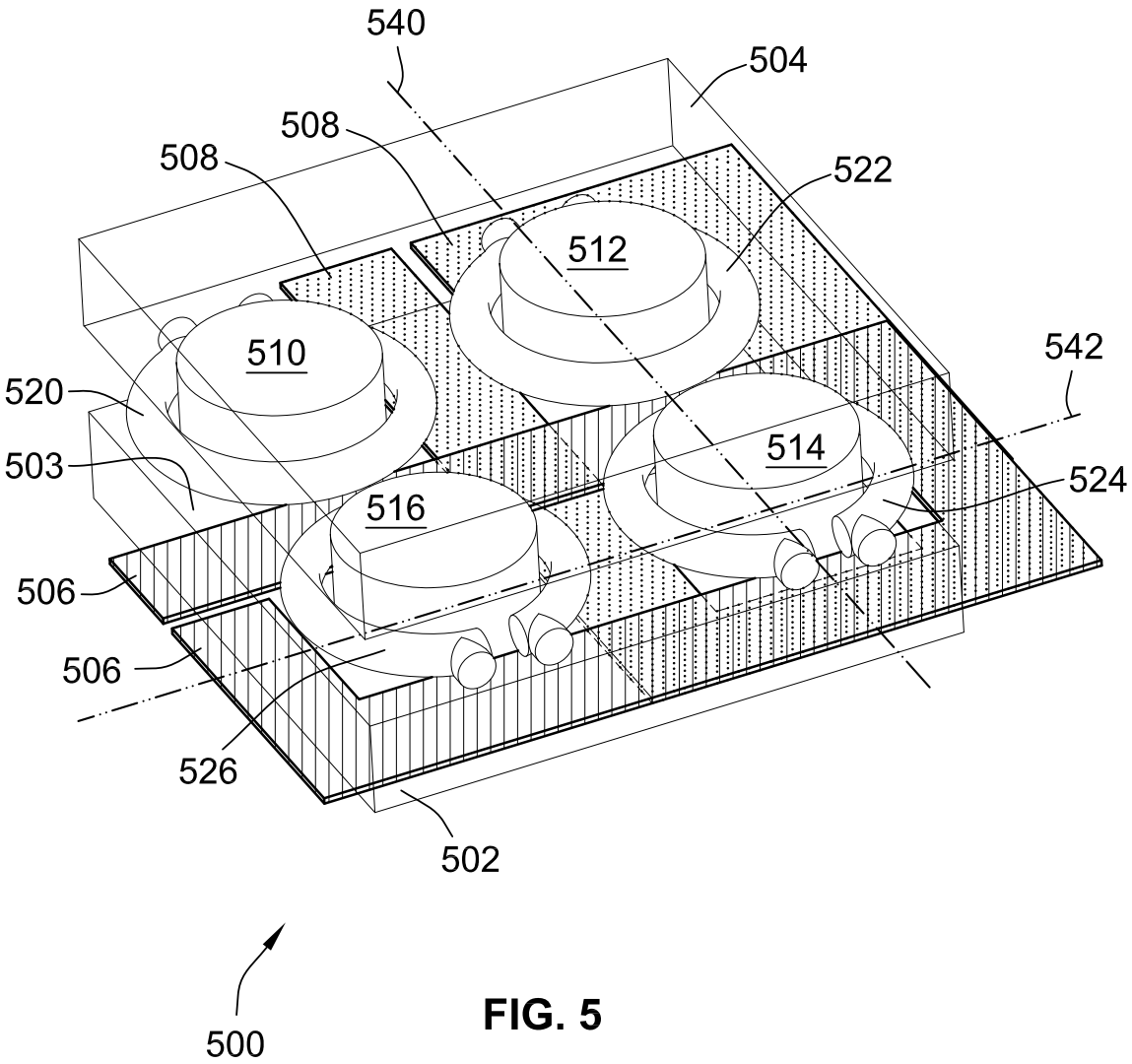
540
504
508
508
522
512
510
542
520
514
503
524
516
506
506
526
502
500

FIG. 5

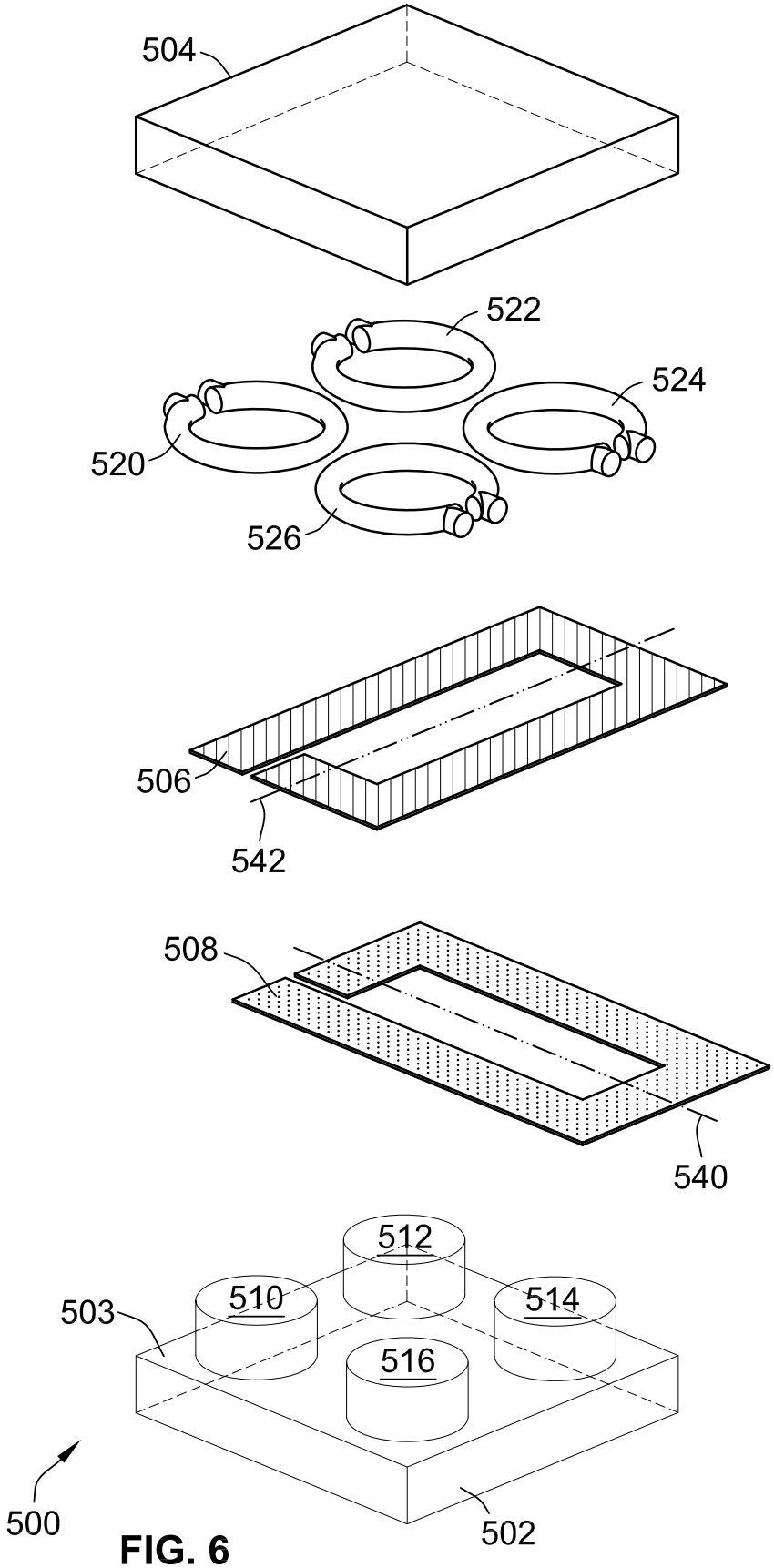

FIG. 6

FIG. 7a)

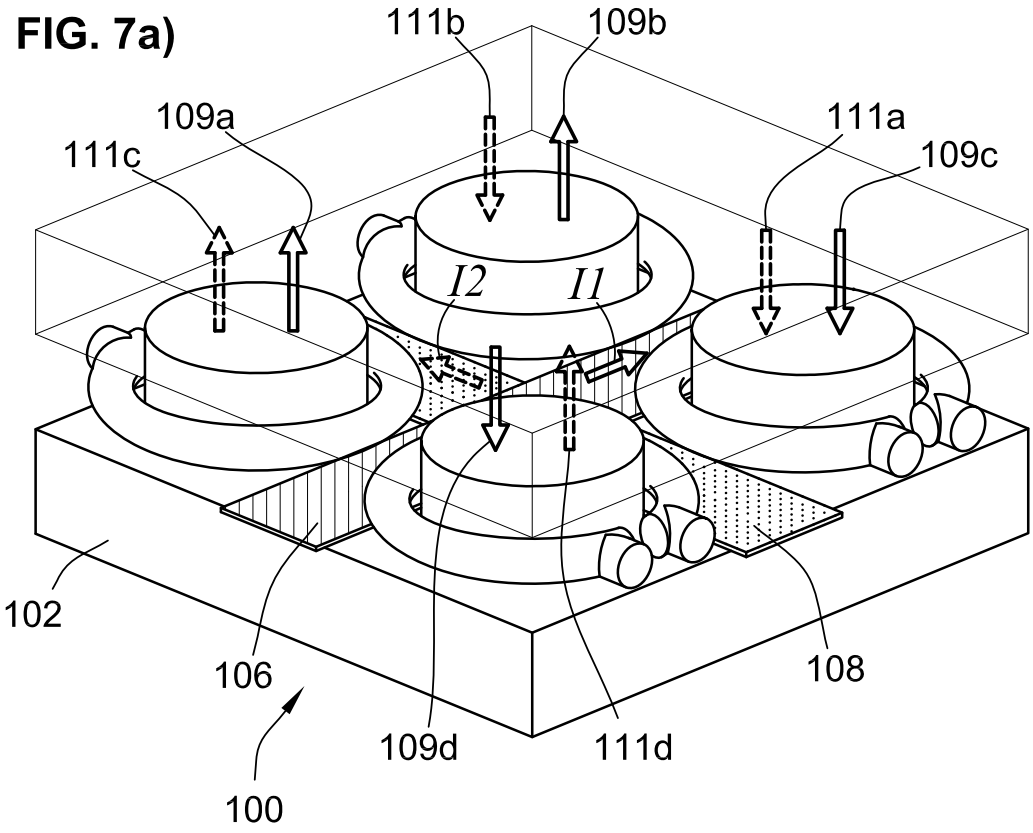
111b
109b
109a
111a
111c
109c
I2
I1
102
106
108
109d
111d
100

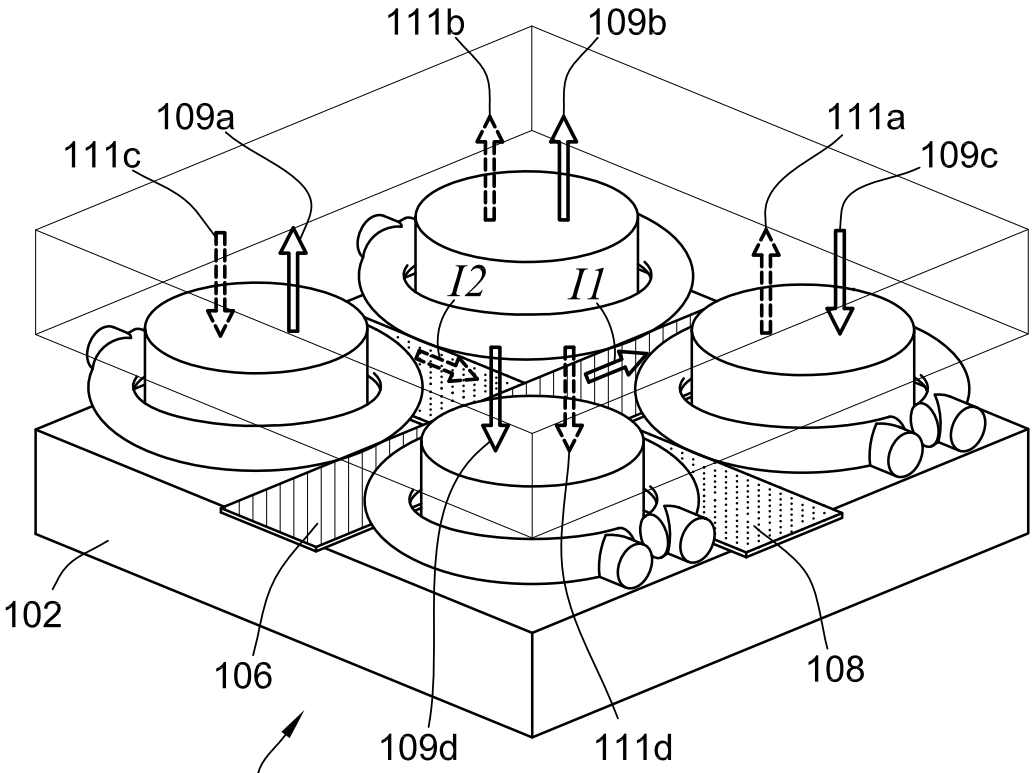
111b
109b
109a
111a
111c
109c
I2
I1
102
106
108
109d
111d
100

FIG. 7b)

FIG. 7c)

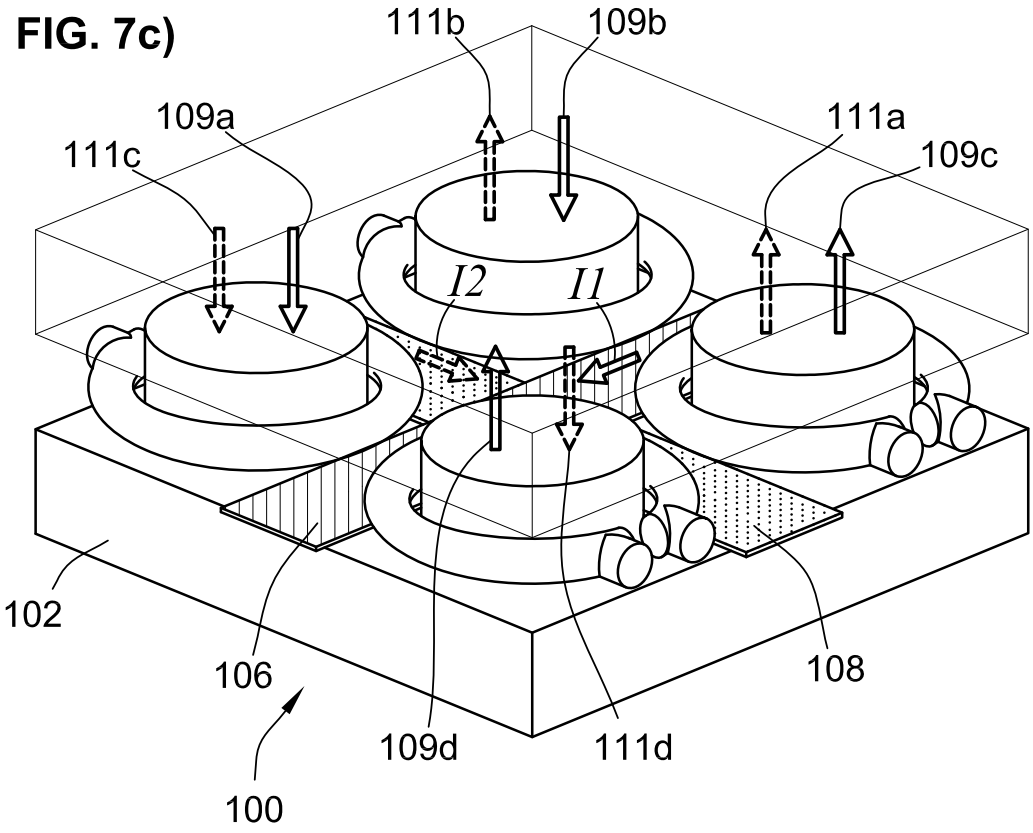
111b
109b
109a
111a
111c
109c
I2
I1
102
106
108
109d
111d
100

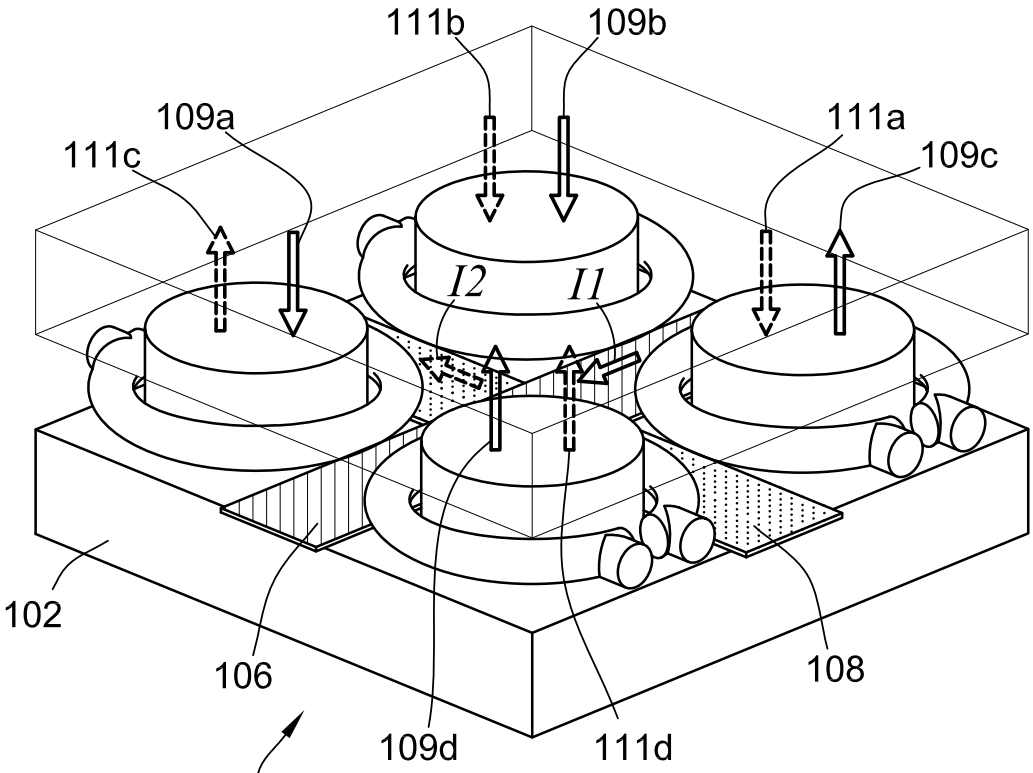
111b
109b
109a
111a
111c
109c
I2
I1
102
106
108
109d
111d
100

FIG. 7d)

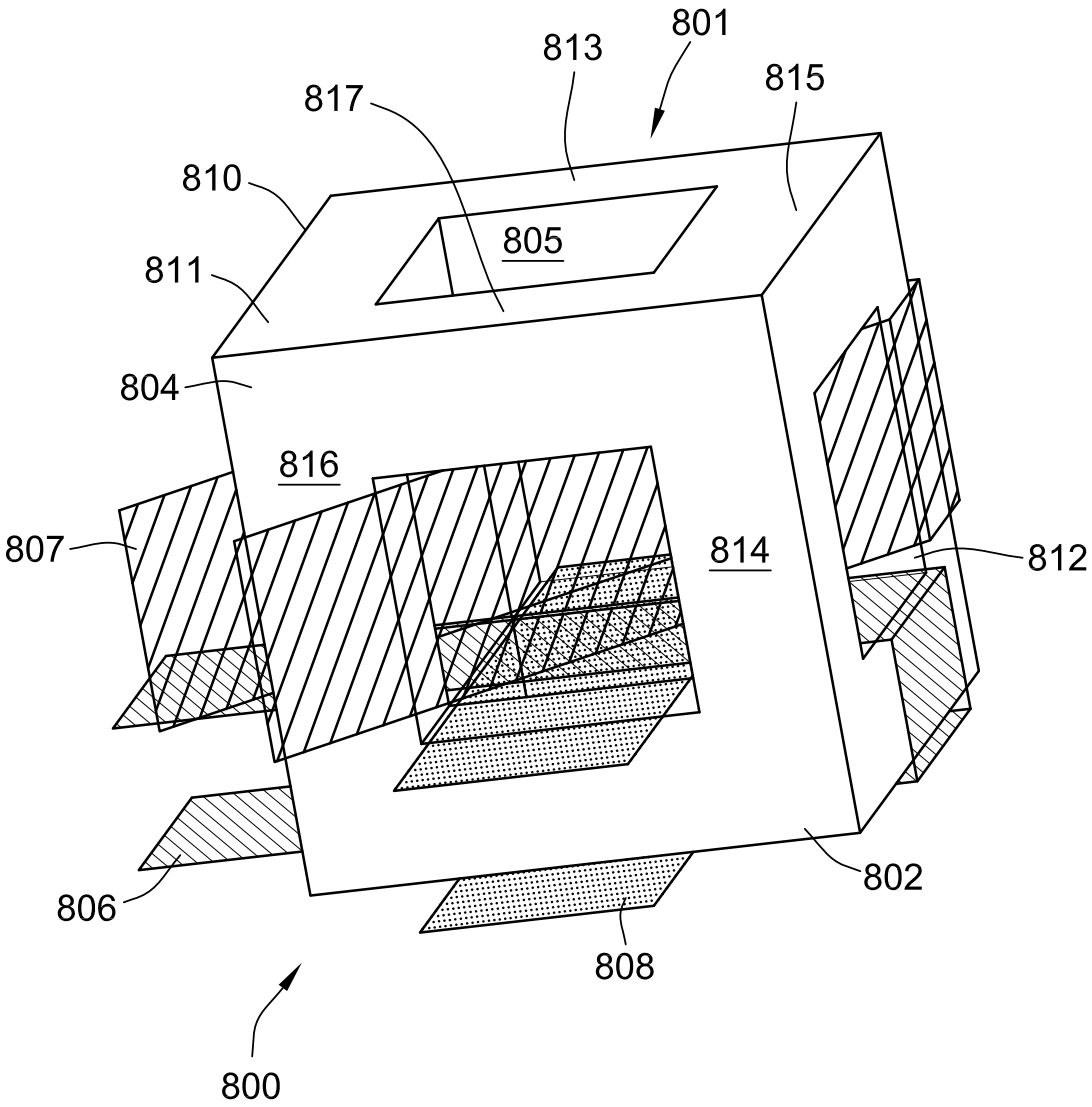

FIG. 8

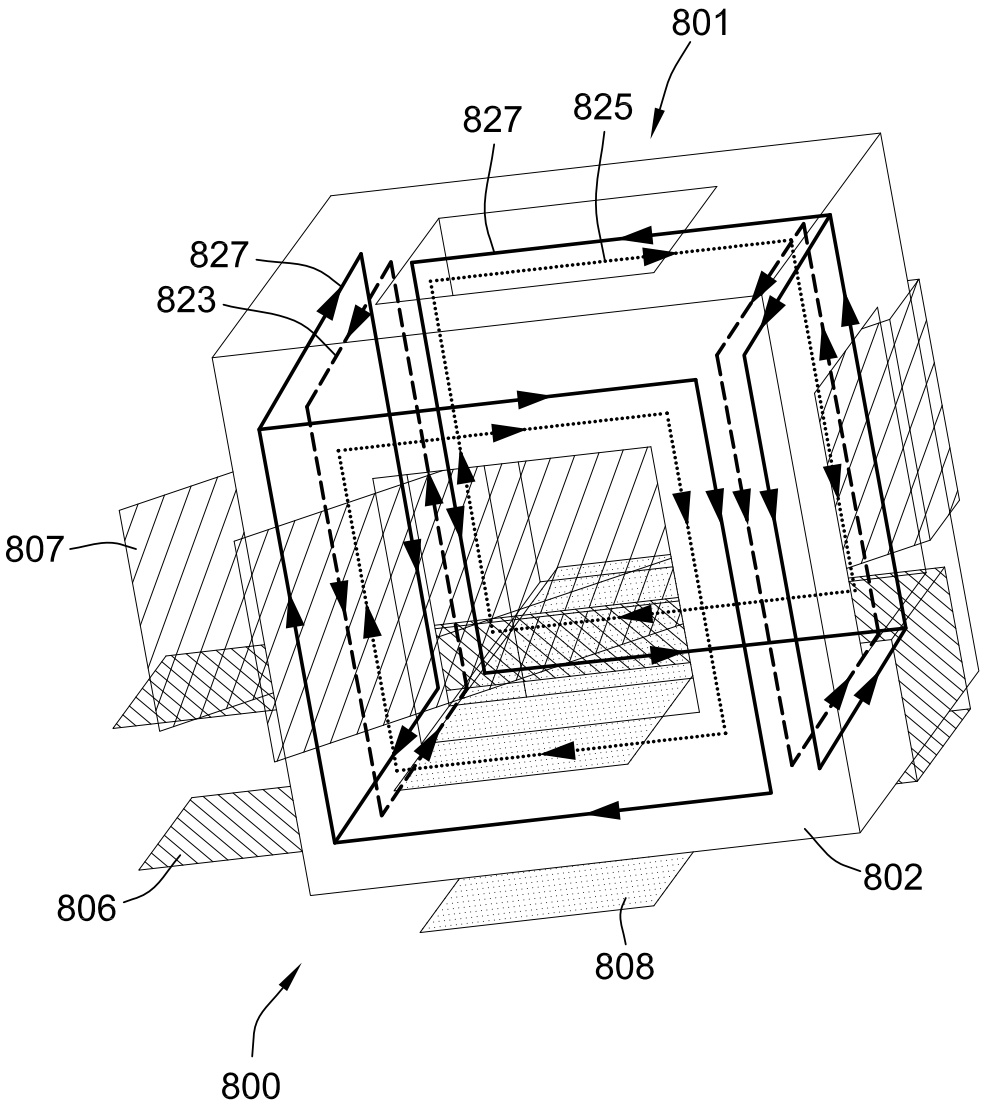

FIG. 9

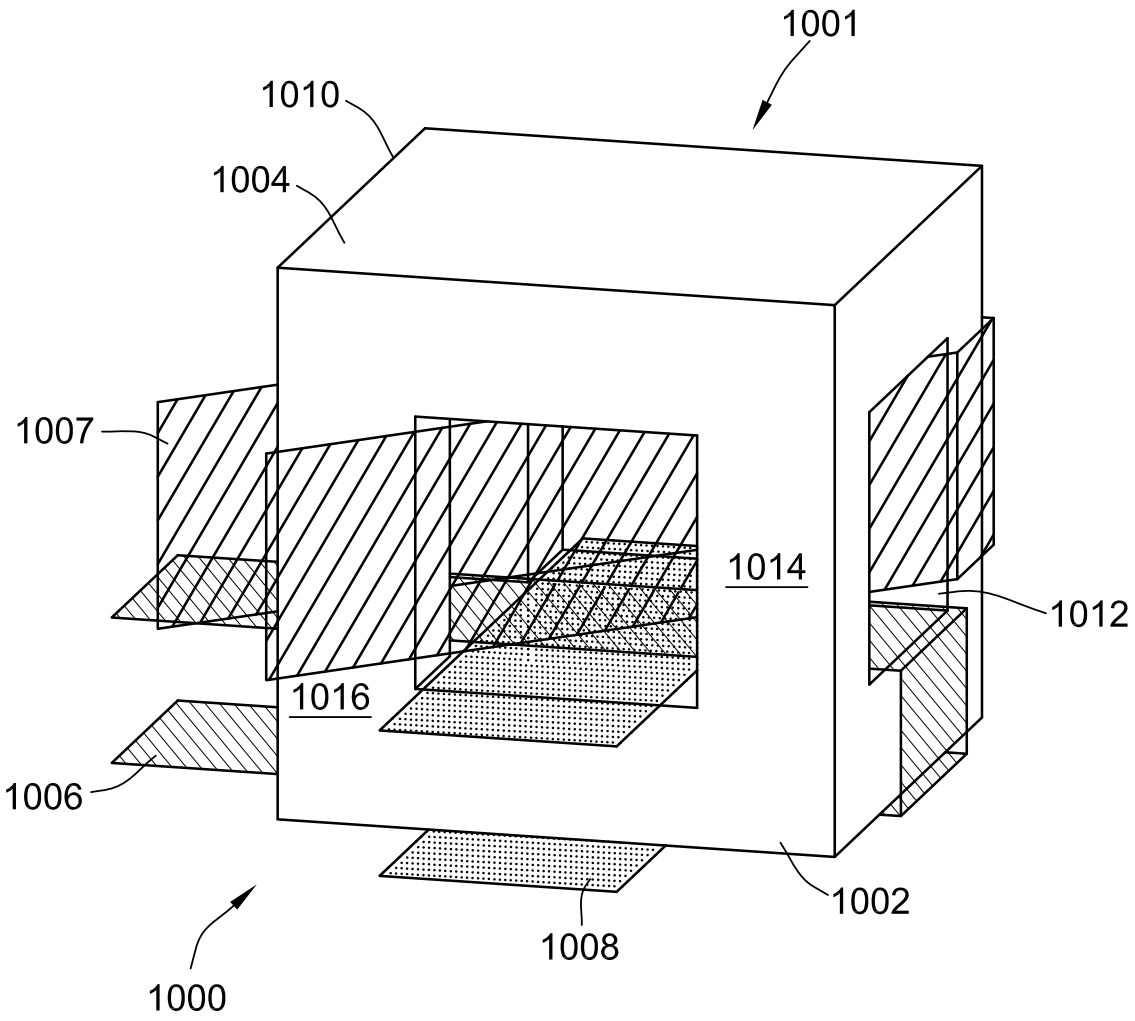

FIG. 10

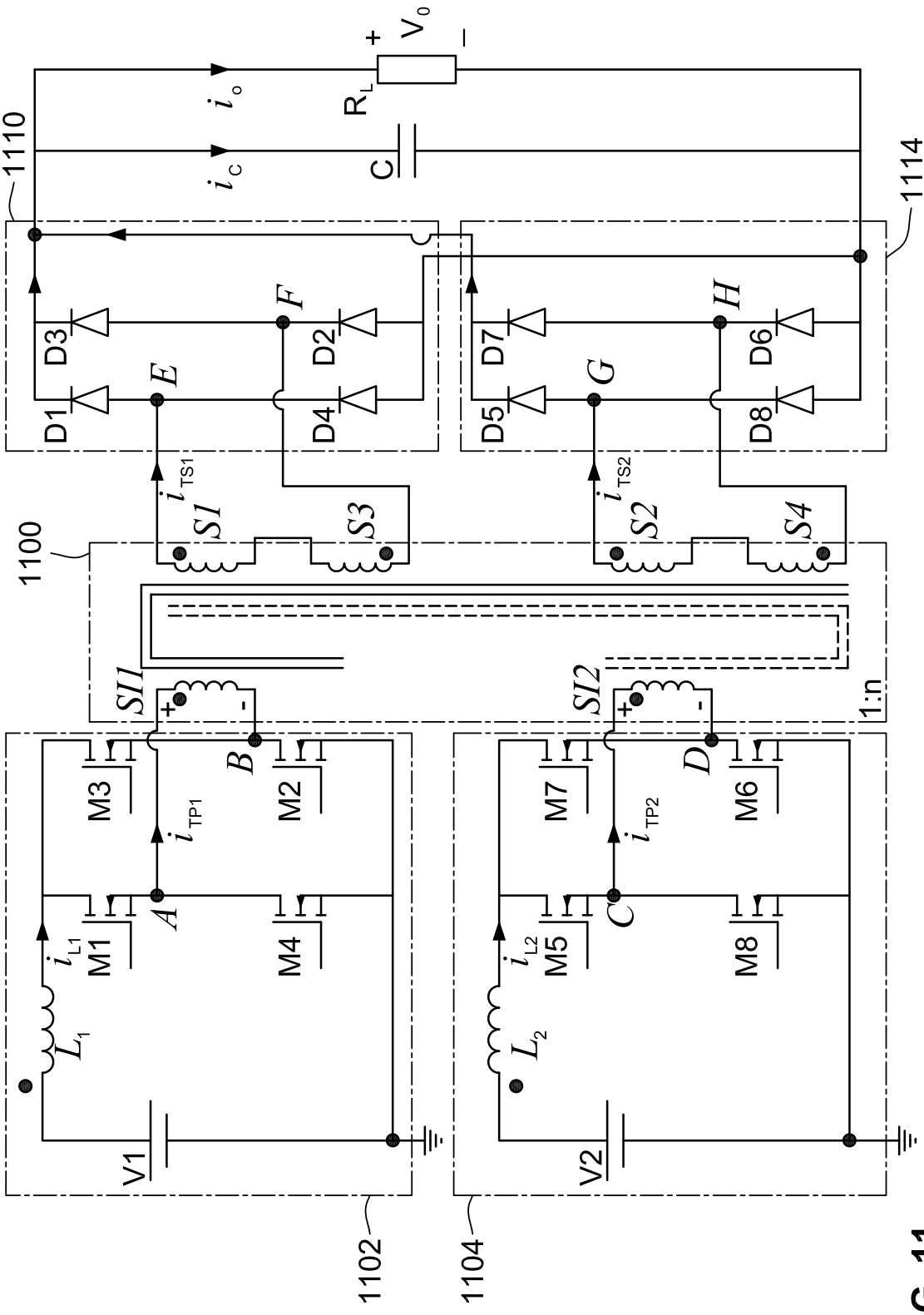
1110
1114
1100
1102
1104
i_o
i_C
R_L
C
V_0
+
–
D1
D2
D3
D4
D5
D6
D7
D8
E
F
G
H
i_{TS1}
i_{TS2}
S1
S2
S3
S4
SI1
SI2
1:n
A
B
C
D
i_{TP1}
i_{TP2}
M1
M2
M3
M4
M5
M6
M7
M8
i_{L1}
i_{L2}
L_1
L_2
V1
V2

FIG. 11

FIG. 12a)

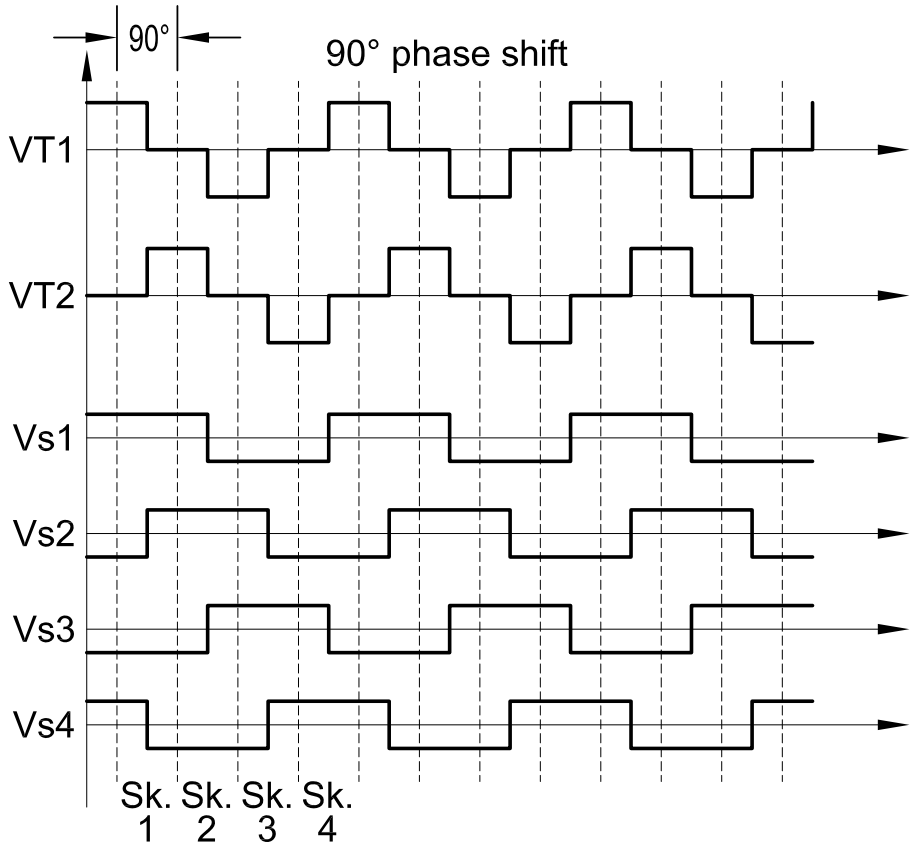

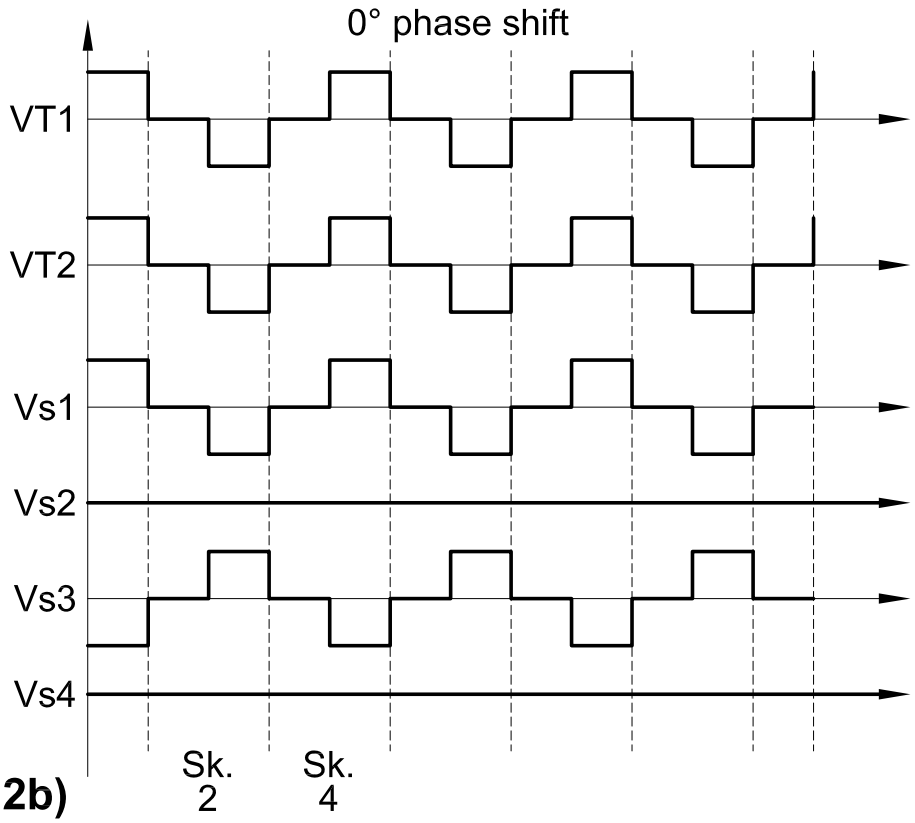

FIG. 12b)

FIG. 13a)

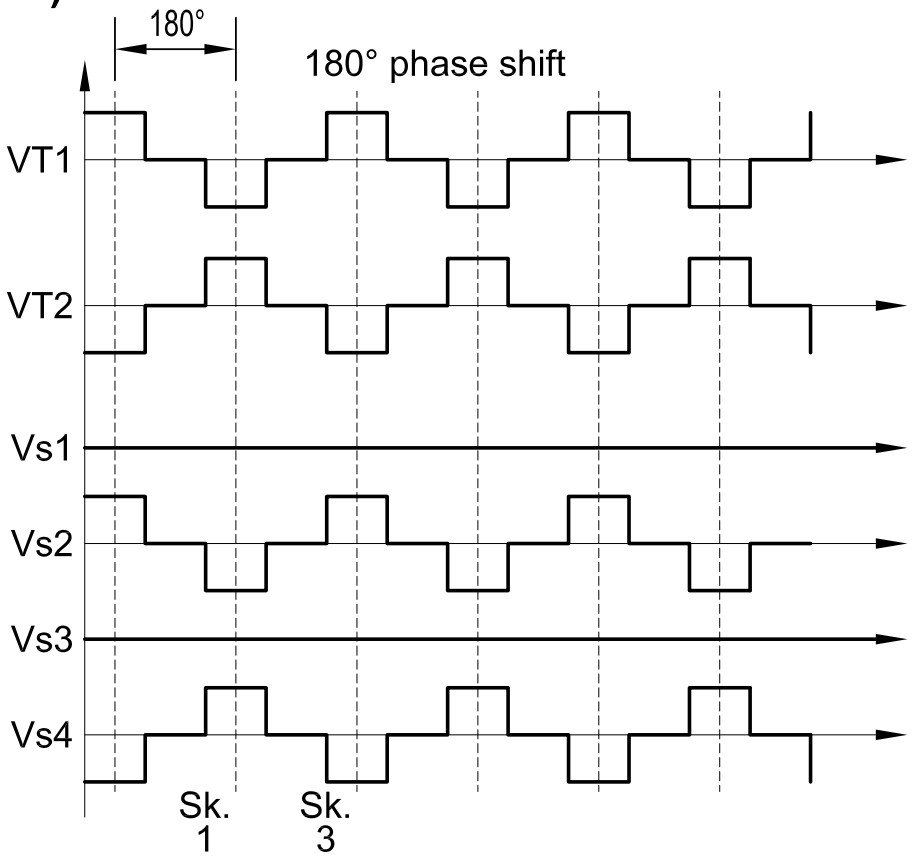

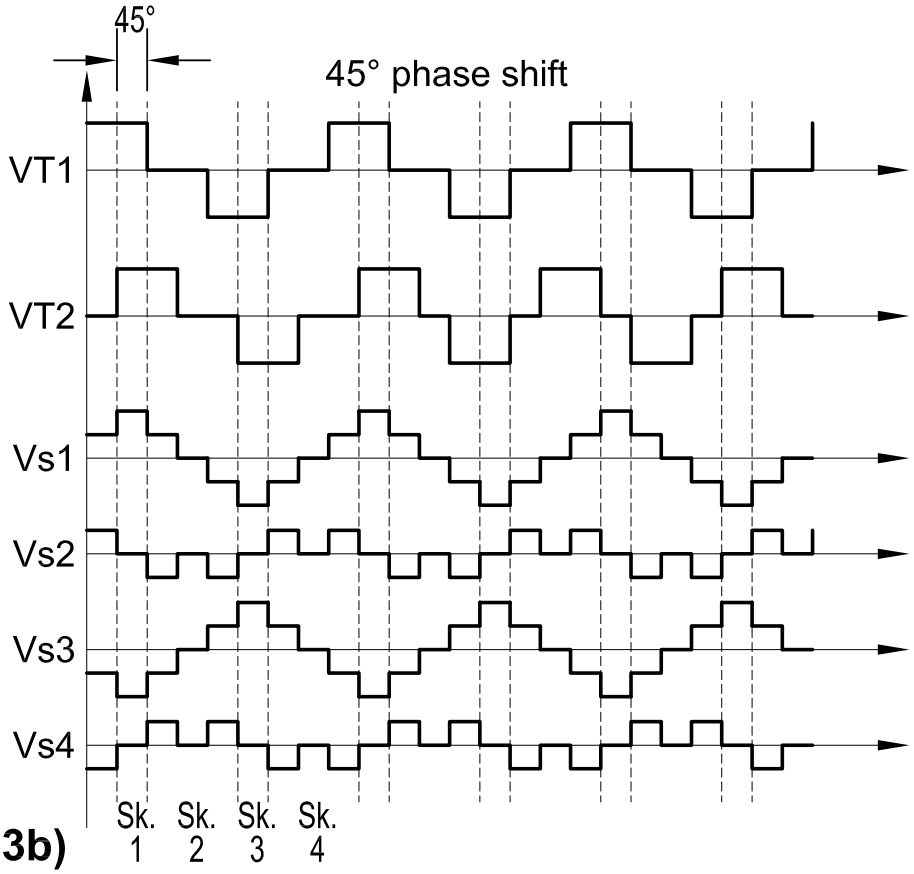

FIG. 13b)

www.elektro.dtu.dk
Department of Electrical Engineering
Electronics Group
Technical University of Denmark
Ørsteds Plads
Building 348
DK-2800 Kgs. Lyngby
Denmark
Tel: (+45) 45 25 38 00
Fax:(+45) 45 93 16 34
Email: info@elektro.dtu.dk

ISBN: 978-87-92465-88-7